



**School Of Mechanical, Materials and Manufacturing Engineering**

***The Energy Absorption of Damaged Braided and  
Non-Crimp Fibre Composite Material Structures***

**Kristofer John Bottome**

*M.Eng(Hons)*

Thesis submitted to the University of Nottingham for the degree of Doctor of  
Philosophy – April 2005

# Contents

**Abstract** vi  
**Acknowledgements** vii  
**Glossary** viii  
**Nomenclature** x

**1.0 Introduction** ..... 1

**2.0 Literature Review**..... 9

**2.1. Energy Absorption**..... 9

**2.2. Modes of Failure of Composite Tubes** ..... 11

**2.3. Engineered Fabrics** ..... 14

2.3.1. Non Crimp Fabric (NCF)..... 14

2.3.2. Braided Fabrics ..... 18

2.3.2.1. Properties of Braided Composites ..... 19

2.3.2.2. Energy Absorption and Failure Mode..... 23

**2.4. Predictive Techniques for Calculating SEA** ..... 25

2.4.1. Energy Absorption Calculation..... 25

2.4.2. Interlaminar Shear Strength ..... 27

**2.5. Induced Damage**..... 33

2.5.1. Holes and Stress Concentrations..... 33

2.5.2. Impact Damage ..... 40

2.5.2.1. Impact Damage Detection..... 42

2.5.2.2. Fracture and Crack Growth..... 43

2.5.2.3. Compression After Impact (CAI) Strength..... 45

2.5.2.4.	Improving Impact Resistance .....	46
<b>2.6.</b>	<b>Strain Rate Effects .....</b>	<b>48</b>
<b>2.7.</b>	<b>Applications .....</b>	<b>50</b>
<b>2.8.</b>	<b>Summary of Literature Review .....</b>	<b>53</b>
<b>3.0</b>	<b>Experimental Methods .....</b>	<b>55</b>
<b>3.1.</b>	<b>Experimental Conditions.....</b>	<b>55</b>
<b>3.2.</b>	<b>Materials .....</b>	<b>55</b>
3.2.1.	Reinforcements .....	56
3.2.2.	Matrix.....	56
<b>3.3.</b>	<b>Specimen Geometry .....</b>	<b>57</b>
<b>3.4.</b>	<b>Manufacturing.....</b>	<b>58</b>
3.4.1.	Fibre Volume Fraction .....	59
3.4.2.	Preforming of NCF Fabric Tubes .....	61
3.4.3.	Manufacture of Braided Preforms .....	62
3.4.4.	Moulding.....	66
<b>3.5.</b>	<b>Sample Preparation .....</b>	<b>67</b>
<b>3.6.</b>	<b>Test Methods .....</b>	<b>69</b>
3.6.1.	Quasi-Static Tube Crush .....	69
3.6.2.	Dynamic Tube Crush .....	71
3.6.3.	Ultimate Compressive Strength (UCS).....	73
3.6.4.	Interlaminar Shear Stress Testing .....	74
3.6.5.	Stress Concentration Factors (SCF).....	77
3.6.6.	Test Matrix.....	79

<b>3.7. Post Test Procedures.....</b>	<b>80</b>
3.7.1. Microscopy of Crush zone .....	80
3.7.2. Validation of Braided Carbon Samples .....	81
<b>4.0 Results .....</b>	<b>82</b>
<b>4.1. Carbon tubes .....</b>	<b>83</b>
4.1.1. Resin Comparison with Biaxial Tubes .....	83
4.1.2. Braid Type. ....	86
4.1.2.1. Triaxial Tubes .....	86
4.1.2.2. Biaxial and Inter-ply .....	89
4.1.2.3. Triaxial with Inter-ply.....	91
4.1.3. Braid Angle.....	93
4.1.4. Damage Analysis .....	96
<b>4.2. Glass Tubes.....</b>	<b>101</b>
4.2.1. Sample Classification.....	103
4.2.2. Architecture and Rate Effects .....	104
4.2.3. Higher Rate Effects.....	110
4.2.4. Resin Comparison.....	112
4.2.5. Micrographs. ....	114
4.2.6. Ultimate Compressive Stress .....	135
4.2.7. Stress Concentrations.....	138
4.2.7.1. Holes .....	138
4.2.7.1.1. Initial testing .....	138
4.2.7.1.2. Holes at 25mm from Chamfer .....	142
4.2.7.2. Failure Stress Comparison .....	151
4.2.7.3. Experimental Determination of Stress Concentration Factors.....	156
4.2.8. Impact Damage .....	164
4.2.8.1. Impact Damage at 45mm from Chamfer .....	164
4.2.8.2. Impact Damage at 30mm from Chamfer .....	168
4.2.9. Compression After Impact Strength (CAI).....	181
4.2.10. Interlaminar Shear Strength .....	188

4.2.11. Interleaf .....	191
<b>5.0 Conclusions .....</b>	<b>197</b>
<b>6.0 References .....</b>	<b>204</b>
<b>Appendix .....</b>	<b>213</b>
<b>Appendix 1: Braided Composite Manufacturing.....</b>	<b>213</b>
<b>Appendix 2: Predicted In-Plane Axial and Transverse Tensile Stiffness of <math>\pm 45^\circ</math>     Braided Carbon/Vinyl Ester Using Rule of Mixtures and Laminate Theory.....</b>	<b>215</b>
<b>6.1. Theoretical Work – Stress Concentrations.....</b>	<b>220</b>

## Abstract

The effects of pre-existing damage on the mode of failure and energy absorption characteristics of Non-Crimp Fabric (NCF) and biaxially braided tubular sections under axial loading were considered. Loading rate effects were incorporated by testing at quasi-static rates and impact rates up to  $7\text{ms}^{-1}$  and the pre-existing damage was simulated through stress concentrations and out-of-plane impact damage. Circular and square geometries were tested, and a range of NCF and braided fibre architectures were investigated.

A number of failure modes were exhibited. NCF tubes were seen to splay at static and impact rates; at impact rates a reduction in Specific Energy Absorption (SEA) was recorded. Braided tubes failed in a combination of buckling and splaying at static rates. Under dynamic conditions all braided samples splayed and where a change in failure mode was seen, SEA was increased. Both NCF and biaxially braided tubes have been shown to offer a much lower SEA than Continuous Filament Random Mat (CoFRM) samples.

A threshold size of damage was observed, where, typically, below that threshold the SEA was unaffected by the damage, and above that size the tube would fail globally. The NCF tubes exhibited an improved damage tolerance over CoFRM and braided samples. The braided tubes showed a poor damage tolerance at quasi-static rates although results suggest that the architectures with high axial fibre content will have a higher damage tolerance.

It has been shown that modelling damaged areas of tubes as a cut-out is a conservative approach to finding failure levels. Peak stress was seen to be the dominant factor in determining loading at global failure as samples could fail even though the crushing stress is less than the failure stress. Previous work upon Interlaminar Shear Strength (ILSS) and SEA has been investigated and shown to overestimate energy absorption for tubular specimens and found to apply only to samples that fail by progressive crush or fragmentation; for those that do fail in this mode a link between ILSS and SEA has been stated.

A technique for determining SEA and for predicting the effect of a SCF on failure mode of composite tubes has been proposed using UCS (Ultimate Compressive Strength) data and SCF (Stress Concentration Factor) data.

## **Acknowledgements**

The Author would like to thank the following:

Dr N.A. Warrior for his assistance and supervision throughout the research period,

The Automotive Composites Consortium (ACC) of the United States Council for Automotive Research (USCAR) the Engineering and Physical Sciences Research Council (EPSRC) and the University of Nottingham who provided funding for this programme,

R.A Jeryan, A.G.Caliskan, and other members of the Energy Management group of the ACC for their technical contributions,

The EPSRC for use of the Kodak HS4540 high speed camera loaned from their instrument pool,

The School of Mechanical, Materials and Manufacturing (M3) for use of their facilities,

Members of the University of Nottingham Composites Group, in particular Mike Ribeaux. Thomas Turner, Richard Fernie, Lee Harper, Graham Aitchison for their assistance,

The technical staff at the University of Nottingham, Roger Smith, Dave Smith, Paul Johns and Geoff Tomlinson for all their help and support,

Dr J.M Barton, Trystan Emery and Eric Roszkowiak of the University of Southampton for their guidance and assistance with the thermal imaging study,

Finally, my family and friends for their ongoing support, encouragement and words of confidence throughout my time at the University of Nottingham.

## Glossary

ACC	Automotive Composites Consortium
Binder	Cohesive substance used for ensuring fibres in a reinforcement preform remain ordered
BS	British Standard
CAI	Compression After Impact
CoFRM	Continuous Filament Random Mat
CRP	Carbon Reinforced Plastics
CSM	Chopped Strand Mat
Curing	Process of polymerization of the resin changing it from liquid to solid
DCB	Double Cantilever Beam test
E-glass	Electrical glass, most common type of glass used in reinforcements
ESEM	Environmental Scanning Electron Microscope
FRP	Fibre Reinforced Plastic
Filament	Single Fibre
GRP	Glass Reinforced Plastics
IFW	Instrumented Falling Weight
ILSS	Interlaminar Shear Stress
Initiator	Also known as Trigger, external or integrated feature to induce progressive crush in a specimen
Isotropic	A material having uniform properties in every direction
Load Cell	In this study a piezoelectric element that compresses and produces an electrical signal under load
Preform	Arrangement of fibres shaped to fit the mould cavity

Quasi-static	Tests undertaken at a low rate to approximate the static behavior of a sample
Reinforcement	Fibres used to provide the strength in a composite
RTM	Resin Transfer Moulding
SEA	Specific Energy Absorption
SRIM	Structural Reaction Injection Moulding
SSCS	Steady State Crushing Stress
Stress Concentration	A geometric feature providing a stress raiser in a structure e.g. a hole
SCF	Stress Concentration Factor (also defined as $K_c$ )
Stress Whitening	The area of damaged composite around the impact point, also referred to as damage zone
Thermoplastic	A polymeric material softened by the action of heat and hardened by cooling in a reversible process
Thermoset	A polymeric material hardened by an irreversible chemical reaction
Tow	A group of filaments bunched together
UCS	Ultimate Compressive Strength
Warp	The direction along the roll of reinforcement material
Weft	The direction across a roll of material
Wet-out	Contact between fibre surface and matrix after polymerisation.

## Nomenclature

		S.I.Units
$a$	Acceleration	$\text{ms}^{-2}$
$a$	Characteristic length	m
$A$	Cross-sectional Area	$\text{m}^2$
$C$	Mean circumference of shell (p25)	
$d$	Diameter of hole	m
$D$	Diameter of tube	m
$E$	Elastic or Young's modulus	Pa
$E_s$	Specific Energy Absorption	$\text{kJ.kg}^{-1}$
$E_{x \text{ or } y}$	Elastic or Young's modulus in x or y directions	Pa
$F$	Force	N
$G$	Fracture toughness	
$G_{yx}$	In-plane shear modulus in y-x plane	GPa
$g$	Acceleration due to gravity	$\text{ms}^{-2}$
$K_T$	Stress Concentration Factor	
$K_c$	Fracture Toughness	
$L$	Length	m
$m$	Mass	kg
$OD$	Outer Diameter	m
$P_{max}$	Maximum stable crushing force	N
$R$	Inner radius of tube	mm
$R_{ad}$	Adhesive energy per unit area of layers	kJ
$r \text{ or } a$	radius of hole	m
$s$	Crush distance (p25)	m

$s_1$	related shell shortening corresponding with formation of centre intra-wall crack	
$s_2$	relative shell shortening corresponding to completion of wedge formation	
$t$	Tube wall thickness	m
$V$	Speed	$\text{ms}^{-1}$
$V_f$	Volume Fraction (Fibre)	
$\nu$	Poisson's ratio	
$W$	Width of square tube	m
$W$	Energy absorbed (p25)	J
$\varepsilon$	Strain	
$\sigma$	Stress	Pa
$\sigma_\theta$	Tensile fracture stress	MPa
$\sigma_c$	Critical Stress	MPa
$\sigma_c$	Crush Stress (p156)	MPa
$\sigma_{f \text{ or } 0}$	Failure Stress	MPa
$\sigma_p$	Peak Stress	MPa
$\theta$	Fibre Angle	
$\rho$	Density	$\text{kgm}^{-3}$
$\mu_{S1}$	Friction coefficient between platen and fronds	
$\mu_{S2}$	Friction coefficient between wedge and fronds	
$\tau$	Shear Stress	MPa
$\tau_{max}$	Max Shear Stress	MPa

## 1.0 Introduction

Composite materials are typically constructed from high modulus fibre reinforcement in a brittle matrix, which as a composite structure will display significantly improved properties over the individual constituents. It is the fibres, in the reinforcement architecture, that provide the main load bearing component and these can be arranged in many ways. Random fabrics such as Compound Filament Random Mat (CoFRM) or Chopped Strand Mat (CSM) offer low cost and a degree of in plane isotropy, whilst unidirectional fabrics offer high in-plane strengths and are useful for applications where the direction of the load is known. For example, by manufacturing a tube with the fibres woven into a 45° angle, the torsional stiffness will be greatly improved due to the fibres lying along the load path.

Typically, composites have been of the carbon/epoxy type and have shown major advances over metallic materials due to high specific strengths. The increased use of composites has, however, been hindered by the high cost associated with the labour intensive manufacturing process and the cost of the raw materials themselves. Initially, random fabrics gained popularity but recently the drive for improved properties and reduced cost has led to further research into braided and Non-Crimp Fabrics (NCF). These offer potential for net-shaped preforms, reduced manufacture times and a reduction in labour cost.

The automotive sector has been a major influence in the development of cost effective composites in recent years. The need for increased fuel efficiency, coupled with decreased weight and increasing safety requirements, has led to composites being considered for energy absorbing structural components in transport applications. The prohibitive cost of the traditional aerospace composites has restricted use to the high performance automotive field but it is hoped that the newer cheaper manufacturing methods will increase composites use and allow optimised designs to be created in complex shapes.

A structures ability to absorb impact energy efficiently whilst allowing the occupant to survive is known as crashworthiness, which is increasingly important in automotive design and manufacture. Tests such as the Euro NCAP [1] bring safety and survivability into the public perception and are increasingly becoming criteria for differentiating one car over another. The established means of comparing suitability of structures and composites for

crashworthiness applications is through the specific energy absorption (SEA) of the structure. The SEA is measured in kJ/kg and defines how much energy is absorbed per kg of material and is a useful tool in comparing how different materials perform. For a typical sample the energy absorbed by the element is the area under the load deflection curve (Figure 1, Figure 2). If the mass of the crushed length is known, then the SEA can be simply calculated by dividing the energy absorbed by the crushed mass.

In a typical car, the primary energy absorber is the bumper. This absorbs the energy of the low speed, small energy impacts, typically from a parking incident. At higher speeds, it is the job of a specific structure, the crumple zone, to absorb the energy of the impact whilst ensuring the occupants survive through preserving the passenger cell integrity and reducing the deceleration forces felt by the occupant.

The motivating factor for application of these materials is safety. The Euro NCAP test (mentioned earlier) is undertaken at a speed of 40mph ( $17.78\text{ms}^{-1}$ ). The frontal impact is offset so effectively only half of a car's frontal structure will absorb the energy. A typical family car may have a mass of 1300kg equating to approximately 205kJ needed to be absorbed in an impact. For a structure with a higher SEA, the equivalent mass will be smaller than a structure with a lower SEA to absorb the same level of energy. Reducing mass is beneficial in improving performance and fuel economy but also reduces the amount of energy needed to be absorbed in an impact; a 100kg reduction in mass reduces the energy absorption requirement by 15.8kJ.

Composites have the potential to absorb significantly higher amounts of energy than metallic elements through the crushing failure mode. Traditionally, metals are used in crashworthiness applications; they absorb energy by plastic deformation through progressive folding (Figure 1) which leads to high levels of deceleration felt by the occupants. Farley [2] describes metal tubes as being able to crush only to 50% of their original length due to the folding mode before bottoming out and the load increasing sharply, whereas Jones[3] describes stroke efficiency (crush length before bottoming out, the point at which the load increases rapidly) for steel tubes to be in the region of 75%. For CoFRM materials the stroke efficiency has been reported to be over 80% [4]. Typical values of SEA for metallic structures are  $45\text{kJ}\cdot\text{kg}^{-1}$  for steel and  $60\text{kJ}\cdot\text{kg}^{-1}$  for aluminium alloys [5].

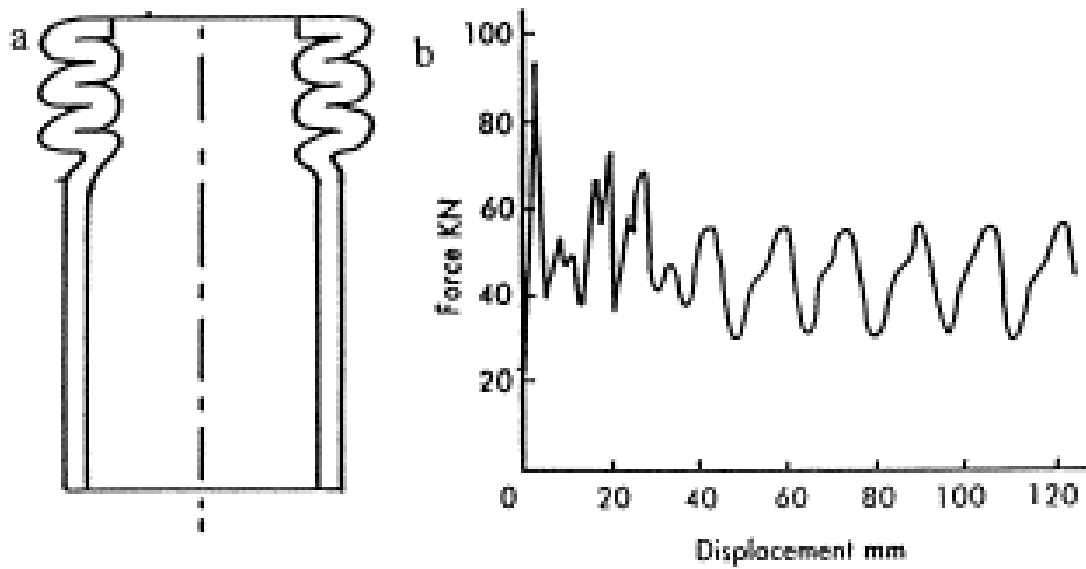


**Figure 1 Progressive failure of axially compressed metal tube and its force displacement curve[6]**

In an ideal energy absorber the load will rise steadily till it reaches a maximum crushing load. The absorber will then continue to absorb energy at this level until all the energy of the impact has been dissipated. The constant load and hence constant deceleration are tailored to be the minimum possible to reduce damaging deceleration effects on the occupant.

Composites can fail in a similar manner to an ideal energy absorber; an initiator allows the load to rise steadily till it reaches the steady state crushing load. Due to their nature and mode of failure, composites have the potential to be able to crush for a greater proportion of their length before the material compacting causes the load to rise significantly (Figure 2).

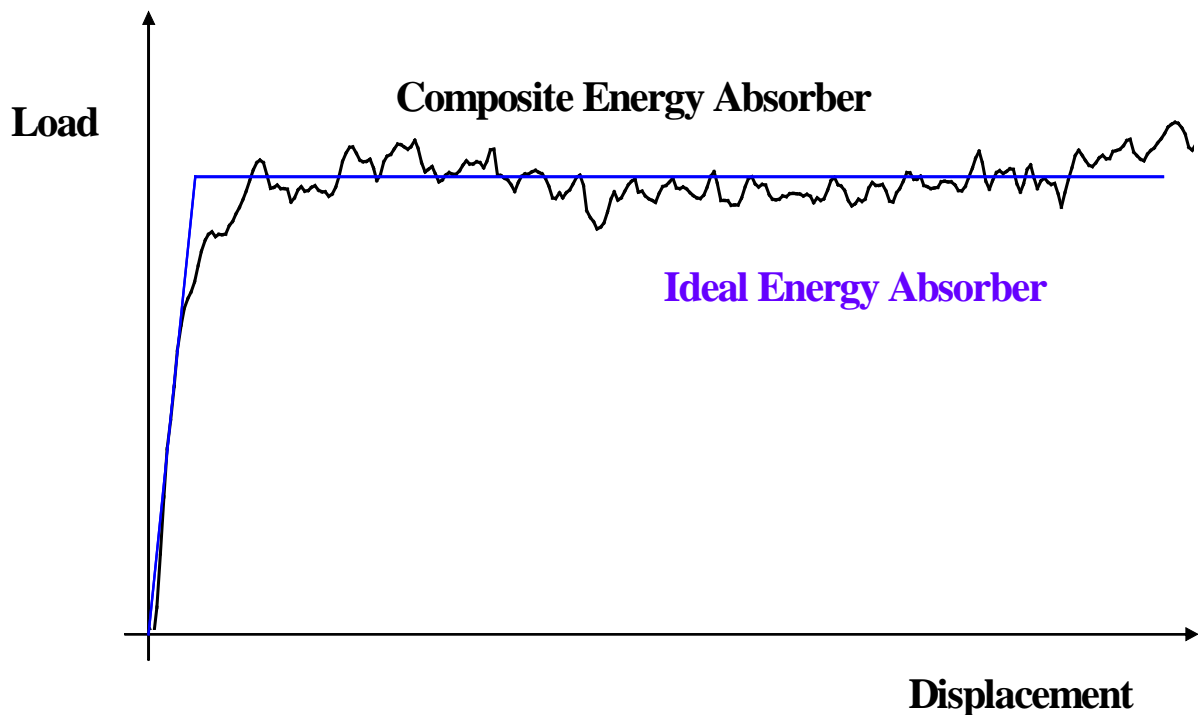


**Figure 2 Load Displacement Graph For Energy Absorbers**

Currently, there exists a large library of data regarding laminated composites in this application, however, there is a much smaller resource covering the properties of braided composites and other machine made fabrics, such as woven and Non Crimp Fabrics (NCF). Recently, there has been an effort to increase the understanding of the mechanical properties both statically and dynamically.

There are significant gaps in the knowledge of the effects of damage on composite specimens, in both braided and NCF fabrics. The effects of geometry and lay-up are not fully understood. If these types of fabrics are to be considered for practical energy absorbers, due to the possibilities offered in reducing cost and improving mechanical properties over traditional composites, then further investigation is required.

Ribeaux[7] investigated the effects of stress concentrations and damage upon CoFRM tubes. Typically these were wound on a pre-forming machine in a spiral pattern (see Figure 3), which is an impractical method for manufacture of large composite structures. The inherently low in-plane properties make this type of material unsuitable for energy management properties.

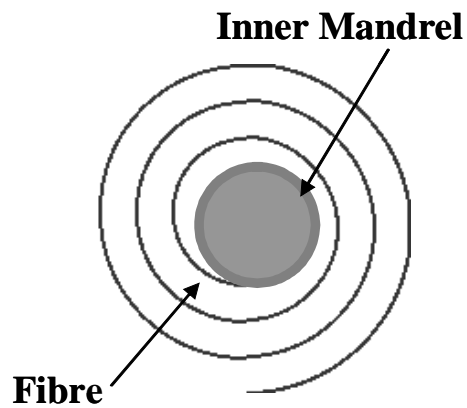


**Figure 3 Fibre Rolled in a Spiral Pattern**

NCF fabrics offer potential for use in energy management structures. In this study NCF tubes were manufactured in a similar way to the CoFRM tubes, with the fibre preformed around a mandrel. In high volume applications, NCF structures can easily be manufactured in a press and then joined to form the required shape (see Figure 4). Other suitable materials include biaxial and triaxial braids due to their high in-plane properties and method of manufacture.

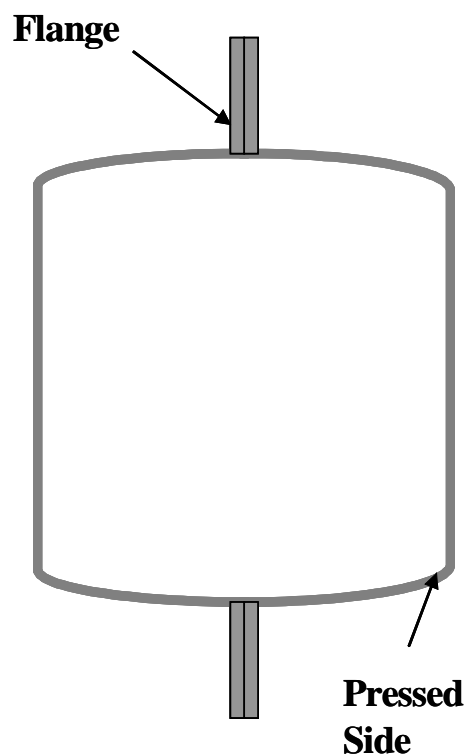


**Figure 4 Typical Press Manufactured Component**

The first aim of this work is to provide an understanding of the effects of non-service damage upon composite energy absorbers and to establish performance guidelines. Non-service damage refers to damage that occurs when the energy absorber is not used for its primary purpose. This could be a hole drilled in the tube wall to provide a fixing or locating point for another component, a stone chip thrown up from the road impacting with the energy absorber, or a mechanic dropping a tool onto the component. To represent stress concentrations in this study, a hole was drilled through the wall thickness of the tube perpendicular to the major axis of the tube. Non-service damage was replicated by impacting the side of the tubes with a hemispherical tup attached to a falling weight.

It has been well established in the literature, e.g. Hull [8], that changing any one variable (matrix, fibre, t/D ratio, rate etc) can affect the SEA significantly and that these variables are often independent of one another. This, therefore, required a large number of samples in order to assess the contribution of any one individual factor.

Large tubes were used to investigate the effect of the matrix and architecture upon the energy absorption of samples braided with cost effective automotive grade carbon fibre tows. The dimensions are described later. These large tubes have previously been shown to be impractical for dynamic testing [7] so smaller diameter tubes were manufactured in order to test at dynamic rates (i.e. test rates  $1\text{ms}^{-1}$  and above). With the corresponding reduction in size of tube, the tow size of the braided fibre needed to be reduced in order to ensure wet-out and correct sizing. One of the aims is to test cost effective solutions so glass/polyester tubes were used. In order to examine the effects of geometry, square samples were manufactured with NCF.

The specimens tested in this project were crushed between two parallel ground steel crush platens. A 45° bevel chamfer was machined onto the samples to act as an initiator to induce progressive crush (see Figure 5 for illustration). Without any initiator the samples would fail globally by compressive shear, rendering them useless for energy absorption purposes. Under axial compression, the sample will crush the length of the chamfer. The load will steadily increase until a peak load is reached and then reduce slightly to a steady state load. From this steady state load, the Steady State Crushing Stress (SSCS) can be calculated. A similar process is observed for both quasi-static ( $0 \text{ ms}^{-1}$ ) and dynamic ( $5\text{ms}^{-1}$ ) test rates.

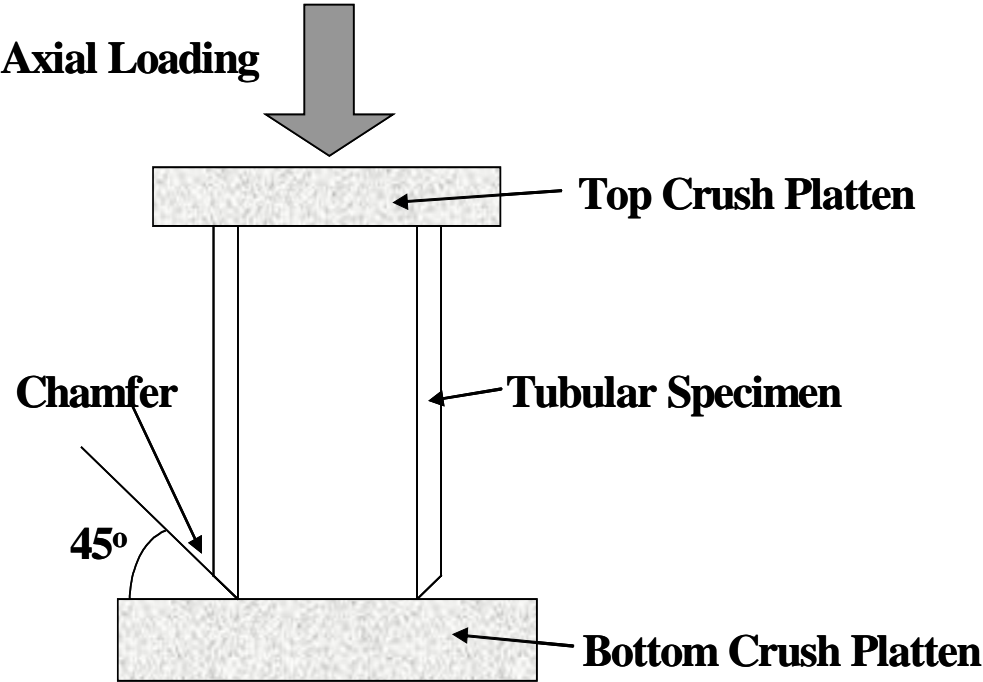


**Figure 5 Schematic of Test Sample**

The tube will continue to crush progressively unless a stress raiser is present (in this study a hole or area of impact damage) and these can cause local buckling or fast fracture (global collapse) to occur (see Figure 6).

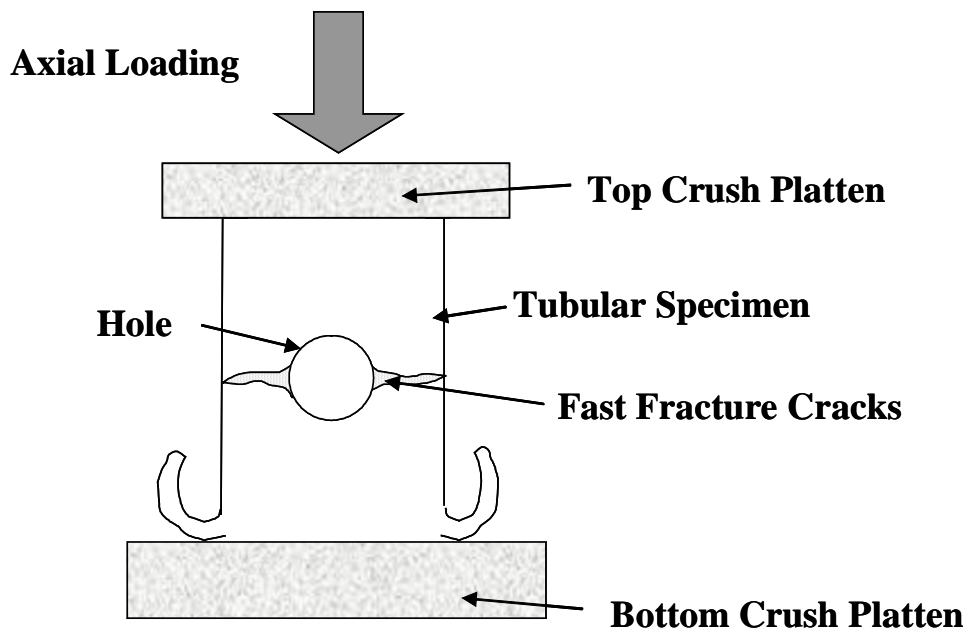


**Figure 6 Specimen Showing Global (Fast Fracture) Failure**

In order to predict whether a sample will fail analytical methods have been investigated. Ribeaux [7] investigated Ultimate Compressive Strength (UCS) and noted that samples that failed globally appeared to crush at a greater percentage of the UCS. Here this study is extended to compare the failure stress associated with global failure and the peak stress of the samples.

Daniel et al [9] have linked Inter Laminar Shear Strength (ILSS) to SEA and suggest that this is a key parameter in determining SEA. In this study ILSS was measured for tubular specimens and compared to the SEA level to assess the validity of their conclusions. SEA is important because from this value, the crushing stress can be calculated, if information about the mass of the tube is available.

Methods for determining the Stress Concentration factor around the hole have been investigated and evaluated in comparison to the experimental results. A comparison of impact damage and hole size has been undertaken.

This work aims to provide a clearer understanding of when structures will fail and if this can be predicted using simple analytical methods.

## 2.0 Literature Review

The key parameter for an impact or crashworthiness structure is energy absorption level. This is used as the yardstick by which structures and materials are compared and is known as the Specific Energy Absorption.

### 2.1. Energy Absorption

A typical ideal energy absorber, described by Harte et al[10], has a long flat load deflection curve where the absorber crushes plastically at a constant force.(Figure 7) Tubes, shells and honeycombs provide a failure mode satisfying this.

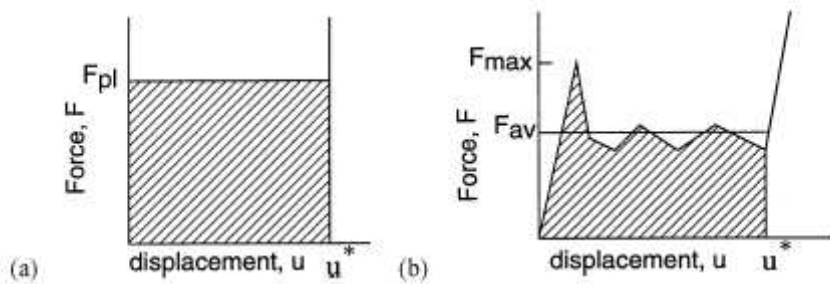


**Figure 7: a) An ideal energy absorber, b) Typical force deflection curve of practical energy absorber. [10]**

Where  $F_{pl}$  = plateau force,  $F_{max}$  = peak collapse force,  $F_{av}$  = average crush force

Mamalis[11] amongst others [12] have investigated energy absorption in glass fibre/vinyl-ester hour-glass shaped tubular specimens and noted that mean post-crushing load and energy absorbed are mainly affected by the crushing length (the length/displacement the specimens crush over. see displacement  $u$ , Figure 7), whilst the axial length of the shell has no significant effect on these crashworthiness characteristics. Their observations suggest that the contribution of frictional conditions between wedge/fronds and fronds/platen contribute to the energy absorption capability of the structure.

Mamalis et al [13] also describes the 3 distinct stages of the ideal deformation pattern;

- Stage 1, initially the specimen behaves elastically and the load rises to a peak value then falls abruptly. At this stage, an intra-wall crack is formed at the end of the shell adjacent to the loading area.
- Stage 2, the load increases with increasing deflection associated with the formation of lamina bundles bending inwards and outwards. A triangular debris wedge is formed due to the friction between bent bundles and the platen. The wedge formation is complete when the load starts oscillating.
- Stage 3, stable crush with the formation of inward and outward fronds which spread radially in the form of a mushrooming failure. The external fronds develop axial splits due to the developed tension. Axial fibres bend inwards or outwards without fracturing whilst fibres aligned in the hoop direction can only expand outwards by fracturing and inwards by fracturing or buckling. Delamination occurs as a result of shear and tensile separation between plies.

Another contributing factor to energy absorption is friction. Laananen and Bolukbasi[14], in looking at the energy absorption of composites stiffeners, noted up to a 50% increase in energy absorption capability when the specimens crush on a rough, rather than a smooth surface. However, much of their work was undertaken on analysis of flat plate specimens, though their work with angled sections and channels showed they crushed in a similar mode to the flat plate specimens. Others [15, 16] have also investigated the effect of surface roughness on the platen and noted that friction can account for more than half the energy absorption capability of the structure.

## 2.2. Modes of Failure of Composite Tubes

Composites are inherently brittle and show little plastic deformation. The elastic energy, which is stored before the fracture, becomes the surface energy of the fractured parts and kinetic energy of the fractured parts. Fragmentation of the material, fibre breakage, matrix breakage interfacial debonding, delamination and crack nucleation and growth are all involved during a collapse of a component, causing a complex problem for describing the material behaviour [17-22].

Three modes of crushing failure for composites have been identified in the literature. Mamalis et al [11] define these as;

- Mode I, Progressive crushing with micro-fragmentation of the composite material, associated with a large amount of crush energy
- Mode II, Brittle fracture of the component, resulting in catastrophic failure with little energy absorption
- Mode III, Progressive folding and hinges formed similar to the crushing behaviour of thin-walled metal and plastic tubes, showing a medium energy absorbing capacity.

In a later paper, Mamalis et al [19], define Mode II as local shell buckling and Mode III as Mid-length collapse, both being unstable failure modes. They suggest thinner tubes are likely to fail by local tube wall buckling. Delamination between the plies can occur, however this is often attributed to be due to micro structural defects of the composite material [23] and can be seen in many of the failure modes.

The progressive crush mode, mode I, features splaying initiated by an annular wedge of highly compacted and fragmented debris forced axially through the tube wall. This is referred to as the debris wedge and is formed during crushing of the trigger. During the crush, the debris wedge deflects delaminated strips from the wall outward in the form of fronds [15]. Hull [24] reported that the splaying mode is observed in structures containing a high percentage of axial fibres.

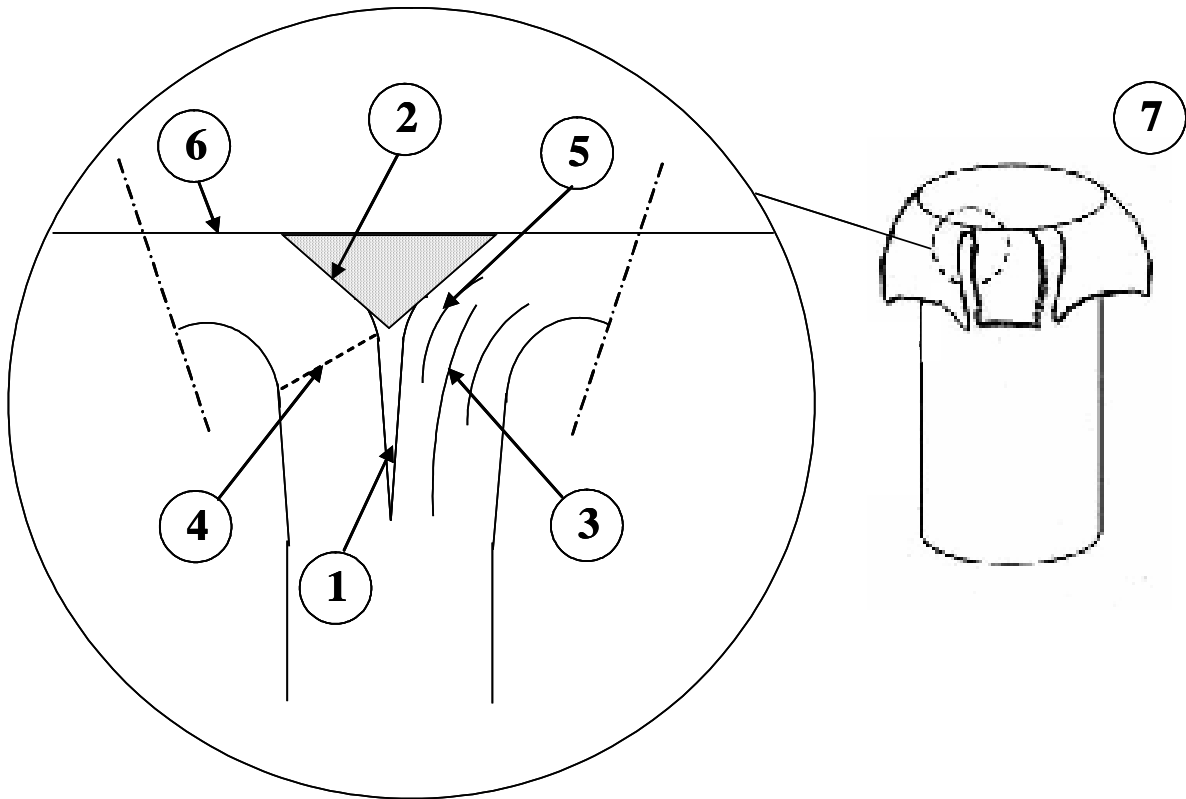


**Figure 8 Splaying Crush Mode Schematic (Redrawn from [24])**

Factors contributing to energy dissipation (see Figure 8) [24] include:

- 1 Propagation of mode I opening crack at the apex of the Debris Wedge
- 2 Frictional resistance to penetration of the debris wedge between internal and external fronds
- 3 Delamination in fronds deflected through a small radius of curvature by the debris wedge
- 4 Multiple transverse cracking through individual plies caused by flexural damage at the delamination
- 5 Frictional sliding resistance between adjacent plies
- 6 Frictional resistance between fronds and crush platen.
- 7 Propagation of axial splits between fronds. The spacing is governed by the initial external curvature of the tube
- 8 Multiple longitudinal cracking through the individual plies of the fronds facilitating transverse flattening. (Not shown on figure)
- 9 Fibre breakage (Not shown on figure)

Of these factors, five are fracture mechanisms and three are frictional processes. As mentioned in the previous section, it has been noted that frictional effects can account for 50% of the total energy absorption. Work undertaken by Berry [25] and Keal [26] found that these fracture mechanisms account for approximately 1/3 of the overall energy absorption of fibre glass and filament wound composite tubes. Farley [2, 27-29] has reported that, for the splaying mode of failure, the principle mode of energy absorption is through matrix crack growth.

Thornton [30, 31], Jimenez et al [32], Hull and Coppola [33, 34] and Cooper [35] have all looked at the effects of the geometry of the crush initiator upon tubes. An initiator is essential in promoting a stable crush mode of failure. Without an initiator (or trigger), the composite will fail globally through a fast fracture failure, thus it will not perform as an energy absorber. Types of initiator include integrated bevel tulip and notch triggers or external methods including plug/external ring initiators to force the tube to crush in a certain manner. These latter methods have been seen to significantly increase the energy absorption capability of the crushed tubes [36].

The buckling/folding failure mode associated with axially crushed metal tubes can also be seen observed in certain composite specimens. These are predominantly braided tubular specimens with shallow fibre angles or purely tubular specimens with purely axial fibres.

Work has been undertaken on the through thickness effects and Daniel et al [9] have noted that an important way of improving the energy absorption properties for of composites during crushing is to increase the inter-laminar and through-thickness strengths of the materials.

## **2.3. Engineered Fabrics**

Whilst work has been undertaken to reduce the manufacturing time of traditional carbon fibre composites, (e.g. Mills[37]) bigger improvements lie in the adoption of machine-manufactured, engineered fabrics. These textile based fabrics offer potential for reduced cost through savings in manufacturing costs. Increased automation of the lay-up process is possible, reducing the reliance on expensive hand labour. Potentially, engineered fabrics offer increases in interlaminar strength properties and delamination, although it is generally considered that a reduction in in-plane stiffness and strength properties occurs because of the undulation of the fibre paths [38].

### **2.3.1. Non Crimp Fabric (NCF)**

NCF fabrics are made from stitching layers of fibres together, typically, in two or more different directions (see Figure 9). NCF fabrics have the potential to improve damage resistance of laminates over traditional methods due to stitching, whilst offering benefits in reducing manufacturing costs as a result of the rapid lay-down of the material in comparison with prepreg composites [39]. Drapier and Wisnom [40] suggest that the cost reduction improvement in NCF fabrics comes from the easier handling and lay-up process and the use of cheaper tows. Bibo et al [39, 41, 42] compare the cost of prepreg laminates and NCF fabrics for a simple 300x600mm plate. They suggest that the labour cost can be cut in half and the total cost could be reduced by about 35% when materials costs are taken into account.

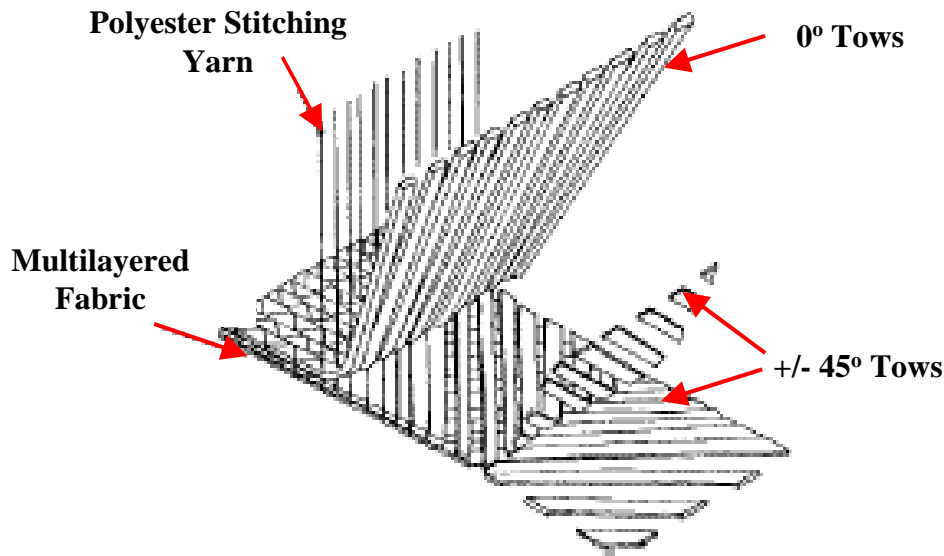


**Figure 9: Typical Non Crimp Fabric[40]**

Yang et al[43] investigated the stitching density. They observed that stitching density affected the bending behaviour; higher stitching density lowered the bending strength. Their results indicate that NCF laminates have a compressive strength of up to 15% higher than comparable sized woven composites, as a result of decreased waviness in the fibres. The stitching also been shown to improve the delamination resistance.

The stitching pattern and tension have been shown to affect the waviness of the fibre tows in the preform, (Leif et al[44]) and results imply that the strength and stiffness of the composite are insensitive to the stitch pattern for tensile and compressive loading.

Bibo et al[39, 41, 42] suggest that the primary strength reducing factor arising from impact damage is internal delamination fractures, at least during compression loading. However, surface damage does occur, with fibre volume fraction being the dominant factor controlling penetration impact. They also note that NCF laminates are relatively notch insensitive and laminates, with both small and large holes, exhibit similar net section compression strength.

The fracture mechanisms in NCF fabrics are shear/transverse and delamination fractures, influenced by the fabric architecture. The small changes in meso-structure create a complex

network of paths and tow-nestings providing crack bridges which may limit the propagation of fractures.

Lundström[45] and Drapier [46] have investigated permeability of NCF composites and suggest that neither the stacking sequence nor stitching pattern influence the transverse permeability, but it is the stitching density that has the largest influence – an important factor in the ability to produce consistent high quality composites, as this helps determine manufacturing conditions

The EU funded TECABS [47], (The Technologies for Carbon-fibre reinforced modular Automotive Body Structures) project looked at creating a cost effective automotive floor pan for large volume (~50 per day) production. 24k tows of carbon fibre were stitched into an NCF fabric. These were then preformed in a press to form the floor-pan preforms. The NCF preforms were assembled in an injection mould together with braided preforms and foam cores for the structural chassis rails and sills. The final floor pan was produced by injecting epoxy resin into the mould using a special high-speed low-cost resin-transfer moulding (RTM) process (see Figure 10).

This shows the benefits of both braided and NCF fabrics and how they combine in a structure. The results of this study can be applied directly to their work.

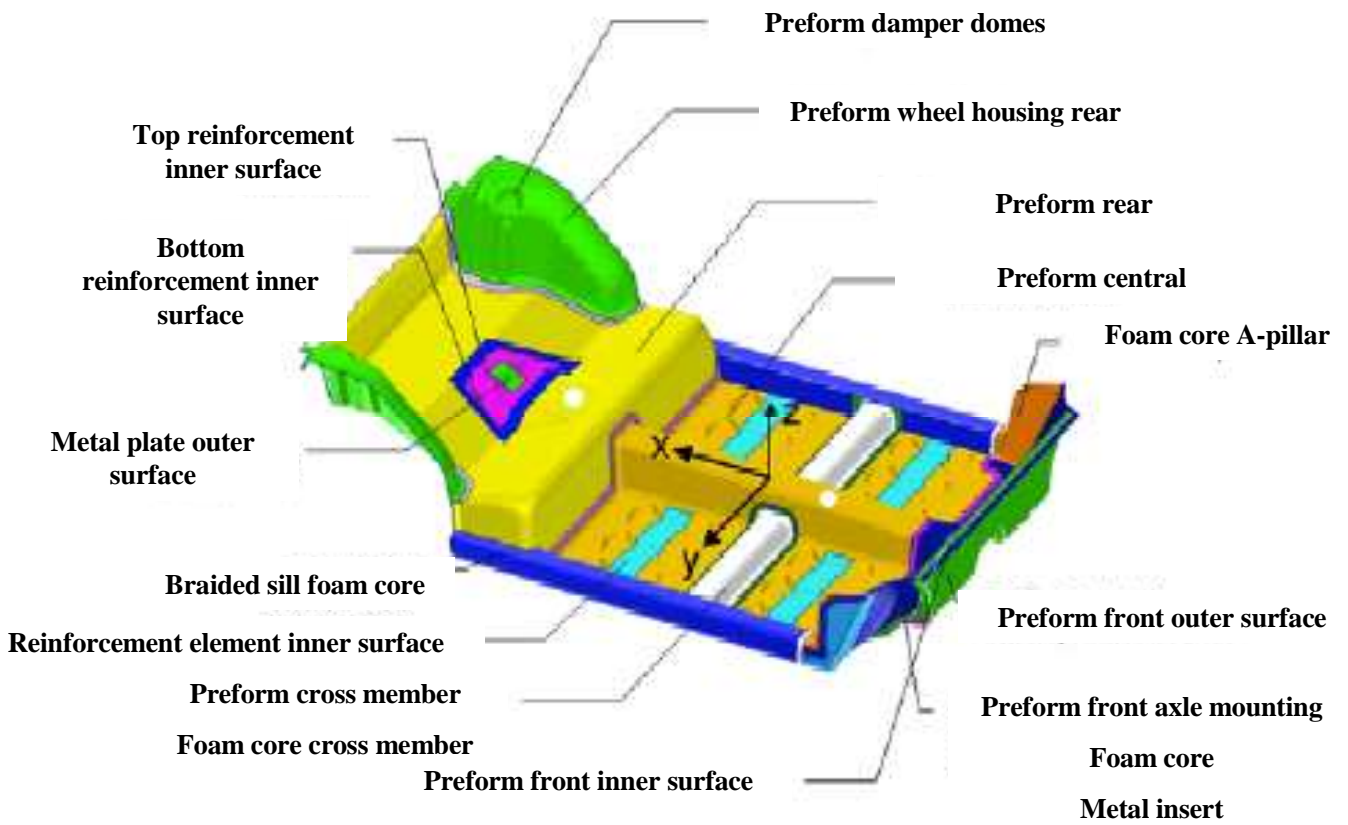
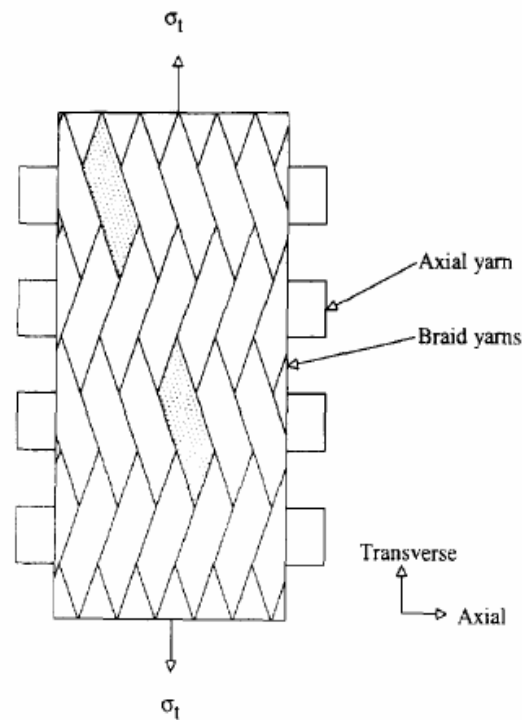


Figure 10 TECABS Floor plan [47]

### 2.3.2. Braided Fabrics

Braided composites are manufactured using a textile manufacturing technique. Bundles of fibres or tows are braided together using a machine to form biaxial or tri-axial braids. Biaxial braids only consist of the braid fibres, whereas tri-axial braids have the addition of interwoven axial tows.



**Figure 11 Tri-axial Braid Schematic Showing Axial and Braid Tows [38]**

The architecture of a tri-axial braid is illustrated in Figure 11 and described by Falzon et al [48]. It comprises of three interlaced tows, or yarns. Two sets of the tows are in the bias direction, known as the braider tows (which are braided in a 2x2 pattern). The third axial tow runs in the longitudinal direction and is interwoven between the other two braider tows. The orientation of the braider tow to the axial tow is known as the braid angle.

### 2.3.2.1. Properties of Braided Composites

The advantages of braided fabrics are stated by Mouritz et al [49, 50]. Braided preforms have higher levels of conformability, drapability, torsional stability and structural integrity, which makes it possible to produce composite structures with intricate geometries to near-net-shape. This can lower the manufacturing cost considerably because the amount of fabric handling and material scrap is reduced, as is the need for extensive machining and joining. Other people (e.g.[51]) have investigated manufacture of braided tubes with foam cores and have reported some success but this is an inconsistent process with poor and inconsistent sample quality.

Work by Swanson and Smith [38], on in-plane strength properties of  $\pm 45$  braided carbon/epoxy cylindrical specimens, describes 2-D braided composites as having lower strength in the axial direction fibres and significantly lower strengths in the braid direction fibres than laminar composites in tensile testing. They note that the axial strength of braids appears to be up to 30% lower than comparable laminates constructed from uni-directional fibres and only part of this was due to different volume fractions. The most significant strength loss occurs in the braid yarns where they were achieving a 60 – 70% drop in value. Depending upon the application this may be significant, although most structural elements carry loads in a singular direction.

Both results are echoed by the research of Falzon and Herzberg [48] who suggest that the reason for the loss of strength may be due to fibre damage in the braiding process and fibre waviness, although this does not affect Poisson's ratio (the reason being that this is a ratio between transverse strain and longitudinal strain, which cancels the influence of fibre damage and fibre waviness on each strain). In their tests, they found there was a reduction in tensile strength, due to damage in the braiding process, of up to 20%. In compression, they found similar results with a decrease in strength of up to 40% depending on the specimens used. The reason for this was attributed to a change in failure mechanism from micro buckling to kink band formation. This mode of failure occurs at lower load levels thus reducing the compressive strength of the samples.

In regards to Poisson's ratio, Sun and Qiao[52] noted that Poisson's ratio decreases with braid angle, and added that it increases non linearly with volume fraction. The addition of axial fibres increases tensile strength and tensile modulus. They based their analysis on an idealized unit cell of an assembly of unidirectional laminae with unique fibre orientations. Each lamina was treated as being transversely isotropic.

Neumeister et al [53] found that weaving can enhance longitudinal strength despite introducing higher fibre stresses and fibre defects. They discover that fibre strength is important because global failure is initiated from clusters of individual failed fibres, and failure is often associated with shear splitting from weak regions, flaws or defects. Importantly, the composite strength relies on the capacity of the structure to restrict growth of shear cracks linking weakened regions. In braided composites, the interweaving provides this structure, and they are geometrically uniform, showing less variation in mechanical properties than laminate materials.

Work on interlaminar fracture toughness by Mouritz et al[49] suggests that that this may be affected by fibre angle but that further work is required to establish a link.

Tang and Postle[54] introduce the concept of normalized pitch length (NPL), which represents the structural parameters of the braid and is created from the volume fraction required. From decreasing functions of this NPL, the braiding angles of the unit cells of the braid can be derived. The NPL can be designed from knowledge of the fibre and matrix properties. This allows the braided composite to be designed to maximise the engineering properties. They also say that the fibre volume fraction can be predicted using these models, which has been linked to energy absorption.

In 2-D braiding, the tows are intertwined with a wave like undulation. With 3-D braiding, the fibres have a more complicated arrangement and crimp. This arrangement could create irregular and possibly looser packing. This should lower the moduli and reduce the strength of the composite. Thus, crimp needs to be minimised in straight axial tows. Kuo et al discuss this.[55] They continue to say that when two tows are in contact the one with lower tension undergoes more deformation and thus tensioning is critical. When the fabrics are removed from the forming fixture, the tension is removed and the fabrics become sensitive to external influences. They conclude that theoretical and experimental data indicate that pitch length (the distance between two similar points in the braid) and braid size affect the moduli marginally, even though shorter pitch lengths result in a denser fabric. The axial modulus tends to be influenced by the axial tows. De-bonding and sliding in the early stage of loading can reduce the flexural properties.

Smith and Swanson [56] note that the architecture with the most uniform yarn widths and spacing exhibit the highest braid-direction failure strain and that architectures with larger yarns exhibit higher strain variations. They also agree that fibre waviness affects the strengths of the material, but suggest that spacing of the fixed yarns affect the local compliance directly, and since strength is controlled by ultimate fibre-direction strain changes in compliance cause changes in strain variation, providing an explanation for the lower average failure strains in braided composites.

Further work has shown that braided tubes demonstrate higher shear strength and resistance to torsional instability due to interweaving of the braid fibres as noted by Karbhari and Haller[57]. These cause local fragmentation and tearing instead of longitudinal tearing and interlayer splitting seen in fabric samples.

Wu[58] and Pandey and Hahn [59, 60] have investigated 4-step braided composites, and suggest their suitability for load bearing applications, but these are more complex to manufacture and are not covered in this study

Wang and Wang[61] looked at the microstructure properties of braided fabrics. They noted that although several methods for deriving effective properties of braided composites exist, they involve considerable simplification of the true microstructure. They developed a model using volume averaging of stiffness or volume averaging of compliance techniques to better create the complex structure of a braided composite, and although they composed the structure from the same basic units, the compositions were different for larger structures hence the properties were different. They concluded that the preform as a whole does not have uniform properties, as the cells in the interior regions are different to those on the boundaries.

### 2.3.2.2. Energy Absorption and Failure Mode

For braided composites, failure mode, energy absorption and fibre architecture are all linked. Karbhari et al [62, 63] noted that an increase in the number of braided layers in the preform increases the amount of energy absorption for the tube. The most efficient architecture they found was using a tri-axial braid with carbon fibres in the axial direction. Chiu and Liu[64, 65] in their work have noted that different materials and arrangements demonstrate different failure modes and state that carbon tubes can absorb more energy in crush tests, but Kevlar provides better post crush integrity. They conclude that the constraint forces in the braiding fibres resist the centre wall crack opening and the splaying of fronds. The axial fibres are dominant in energy absorption and the braid fibres affect the crushing failure modes.

Harte and Fleck [66, 67] observed that the failure mode of a braided tube was closely related to fibre angle. For a fibre angle of less than  $35^\circ$  the tubes were found to fail by micro buckling. Micro-buckling is a local instability property of the material involving rotation of approximately 20 fibres within a narrow width. This mode depends on the in-plane shear strength of the composite in the axial direction reaching a threshold level. For angles greater than  $35^\circ$ , the mode of failure was predominantly diamond shape buckling (Figure 12), which involved localised buckling along diagonal lines on the surface of the cylinder. This pattern propagates along the cylinder until the entire length has collapsed. At higher fibre angles they found that elastic modulus, tensile strength and compressive strength drop, but ductility and energy absorption increase.

Others including Chiu et al [65] and Falzon and Herzberg [48] have investigated the failure modes associated with braided tubes and found three different failure modes: splaying, folding, and spiral curling. They note that, predominantly carbon tubes fail by splaying and microfracture whereas Kevlar fails through a buckling mode due to the increased ductility of the Kevlar fibres. In a tri-axial braid, they note that the braiding fibres control the mode of failure, but that the axial fibres that carry the majority of the load. The worst post crush integrity occurred with the splaying mode and the best with the folding mode.

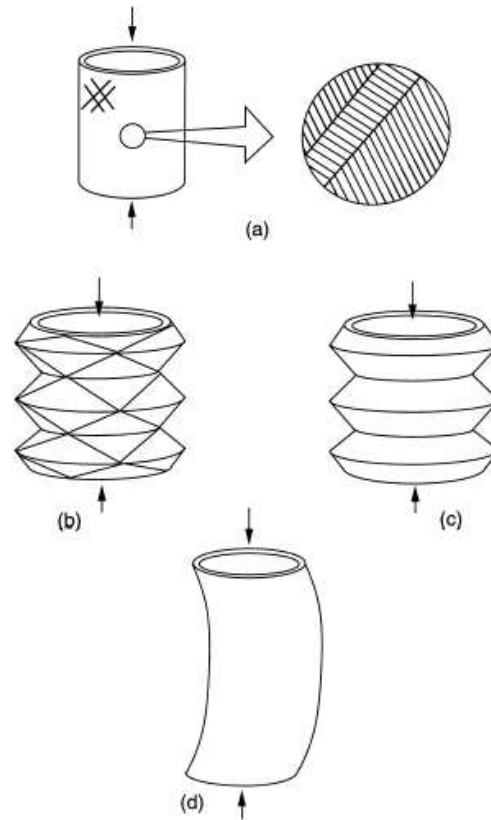


**Figure 12: Four possible modes of buckling for braided tubes. (a) Fibre microbuckling, (b) diamond shape buckling, (c) concertina buckling and (d) Euler macrobuckling [66].**

The failure pattern under quasi-static loading was noted to be an initially non-linear elastic response followed by a sudden drop in the stress at the onset of inelastic deformation. The initial drop is associated with the matrix cracking. In the inelastic region, the braid is flattening and sliding over the axial fibres in the damaged regions. Further drops, they note, are due to propagation of shear fracture through the thickness of the specimen.[68]

Smith and Swanson[69] looked at strength design with the aim of creating a failure prediction that would hold for all braid architectures, however, they note even in laminates this has not been achieved. With their results they suggest that the failure properties can be correlated by using failure strain values in the axial and braid fibres. The investigation of properties can then be found using procedures for investigating laminates.

## 2.4. Predictive Techniques for Calculating SEA

### 2.4.1. Energy Absorption Calculation

Mamalis[11] proposed a theoretical calculation to obtain the energy absorbed for a structure. It is based upon summing the energies dissipated via friction between the wedge and fronds, the energy absorbed by the fronds bending, the energy associated with crack propagation and energy dissipated through axial splitting (equation (1)).

$$W_{total} = k \cdot \sigma_{\theta} \cdot t \cdot C \cdot \left[ \begin{array}{l} \frac{\mu_{s2}(s-s_2)}{\sin \theta} \\ - \mu_{s1} \cdot \mu_{s2} \cdot (s-s_2) \cdot \cot \theta \\ - \mu_{s1} \cdot (s-s_2) + \theta \cdot \frac{t}{4} \cdot \sin^2 \theta \\ + \frac{\theta \cdot (s-s_2)}{\sin \theta} \end{array} \right] + R_{ad} \cdot [(s-s_1) + L_c] \cdot C + 8 \cdot \left( \frac{t}{2} \right) \cdot G \cdot s \quad (1)$$

Where  $k = \text{constant. } 0.07,$

$W = \text{Energy absorbed}$

$\sigma_{\theta} = \text{Tensile fracture stress,}$

$t = \text{Wall thickness,}$

$C = \text{mean circumference of shell,}$

$\mu_{s1} = \text{Friction coefficient between platen and fronds,}$

$\mu_{s2} = \text{Friction coefficient between wedge and fronds,}$

$R_{ad} = \text{Adhesive energy per unit area of layers,}$

$G = \text{Fracture toughness,}$

$\theta = \text{Semi-angle of the wedge}$

$s = \text{Crush distance}$

$s_1 = \text{related shell shortening corresponding with formation of centre intra-wall crack}$

$s_2 = \text{relative shell shortening corresponding to completion of wedge formation}$

This theoretical model predicts the mean post-crushing load and energy absorbed to within  $\pm 10\%$  of the experimental results presented in the paper, although they suggest that the dynamic results are over estimated by 20% compared to the static (here attributed to higher dynamic friction coefficients). They finish by saying that the analysis predicts that the debris wedge supports the majority of the crush load.

## 2.4.2. Interlaminar Shear Strength

In his work for NASA, Farley[70] investigated the effect of volume fraction on mechanical response of tubes. He concluded that as fibre volume fraction increases, the spacing between the fibres in the matrix decreases. This results in higher interlaminar stresses and as a result, lower interlaminar strength causing failure by laminar bending and splaying of layers.

Interlaminar shear is an important property of laminated structures because they display weak matrix dominated properties. ILS stresses develop due to a mismatch in the mechanical properties between laminae and develop at free edges, notches, ply drops and bonded and bolted joints [71]. Delamination is critical in many composite applications. ILSS (Inter Laminar Shear Strength) is often measured using the short beam shear (SBS) test or three-point bend test ASTM D2344 (see schematic of apparatus Figure 13).

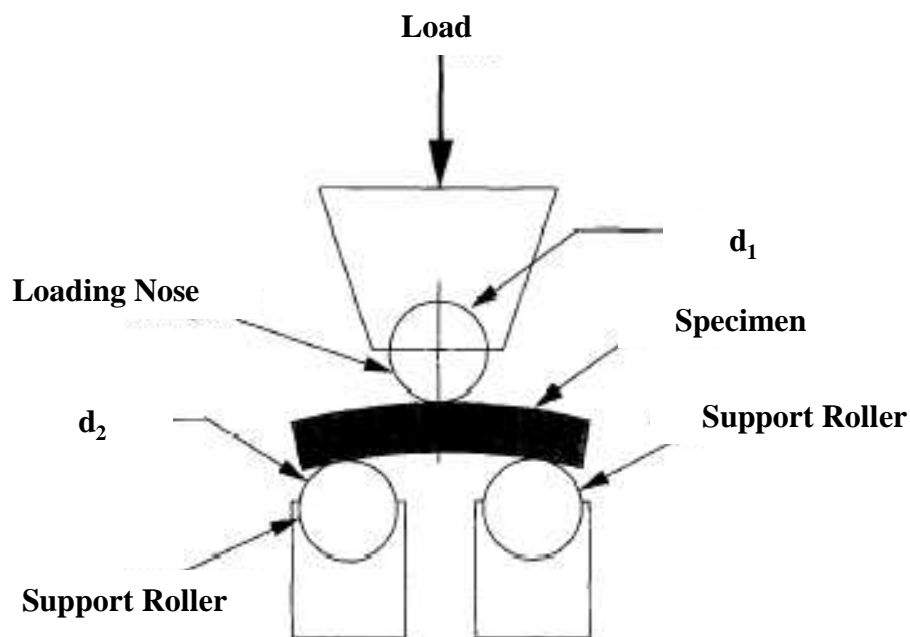


**Figure 13** Schematic of SBS method configuration [72]

The SBS test has its disadvantages and drawbacks. Concerns with this test arise because of the highly localised damage caused by the loading rollers. The method is also criticised because a pure shear stress state is not induced anywhere within the test specimen, and the material can fail in compression or tension. Rosselli and Santare [72] propose use of an Interlaminar Shear Device (ISD), which can be seen in Figure 14. An advantage of this

method is that it measures the shear strength parallel to the fibre direction. This shearing load corresponds directly to mode II fracture, which involves sliding or in-plane shear, and tests have shown that the ISD gives a simpler and more defined shear stress distribution. (See Figure 15, Figure 16)

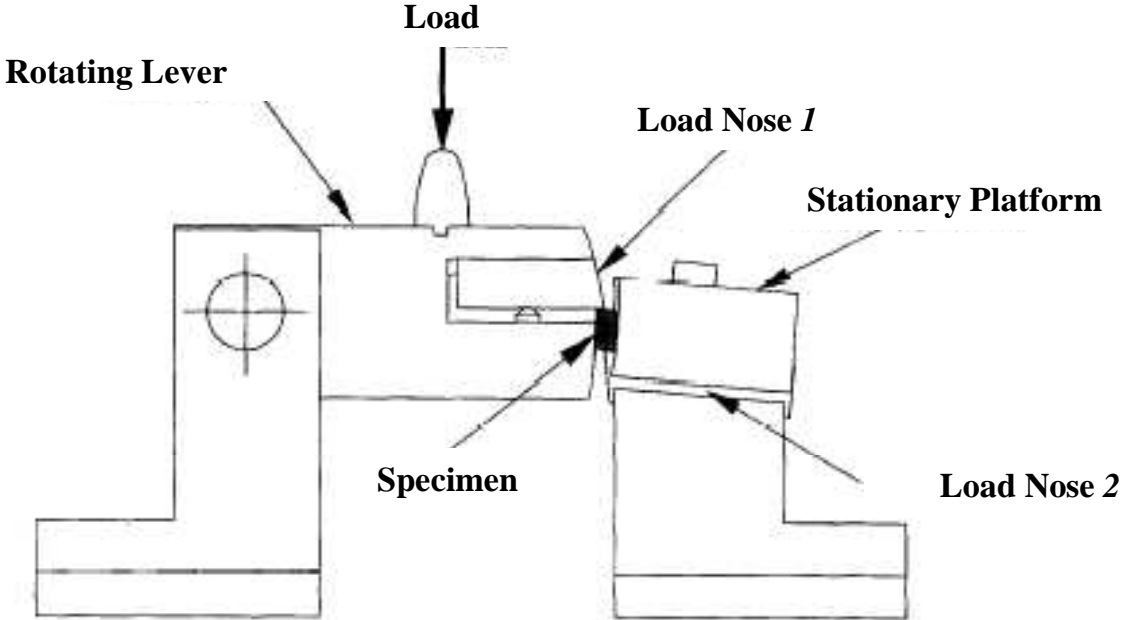


Figure 14 Schematic of ISD apparatus [72]

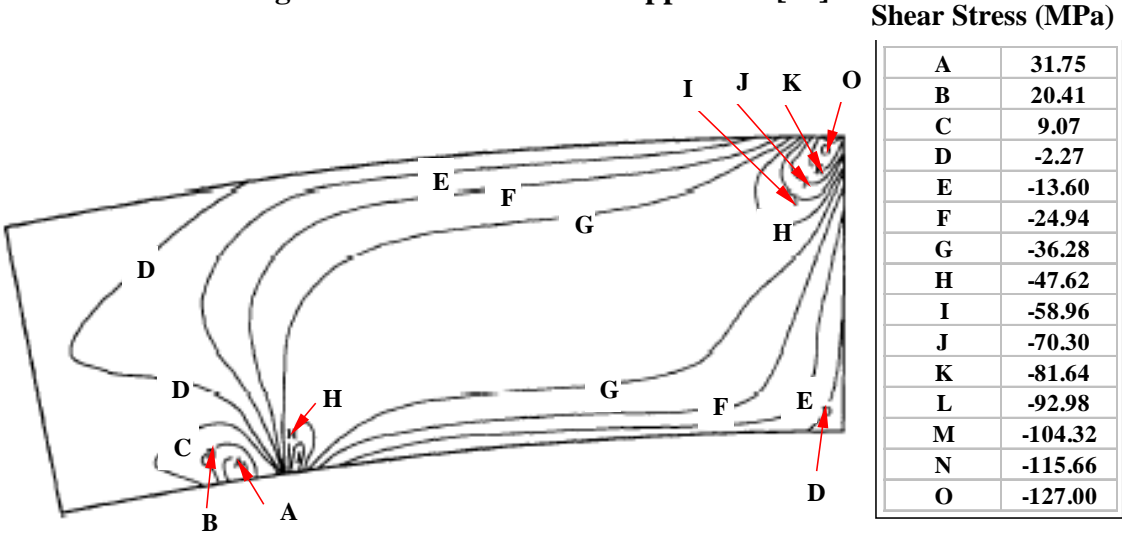
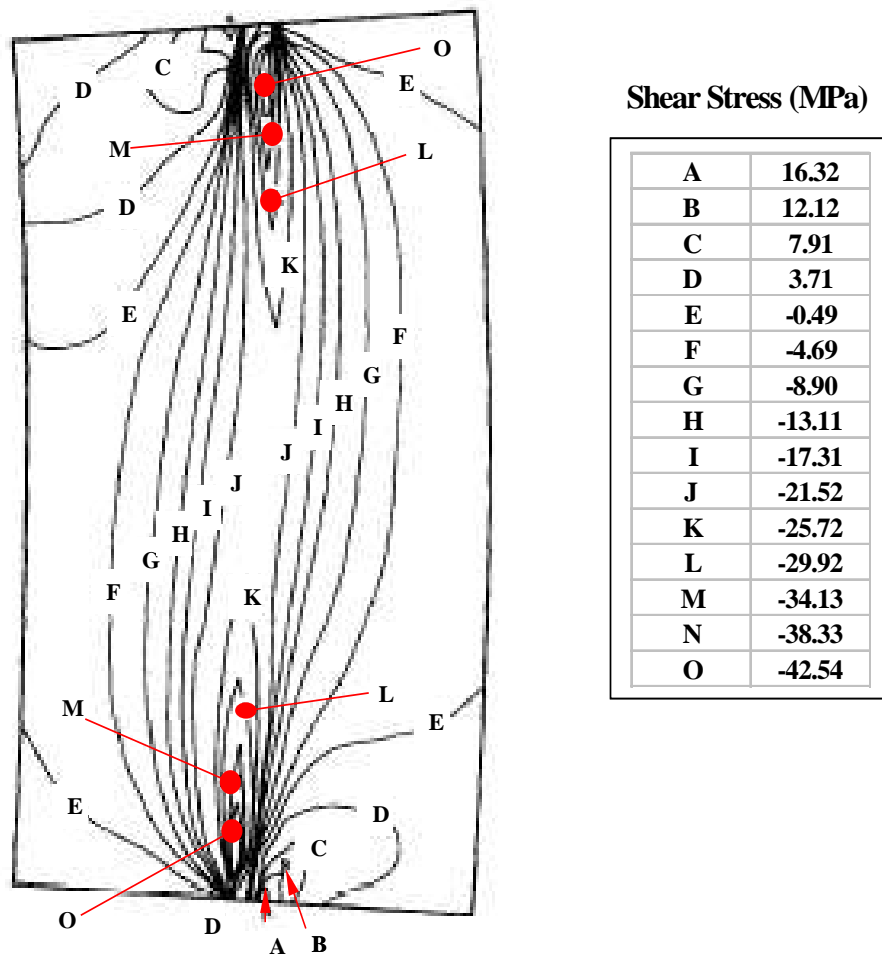
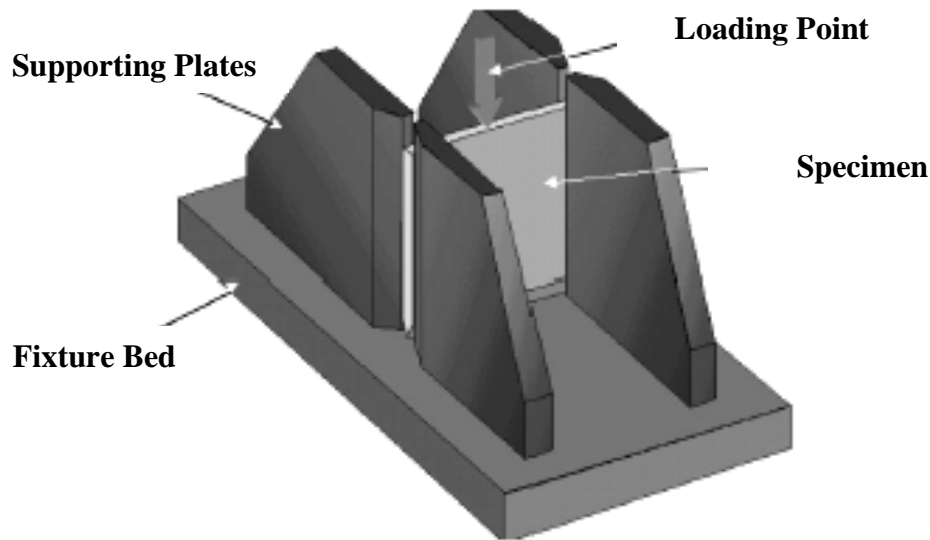


Figure 15 Shear stress contour plot of SBS model [72]



**Figure 16 Shear stress contour plot of ISD model [72]**

ILSS is described as being a key parameter in controlling fracture process and hence energy absorption of a composite by Daniel et al [9, 73]. They used a test rig which measured the crush behaviour of a plate (Figure 17) giving the Steady State Crushing Stress (SSCS). This rig used anti-buckle guides to ensure that all samples could not buckle under the test conditions.



**Figure 17 Test Rig Schematic**

A range of materials were tested, and the volume fractions were kept to approximately 50%. The interlaminar shear strength was measured using the short beam shear method described earlier. When plotting a graph of SSCS against ILSS for each sample, they noted that SSCS rose linearly as ILSS was increased. Their findings suggest that ILSS or through thickness properties control the fracture process and hence the energy absorption of the structure. They restrict this relationship to laminates with similar volume fractions, resins, fibres, laminate thicknesses of the order of 3-4mm, and suggest that if the failure mode changes to a fragmentation mode this relationship could change. They conclude that the route to improved crush resistance may lie in increasing the through-thickness properties by stitching or other methods.

In their later study [73] Daniel et al looked at the effects of ILSS upon tape and woven carbon/epoxy prepreg laminates, and again found a clear correlation between ILSS and SSCS (Figure 18).

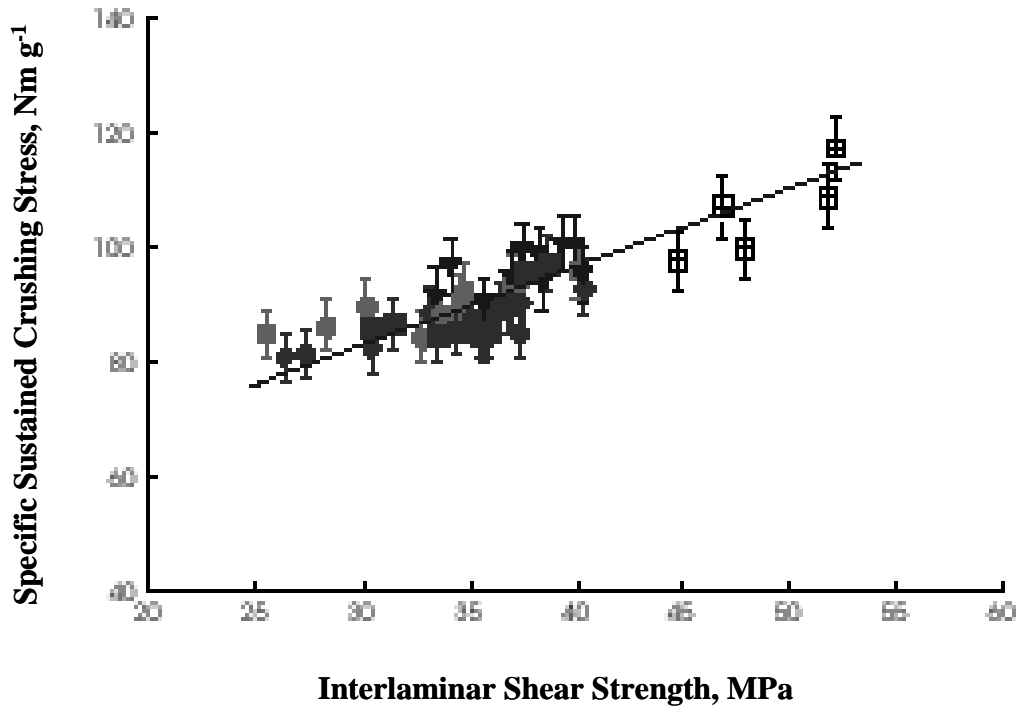


**Figure 18 Graph of SS-CS (Nm.g<sup>-1</sup>) vs. Interlaminar Shear Strength (MPa) for all specimens from [73]**

Here they include a trend line where an ILSS of 43 MPa gives an SS-CS of approximately 100Nm.g<sup>-1</sup>; and an ILSS of 50MPa gives an SS-CS of 110Nm.g<sup>-1</sup>.

Using these approximate values, an equation of the line can be found:

$$SSCS = 1.4 \times ILSS + 38.5 \quad (2)$$

It is interesting to note that the line does not pass through the origin (i.e. When  $ILSS = 0$ ,  $SSCS = 38.5 \text{ Nm.g}^{-1}$ ).

The importance of interlaminar shear strength properties on the energy absorption was linked to the fracture mechanisms operating during the crushing process. A major split is formed through the centre of the laminate, the centre wall crack. This allows the material to form fronds that bend and microcrack to either side under the action of the applied force induced by the loading platen and frictional effects at the frond-platen boundary.

In explanation as to why ILSS is a dominant factor, they suggest it is possible that the primary mechanism of energy absorption is the extensive fragmentation of the laminate that occurs during the bending stage of deformation. Here the material is deforming under the action of frictional forces set up with the loading platen. At this stage fibre orientation and in-plane modulus become relatively unimportant. The amount of energy absorbed will therefore depend on the amount of stored elastic energy prior to bending fracture commencing in the laminate and this in turn will be controlled by the interlaminar shear strength. The ILSS will control the extent that the laminate splits and this will determine the radius of curvature of the fronds as they bend out from the laminate. If the interlaminar shear strength is low, then a long split will occur and the frond will only be forced to sustain a relatively low crack density in order to conform to the deformation. If the ILSS is high then a reduced split will occur and a greater local crack density will be required to facilitate the bending of the frond during the crushing process.

## **2.5. Induced Damage**

Recent studies have begun to investigate the effects of stress concentrations and impact damage. Ribeaux [7] in his work upon CoFRM glass fibre/polyester tubes reported a threshold level for induced damage, below which the damage causes no ill effects on the energy absorption capability of the tube. Above this value the induced damage causes the structure to fail globally reducing the energy absorption capability significantly. Ribeaux suggested that, as a means of predicting failure, the samples that failed globally had a SSCS, which was a higher percentage of the Ultimate Compressive Stress (UCS) than those that crushed progressively.

Holes are necessary for many purposes; bolt holes are important and are often used to join structures or to mount components onto structures. The manufacture of the holes themselves can cause defects such as delaminations, chip-outs of the fibre etc. Persson [74] and others have looked at methods of machining and note the importance of hole manufacture and use of sharp drill bits.

### **2.5.1. Holes and Stress Concentrations**

For analysis, a hole is treated as a stress concentration and has an associated stress concentration factor (SCF) or  $K_T$  where  $K_T$  is defined as the ratio of maximum stress in the presence of a geometric irregularity to the stress that would exist at the same point was the irregularity not present.

Much research has been undertaken into the effects of circular holes and notches in flat plates e.g. [75] however, relatively little has been undertaken on the effects of the holes upon composite cylinders. Lekkerkerker [76] investigated the stress distribution around a circular holes in a cylindrical shell. His analysis is based upon thin shell theory where the stresses are described by two functions of the geodesic coordinates  $x$  and  $y$ .

He defines an explicit parameter  $\mu$ , which is a function of the radius of the hole, the thickness and diameter of the cylinder. It used as a parameter in his mechanical analysis to calculated the membrane stresses around circular holes in cylindrical shells.

It is given by

$$\mu = \frac{4\sqrt{12(1-\nu^2)}}{2} \times \frac{a}{\sqrt{2R}} \quad (3)$$

Where

$a$  = radius of hole in shell

and  $R$  = Inner radius of shell (also defined as Radius of middle surface of pipe in other literature)

This value also is used to provide bounds by which the analysis can be validated with respect to hole size, cylinder size and thickness. For values of  $\mu < 1$  his test results agree with the theoretical results. For the tension and torsional cases, his results show that as  $\mu$  increases the membrane stress increases. From  $\mu = 1$  the increase is linear. The bending stress also increases until it reaches a plateau. The bending stress is indicated as being positive if it is a tensile stress at the outside of the cylinder. The theoretical results diverge from the experimental at  $\mu = 1$ ; this means that theory is overestimating the membrane stresses in the cylinder, and possibly the magnitude of the bending stress. This means it is providing a conservative stress concentration factor.

Bull [77] used Lekkerkerker's work as a basis for experimental and finite element analysis of circular holes in circular shells. The earliest work in this field simplified the solution to that of an infinite plate containing a cut out subject to an appropriate stress system at infinity. The assumption was that the curvature of the shell has little affect on stress concentration (Houghton and Rothwell [78]). The next development took the plate and bent it to form a panel. The loads were applied via stiff end plates, which avoided bending the panel as a unit. The results compared reasonably well with flat plate theory, as long as  $R/a$  was large and the loading system did not bend the panel as a whole. Bull's work used a number of restrictions to

arrive at specimen dimensions. Thin shell theory required  $R/t > 20$ .  $R$ ,  $a$ ,  $t$  and  $\mu$  values had to be such that results could be compared to existing data. The shell has to be of sufficient length that stresses induced by the hole are negligible at the end of the pipe. Three loading cases were used, axial compression, 3-point bending and torsional testing. Finite Element analysis with a model of 1805 degrees of freedom gave the theoretical data. The conclusions of this work are that the addition of a hole in a shell introduces bending and membrane stresses that are not present in a cylindrical shell without a hole. As the  $a/R$  ratio, increases the effects of the hole are unconfined to the area within a small radial distance from a hole. If  $R/a < 4$  then curvature of shell will induce additional stresses above those found in a flat plate with a hole.

Van Tooren et al [79] expanded the theory to look at the effects of curvature on the stress distributions of cylinders with a circular cut-out. They were concerned with windows in aeroplane fuselages and the effects of stress upon composite sandwich structures. They used shallow shell theory and Lekkerkerker's work as a basis for their work. They suggest the main difference between curved and flat isotropic plates weakened by a hole is the occurrence of-out-of plane bending. They model the cylindrical shell as a spiral shell i.e. the plate is modelled as an infinite plate with a constant curvature.

Their results suggest that increasing the curvature increases the tangential stresses around the cut-out, due to an increase in membrane and bending stresses. The membrane stresses increase with increasing curvature because the cross sectional area of the cylinder becomes smaller for a smaller radius. They conclude cut-outs cause large stress-concentrations and their magnitude is highly dependant on the curvature parameter. Importantly, for a cylindrical application, the stress concentration is considerably higher than in an equivalent flat plate with an equivalent loading.

Quinn and Dulieu-Barton [80] and their work on determination of Stress Concentration Factors (SCFs) furthered this study. They used thermoelastic stress analysis to obtain SCFs for a variety of holes in cylinders. They use both SPATE (Stress Pattern Analysis by the measurement of Thermal Emissions) and Deltatherm (a propriety thermal stress analysis system) to analyse the specimens. Their work confirms other research that maximum SCF increases with increasing hole size. With oblique holes they found that the stress distribution around the oblique hole was similar regardless of loading case and combined compression and

bending gives a larger SCF than those from uniaxial compression or tension. They state that predictions of the maximum SCF at holes in cylinders using flat plate data showed good agreement with thermoelastic results.

Wu and Mu[81, 82] have looked into stress concentrations for cylinders with circular holes in tension. They state that the failure stress, taking into account the cross-sectional area, is typically much less than the UTS of the same material without the notch or the hole. They predict failure using  $SCF / K_T$  without considering cracks around the hole.

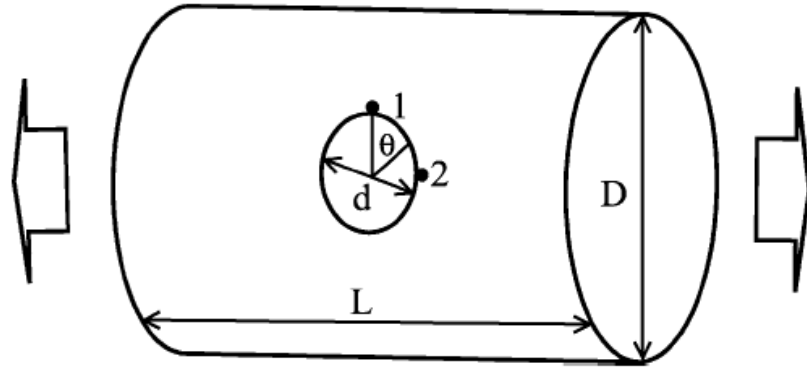


**Figure 19: A pipe with a hole under uniaxial tension[81]**

In cylinders and pipes the hole is located on the circular surface of the cylinder rather than on a flat surface. The effects of curvature need to be considered. For an isotropic cylinder with

$\frac{d}{D} \ll \sqrt{\frac{2t}{D}}$  and under axial loading, see Figure 19, the SCFs at point 1 and 2 are given by:

$$\begin{aligned}
 K_{T,i,c,u}^{\infty,1} &= 3 + \sqrt{\frac{3(m^2 - 1)}{m^2} \frac{\pi}{8} \frac{d^2}{Dt}} \\
 K_{T,i,c,u}^{\infty,2} &= - \left( 1 + \sqrt{\frac{3(m^2 - 1)}{m^2} \frac{\pi}{8} \frac{d^2}{Dt}} \right)
 \end{aligned}
 \tag{4}$$

Savin's SCF Equations from [81] are given in (4)

Where  $m = \frac{1}{\nu}$

For the cylinder under uniaxial tension, the SCFs are calculated by the SCFs of the finite-width isotropic plates multiplied by the ratios of:

$$K_{T,i,c,u}^{\infty,1} \text{ to } K_{T,i,p,u}^{\infty,1} \text{ or } K_{T,i,c,u}^{\infty,2} \text{ to } K_{T,i,p,u}^{\infty,2} \quad (5)$$

They conclude that the SCFs only depend on the dimension ratio defined as the hole diameter to plate width for plates, or the hole diameter to cylinder diameter for cylinders.

Kaltakci [83] determined stress concentrations around circular cut-outs for anisotropic glass-epoxy and graphite-epoxy composites using Modified Distortion Energy and Tsai-Hill failure theories. In orthotropic and anisotropic plates containing circular holes, the failure takes place as a result of various stress components including stress concentration. For an isotropic plate the failure is usually due to the stress concentration. His research revealed that the strength of composite plates is considerably affected by the orientation of the load to the fibres and that the stress concentration is affected considerably by the fibre orientation angle. For cases where the load was parallel to the fibre orientation angle the negative effects of circular cut-outs on the plates' strength were found to be the maximum. He also noted that the maximum stress concentration factor and its location are not always dependant on the magnitude and location of the stress causing failure.

Pandita et al [84] used a strain concentration method to calculate the stresses around the holes, and compared the stress concentration found with this to the theoretical value calculated by earlier solutions. Yao et al [85] studied eccentric holes and noted that the influence of hole diameter is much larger than off-set distance on the stress-strain relationship of the composite material.

Cowley and Beaumont [86] used Penetrant-enhanced radiography to observe damage resulting from SCFs in polymer composites. Here damaged specimens were soaked in an appropriate penetrant, which impregnates any matrix micro-cracks or interfacial ply delaminations. A clear image of the individual modes could be seen on the x-rays. At elevated temperature, fracture stress was seen to decrease and they concluded that weakening of the un-notched section of the laminate coupon was the dominant mode, which over-rode the blunting effect of the notch by enhanced splitting at the tip.

When looking at the effect of a filled hole in a composite Williamson et al [87] observed that the filled hole can restrict the microbuckling of fibres, giving a higher strain to failure in compressive loads. They suggest that current designs are conservative because of this. If the loading is compression, higher design strains than those used can be sustained. They note that the extent to which this result is used depends on close attention to detail of tolerancing. They suggest that losing a bolt, misaligning a bolt or making the hole larger would be dramatic in components subjected to an extreme compressive loading, with a reduction in strain to failure of up to 50%.

## 2.5.2. Impact Damage

Polymer matrix composites are known to be susceptible to internal damage caused by transverse loads even under low-velocity impacts. The composites can be damaged on the surface; importantly they can be damaged below the surface by relatively light impacts causing barely visible damage. Whilst reviewing the low velocity impact properties of composites, Richardson and Wisheart[88] note that poor post impact compressive strength is their biggest weakness. This is due to local instabilities resulting from delaminations causing a large decrease in compressive strength. It is the ease at which these delaminations are caused that is the problem.

Four failure modes have been identified in low-velocity impact [88-90].

- 1) Matrix mode. Cracking occurs parallel to the fibres due to tension, compression or shear, induced often by a low-velocity impact.
- 2) Delamination mode – Usually produced by interlaminar stresses, a crack running in the resin rich area between each ply of material usually occurring after a threshold level
- 3) Fibre mode – occurs under the impactor due to indentation effects and locally high stresses; in tension is seen as fibre breakage and in compression buckling.
- 4) Penetration – here the impactor will completely perforate the impacted surface.

Penetration and delamination have been described as the primary modes of damage in impacted composite structures [91, 92]. In high velocity impacts, the impactor can completely penetrate the structure without creating a large delamination zone. Corum et al [93] note that for carbon-fibre laminates the damage produced with a low speed pendulum was approximately twice the size produced by a gas-gun projectile, both having the same kinetic energy. In a constant energy situation, a low velocity impact with a heavy object induces an overall target response, whereas a high velocity impact by a light projectile induces local target deformation, resulting in energy dissipated over a much smaller area close to the point of impact [91].

Naik and Meduri [94, 95] state that the through-thickness reinforcement of 3D composites makes them more resistant to delamination, they display better resistance to crack propagation and less notch sensitivity when compared to laminated composites. They use an Interlaminar failure function I, where,

$$\left(\frac{\overline{\sigma}_{3t}}{Z_t}\right)^2 + \left(\frac{\overline{\sigma}_{3c}}{Z_c}\right)^2 + \left(\frac{\overline{\tau}_{23}}{S_{23}}\right)^2 + \left(\frac{\overline{\tau}_{31}}{S_{31}}\right)^2 = I \quad (6)$$

Here,  $\sigma_3$ ,  $\tau_{23}$  and  $\tau_{31}$  are the stress components and Z,  $S_{23}$  and  $S_{31}$  are the corresponding strength values. T and c subscripts refer to tensile and compressive values. This equation is based upon a through-thickness quadratic failure criterion as proposed by Brewer-Lagace [96]. The delamination initiation occurs when the value of I just exceeds unity. They observe that a rational mixing of uni-directional and woven fabric layers helps in decreasing the overall failure function, indicating that mixed composites are more damage resistant, and conclude that 3-dimensional woven composites have superior impact damage resistance properties.

This superior damage resistance has been seen in braided tubes, but as Karbhari et al and others [97-99] have noted, the effect of damage prior to crushing is significant, Figure 20.

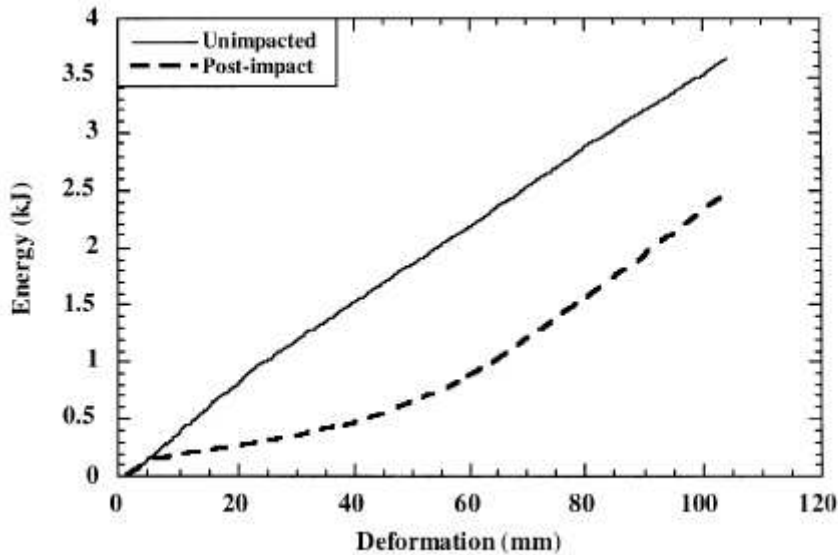


**Figure 20: Schematic representation of relationship between energy absorption and deformation level for tubular samples [97]**

They tested a range of cylindrical samples, all moulded with vinyl-ester resin. Their fibres were glass, carbon and Kevlar and they used combinations of these in biaxial and triaxially braided  $\pm 45^\circ$  samples. The samples were damaged by impacting with a drop weight, which left micro-cracking in an elliptical region around the point of contact. Their results note that carbon fibre composites generically have significantly lower damage tolerance than glass or Kevlar reinforced composites. In the tests, tri-axial braids show greater damage because of propagation along axial yarns.

### **2.5.2.1. Impact Damage Detection**

For characterisation and detection of damage a number of techniques are used, from simple observation with the naked eye to Thermoelastic Stress Analysis. This technique uses a small infrared detector to measure small surface changes in temperature produced when a component undergoes cyclic loading. These changes in stress can be related to the sum of the principal stresses using a calibration constant. Cunningham et al [100] studied this technique and highlight the importance of the surface layer upon the thermoelastic readings. With a resin-rich epoxy layer the thermoelastic signal becomes a function of the global stiffness of the coupon, and hence the ply lay-up, and not the orientation of the surface. Clarke and Pavier [101] looked at using x-rays with a penetrant added to the composites after failure to measure damage. They note that an opaque penetrant, such as zinc iodide, greatly improves the contrast of the damaged area. Olsson et al [102] used digital speckle photography to measure strain fields in the laminates in order to validate an inverse method where elastic properties of inclusions are determined by matching computed and measured displacements.

Scaling effects in samples have also been considered by Swanson [103] and others. The structural response of structures often needs to be studied experimentally, so for cost, time and convenience reasons it is desirable to use scaled models in these experiments. The problem arises how the results obtained apply to the final prototype. Delamination depends on absolute size of the structure and damage area, and propagation is governed by energy release rates, as expected with fracture mechanics considerations allowing for accurate scaling predictions. Fibre breakage is more complex and it has been suggested that this could be predicted using fibre direction stress or strain. Data from Swanson [103] suggests that the size of the specimen does not have a large effect on fibre values of stress or strain over the range

of samples tested, but that the applied strains are under-predicted in larger specimens using linear analysis.

### 2.5.2.2. Fracture and Crack Growth

In tension Edgren et al [104] label the damage in 4 categories: longitudinal cracks; half cracks; whole cracks; and double cracks (see Figure 21).

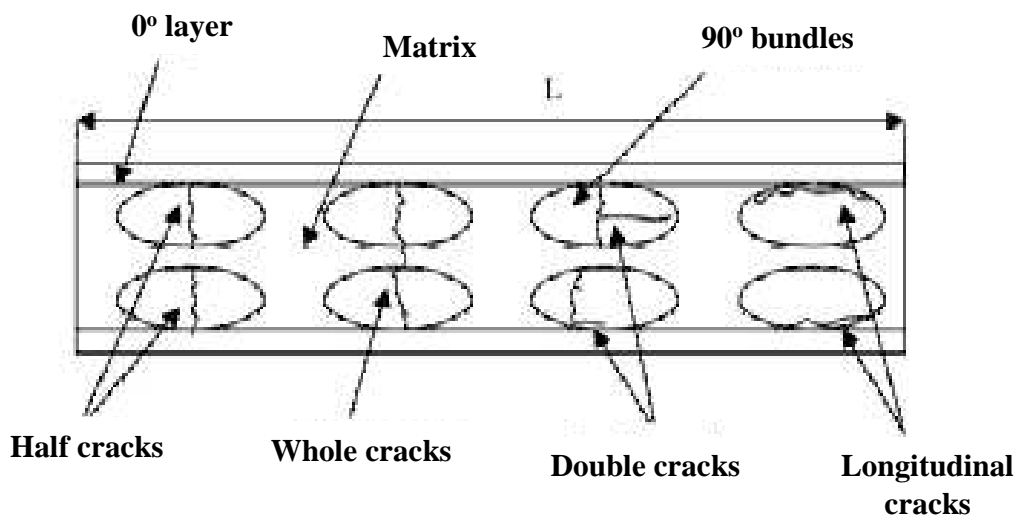


**Figure 21. Schematic showing 4 crack types in NCF laminates [104].**

Their specimens were constructed from 0-90 NCF carbon/vinyl-ester laminates and cut into 230x23x1mm thick strips. Their results showed half cracks were contained in a single fibre bundle and occur first at a strain of approx 0.4% and dominate over other crack types. The other crack types initiated at strains of  $> 0.5\%$ . Their experiments showed that damage has little effect in longitudinal modulus, but a large effect on Poisson's ratio. They show mechanical degradation is ruled by Crack Opening Displacement (COD), and this is dominated by the small half cracks in the  $90^\circ$  layer. This is beneficial as resulting reductions in mechanical properties are less than those expected for 'prepreg' composites.

Fracture toughness and crack growth are also important in damage growth. With increasing rate crack growth was found to change from an unstable stick-slip manner to a continuous manner. The damage zone can be described through assuming characteristic length  $a$ . The fracture toughness,  $K_c$  is calculated from equation (7)

$$K_c = \sigma \cdot \sqrt{\pi(L + a)} \quad (7)$$

Where  $L$  is original crack length. The critical value of stress  $\sigma_c$  is given by

$$\sigma_c = \frac{K_c}{\sqrt{\pi(L + a)}} \quad (8)$$

By substituting  $L = 0$ , the tensile strength for laminates is calculated, when combined they can be written as

$$L = a \cdot \left[ \left( \frac{\sigma_0}{\sigma_c} \right)^2 - 1 \right] \quad (9)$$

If a graph is plotted of the above, the slope gives  $a$ , the characteristic length of the curves, from which the fracture toughness can be calculated. Xiaoping et al [105] conclude that  $K_c$  increases with increasing loading rate.

### 2.5.2.3. Compression After Impact (CAI) Strength

Falzon and Herzberg [106] have undertaken work on the strength of composites after impact of carbon/epoxy  $0\pm 45^\circ$  triaxially braided flat plaques. They investigated the damage resistance and tolerance of braid after a low-medium energy (up to  $7\text{Jmm}^{-1}$ ) impact test. The samples were then tested compressively to measure their Compression After Impact (CAI) strength. They note after visual inspection, that the damage was mainly due to delamination of the plies. On the surface of the specimens there was evidence of compressive cracking, as an indentation in the samples impacted with energy exceeding  $3\text{J/mm}$ , and they note that the cracks propagate along the fibre directions, but stop at tow crossover points.

In modelling the CAI they assumed the damage area does not carry any load, thus can be treated as an elliptical hole, as the damage behaviour is similar to that observed by specimens with a hole in compression. They used a simple closed form solution with two different failure criteria to approximate the CAI. The two models used were the point stress and average stress models. They note that comparison between predicted and measured CAI are within 10% of each other. In a later paper, Khondker [107] idealised the impact in a woven composite as a hole in order to calculate the CAI. Corum et al [93] also used the assumption that impact-induced defects introduce the same strength reduction as a hole of the same size.

CAI is also improved by increasing translaminar reinforcement [108-110], examples include through interleaving or stitching through the laminate thickness. Walker et al [108] noted this in their work on improving impact resistance of carbon fibre/epoxy prepreg plaques. They describe a composite structure as absorbing an impact in two different ways; firstly through absorption of energy through the creation of damaged areas and secondly via an elastic non-failure response. This second way of temporarily storing the energy potentially offers the greatest potential of reducing damage during impact. Three methods have been used to increase impact resistance, toughened resins, short fibre addition and interleaving materials. Both Toughened resins and interleaving work by limiting crack growth in the composite. This occurs through plastic deformation, by incorporating materials that are highly elastic into the composite. They note benefits of translaminar reinforcement include increasing CAI by up to 50% and increasing Mode I fracture toughness by a factor of 30 but they note a decrease in in-plane stiffness, tensile and compressive properties. The addition of an interleaf generates

highly localised damage compared to an un-reinforced laminate featuring significant global damage with little local damage to the impact zone. Masters[109] noted impact resistance of graphite/epoxy systems to improve by up to 80% through the ability of an interleaf to alter the pattern of impact damage development. Here transverse cracks develop within the lamina but are arrested at the laminar interfaces. The interleaf also helps to reduce impact-induced delamination. Mode I and Mode II interlaminar fracture toughness are also increased by up to 10 times as seen by Larsson[110], who noted stitching reduces in-plane tensile strength by 20-25% and modulus of elasticity by nearly 15% but increases delamination energy of impact by up to 20 times compared to unstitched laminates.

#### **2.5.2.4. Improving Impact Resistance**

Ribeaux [7] and Warrior et al [111] studied the effects of interleaving upon the energy absorption of tubes. They noted that the Mode I fracture toughness ( $G_{IC}$ ) was increased. However, there was a decrease in energy absorption of a CoFRM tube with interleaves, under axial loading, of between 18 to 48%. Ribeaux[7] attributed this to a reduction in the coefficient of friction in the crush zone (from 0.36 to 0.22 in the samples tested with the addition of interleaves). The introduction of interleaves also reduced the stick-slip in the crush zone and brought about a smoother load response. The effects upon energy absorption were also altered. At higher rates the energy absorption was seen to increase, reversing the trend seen in non-interleaved samples, and an improvement in the damage tolerance of samples by up to 9 times was observed. Zhong and Jang [112] found that the total energy absorbed increased by 3 times in the interleaved samples over the control specimen, however, this is the energy absorbed during impact with a projectile rather than an impacted tube which is subsequently then crushed.

Wisheart[88] and others [112, 113] suggest toughened resins or thermoplastics as a solution to reducing delamination and impact effects, but it is the fibres themselves that have the greatest bearing on the impact. Much work has been performed in this area upon 2d plates, but there is little work on more complex geometry such as tubes. If these methods are to gain widespread acceptance then more progress is required in these areas.

Explosives and ballistic work has been studied frequently [114-116]. Tang et al[114] have looked at explosive impact work on specimens. They use a rubber buffer on the specimens to decrease the blast wave, and they used a transducer to measure pressure and blast velocity. A Scanning Electron Microscope (SEM) is used to investigate damage size and mechanism. Under static loading the form of damage is delamination and cracks propagate in a zigzag pattern. They state that after the blast wave transfers to the specimen, a tension wave is reflected on the back. This produces a triangle shaped damage region. The SEM results reveal carbon epoxy damage mechanisms include fibre debonding, delamination and kinking of the fibres. The braided bundles exhibited failure across the bundle width, parallel to the fibre or boundary until a crossover point was reached. Glass fibre composites showed lower impact damage to carbon-fibre composites, which was explained by glass having poor interface bonding. This increased the crack propagating path and absorption energy, and decreased stress concentration, all of which aid impact resistance during their explosive tests.

## 2.6. Strain Rate Effects

Impacts can be classified into three categories; low velocity impact, high velocity impact and hyper velocity impact. An impact can be classified as low velocity if the contact period of the impactor is longer than the time period of the lowest vibrational load (speeds in the range of  $0-150\text{ms}^{-1}$ ) [117, 118]. In low velocity impact, the stress waves generated outward from the impact point have time to reach the edges of the structure causing full vibrational response. It is this low velocity impact that is investigated in this study.

Much of the previous work on strain rate involves laminate and ductile metallic materials, but recently strain rate effects have begun to be investigated with more types of composites. Typically, a split Hopkinson's pressure bar (SHPB) is used or modifications on this [119-122], although other methods have been used such as Ballistic Testing, servo hydraulic machines, and instrumented falling weight (IFW) or drop towers [4, 123].

Results have noted that the compression strengths and failure strains are strongly dependant on the specimen geometry, considerable increases in strength and stiffness occur with the increase in strain rate and that the high strain rate response was found to be highly material dependant. This was noted by Akil et al and others [121, 122] who observed that the modulus was more strain rate sensitive in the through-thickness direction whilst a higher strain rate sensitive failure was found in the in-plane direction. They attributed this to the matrix dominated properties in the through thickness direction stating that the strain rate sensitive mechanical behaviour is attributed to the strain rate sensitive matrix properties.

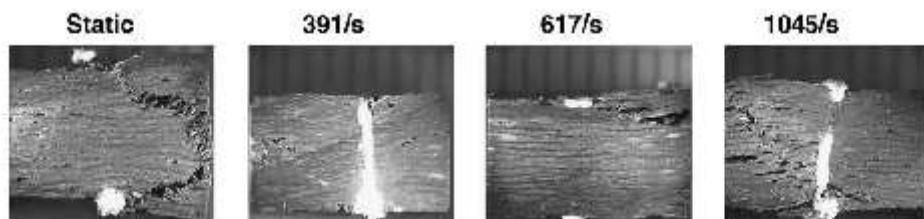


**Figure 22. Optical Micrographs of stitched satin weave laminate loaded in fill direction at differing rates [120]**

Hosur et al[120] noted that peak stress and modulus were higher for dynamic loading when compared to static loading in case of both stitched and unstitched plain and satin weave samples, but failure strain was found to be 2-3 times higher in case of static loading. An example of their experimental results can be seen in Figure 22.

Khan et al [124] looked at the effects of rate upon the resin. They studied polyester and vinyl-ester resins and suggest that an increase of up to 40% in maximum stress were observed with increasing strain rate, that modulus remains constant at strains of up to  $0.1s^{-1}$ , and rose linearly between rates of  $0.1s^{-1}$  to  $10s^{-1}$ . The cubic specimens tested initially deformed in a linear elastic manner, followed by the onset of in-elastic behaviour, described as visco-elasticity. At higher strain rates the polyester fractures by shattering in a brittle manner, coinciding with a rapid drop in stress level suggesting the polyester is unable to relax at higher rates. Their results also suggest that rule of mixtures is a poor way of predicting strength of a material as it does not take into account voids, fibre/matrix interface strength, fibre orientation and discontinuity of fibres.

## 2.7. Applications

Aerospace has been the traditional application for composite materials. The challenge is to introduce composites into affordable everyday usage. High-end automotive use has followed the aerospace trend of labour intensive, hand lay-up carbon fibre. An example of this is the Lamborghini Murcielago, which uses an entire carbon/epoxy body except for the roof structure. In this application the use of composites allows for a weight saving of 34kg or 40% over its predecessor [71].

As noted earlier, composites are ideal for crashworthiness applications. For effective use as a crash energy absorber, any structure must be designed to absorb energy in a controlled manner such that the deceleration is less than  $20g$ , where  $g$  is acceleration due to gravity. Above this the brain can be irreversibly damaged due to movements inside the skull cavity [6]. Savage et al [117] describe such a situation. In Formula 1 motor sport an impact between a BAR Formula 1 car and a barrier at a speed of 182mph created a peak load of 32g. The composite crash structures absorbed this energy and allowed the driver to walk away unhurt.

For use in a more mainstream automotive application, Hamada[125] shows braided composite I beams to possess suitable bending properties for use as side impact members, and with the introduction of a trigger, progressive crush characteristics. He concludes that I beams are useful energy impact absorbers in lateral and frontal conditions. In later work Hamada [126] clarifies his results; the structure of braided I-beams are suitable for progressive crushing because axial fibres are constrained by the braid fibre. Braided beams are noted to possess excellent bending properties compared to conventional aluminium, and the H/A (hoop to axial ratio) of fibres can be greatly varied and optimised for braided composites, contributing to design flexibility. An optimum value of (H/A) for a (0/90) tube is suggested to be a ratio of 0.25.

A non automotive use of composites in a crashworthiness application is for helicopter sub-floor structures [127, 128]. The chief concern for crashworthy sub-floor design is to absorb maximum energy within the limited space available, while keeping the peak loads transmitted to occupants to a minimum, i.e. the same requirements as an automotive crash structure (see Figure 23 for an example).

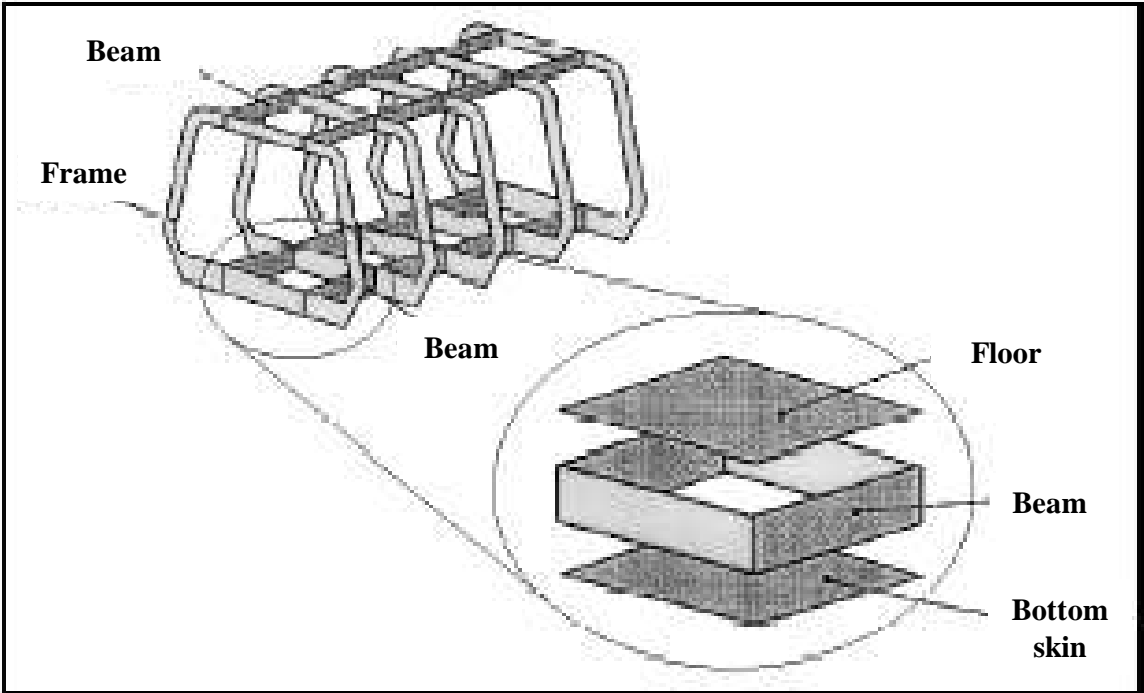


**Figure 23 Typical Composite Helicopter Structure [127]**

Dreschsler and others [129, 130] suggest that CFRP and GFRP are suitable for use in automotive, rail and aerospace crashworthiness applications. These materials with high SEA levels above steel and aluminium are strong candidates for bumper beams, crash boxes, front members and rockers. To make composites more attractive to OEMs (Original Equipment Manufacturers), feasible components must provide sophisticated functions in addition to weight reduction and provide cost reductions compared to state of the art aerospace grade materials.

Composites use is seen in the Aston Martin Vanquish (Figure 24), which uses carbon fibre extensively for structural and crashworthiness applications along with the BMW M3 and the Mercedes McLaren SLR. Composites have been traditionally glass-fibre random & CSM composites, but aerospace technology was adopted for motor sport in the early 1980's with prepreg carbon/epoxy systems appearing in high-end road cars. Typical composite structures are tubular beams for crash, impact and body chassis members usually produced from carbon.



**Figure 24 Aston Martin Vanquish Showing Composite Materials Use [131]**

## **2.8. Summary of Literature Review**

### *Architecture*

Many results have shown that stacking sequence and fibre architecture can affect SEA significantly.

### *ILSS*

Daniel et al[9] suggest that ILSS is a key parameter in determining SEA. There are problems with their work as the method used to obtain their experimental data is for simple plate geometry and the effects of failure mode are ignored. Their test is based upon a rig that ensures all samples fail by splaying which is not seen in all tubular specimens. This suggests there is further scope for work to be undertaken to establish the validity of their theory.

### *Rate*

The works of Fernie[4] and others[132] on the effect of rate upon SEA are inconclusive. Generally the change in rate affects the energy absorption adversely [133] but in certain cases the energy absorption increases with rate and in others appears to peak at a rate of  $5\text{ms}^{-1}$ . The first result can be attributed in some cases to a change in the mode of failure but the second seems to be an anomaly.

### *SCF's*

The effects of notches and holes have been investigated, but no design rules or effects of stress concentration factors have been properly established for composite tubes; and there appears to be some disagreement in the literature how to apply scaling and conversion factors to damaged areas of composite materials.

## *Impact*

Data has been given for CoFRM tubes regarding damage and threshold levels, but how this applies to other reinforcement architectures is unclear. Common practice is to assume that a damaged area is equivalent to a hole of a similar size; however, this is overly simplistic and tends to overestimate the effects of the damaged zone. In addition, predictions of how a material will fail with damage have not been investigated for tubular specimens.

These areas will be investigated in this study.

## **3.0 Experimental Methods**

In order to investigate the issues mentioned in the previous section a number of experimental investigations needed to be undertaken. This chapter describes the methods used.

The majority of this work was crush testing of composite tubes. Quasi-static and dynamic test conditions were used, fibre volume fractions were calculated for each type of tube, failure modes were observed with digital cameras, high-speed digital cameras and through micro-graphing. Ultimate Compressive Strength (UCS) testing was undertaken and finally ILSS testing was undertaken.

### **3.1. Experimental Conditions**

Similar work for CoFRM tubes was presented by Ribeaux [7]. He produced glass/polyester circular and square tubes, tested at a quasi-static rate and  $5\text{ms}^{-1}$ . The samples were pre-damaged and the effects of the damage were investigated. This was used as a basis for comparison for this study. To ensure the validity of any comparisons the resin and specimen dimensions were kept to the specifications he used. These are described later in this chapter.

### **3.2. Materials**

As a result of the through-stitching process, the tow sizes and spacing in the plies of the NCF vary between the layers, thus allowing for a number of different fibre orientations.

- (a) - Axial weft fibres on the outside of the outer layer, 0-90
- (b) - Weft Fibres circumferentially on outside of the outer layer, 90-0
- (c) - Weft Fibres circumferentially on inside of the outer layer, 90-0 Axial Outer (AO)
- (d) - Axial weft fibres on the outside of the outer layer, 0-90 Hoop Outer (HO),
- (e) - Fibres orientated at  $45^\circ$  to the major axis of the tube

### 3.2.1. Reinforcements

The NCF fabrics used were Brunswick Technologies Inc. (BTI) ELT566 balanced  $0^{\circ}/90^{\circ}$  E-glass non-crimp fabric of density  $566 \text{ gm}^{-2}$  ( $283 \text{ gm}^{-2}$  of fibre in each axis). During the performing process a thermoplastic additive (7% by mass DSM resins Neoxil 940) was added as a binder to aid the performing process.

The carbon fibres used in braiding the large tubes were Tenax STS 5631 with linear density of 1600 tex and 24000 filaments. The glass fibres used in braiding the small tubes were Hybon 2002 600 tex E-glass continuous filament rovings

Other reinforcement materials used were CoFRM E-glass, with areal mass of  $450 \text{ gm}^{-2}$  (Verotex Ltd. U750-450), along with a quasi-unidirectional E-glass fabric, BTI ELPB 567 with density  $567 \text{ gm}^{-2}$ .

The interleaf film used was plastic urethane (Sarna-Xiro XAF36.404 at  $100 \text{ gm}^{-2}$ ) with a film thickness of  $80 \mu\text{m}$ .

### 3.2.2. Matrix

The polyester matrix used was unaccelerated orthophthalic polyester Reichold Norpol 420-100 (41-45% styrene content) supplied by K&C Mouldings, with 0.5% Akzo-Nobel NL-49P accelerator and 1% Akzo-Nobel methyl ethyl ketone peroxide (MEKP) Butanox M50 catalyst.

The vinyl-ester matrix used with the carbon tubes was rubber modified bisphenol-A epoxy based (Reichold Dion 9500, supplied by K&C mouldings) cured by 1.25% Butanox LPT catalyst and 0.5% NL-51P accelerator.

The epoxy matrix for the carbon tubes was Crystic Kollernox D5136 supplied by Scott-Bader with curing agent Crystic Kollercure D5130 at a ratio of 100 parts D5136 to 26 parts D5130.

### 3.3. Specimen Geometry

Previous work by Curtis[134] and Duckett [135] upon tubes with an outer diameter of 88.9mm and a wall thickness of 4mm produced samples that absorbed approximately 2900J in 30mm under quasi-static test conditions. These dimensions were used for the preliminary specimens for investigating the failure modes of braided carbon. However, as discussed by Ribeaux, this size of tube is impractical for testing at dynamic rates. The drop tower available had a maximum payload of 45kg, which at a height of 1.27m (equating to  $5\text{ms}^{-1}$  or 11.2mph) gives potential drop energy of 561J i.e. significantly less than the energy absorbed by Curtis and Duckett's specimens. In order to ensure steady state crush, approximately 30mm of crush is required. To maximise SEA a D/t ratio of 16 is required. This led Ribeaux to use tubing with an outer diameter of 38.1mm and a wall thickness of 2mm, used as the basic size for the majority of the E-glass tubes in this study.

### 3.4. Manufacturing

The circular tube moulds were originally manufactured with the outer mandrel made from bright seamless steel hydraulic tubing with inner diameters of 88.9 and 38.1mm for the large and small tubes respectively. The wall thickness of the large tubes under test was 4mm, and for both the circular and square glass tubes it was 2mm. In order to provide these wall thicknesses, the inner mandrels were manufactured with a ground surface finish. Two end caps hold the mandrels concentrically, ensuring a uniform cavity and seal the mould. (see Figure 25)

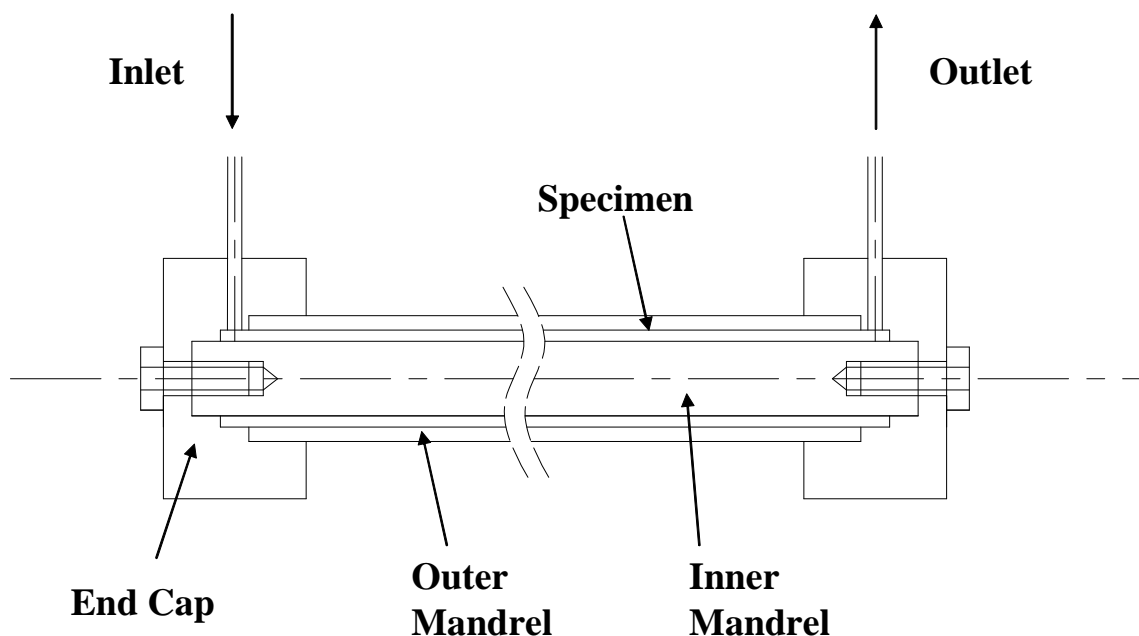


**Figure 25 Schematic of Tube Mould**

The design of the tube moulds allows for a 500mm long composite tube to be manufactured. This enables five 80mm samples to be cut from the tube with enough spare to use for volume fraction test work.

Existing square tube moulds were utilised for the manufacture of square glass tube samples (Ribeaux [7]). The moulds produced a square tube with a uniform wall thickness of 2mm and width of 30mm in lengths of 500mm.

### 3.4.1. Fibre Volume Fraction

Presented here are the results for the fibre volume fraction for the large carbon tubes (Table 1) and the small glass tube data (Table 2, Table 3). Included is the number of layers of fibre for each tube.

**Table 1 Large Carbon Tube Data**

Fibre architecture	No of layers	Volume Fraction (%)	Proportion axial to braid % (approx)
Biaxial $\pm 30$	7	37.0	-
Biaxial $\pm 45$	4	27.6	-
Biaxial $\pm 45$ + Interply	4+3	39.0	39
Biaxial $\pm 60$	4	44.9	-
Biaxial $\pm 75$	3	47.1	-
Triaxial $\pm 45$	4	32.3	31
Triaxial $\pm 45$ + Interply	3+2	34.4	47

The numbers of layers of braid were chosen to ensure that there were no resin rich outer layers in the specimens (see section 3.4.3 for more information).

**Table 2 Small Glass NCF Tube Data**

Fibre architecture	No of layers	Volume Fraction (%)
NCF 0-90	3	33.1
NCF 90-0	3	31.3
NCF $\pm 45$	3	30.3
NCF 0-90 (HO)	3	33.1
NCF 90-0 (AO)	3	31.3

**Table 3 Small Glass Braided Tube Data**

Fibre architecture	No of layers	Volume Fraction (%)	Proportion axial to braid % (approx)
Biaxial ±30	7	33.4	-
Biaxial ±45	5	37.3	-
Biaxial ±60	4	41.3	-
Triaxial 0±30	6	31.3	37
Triaxial 0±45			31
Triaxial 0±60	4	42.2	24

This data was obtained by carrying out resin burn off tests on samples cut from tubular specimens using an established method [7] similar to ASTM standard D2584-94. Samples were typically in the range of 3-5g and were weighed to an accuracy of ± 0.01g using a mass balance. The glass samples were placed in an electric furnace (or burn-off oven) at 625°C for 1 hour to remove the resin. Samples were then weighed again and mass fractions calculated using the following calculations:

$$\text{Mass of Residue} / \text{Mass of Specimen} * 100 = \text{Fibre Mass Fraction} \quad (10)$$

$$\text{Mass of Residue} / \text{Density of Fibres} = \text{Volume of Fibres} \quad (11)$$

$$\text{Volume of Fibres} / \text{Volume of Specimen} * 100 = \text{Fibre Volume Fraction} \quad (12)$$

The specimens were measured to provide dimensions to calculate the volume, and at least 6 samples of each type were tested to ensure the effect of variation between tubes was negligible (see Table 4 for constituent information).

**Table 4 Fibre and Resin Density Data**

Material Type	Density (kg/m <sup>3</sup> )
Norpol 420-100 polyester Resin	1100
Tenax STS carbon fibre	1790
Density of E-glass	2600

### **3.4.2. Preforming of NCF Fabric Tubes**

The inner and outer mandrels were prepared by applying a minimum of five coats of Chemlease PMR-90 release agent to surfaces to ease removal of the finished composites from the tube moulds.

The fibre was cut to size, 350 x 500mm for the small tubes giving three layers of fabric in a 2mm wall space cavity, and weighed. 7% by mass of the binder was then applied to the fabric and heated.

This part of the manufacturing process evolved from work by [136, 137] on pressurised roller techniques. A pre-forming rig was used to allow the fibre to be rolled onto the inner mandrel directly, with toggle clamps to clamp the mandrel down onto a spring loaded roller. This compresses the preform whilst enabling easy assembly and disassembly.

Heat from a hot air gun and pressure from the roller consolidated the preform.

The preform was then removed from the rig and inserted into the outer mandrel. The end-caps were fitted and tightened to ensure there was no leakage. O-ring seals were used to provide sealing all around the preform.

### 3.4.3. Manufacture of Braided Preforms

The braiding follows a slightly different process to the NCF fabrics. End fittings were manufactured to allow the inner mandrels to pass through the braiding machine. The mandrels were coated with mould releasing agent as before and then fibre was braided directly onto them. The braiding machine used was a single axis 48 carrier braiding machine with the ability to braid triaxially with the addition of 24 axial fibres. Once complete the moulds were once again put together ready for injection.

Three different types of preform were created for the large (88.9mm) carbon tubes. The original biaxial type, a triaxial type with 24 axial fibres woven into the braid fibre and a third type with 55 axial fibres (interply) laid between the layers of braided fibres (see Figure 26).



**Figure 26 48 Carrier single axis braiding machine with carbon fibre and 55 axial fibres connected.**

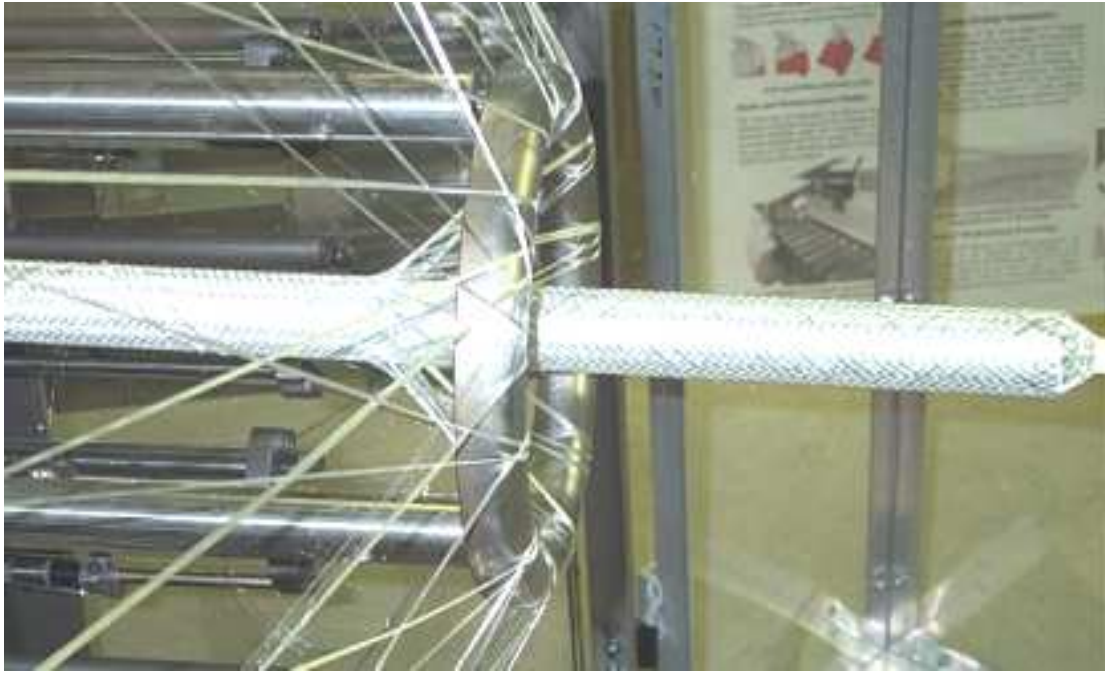


**Figure 27 Braiding of Ø38.1mm E-Glass Tube**

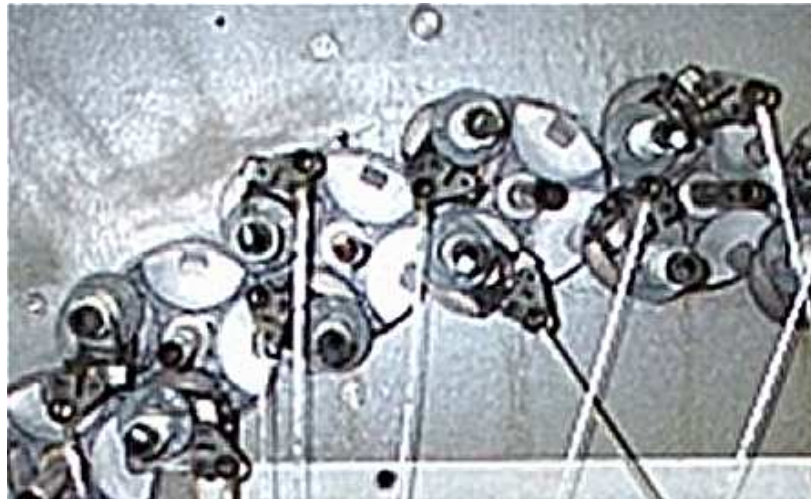
The lay up of these braided tubes was a function of machine variables such as speed of braider and speed of mandrel, and physical dimensions of the mandrel and braiding ring. Thus coverage of the mandrel was different at differing braid angles resulting in differing pitch lengths. In order to ensure a full cavity different numbers of layers were required

Figure 27 through to Figure 30 an example of the braiding process with a Ø38.1mm E-glass tube can be seen.

For further methods of braided composite manufacture see Appendix 1: Braided Composite Manufacturing



**Figure 28 Braiding of Ø38.1mm E-Glass Tube**



**Figure 29 Spools and Carriers**



**Figure 30 Braiding of Ø38.1mm E-Glass Tube**

### 3.4.4. Moulding

Tubes were moulding using the Resin Transfer Moulding (RTM) technique at room temperature. The inlet of the tube mould is connected to a pressure pot containing the mixed resin. The resin is forced through at pressure. The outlet is vented to atmosphere with a bucket to catch the resin flushed through. The pressure required to force the resin through was in the range of 2.5 bar, for some NCF fabrics, up to 6 bar, for the high fibre content braided fabrics. The moulds filled in approximately 7 minutes and resin was flushed through for a further 20 minutes to ensure there were no voids or air pockets left in the composite. The mouldings were cured overnight at room temperature and post-cured for 2 hours at 80°C. A schematic of the moulding process can be seen in Figure 31.

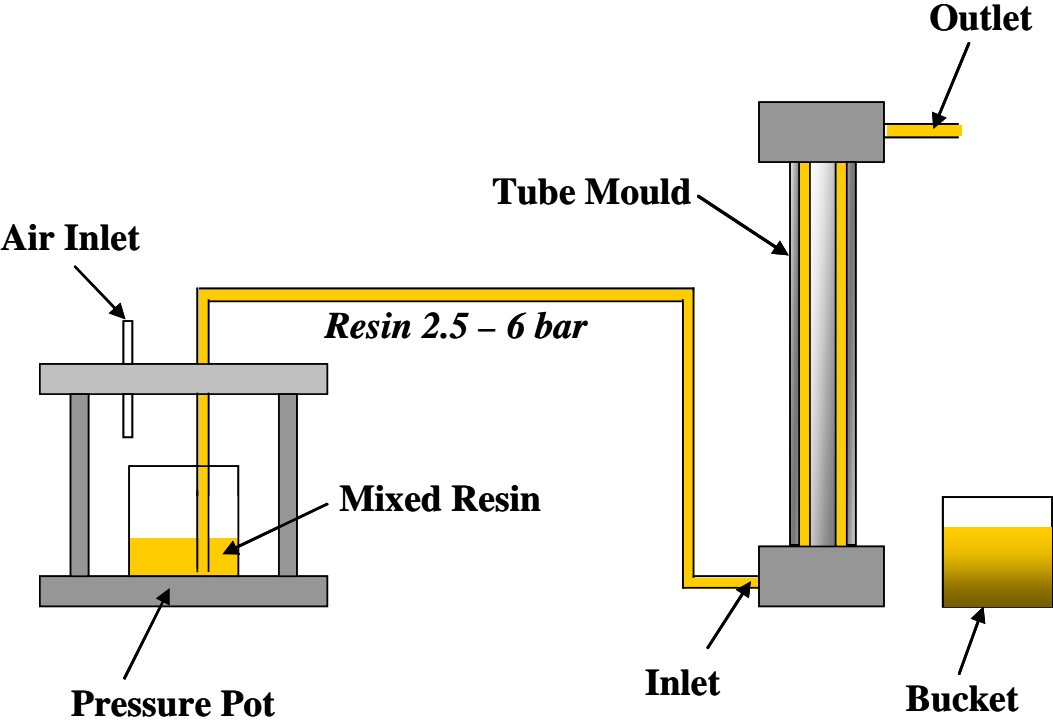
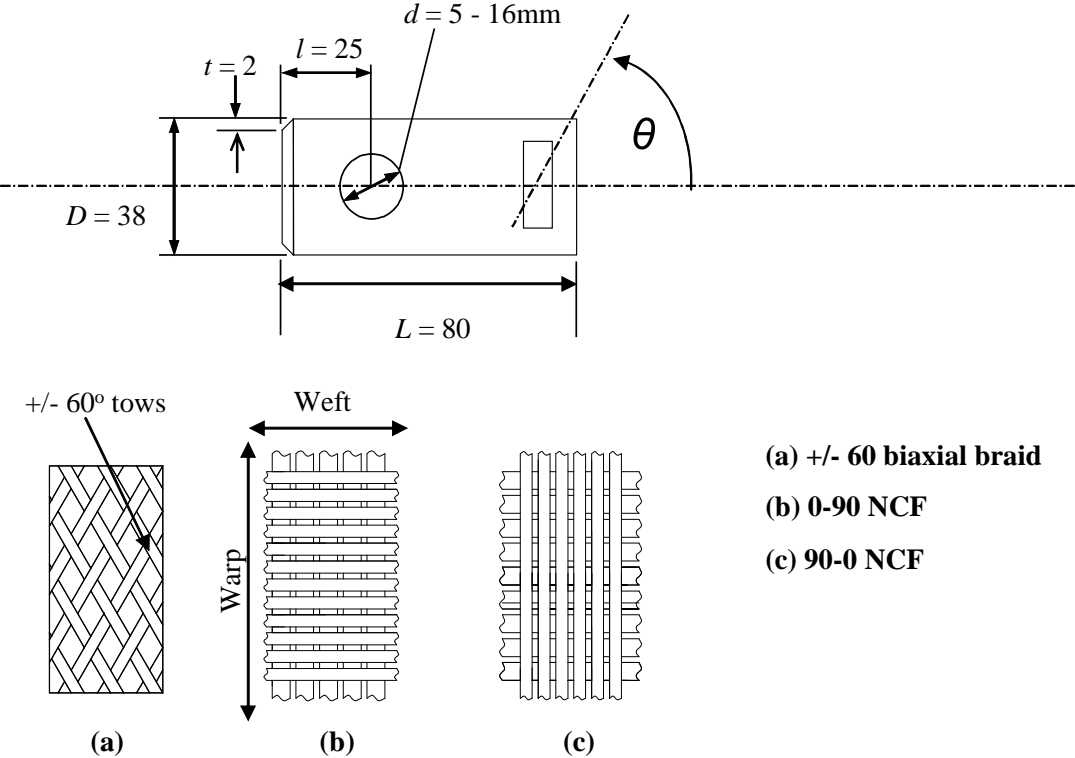


Figure 31 RTM Moulding Process

### 3.5. Sample Preparation

The specimens were cut from the tube using a diamond tipped cutting saw to a length of 80mm. A 45° chamfer was machined using a lathe onto one end of each specimen to act as a stable crush initiator.

Holes were machined with spur drills of diameters 5, 10 and 16mm at axial positions of 15, 25 or 45 mm relative to the chamfered end (see Figure 32). Drills were regularly replaced to avoid causing extra damage, such as delaminations, tearing of fibres, matrix damage, to the specimens (see section 2.5.1.). The rigs used for the impact damage were used to hold the specimens in position whilst drilling.



**Figure 32 Graphical representation of tube structure with holes (all dimensions in mm).**

Impact damage was applied by dropping a fixed weight from a controlled height using a Rosand Instrumented Falling Weight Tower (IFWT). A hemispherical tup of diameter

12.7mm was used as the impactor. Stepped energy levels were chosen in order to find a threshold level at which the tube would fail catastrophically. The levels were in the range 1.5 – 15J. The sample was fixed in a rig that ensured there was no rotation of the tube and the sample could be positioned accurately (see Figure 33).

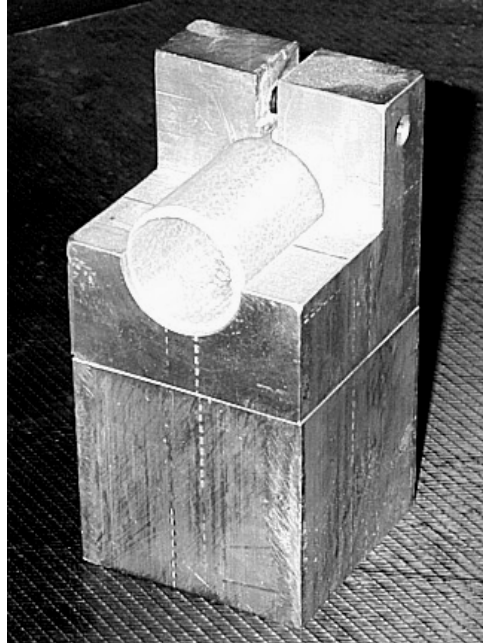


**Figure 33 Sample and impact fixture**

The mass of the impactor and fixture was 5.792kg. Using the formula for potential energy, assuming all energy is transferred / absorbed by the specimen on impact:

$$\text{Impact energy} = \text{mass of impactor} \times \text{acceleration due to gravity} \times \text{drop height} \quad (13)$$

The impact damage was applied at 30mm from the chamfered end.

In reference to non-service damage, a 500g spanner dropped from a height of 1m will have an impact energy of 4.9J, a small stone chipping, kicked up by a car, with mass of 15g travelling at 70mph ( $31.1 \text{ ms}^{-1}$ ) will have an associated energy of 7.25J.

## **3.6. Test Methods**

### **3.6.1. Quasi-Static Tube Crush**

The large tubes were crushed quasi-statically at a rate of 10mm/min using an Instron 8500 servo hydraulic testing machine with a 1000kN load-cell (Figure 35). The samples were crushed onto a ground steel platen and load and displacement data was recorded on a PC directly from the testing machine. All samples were crushed 50mm.

At least 3 samples of each type were tested to ensure that any issues with sample quality were minimised and a more accurate average could be used.

The data presented for SEA in section 4.0 is the mean from these tests along with the standard deviation for these samples from that mean value. The mean crush loads were calculated by finding the average crush load after the first 5mm of crush. The first 5mm was discounted to remove the effects of the chamfer.

SEA was determined by firstly using the trapezium rule to find the area under the load-displacement curve between each time step and hence the energy absorbed in that time step. These were then added together to calculate the energy absorbed for the sample. This was then divided by the by the mass of the crushed length to give the SEA in  $\text{kJ.kg}^{-1}$ .



**Figure 34 Instron 8500 Control Unit with ESH Servo-Hydraulic Test Machine**

The small section tubes were crushed quasi-statically at 10mm/min using an Instron 1195 electro-mechanical loading frame with a 100kN load cell (see Figure 35). Data was collected and processed in the same way as the large tubes.



**Figure 35 Instron 1195 with sample under Quasi-Static Testing**

### **3.6.2. Dynamic Tube Crush**

The Dynamic tests were carried out using the Rosand IFW5, instrumented falling weight machine at an impact speed of 5m/s (see Figure 37). The machine limits allowed impacts in the range of 2-7m/s to be tested. Energy levels were changed by adding mass to the drop fixture, to ensure a minimum of 30mm of crush.

A Kodak HS4540 high-speed video-imaging camera was used to observe dynamic failure modes. The equipment was loaned from the instrument pool of the Engineering and Physical Sciences Research Council (EPSRC). The camera frame rate was set to 4500 frames per second.

The test rig used (see Figure 37) was designed for previous work with a Kistler 9051A 120kN load cell pre-tensioned between the crush platen and the base. The load cell was pre-tensioned with a load of 5kN to reduce vibration in the system.

The sample was attached to the drop weight using cyanoacrylate before being raised to the correct height.



**Figure 36 IFW5 Tower in use**

The force and time data were collected on a PC using an Instronet data recording system at a rate of 40 kHz and processed in a similar way to the quasi-static test data.

This is an established method utilised by Ribeaux[7] Fernie [4] Duckett [135] and Warrior et al [138] using the data collected by the Instronet, which was then further processed by PC. Initially the Force and Time data was calculated from the load-cell outputs, and knowing the masses of the falling sample and impactor, the acceleration at each point was calculated from Newton's third law,  $F=m.a$ , this data in turn was used to calculate the velocity at each corresponding point, from which the displacement was calculated. The load and displacement data was then plotted to create the load displacement curves seen in section 4.0. The SEA was obtained in a similar manner to the quasi-static tubes by firstly using the trapezium rule to calculate the energy absorbed, then dividing this by the mass of the crushed length to give the SEA.

At least 3 samples of each type were tested. The data presented for SEA in section 4.0 is the mean and the standard deviation from the mean for these samples.

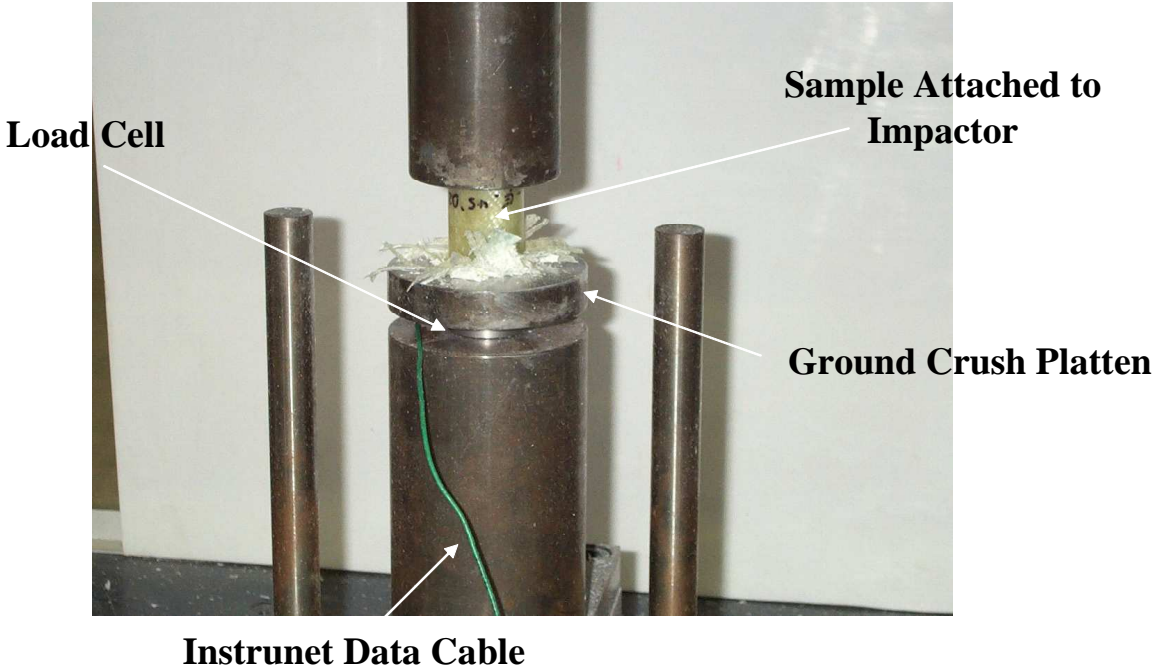


**Figure 37 Dynamic Crush Test Rig**

### **3.6.3. Ultimate Compressive Strength (UCS)**

Tubular samples were tested in a similar manner to those tested by Ribeaux[7]. The samples were placed under compression between two ground crush platens. In order to obtain the ultimate compressive strength for the sample types the specimens were manufactured with no chamfer so that the tubes would fail globally rather than crush.. The samples were tested at both  $10\text{mm}\cdot\text{min}^{-1}$  and  $5\text{ms}^{-1}$ .compressively using the Instron 1195 and Rosand IFWT respectively (both described earlier). The test was judged to be complete once the sample failed globally. The sample failed at the ultimate compressive load of the specimen. This maximum load divided by the closed sectional area of the tube gave the UCS. Tests were undertaken both quasi-statically and dynamically.

### 3.6.4. Interlaminar Shear Stress Testing

This used the method described by Rosselli and Santare [72] for the interlaminar shear device. It involves shearing a specimen to failure along the direction of fibres by applying a compressive load to the ends of the beam. The aim is to measure the shear strength in a plane parallel to the fibre direction. This mode corresponds directly to mode II fracture, which involves sliding or in-plane shear. The original rig involved an offset load on the lever arm (see Figure 14). A modified rig was designed and manufactured so the radius of the test arm matched that of the large tube wall ( $\text{Ø}88.9\text{mm}$ ) with the load applied directly over the test piece to simplify the analysis (Figure 38).

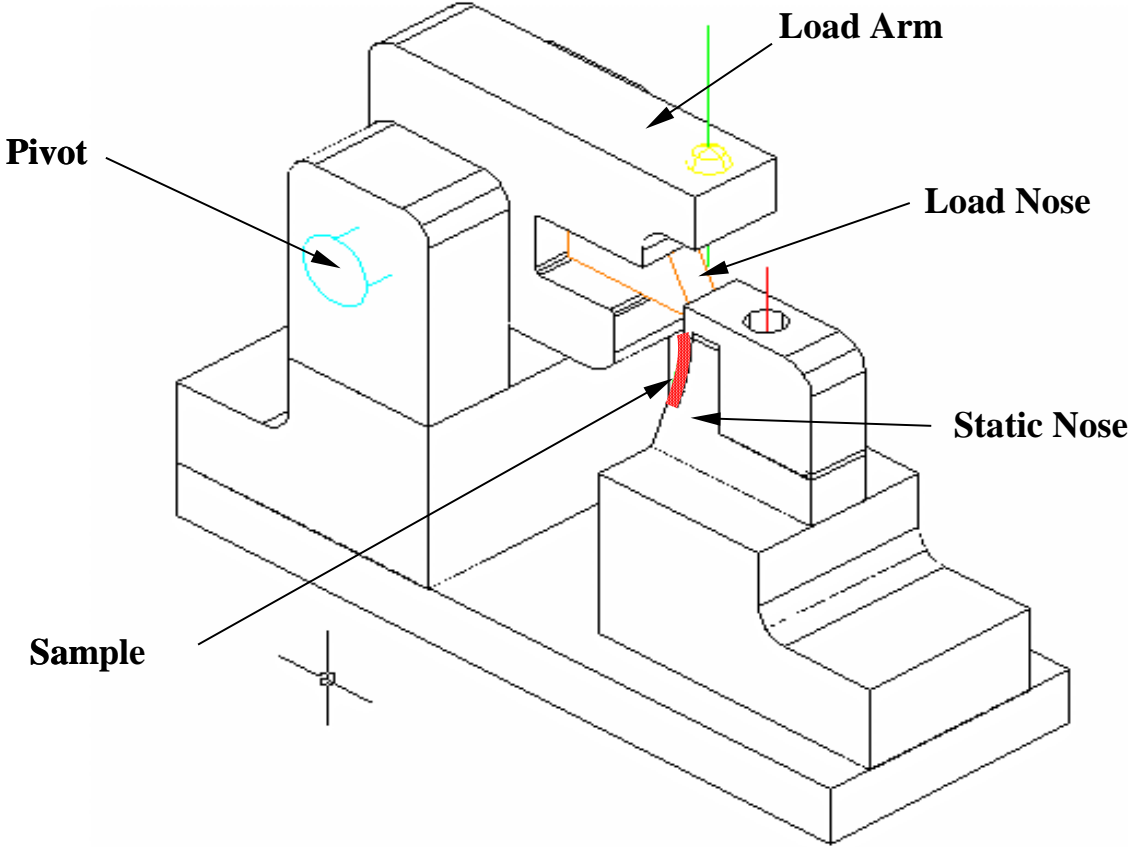
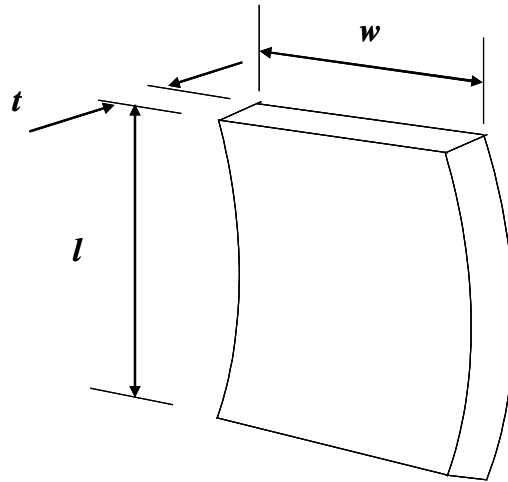


Figure 38 Schematic of ILSS device

The rig was designed to fit in an Instron 1195 loading frame. This would provide the correct loading rate required; 10mm/min, the same as the quasi-static testing for UCS and SEA data.

Slices were cut from the Ø88.9mm tube samples, and then these rings were cut into smaller samples for testing. (Figure 39)



**Figure 39 ILSS Sample**

The initial sample size was  $l = 15\text{mm}$ ,  $w = 10\text{mm}$ .

The samples were fixed to the static platform using cyanoacrylate applied on the rear surface. The load nose was positioned so that it just touched the lower ledge of the sample block. For samples with a  $t < 4\text{mm}$ , a shim was required to ensure that the loaded edge made contact with the centre of the sample. At least 6 samples of each type were tested.

ILSS was calculated using:

$$\tau_{\max} = \frac{P_f}{w.l} \quad (14)$$

Where  $\tau_{\max}$  is interlaminar shear strength,  $P_f$  is the load on the specimen at failure,  $w$  is the width of the specimen and  $l$  is the length of the specimen.

The shear strength is calculated from equation (14) . It assumes that the shear stress through the specimen is uniform, hence the sample fails simultaneously at all points within the delamination area, which requires a homogenous stress distribution and a sample without defects, which Rosselli and Santare[72] admit is almost impossible in practice, but it does give a quick estimate of the average shear stress.

After initial testing it was found a number of samples began to crush rather than shear; i.e. there was no homogenous shear stress, only a crushing stress. In order to induce shear, the shear area needed to be reduced or the contact area increased, increasing the latter would have increased the shear area also, so it was decided to reduce the length. Specimen dimensions of  $w = 10$  and  $l = 10\text{mm}$  were then tested.

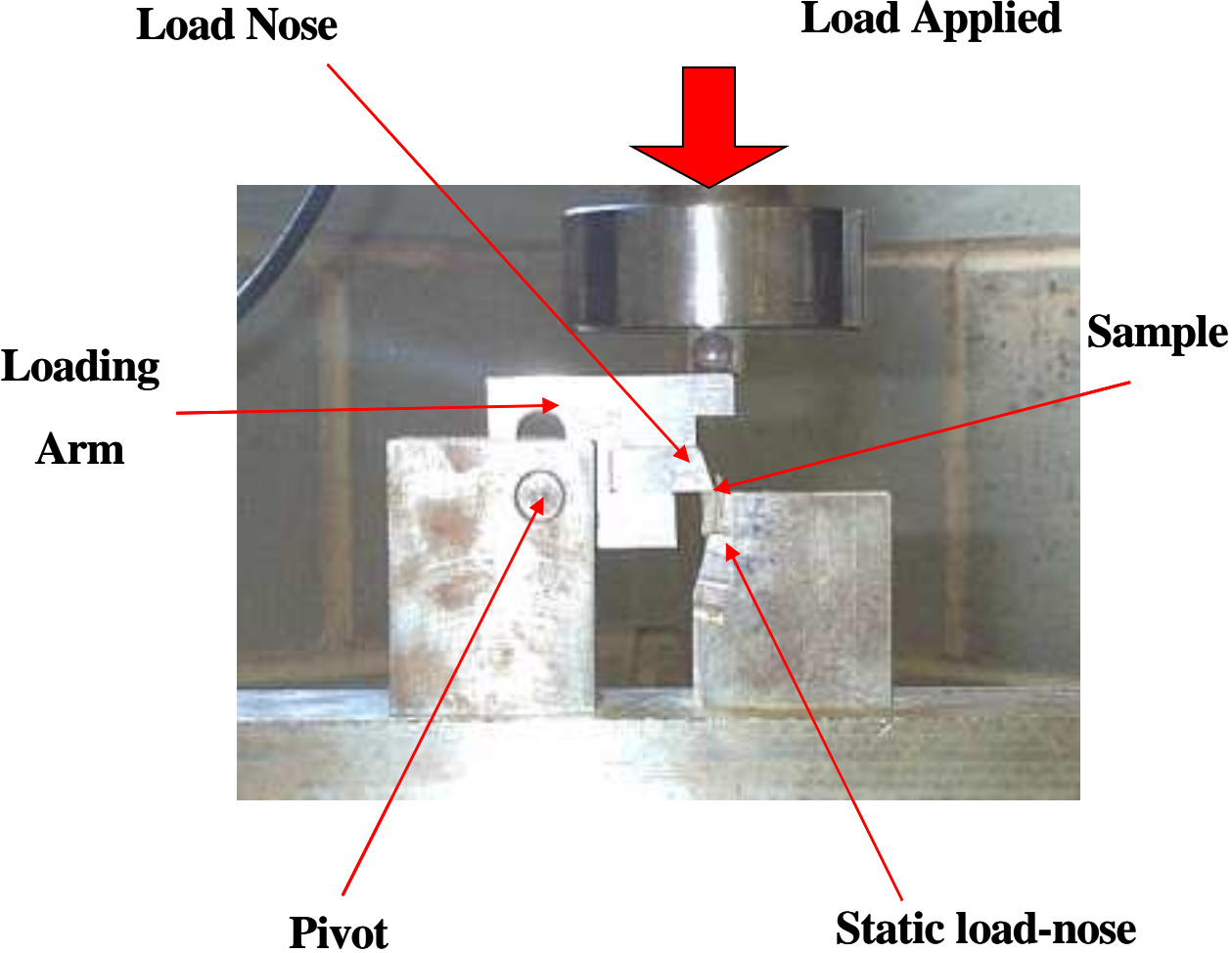


Figure 40 ILSS Rig under Setup

### **3.6.5. Stress Concentration Factors (SCF)**

Using the methods described by Quinn and Barton [80] the stress concentration factor can be found by thermal analysis. A range of test specimens were manufactured and cut to a length of 70mm.

The specimens were loaded in an Instron 8802 servo-hydraulic machine at a loading frequency of 10Hz with a mean load of  $2.3\text{kN} \pm 1.15\text{kN}$  (thus a dynamic loading).

The Delta-therm System was used to measure the stresses. This uses Thermoelastic Stress Analysis (TSA) to produce a full-field stress map by imaging temperature changes with a sensitive infrared camera (Figure 41). All materials change temperature when loaded in compression or tension. These temperature changes are then related to the sum of the principle stresses by means of a calibration constant which is a function of the material used and the infra-red detector characteristics.

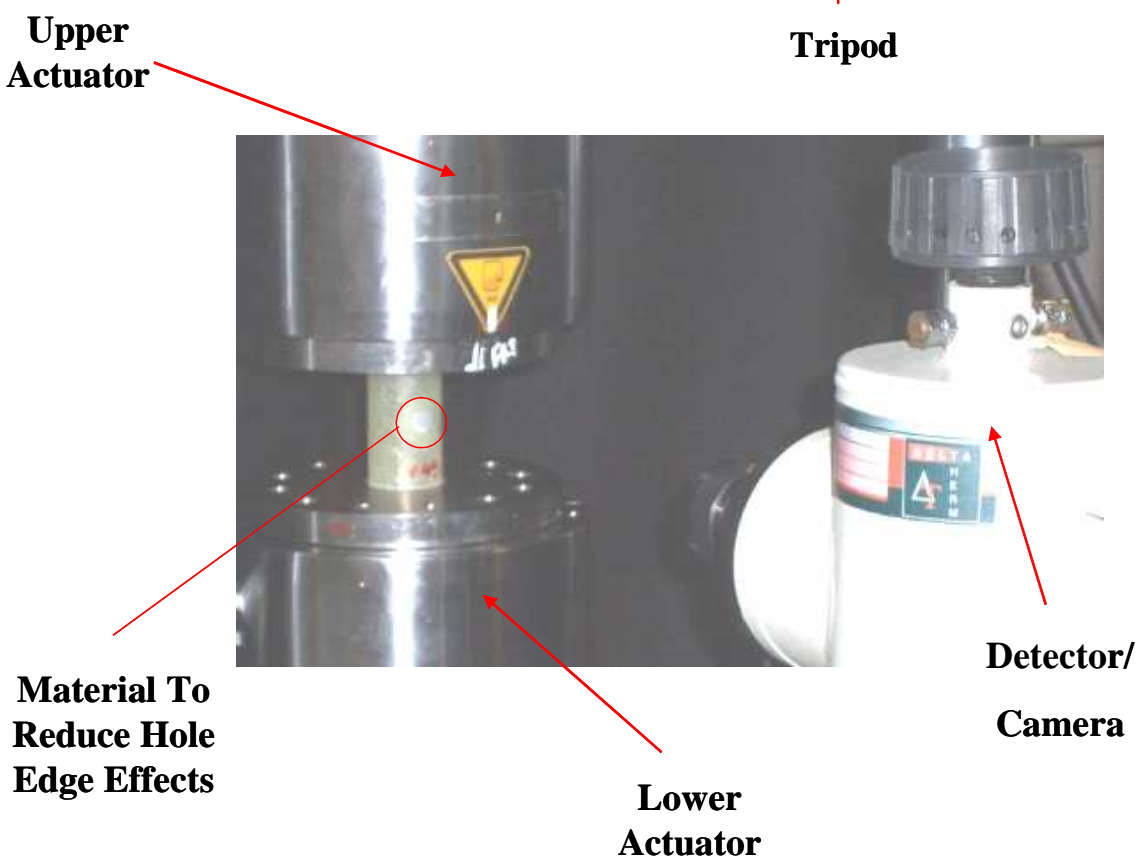
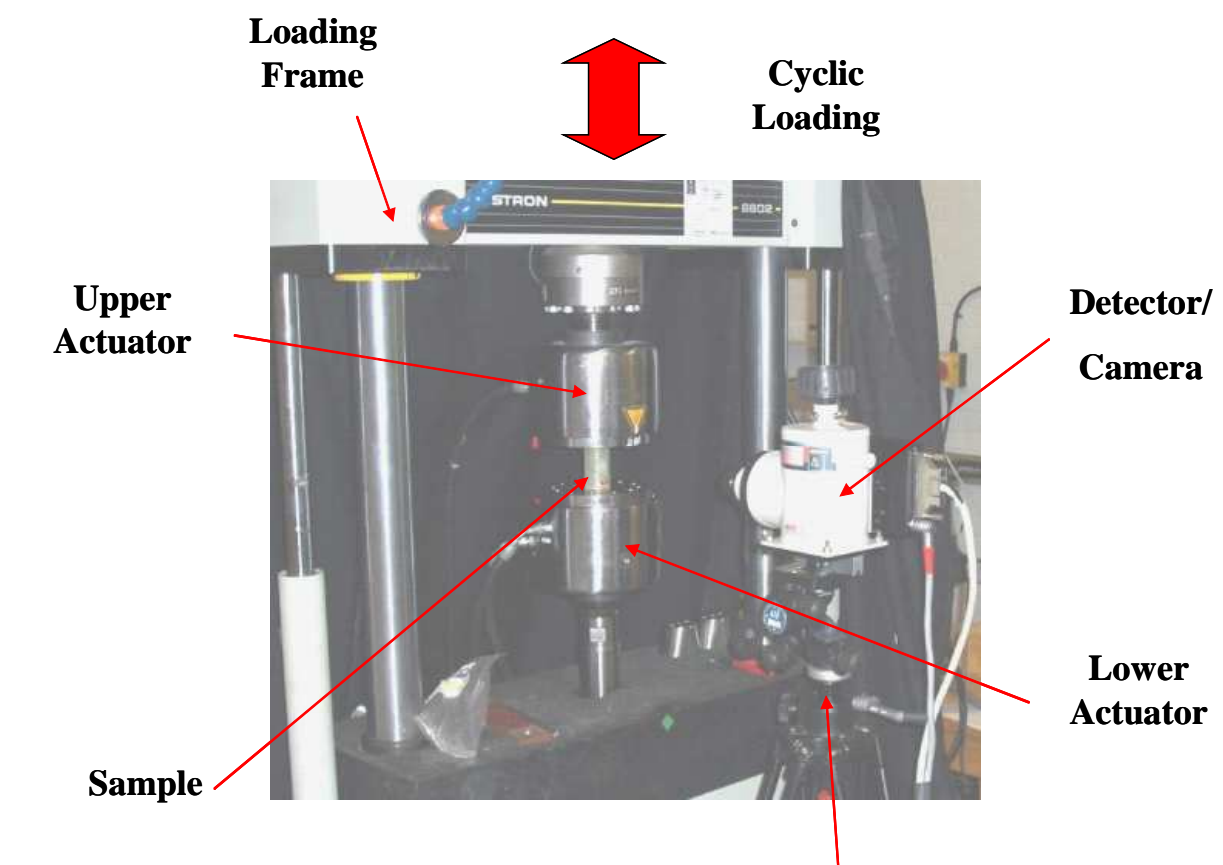


**Figure 41 TSA Apparatus**

### 3.6.6. Test Matrix

The following test matrix (Table 5) shows the fibre, resin and orientations used for the majority of the tube crush work.

**Table 5 Crush Testing Matrix**

Tube	Geometry	Reinforcement		Resin	Orientation	Hole size mm	Hole position mm	Impact level J
		Type	Material					
Ø38.1	O	NCF	Glass	P	0-90	5, 10, 16	15, 25, 45	1.5, 3, 6, 9
Ø38.1	O	NCF	Glass	P	90-0	5, 10, 16	25	1.5, 3, 6, 9
Ø38.1	O	NCF	Glass	P	A-0	5, 10, 16	25	1.5, 3, 6, 9
Ø38.1	O	NCF	Glass	P	+45	5, 10, 16	25	1.5, 3, 6, 9
Ø38.1	O	Braid	Glass	P	Biaxial 30	5, 10, 16	25	1.5, 3, 6, 9
Ø38.1	O	Braid	Glass	P	Biaxial 60	5, 10, 16	25	1.5, 3, 6, 9
Ø38.1	O	Braid	Glass	P	Triaxial 60	5, 10, 16	25	1.5, 3, 6, 9
30x30	□	NCF	Glass	P	0-90	5, 10, 16	25	1.5, 3, 6, 9
Ø88.9	O	Braid	Carbon	V	Biaxial 30	16	30	
Ø88.9	O	Braid	Carbon	P/V/E	Biaxial 45			
Ø88.9	O	Braid	Carbon	V	Biaxial 60	16	30	
Ø88.9	O	Braid	Carbon	V	Biaxial 75			
Ø88.9	O	Braid	Carbon	P/V/E	Triaxial 45			

Resin types: P - Polyester, V - Vinylester, E - Epoxy

Note the glass samples were 2mm wall thickness, the braided carbon were 4mm wall thickness.

### **3.7. Post Test Procedures**

#### **3.7.1. Microscopy of Crush zone**

To understand the failure mechanisms of the specimens an image of the crush zone was required. To achieve this, the samples were cast in resin whilst under load using clear polyester casting resin initiated by 2% Butanox M50. Once cured, the sample was removed from the casting pot, sectioned through the damage zone using a diamond tipped cutting wheel and then trimmed before being re-potted in 40mm diameter casting pots. Finally, the samples were cut and polished to a 13mm thickness, using a Struers Dap-7 polishing machine (Figure 42). This was fitted with Silicon Carbide paper with grit sizes in the range of 240-2500 grit. Alumina additive helped to ensure a smooth final finish.



**Figure 42 Struers Dap-7 polishing machine**

To obtain a complete image of the crush zone a minimum of 30 images were required; these were collected using a Zeiss microscope and Aphelion Imaging software (Figure 43). The resulting digital images could then be collated to produce a collage of the entire crush zone.



**Figure 43 Zeiss microscope and Aphelion imaging software**

### **3.7.2. Validation of Braided Carbon Samples**

In order to establish the validity of the performance of the carbon mouldings, a biaxial  $\pm 45$  flat plaque was moulded with vinyl-ester resin. This was used for coupon testing to find tensile stiffness. The experimental results were compared to theoretical results calculated using laminate theory and the Rule of Mixtures, and were found to lie within acceptable boundaries, see appendix 0

## 4.0 Results

This chapter looks at the experimental findings for the testing work described in chapter 3.0. Firstly, it considers the large braided tube work and looks at failure modes. Then it examines the tube results and develops an understanding of material properties, failure modes, and threshold levels associated with different forms of damage. The threshold level is defined as the level at which the failure mode changes from progressive failure to global failure, and is often associated with a standard deviation of  $> 10\%$  [99]. Below this threshold level the tube will crush and absorb energy as if undamaged. Whilst above this level the tube will see a drop in SEA.

## 4.1. Carbon tubes

The carbon tubes were crushed at a quasi-static rate of 10mm/min. The following section looks at the effects of changing the resin type upon crush mode and energy absorption. The effects of changing the braid type are investigated and the final subsection involves changing the fibre angles in the braid. The data presented in the tables is for the mean SEA and the standard deviation from that mean unless stated.

### 4.1.1. Resin Comparison with Biaxial Tubes

The results present below are for biaxial braided carbon tubes moulded with three different resin types, tested quasi-statically (Table 6)

**Table 6 Biaxially Braided Carbon Data with Different Resins**

Fibre Type	Fibre angle (°)	Resin *	SEA kJ/kg (std Dev %)
Biaxial	45	P	34.8 (11.4)
Biaxial	45	V	47.3 (6.3)
Biaxial	45	E	54.8 (1.4)

\* Where; P = Polyester, V= Vinyl-ester and E = Epoxy

The Load displacement curves for these samples can be seen in Figure 44 and examples of the samples post crush can be seen in Figure 45.

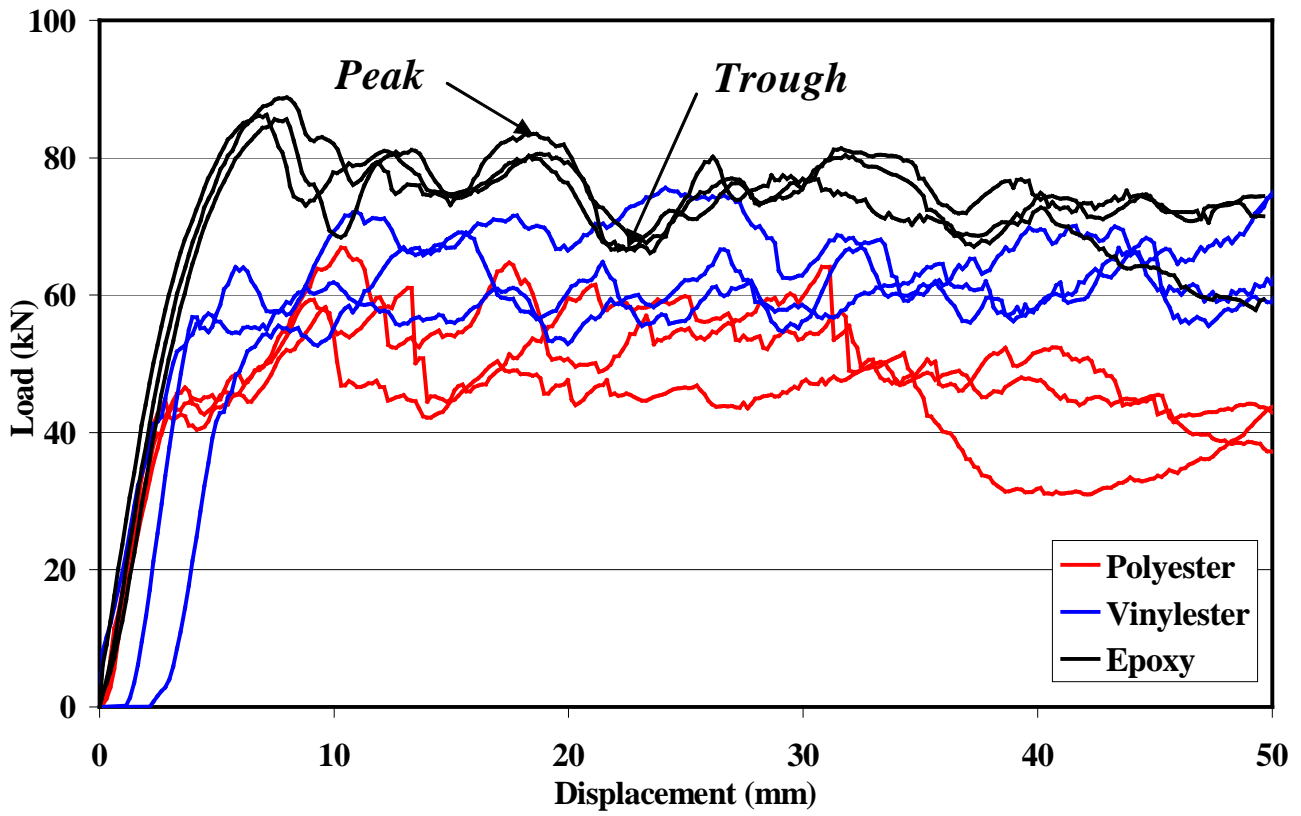


**Figure 44 Load Displacement Curve for Biaxially Braided Carbon Tubes Showing Resin Effects.**



**Figure 45 - Polyester and Vinylester Tubes Post Crush**

These were all manufactured with a fibre angle of  $\pm 45^\circ$  in each layer. The dominant mode of failure amongst the biaxial tubes was buckling, initially the vinylester and polyester tubes began to splay, but after 10-12 mm of crush they began to buckle.

The polyester tubes failed at both ends of the specimen. The vinylester tubes created a small debris wedge during crush, but the majority of the fibres remained intact and undamaged during the crush. The epoxy tubes failed through a pure buckling mode of failure. No debris wedge was observed and all the fibres appeared to be intact. From the post crush images (Figure 46) it can be see that the epoxy exhibits a concertina type folding/buckling mode which is very similar to the modes of failure seen in the metal tubes tested by Fernie [4].



**Figure 46 - Epoxy Biaxial tubes during crush and post crush**

The epoxy tubes showed the highest value of energy absorption, 54.8kJ/kg which is an increase of 36.5% over the value for polyester of 34.8kJ/kg. (see

Table 6)

### 4.1.2. Braid Type.

This section of results is concerned with the braid type. Results for biaxially braided tubes at an angle of 45° were presented in the previous section. The braid types used in this section are triaxially braided tubes, biaxially braided tubes with the addition of axial (inter-ply) fibres between each layer of biaxial braid and triaxially braided tubes with the inter-ply fibres. Each type of braid was tested with all 3 types of resin (see Table 7).

**Table 7 Braided Carbon Data for Different Braid Types with Different Resins**

Fibre Type	Fibre angle (°)	SEA kJ/kg (std Dev %)		
		Polyester	Vinylester	Epoxy
Triaxial	45	37.7 (3.7)	44.6 (6.9)	56.7 (8.4)
Biaxial + interply	45	36.7 (3.8)	45.1 (1.5)	50.8 (5.4)
Triaxial+ Interply	45	34.5 (4.4)	41.8 (3.1)	54.4 (1.9)

#### 4.1.2.1. Triaxial Tubes

The specimens again were braided to an angle  $\pm 45^\circ$  in each layer. The tube specimens failed by a mixture of failure modes. There was some buckling in the tubes as seen by the load displacement curve showing the large peaks and troughs. However, in each of the samples a debris wedge was created, although a high percentage of the fibres remained intact after the crush, and fronds developed on the outer layers giving the appearance of splaying. The percentage of axial to braid fibres was approximately 20%.

The Load displacement curves for these samples can be seen in Figure 47 and examples of the samples post crush can be seen in Figure 48

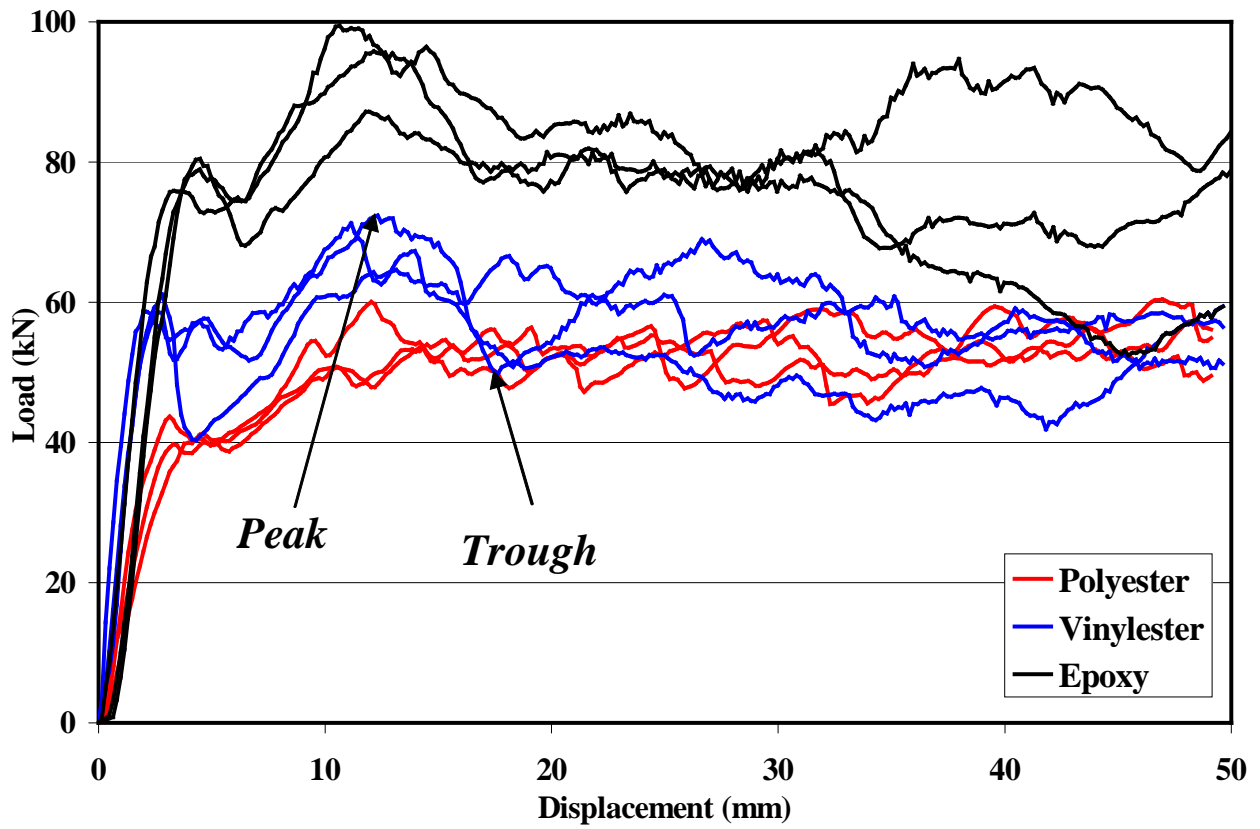


Figure 47 Load Displacement Curve for Triaxially Braided $\pm 45^\circ$  Carbon Tubes



Figure 48 - Vinyl Ester Triaxial Tube Post Crush



**Figure 49 - Epoxy Tri-axial tube during crush and post crush**

In a similar trend to the biaxial tubes, the epoxy tubes provided the highest energy absorption followed by vinylester and polyester. However, the values of SEA obtained showed only a slight increase on the biaxial results (~3%) (see Figure 49 for images).

**4.1.2.2. Biaxial and Inter-ply**

All the biaxial tubes with interply fibres failed through a splaying mode. Fronds were created suggesting that the mode of failure has changed from buckling to a splaying mode. The braid fibres showed some evidence of damage; however, the axial inter-ply fibres were intact after the crush. The inner layer was forced up inside of the tube in all specimens. The epoxy tubes again showed the highest energy absorption, followed by vinylester and polyester. The overall energy absorption levels were similar to those obtained for triaxially and biaxially braided tubes.

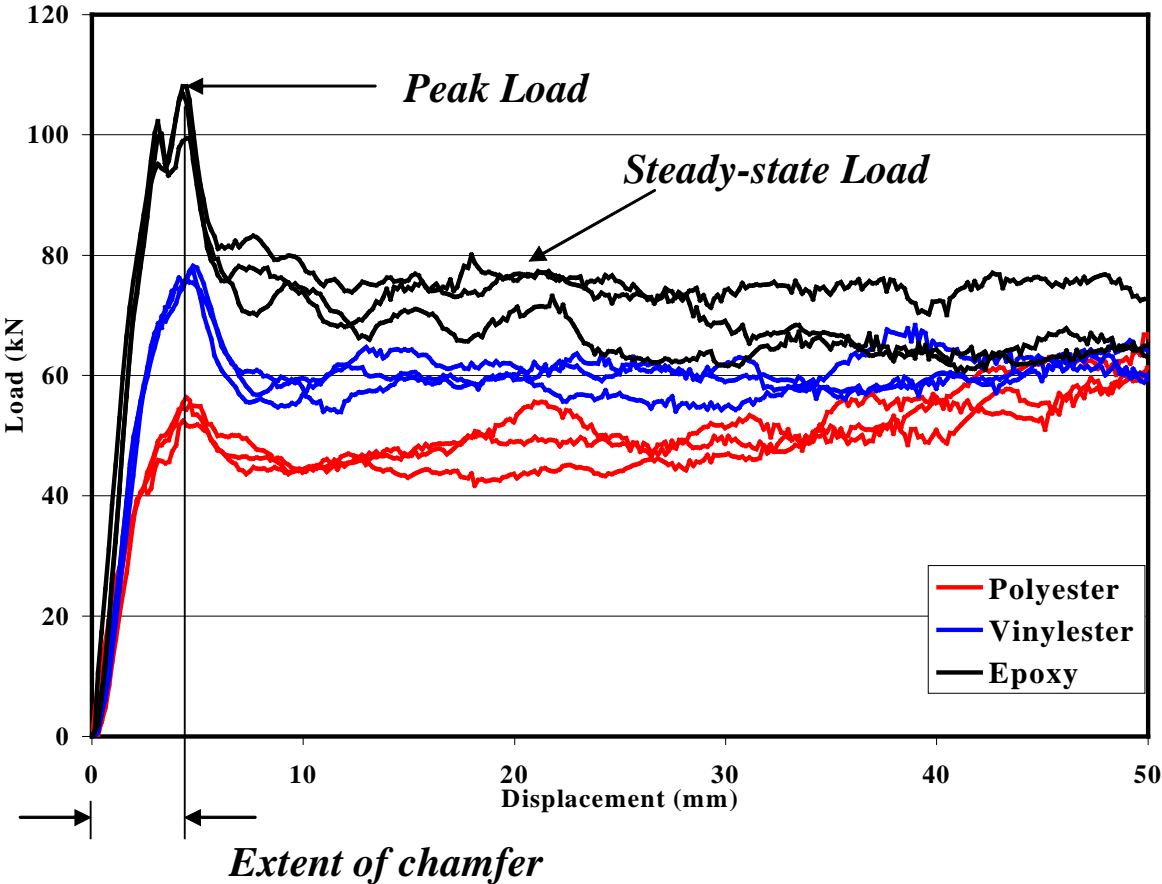


**Figure 50 Carbon Biaxially Braided Tubes with Interply Fibres**

From the load deflection curve (Figure 50) in comparison with Figure 44 it can be seen that the trace is quite different. The load rises steadily as initiated by the chamfer to a peak load and then falls to a steady state load. This peak is due to the interply fibres increasing the in-plane strength of the composite considerably; a decrease in load of this magnitude is not seen

for the biaxial tubes because of the lower axial strength. Looking at the steady state load the biaxial tubes have a trace consistent with a buckling mode of failure, whereas the tubes with the addition of axial fibres show a much smoother trace with smaller peaks and troughs, usually associated with a splaying mode of failure (for samples see Figure 50). In comparing peak loads with the biaxial tubes the addition of axial fibres significantly increases the maximum load. Without the axial fibres the peak load for the epoxy tubes reaches a maximum of 90kN, when the axial fibres are added this increases to 110kN.



**Figure 51 - Polyester and Epoxy tubes post crush**

### 4.1.2.3. Triaxial with Inter-ply

These tubes all failed in a similar manner to the biaxially braided tubes with the interply layer. The tubes initially splayed and then continued to form large fronds throughout the crush. A debris wedge was formed inside the fronds, mainly from the braid fibres. The axial inter-ply fibres were again clearly visible and undamaged after the crush. Figure 52 shows the load displacement curves for these samples.

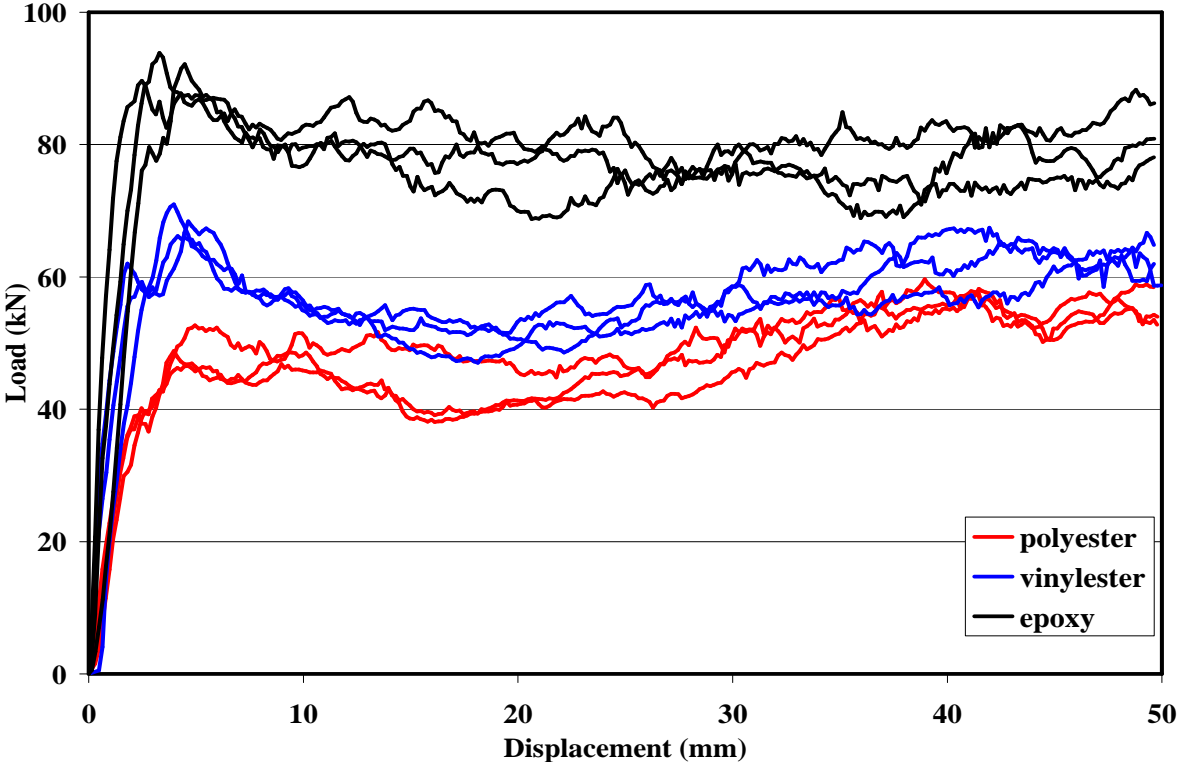


Figure 52 – Carbon Triaxially Braided tubes with Interply

The Polyester tubes showed the lowest level of energy absorption with the epoxy again the highest (vinyl-ester and polyester samples can be seen in Figure 53).



**Figure 53 - Vinyl ester and Epoxy tubes post crush**

There was no significant change in the level of energy absorption between each of the braid architectures or between the different failure modes associated with them, only between the different resin systems.

### 4.1.3. Braid Angle

This section involves biaxial carbon samples braided at different angles. Table 8 provides the SEA data for these.

**Table 8 Braided Carbon Data for Different Braid Angles**

Fibre Type	Fibre angle (°)	Resin	SEA kJ/kg (std Dev %)
Biaxial	30	V	45.9 (0.9)
Biaxial	45	V	47.3 (6.3)
Biaxial	60	V	43.6 (8.6)
Biaxial	75	V	34.1 (5.0)

The load displacement curves for these can be seen in Figure 54.

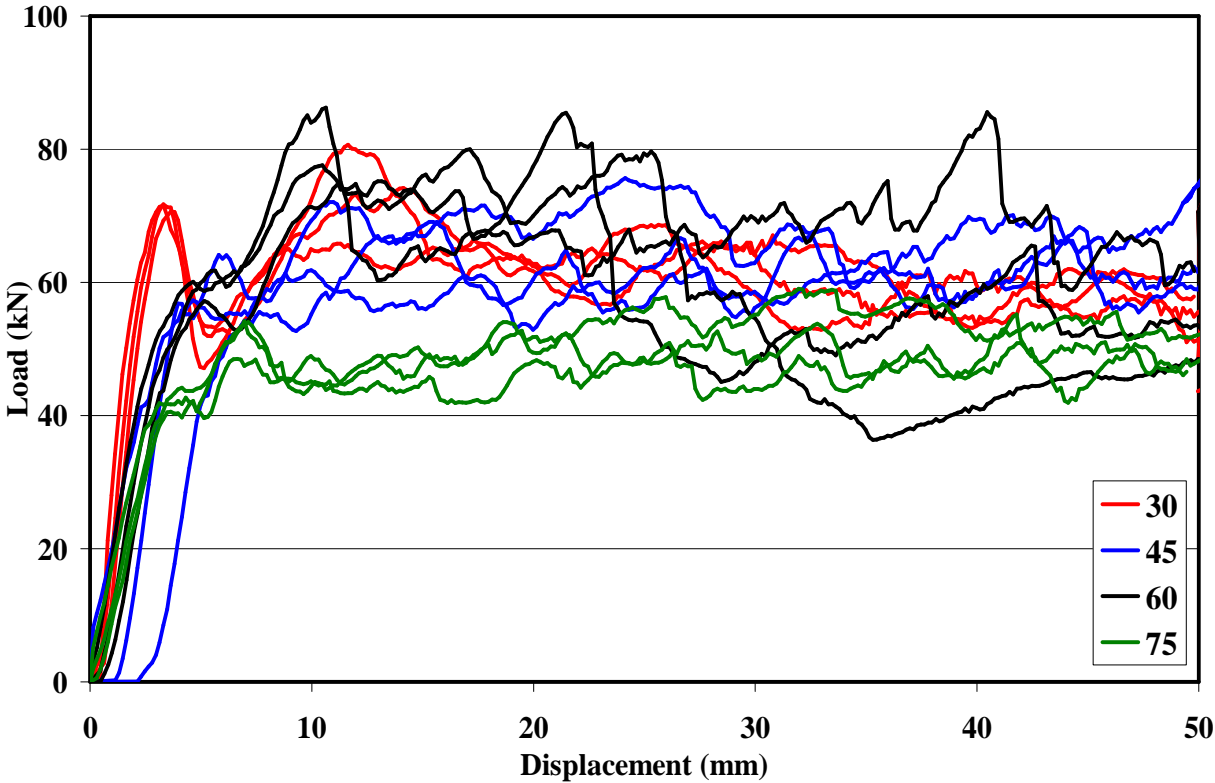


**Figure 54 – Carbon Braid Angle Comparison**

Each tube crushed differently. The 30° tube crushed with a hybrid buckling/splaying mode, with a debris wedge created and clearly visible fronds formed on the outer layer (Figure 55). The 45° tube again splayed initially, but there was some evidence of buckling. The 60° tubes failed by buckling, and 2 specimens developed cracks parallel to the fibres and around the circumference; one of the specimens began to crush/buckle at this point (Figure 56).

In terms of energy absorption, the highest SEA of 47.3kJ.kg was seen in the  $\pm 45^\circ$  samples. The  $\pm 30^\circ$  and the  $\pm 60^\circ$  tubes were within 8.5% of this value. This value suggests that the failure is dominated by the matrix, and that fibre angle has a much smaller effect on energy absorption. The 75° tubes however, showed a much lower SEA. This was attributed to poor wet out due to the higher fibre content. The mode of failure was similar to the 60° tubes, a concertina type buckling.



**Figure 55 Biaxial 30° tube post crush**



**Figure 56 Biaxial 60° tube Post Crush Showing Buckling/Folding**

**4.1.4. Damage Analysis**

A preliminary study was undertaken to compare the effects of tubes with pre-damage to a undamaged tube. This was accomplished by drilling a 16mm diameter hole in the side of a specimen at 25mm from the chamfer. One sample of each type of tube was crushed quasi-statically to evaluate the effects of the hole. The data is presented in Table 9. There is no standard deviation presented for the samples with a 16mm hole as only one sample of each braid type was tested.

**Table 9- Data Table for Specimens with Holes**

Fibre Type	Fibre angle (°)	Resin*	Hole size (mm)	SEA kJ/kg (std Dev %)
Biaxial	30	V	-	45.9 (0.9)
Biaxial	30	V	16	44.1
Biaxial	60	V	-	43.6 (8.6)
Biaxial	60	V	16	40.41

The following figures (Figure 58, Figure 59 & Figure 60) show the difference in failure modes for the samples. The biaxial ±30 tubes showed more splaying and fragmentation, the sample cracked at the edge of the minor axis edge of the hole and propagated along the tows down to the crush zone. The undamaged section can clearly be seen in Figure 58.

These results show that there is no significant change in SEA between the damaged specimens and the undamaged specimens for either of these braid angles with different crush modes although the effects of the hole can clearly be seen in the following figures. It would appear that this size of hole at this position has little effect in quasi static crush upon these tubes, although buckling can be seen clearly in the biaxial ±60 tubes initiated at the hole. This effect can be seen in the load displacement curves (Figure 57).

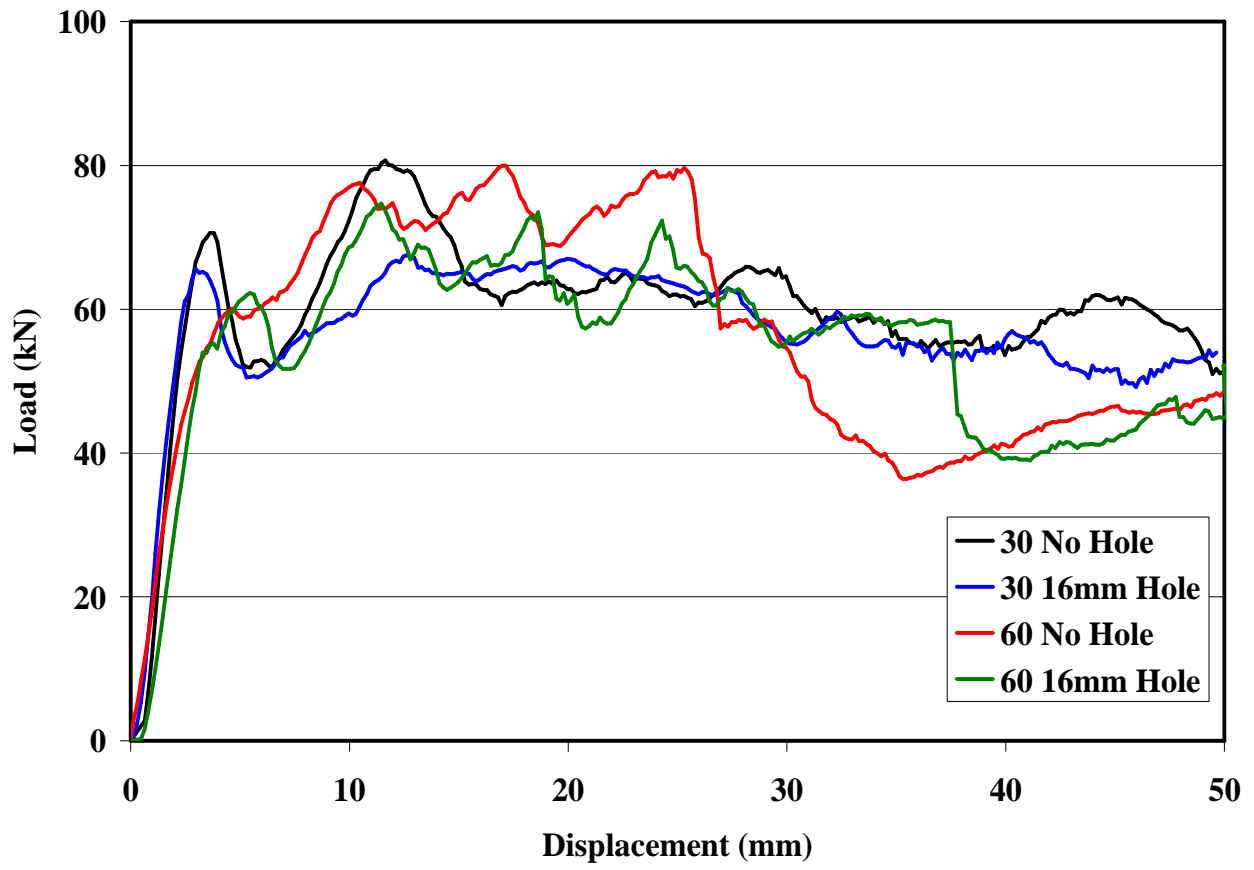
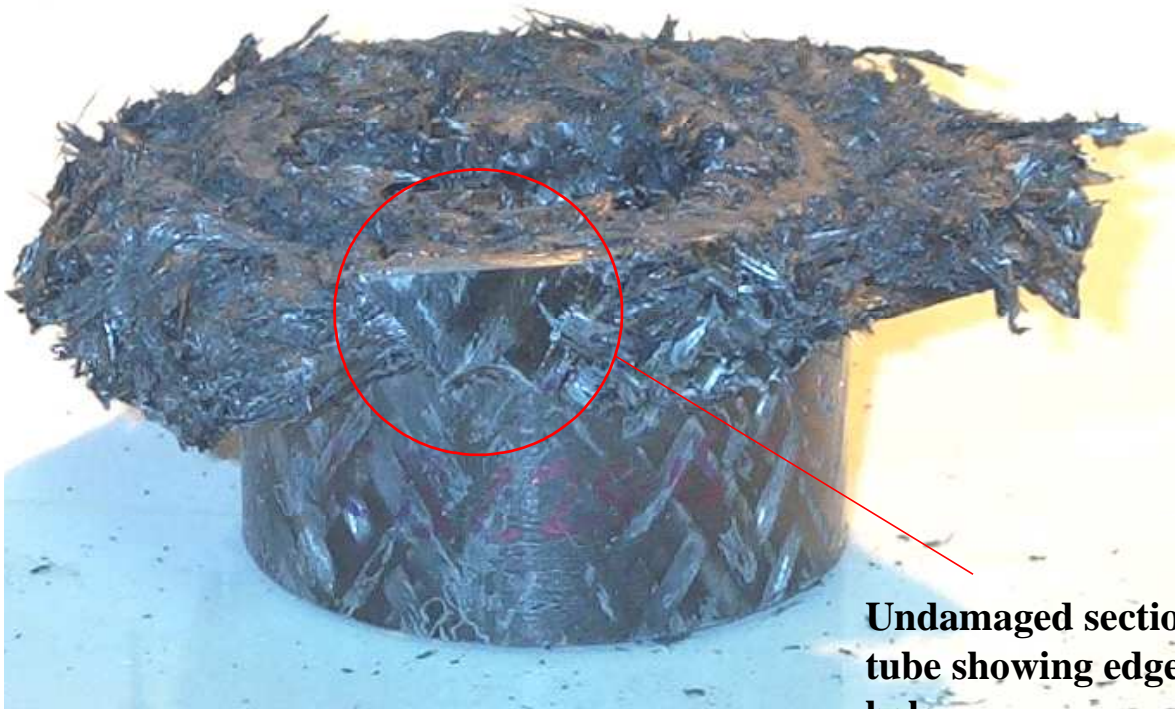


**Figure 57 Load Displacement Curves for Samples With and Without Holes**



**Undamaged section of tube showing edge of hole**

**Figure 58 -  $\pm 30$  Biaxially braided tube with 16 mm hole post crush**



**Figure 59 -  $\pm 60$  Biaxially braided tube with hole during crush, showing cracking/buckling across tube from edge of hole**



**Figure 60 -  $\pm 60$  Biaxially braided tube with hole post crush showing buckling failure**

## 4.2. Glass Tubes

This section looks at the bulk of the test work that involved glass tubes. The tests were undertaken with the Ø38.1mm tubes and the square 30x30mm tubes at a quasi-static rate of 10mm min<sup>-1</sup> and a dynamic rate of 5ms<sup>-1</sup>. The first sub-sections look at undamaged tubes and compares the fibre type, rate and resin effects. The following two sections look at the effects of non-service damage through stress concentrations and impact damage. A way of improving the damage tolerance through interleaves is investigated and the ultimate compressive stress is measured.

At this point, it is useful to note that in this section a number of different failure modes have been seen. These were classified by Warrior et al [98, 99, 139] for continuous filament random mat glass/polyester and NCF composites. In their studies, the tubes failed in 3 distinct and different modes: Failure mode 1 - this was the well-known progressive crushing mode displayed by composites; Failure mode 2 - this was an undesirable global failure, before steady-state crushing load was reached, typically caused by a through-thickness crack originated at the damage zone, and propagating circumferentially causing the tube to split and collapse; Failure mode 3 - progressive crushing was established and a local drop-off in load was observed in the vicinity of the damage zone. This drop-off was larger than one that could be attributed to just the reduction in crushing area of the tube, but was smaller than the large decrease seen in failure mode 2. Cracking was seen, but was self-limiting and the load recovered to the steady-state condition after the crush zone passed through the damaged area.

In this study these definitions of the failure modes will continue to be used. They were determined through observation of the sample under test and the shape of its load displacement curve.

These failure modes are illustrated on a load displacement curve in Figure 61 from [98] and Figure 62

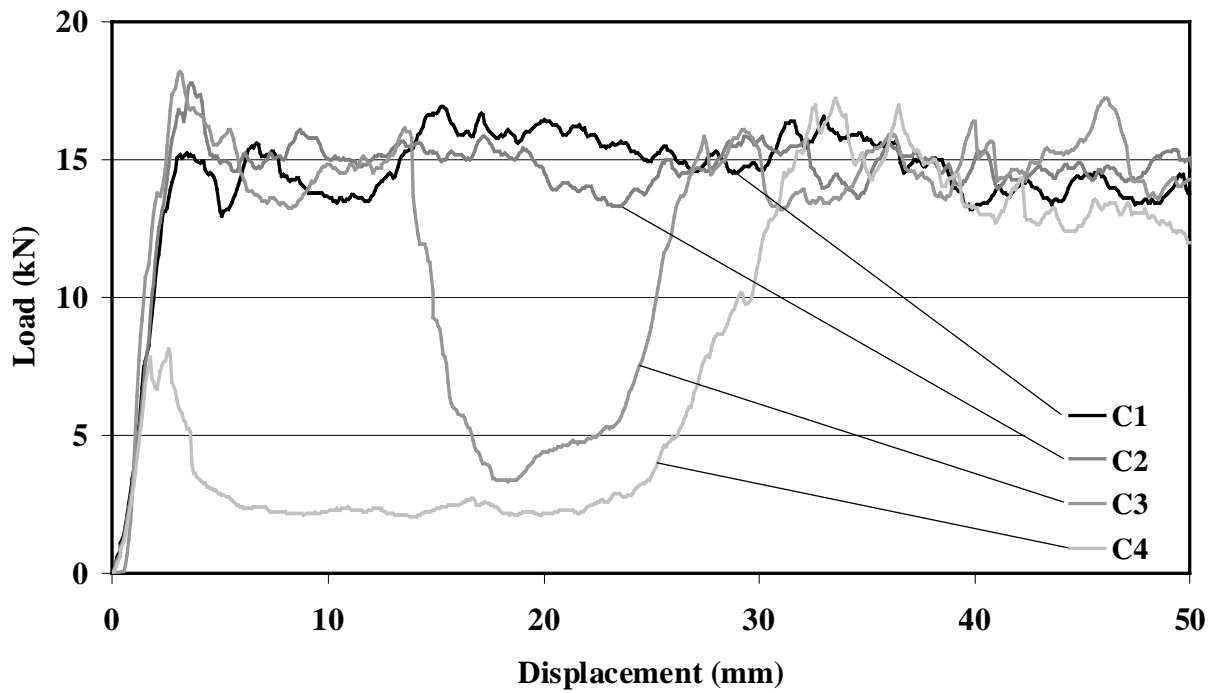


**Figure 61 Load versus displacement curve for 0-90 NCF tubes, showing characteristic failure modes; mode 1, in samples C1&C2, mode 2 (global failure) in sample C4 and mode 3 (local failure) in sample C3 from [98]**

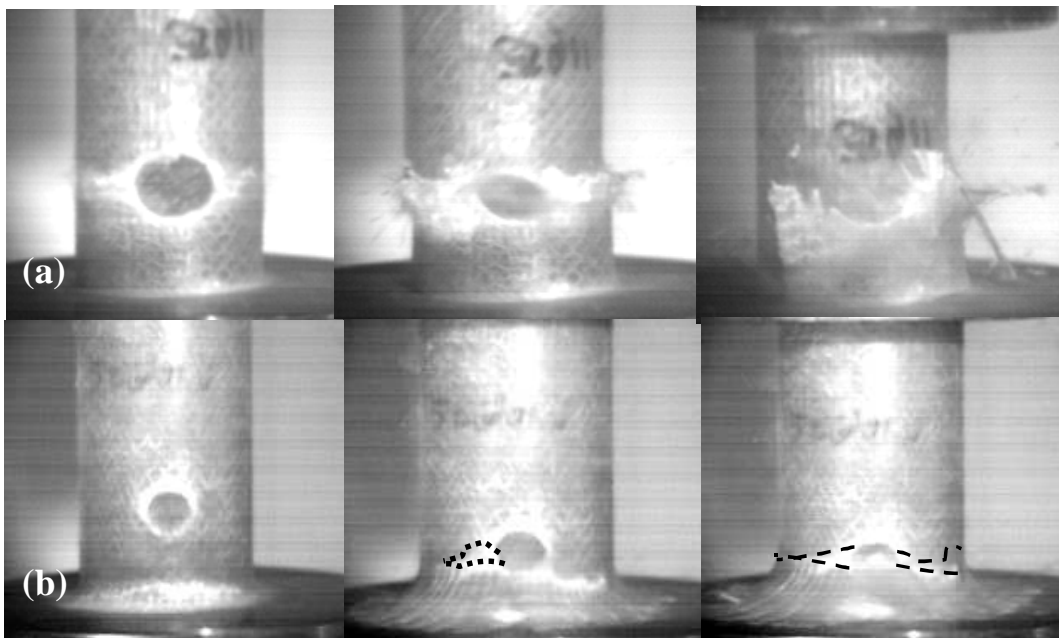


**Figure 62 Showing (a) Mode 2 failure and (b) Mode 3 failure**

### 4.2.1. Sample Classification

In order to simplify classifying and describing the tubes in tables and figures, and alphanumeric numbering system was developed for the small glass tubes.

The prefix refers to the geometry and type of fabric used:

C	-	Circular sample from 0-90 NCF
CiL	-	Circular sample from 0-90 NCF with interleaf
C90	-	Circular sample from 90-0 NCF
C45	-	Circular sample from $\pm 45$ NCF
Q	-	Square sample from 0-90 NCF
CB30	-	Circular $\pm 30^\circ$ biaxial braided sample
CB60	-	Circular $\pm 60^\circ$ biaxial braided sample
CT60	-	Circular $0\pm 60^\circ$ triaxial braided sample

The next information refers to type of damage

M	-	Undamaged sample
5m	-	Sample with 5mm hole
16m	-	Sample with 16mm hole
3J	-	Sample with 3J impact damage
9J	-	Sample with 9J impact damage

The numbers after the letter refer to the position of the damage

15	-	15mm from chamfer
30	-	30mm from chamfer

The final letter, where applicable, refers to quasi-static testing (S) or dynamic testing (D)

## 4.2.2. Architecture and Rate Effects

The mean SEA results, standard deviations and failure modes are presented in Table 10. The information regarding layers and volume fraction can be found in Table 2.

**Table 10 Undamaged Small Tube Test Data**

Fibre Type	Test Ref.	Quasi-static SEA (kJ/kg) (std. Dev %)	Failure mode	Dynamic SEA (kJ/kg) (std. Dev %)	Failure mode	% decrease in SEA with rate
NCF 0-90	C0m	39.0 (2.7)	1	32.7 (2.4)	1	16.2
NCF 0-90	Q0m	39.8 (6.9)	1	28.9 (4.6)	1	27.4
NCF 90-0	C90m	50.4 (1.4)	1	39.8 (5.8)	1	21.1
NCF ±45	C45m	55.4 (8.0)	1	29.6 (7.7)	1	46.6
Braid ±30	CB300m	44.1 (1.1)	1	30.7 (22.7)	1	30.4
Braid ±45*	CB450m	38.8 (3.8)	1	48.4 (1.4)	1	-24.7
Braid ±60	CB600m	45.1 (23.0)	1&3	52.6 (5.1)	1	-16.6
CoFRM*	Co0m	74.6 (3.8)	1	70.2 (4.0)	1	5.8

\*Data from [98, 138]

The undamaged NCF tubes under static and dynamic testing, failed by progressive crushing in the splaying mode. The 0-90 tubes (C1) split into 5 or more fronds. The fronds exhibited significant elastic energy and sprung-back upon removal of the load - the static SEA was 39.0kJ/kg, with a standard deviation over the three test samples of less than 3%. The 90-0 (C901) tubes also split into fronds, however, there was significant curvature of the fronds and the elastic spring-back seen in the 0-90 tubes was not displayed and there was visually more resin break-up and fibre damage in the fronds, – consequently the SEA was higher - 50.4kJ/kg with a standard deviation of 1.4%. The hoop fibres on the external layer of the 90-0 tubes had the effect of constraining the axial fibres, forcing the tube to crush progressively and restricting splaying seen in the 0-90 orientation tubes – resulting in greater accumulation of intralaminar damage giving a higher SEA.

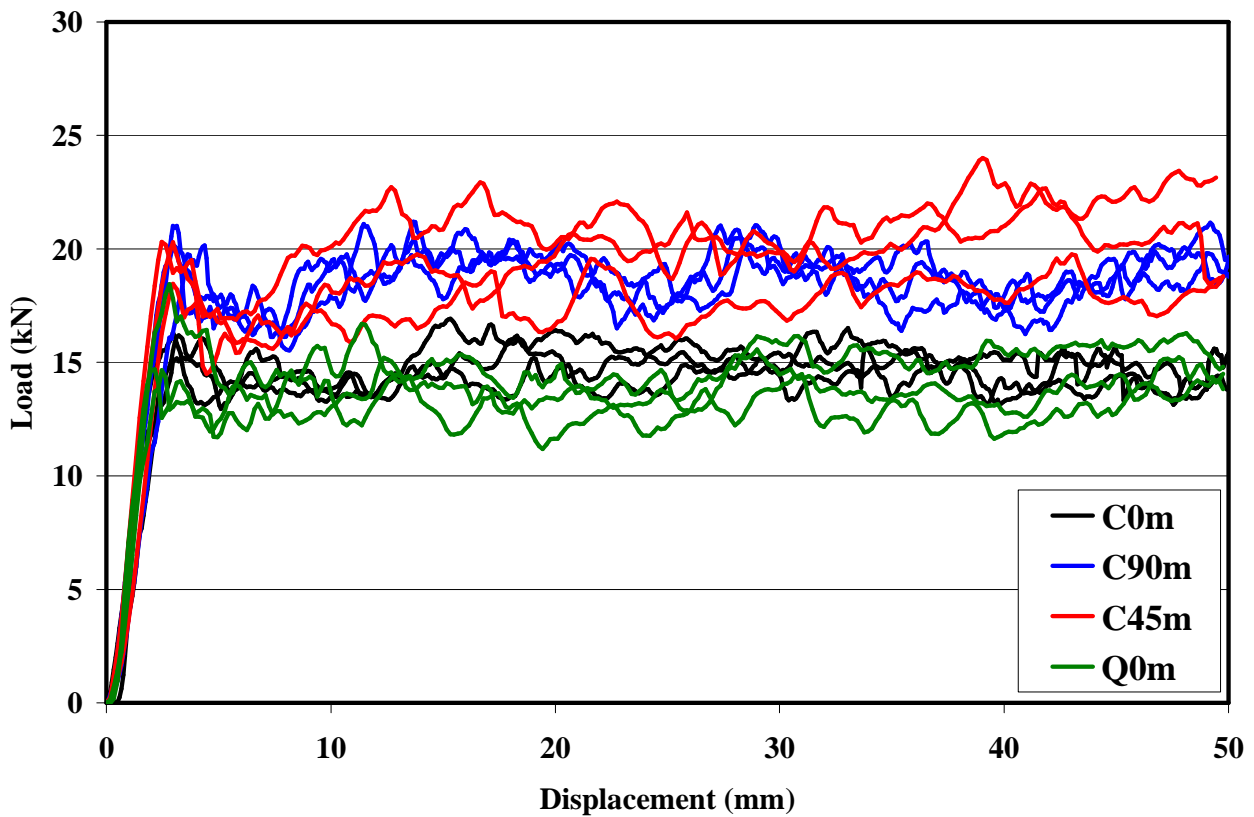


**Figure 63 Load Displacement Curve for NCF tubes**

Comparing the 0-90 and the 90-0 architectures quasi-statically, from the load displacement curves (Figure 63), it can be seen that the 90-0 samples crush at a higher average load of 18-20 kN whereas the 0-90 tubes crush at a load of approximately 15kN, (a crushing stress of 75.4-83.8MPa for 90-0 samples and 62.8 MPa for 0-90 samples). At dynamic rates, the resin was seen to pulverize leaving the fibres unsupported and more able to deform, resulting in a lower SEA (reduced by 16% and 21% for 0-90 and 90-0 respectively). Quasi-statically the NCF  $\pm$  45 tubes showed a splaying mode of crush similar to the 90-0 tubes and absorbed 55.4 kJ/kg of energy (with a deviation of 8.0%), the highest seen for the NCF, but dynamically, the mode of failure is very different. The fibres are unconstrained and splay apart in a spectacular shaped failure absorbing low levels of energy, SEA = 29.6kJ/kg, (a reduction of 46.6% in SEA). (Figure 64)



**Figure 64 Modes of failure of NCF tubes, clockwise from top left, a) 0-90 tube, b) 90-0 tube, c)  $\pm 45$  dynamically loaded d)  $\pm 45$  Quasi-statically loaded**

The square tubes split at the corners, where a stress concentration occurs, into 4 fronds, see Figure 65. Under quasi-static loading the square samples gave a very similar SEA to the circular tubes (39.8kJ/kg). Under dynamic loading the reduction in SEA for Q0m was approximately 27.1%, quasi-static to dynamic, which was a larger than that seen in the 0-90 or 90-0 circular section tubes.

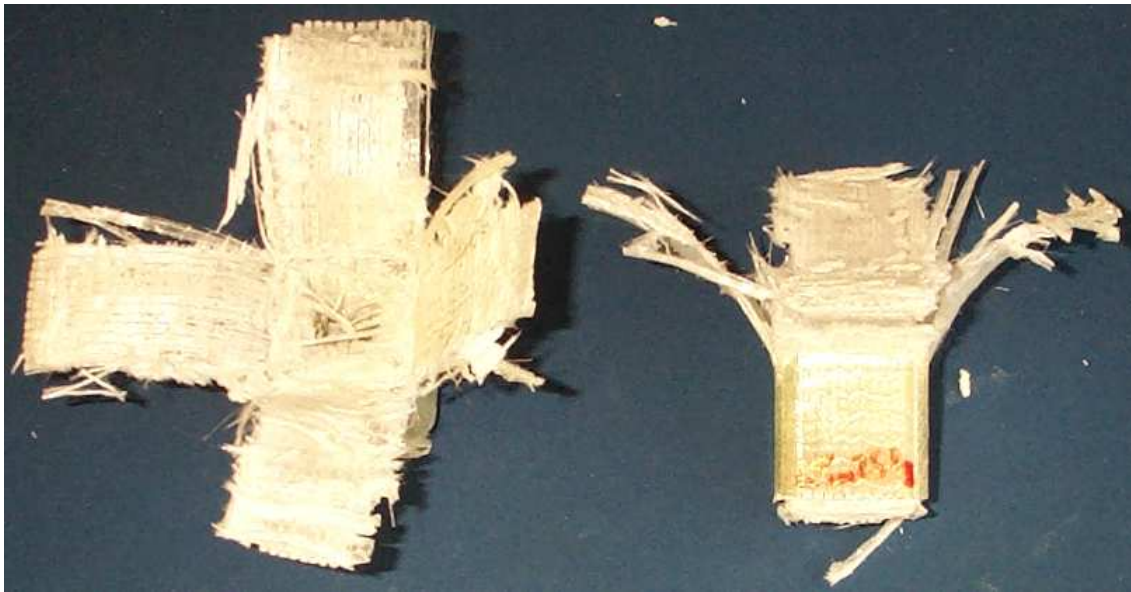


**Figure 65 Mode of Failure of Square NCF tube**

A range of failure modes were seen in the braided tubes. The braided  $\pm 30$  and  $\pm 45$  tubes failed progressively under quasi-static loading with a mixture of local folding/buckling and splaying - the outer fronds splayed whilst the inner fronds folded and buckled. The stroke efficiency was reduced in this mode as the buckles stacked up, prohibiting further crush. Splaying dominated the crush zone morphology in the  $\pm 60$  tubes, where folding was only seen on the inner diameter. For the undamaged braided  $\pm 30$  tube, CB301, the static SEA was 44.1kJ/kg with a standard deviation over the three test samples of 1.1%. For  $\pm 45$  tubes (CB451) the static SEA was 38.8kJ/kg with a deviation of 3.8%, and for  $\pm 60$  tubes (CB601) static SEA was 45.1kJ/kg with a deviation of 23 % - the high standard deviation indicates the change in crush zone morphology between the three test samples. At quasi-static rates the braid angle had little effect on SEA (see Figure 66).

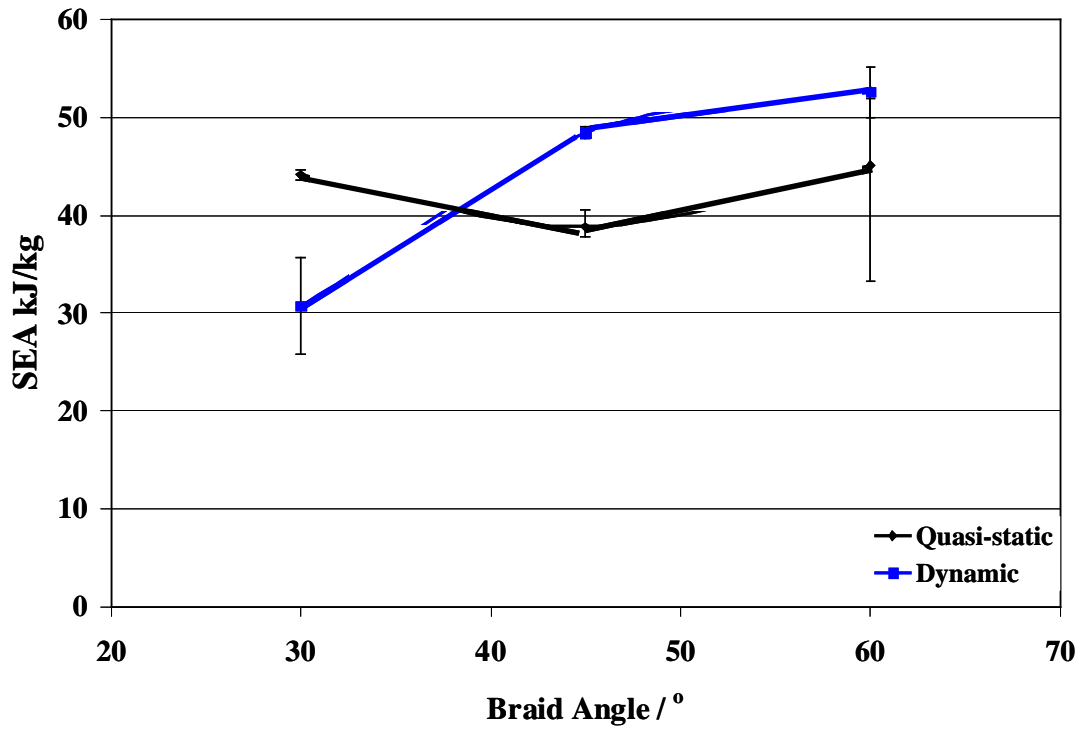


Figure 66 Energy Absorption at Rate for Different Braid Angles

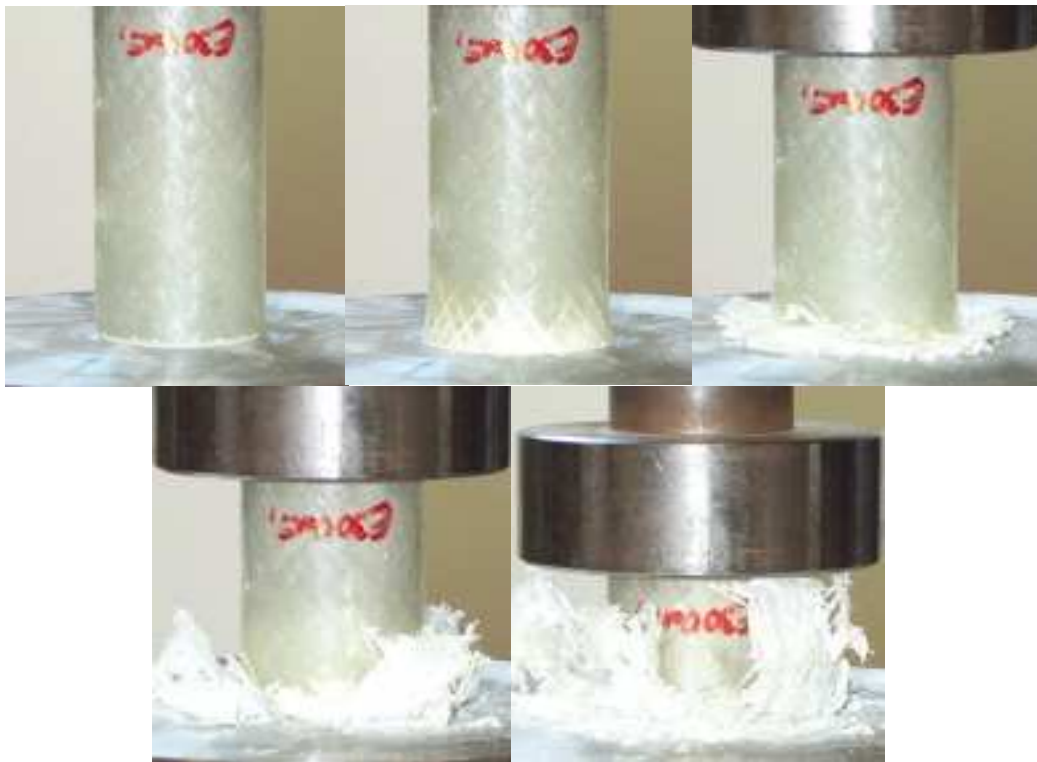


Figure 67 Braided  $\pm 30^\circ$  Tube under Quasi-Static Loading

Dynamically, the modes of failure changed for the braided tubes. The  $\pm 45$  and  $\pm 60$  tubes splayed in a more progressive manner without buckling and folding. This dynamic splaying mode increased the SEA. Figure 67 shows the  $\pm 30$  braided sample under test conditions. The crush zone morphology for  $\pm 30$  showed more splaying, but with some folding on the inner diameter. Dynamically there was a noticeable difference in SEA for the 3 angles.  $\pm 30$  had the lowest SEA of 30.7kJ/kg,  $\pm 45$  was 48.4kJ/kg and  $\pm 60$  was 52.6kJ/kg, although this could be attributed to volume fraction effects here it appears to be a function of angle influenced crushing mode.

### 4.2.3. Higher Rate Effects

Testing was undertaken using the IFW5 drop tower to establish what affect the changing rate had upon the energy absorption to give a clearer understanding than that described by Fernie[4].

The previous section shows the difference between the 0-90 and 90-0 NCF orientations at quasi-static and  $5\text{ms}^{-1}$ . To expand on these velocities, values in the range of  $2\text{-}7\text{ms}^{-1}$  were tested. A Triaxial  $0\pm 60^\circ$  tube was used to test the highest performing braided fabrics (comparing the quasi-static performance from Table 10 and Table 11 illustrates this).

**Table 11 SEA Data for Rate Testing**

Velocity ( $\text{ms}^{-1}$ )	SEA		
	kJ/kg (std Dev %)		
	NCF 0-90	NCF 90-0	$0\pm 60$
0	39.0 (2.7)	50.4 (1.4)	53.8 (0.5)
2	32.6 (5.8)	40.3 (0.9)	50.3 (0.9)
3	31.0 (14.2)	39.9 (4.4)	50.3 (2.7)
4	31.0 (9.7)	40.2 (9.6)	50.6 (2.2)
5	31.1 (2.4)	39.8 (5.8)	50.1 (5.8)
6	31.2 (10.1)	40.4 (3.3)	51.2 (1.8)
7	30.4 (4.2)	40.4 (0.93)	51.2 (1.4)

The limits of the available equipment meant that the maximum velocity attainable was  $7\text{ms}^{-1}$  (approximately 15.8 mph).

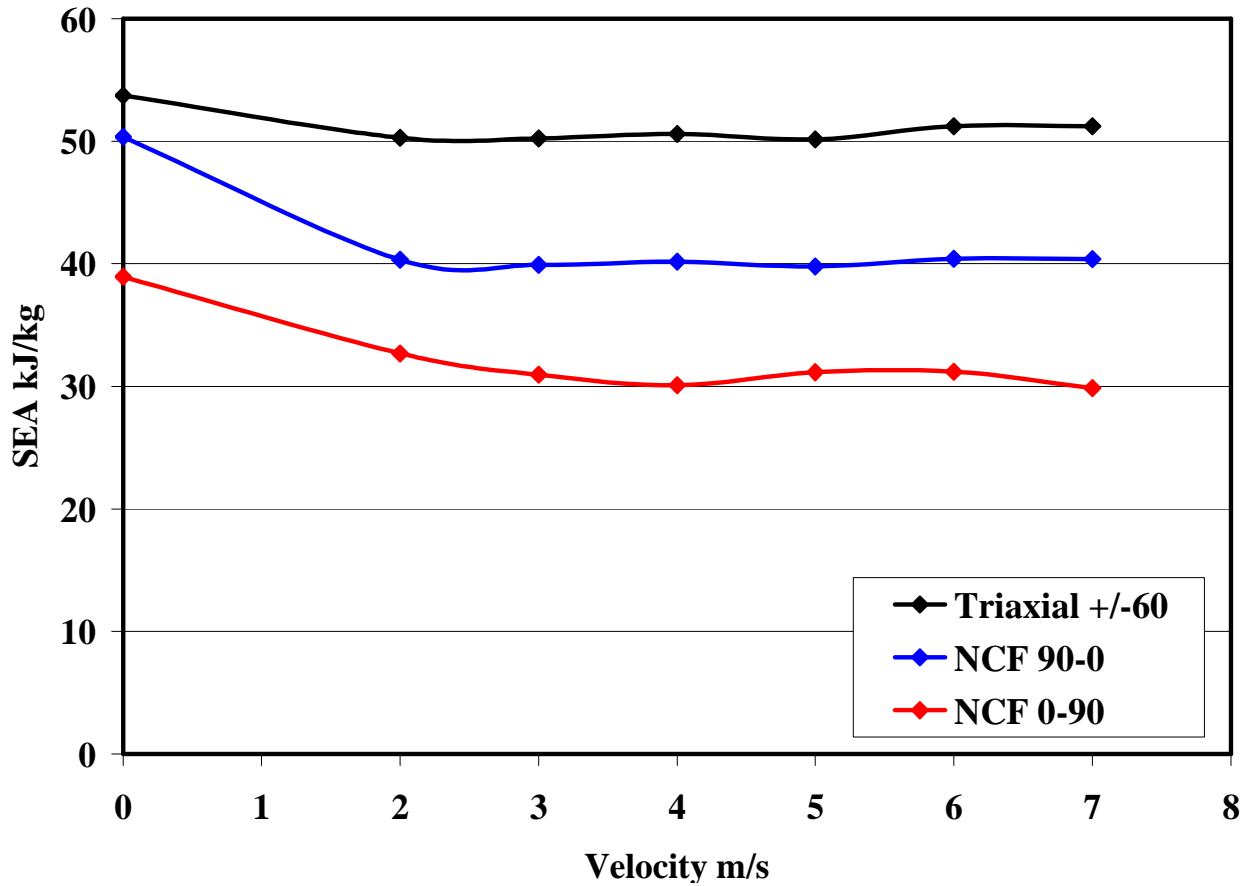


**Figure 68 SEA vs Testing Rate**

Looking at the SEA vs Rate curve (Figure 68) we can observe that there is a drop in load between 0 and 2ms<sup>-1</sup>. As suggested earlier this could be due to the effects of the resin pulverising and allowing the fibres to deform rather than crush. After this initial drop the energy absorption appears to reach a steady state and shows no further drop up to the test limits. This is an important result suggesting that the results of testing at 5ms<sup>-1</sup> will give an indication of the performance at higher rates. This could provide a suitable/economical experimental level for testing “real-life” automotive impacts, although further testing is required to assess the validity of this conclusion.

#### 4.2.4. Resin Comparison

The SEA data for small NCF/epoxy tubes can be found in Table 12, where the prefix CE refers to a NCF tube with Epoxy resin.

**Table 12 Data for Epoxy and Polyester Resin Comparisons**

Fibre Type	Test Reference	Quasi-static SEA (kJ/kg) (std. Dev %)	Failure mode	Dynamic SEA (kJ/kg) (std. Dev %)	Failure mode	% decrease
NCF 90-0	C900m	50.4 (1.4)	1	39.8 (5.8)	1	21.1
NCF 90-0	CE900m	69.9 (9.2)	1	50.6 (6.6)	1	27.6
	%diff	27.8		21.3		
NCF ±45	C450m	55.4 (8.0)	1	29.6 (7.7)	1	46.6
NCF ±45	CE450m	57.1 (5.9)	1	42.6 (6.0)	1	25.4
	%diff	3.0		30.5		

The load displacement curves for the dynamically tested samples can be seen in Figure 69.

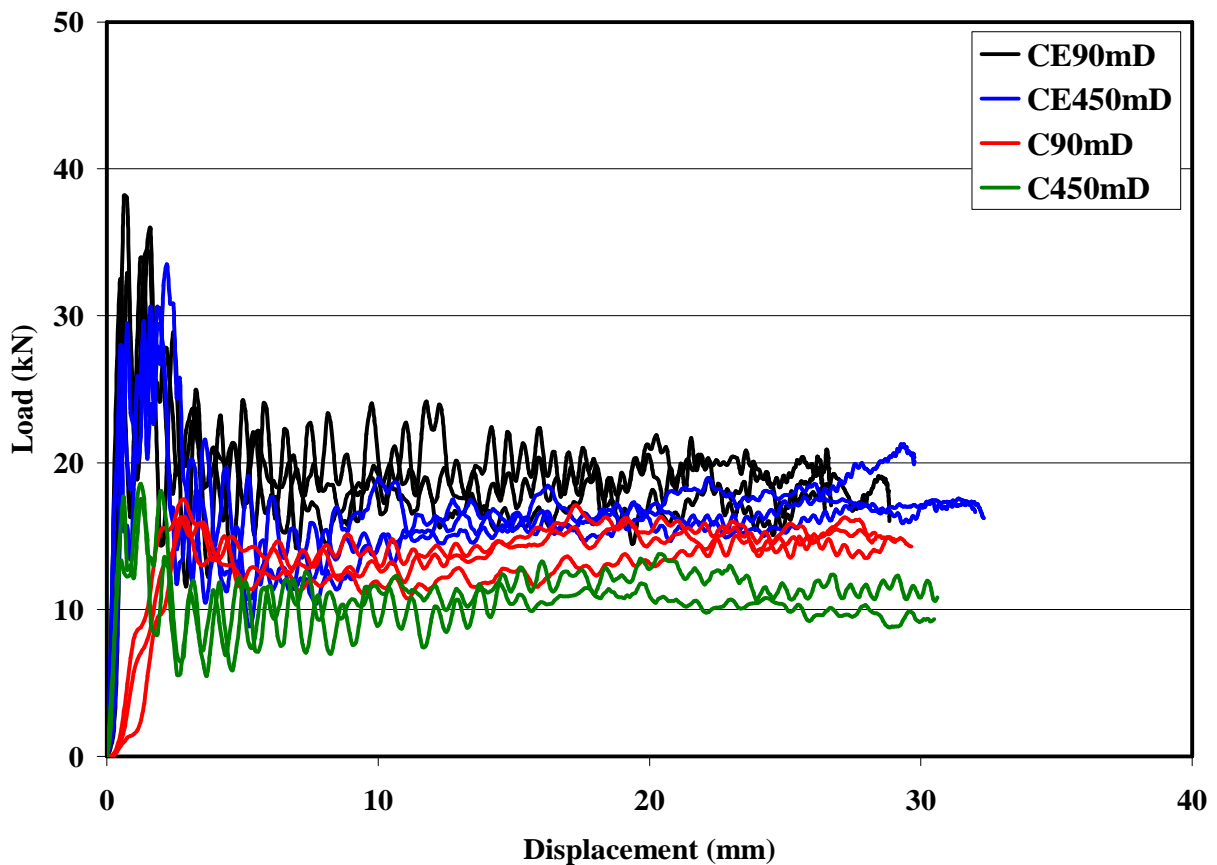


**Figure 69 Dynamic Load Displacement Curve for Resin Comparison**

Using epoxy resin causes a significant improvement in SEA at static rates (up 27.8% for the 90-0 orientation and 3% for the  $\pm 45$  orientation). This agrees with the results of the large carbon tube tests; however, these tests did not show the effects of different resins at rate. From these results it can be seen that the SEA is again improved by using epoxy (21.3% and 30.5% increases for 90-0 and  $\pm 45$  respectively). Importantly these results show that at dynamic rates there is still a significant drop in SEA, 27.6 % and 25.4% over the quasi-static values for the epoxy tubes. However, with the  $\pm 45$  orientation the drop in load was much less severe with the epoxy resin, a splaying type failure was seen and there was more evidence of fibre damage present rather than the spectacular splaying failure seen with polyester resin.

#### **4.2.5. Micrographs.**

The optical micrographs give a visual insight into the crush zone and mode of failure, which allows the ways of energy absorption to be investigated. The micrographs were taken for a range of samples at quasi-static and dynamic rates. Where possible the samples were potted whilst crush load was maintained to preserve the crush zone morphology of the test. This was achieved by applying a constant load with the Instron 1195 after a quasi-static test. For the dynamic samples not picking up the mass carrier on the Rosand IFWT after a dynamic test had the same effect. An overview of each sample can be seen in Figure 70

From the micrographs it can be seen that all the samples exhibit similar basic properties seen in the schematic of the splaying crush mode (Ribeaux [7]). The debris wedge and centre wall crack, associated with the splaying mode of failure, are visible in many samples. Greater curvature is seen in the quasi-static samples and there is more resin break-up and fragmentation can be observed in the dynamic samples, showing further agreement with Ribeaux.[7]

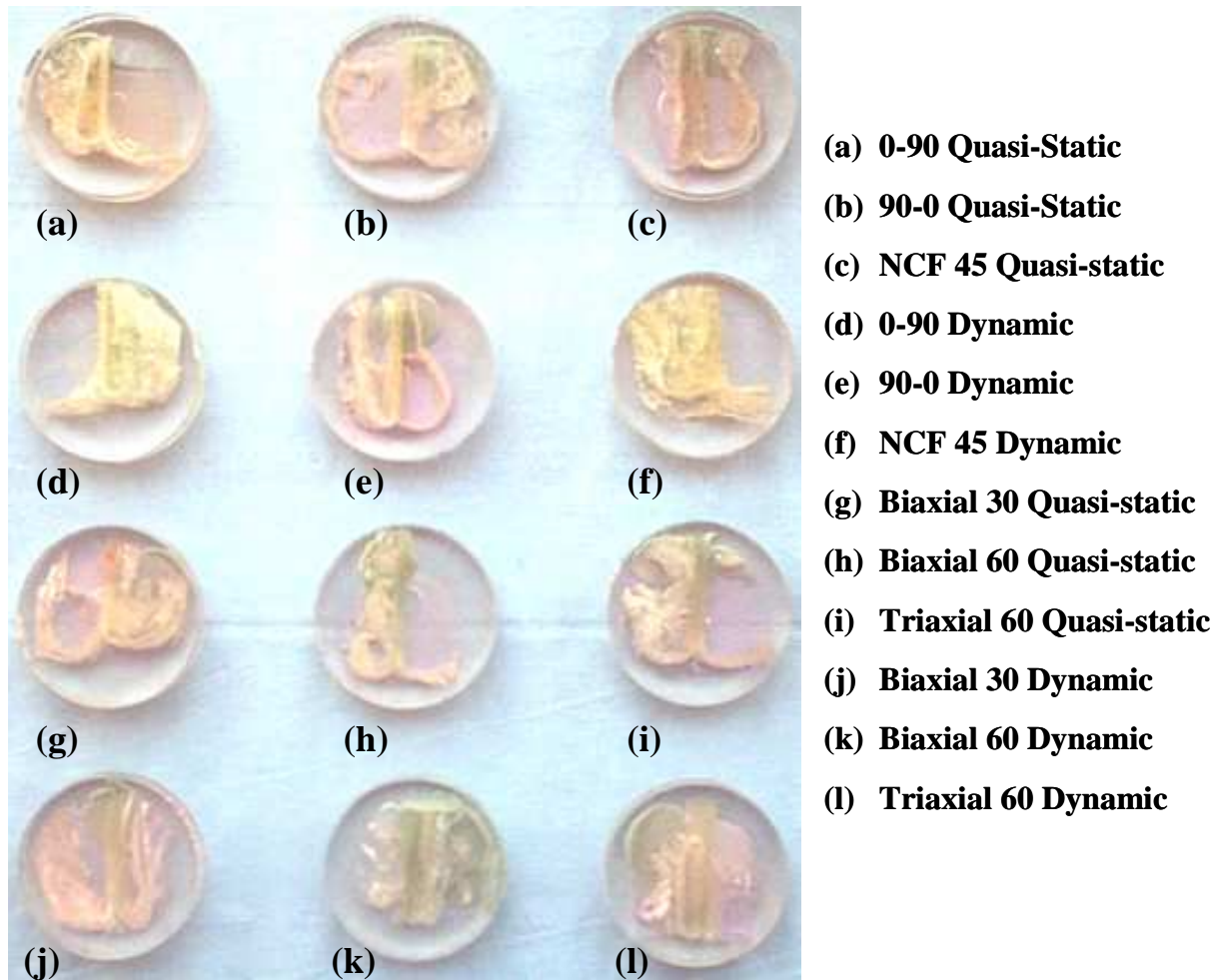


**Figure 70 Potted Samples for Micrography**

From Figure 70 samples (a), (d) and (g) show large amounts of elastic spring-back in the outer fronds.

In general there is much more fibre damage and fragmentation on the inner fronds than the outer layers, see Figure 71 to Figure 88.

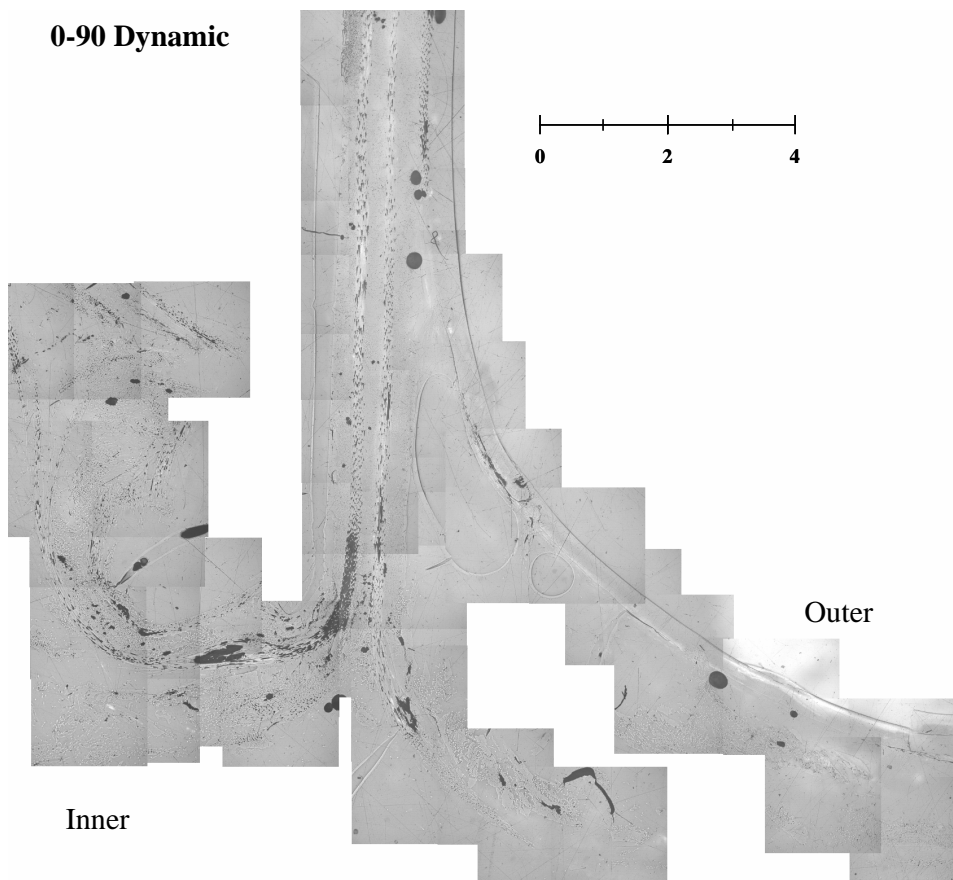
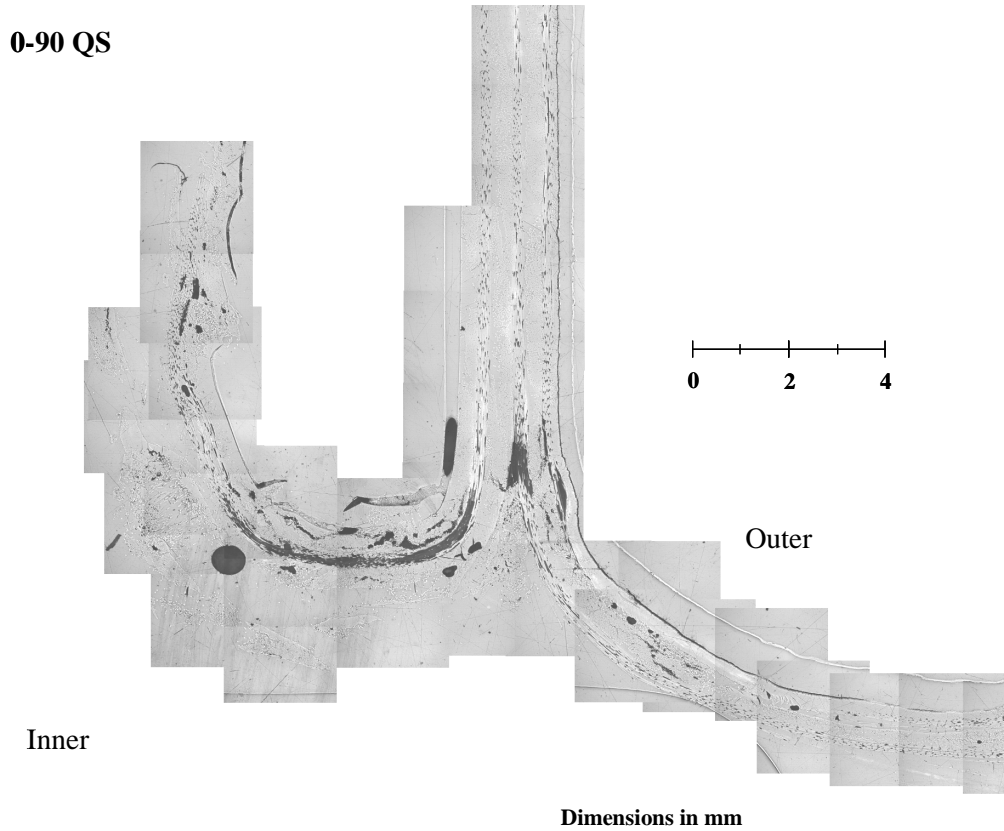


**Figure 71 Micrographs of NCF 0-90 tube at Quasi-Static and Dynamic Rates**

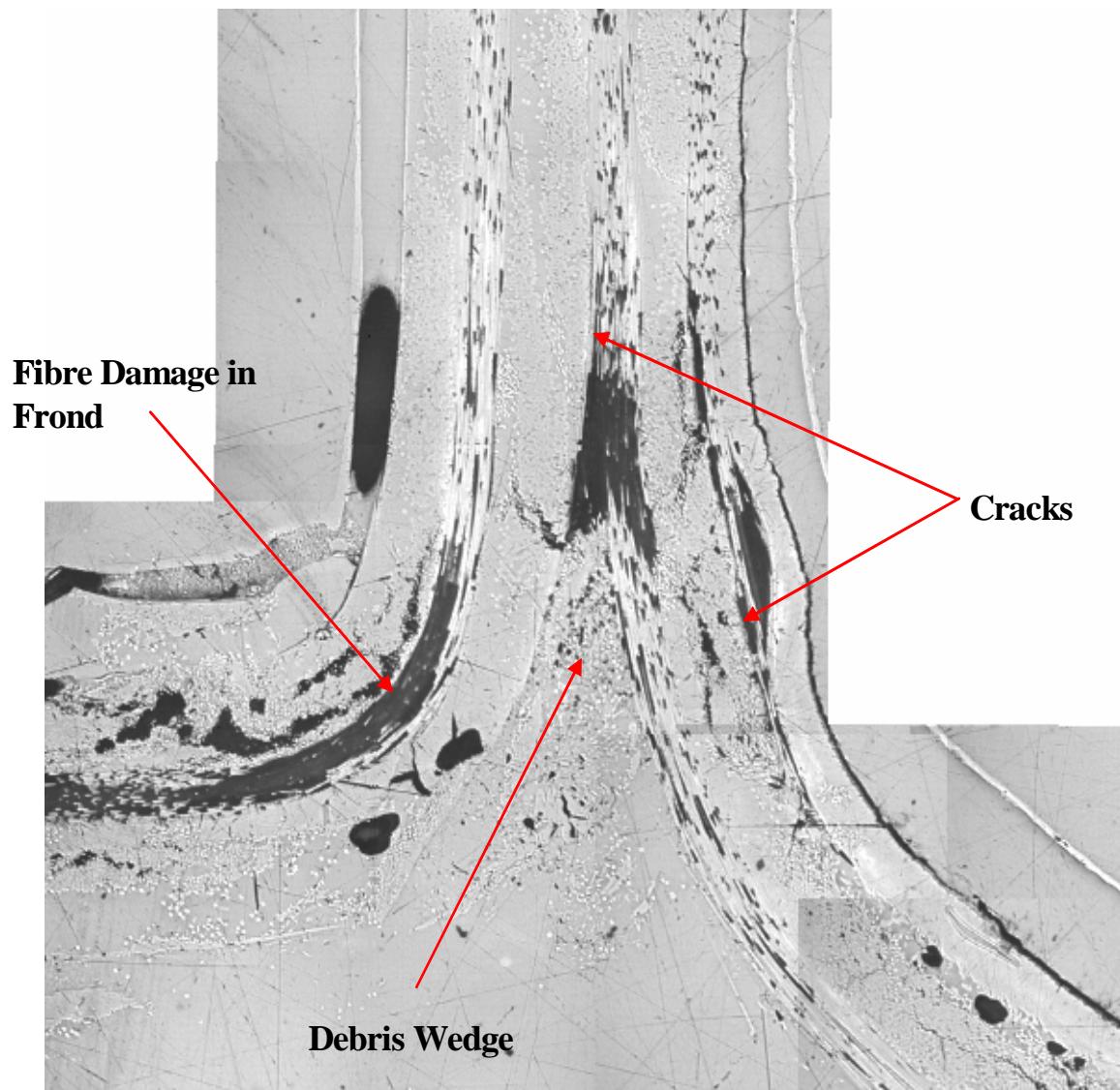


**Figure 72 Micrograph of NCF 0-90 crush zone under Quasi-Static testing**

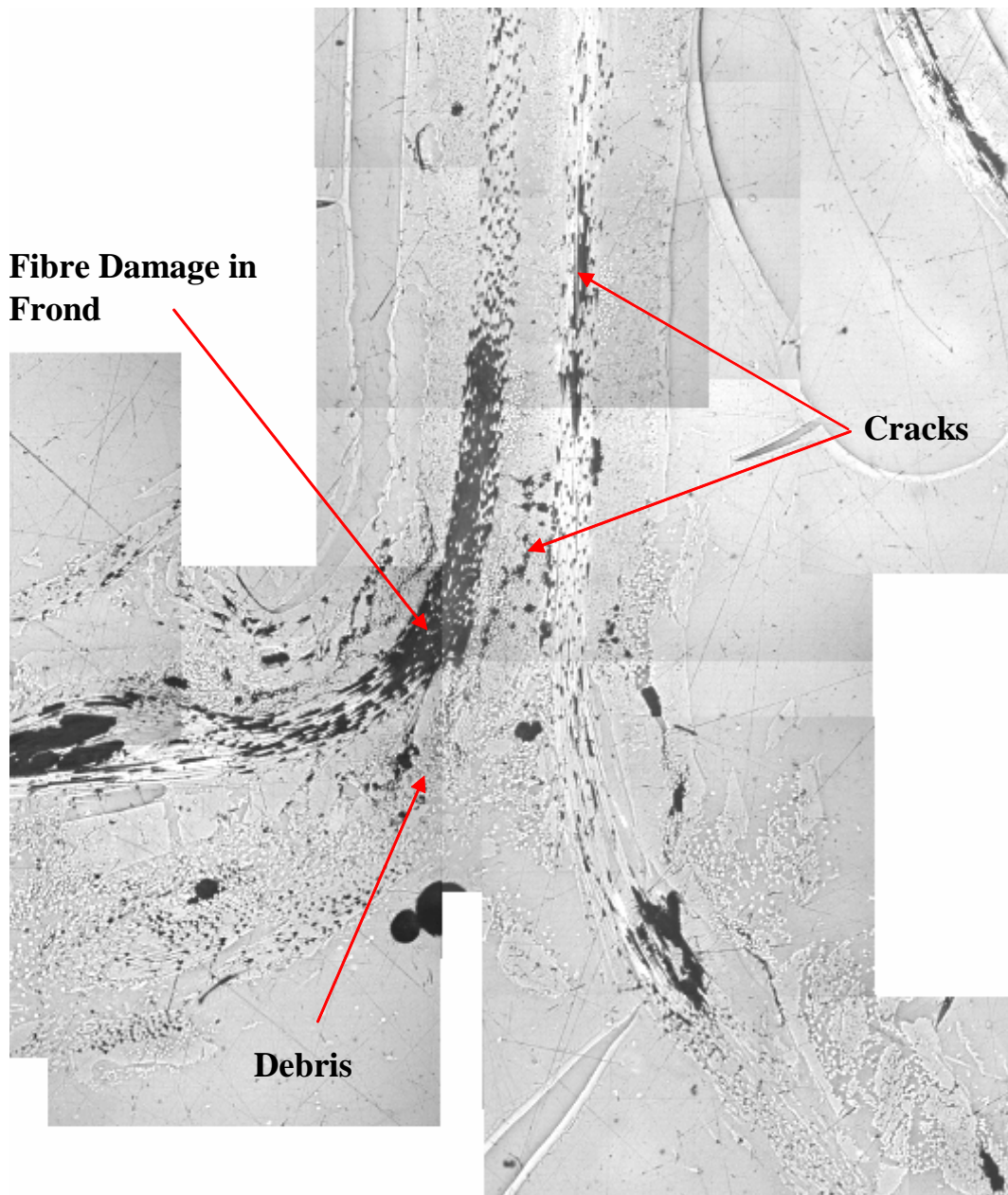
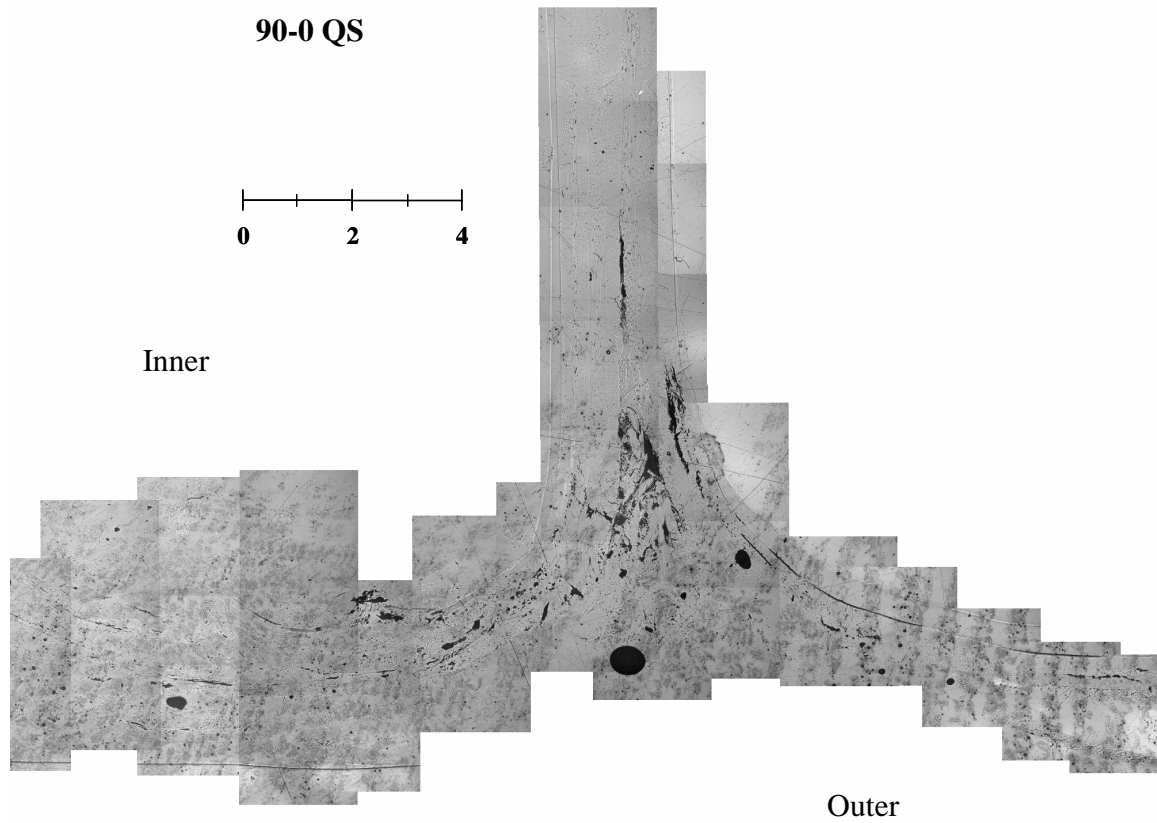


**Figure 73 Micrograph of NCF 0-90 crush zone Under Dynamic Testing**



**90-0 Dynamic**      Dimensions in mm

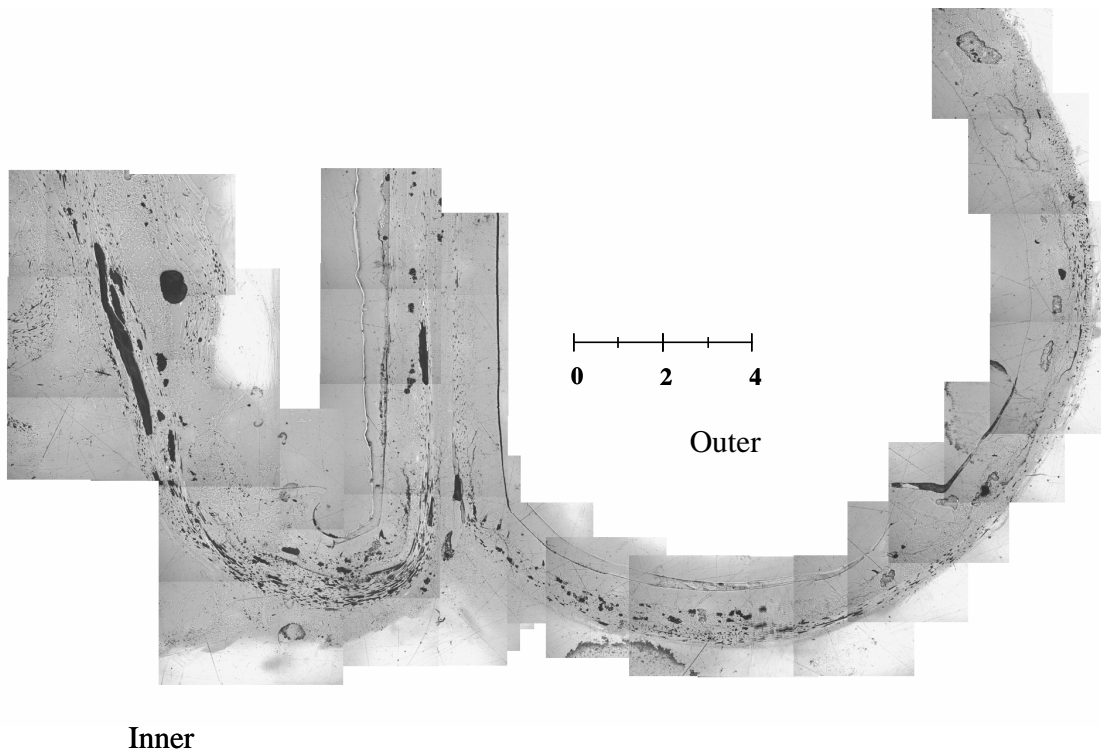


**Figure 74 Micrographs of NCF 90-0 tube at Quasi-Static and Dynamic Rates**

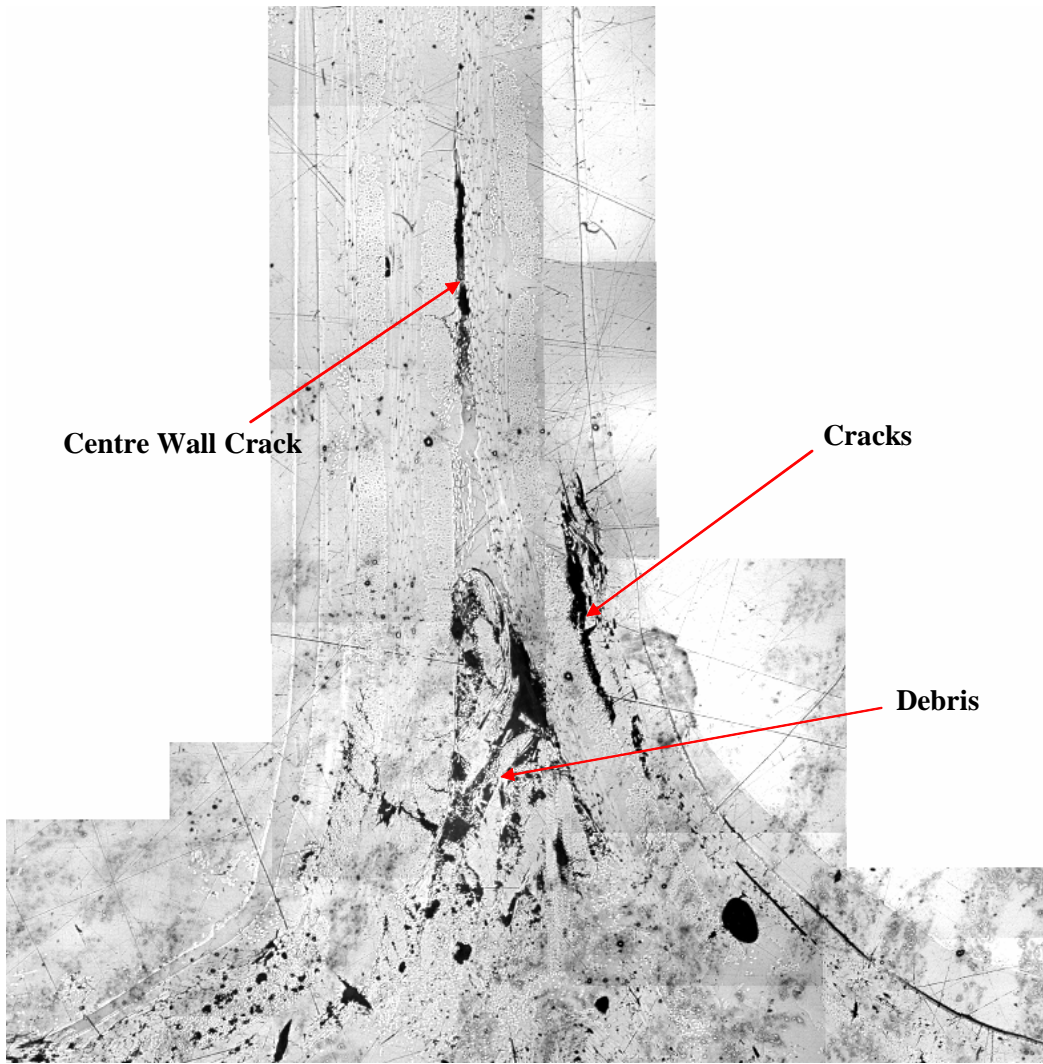


**Figure 75 Micrograph of NCF 90-0 Crush Zone under Quasi-Static Testing**

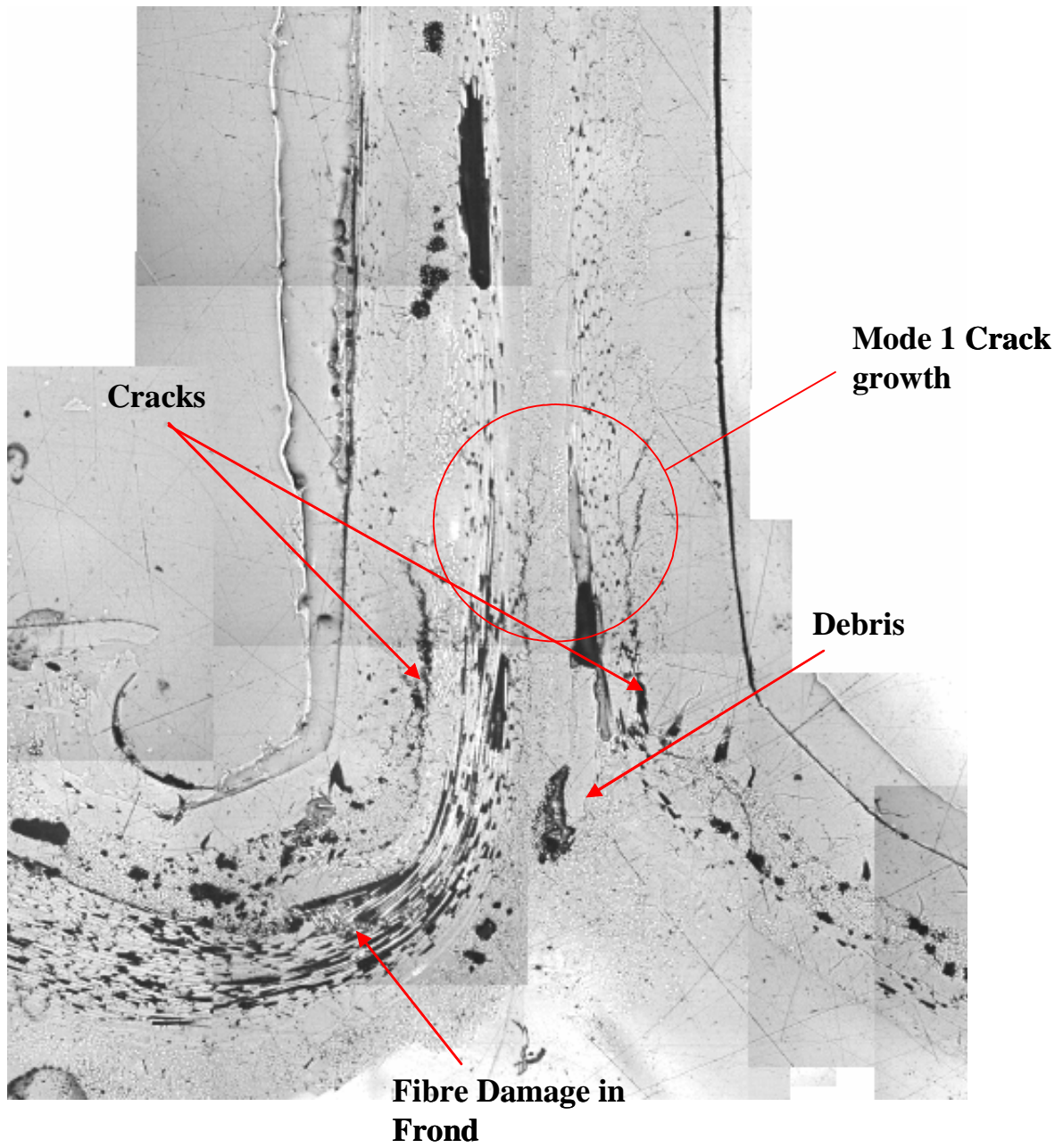
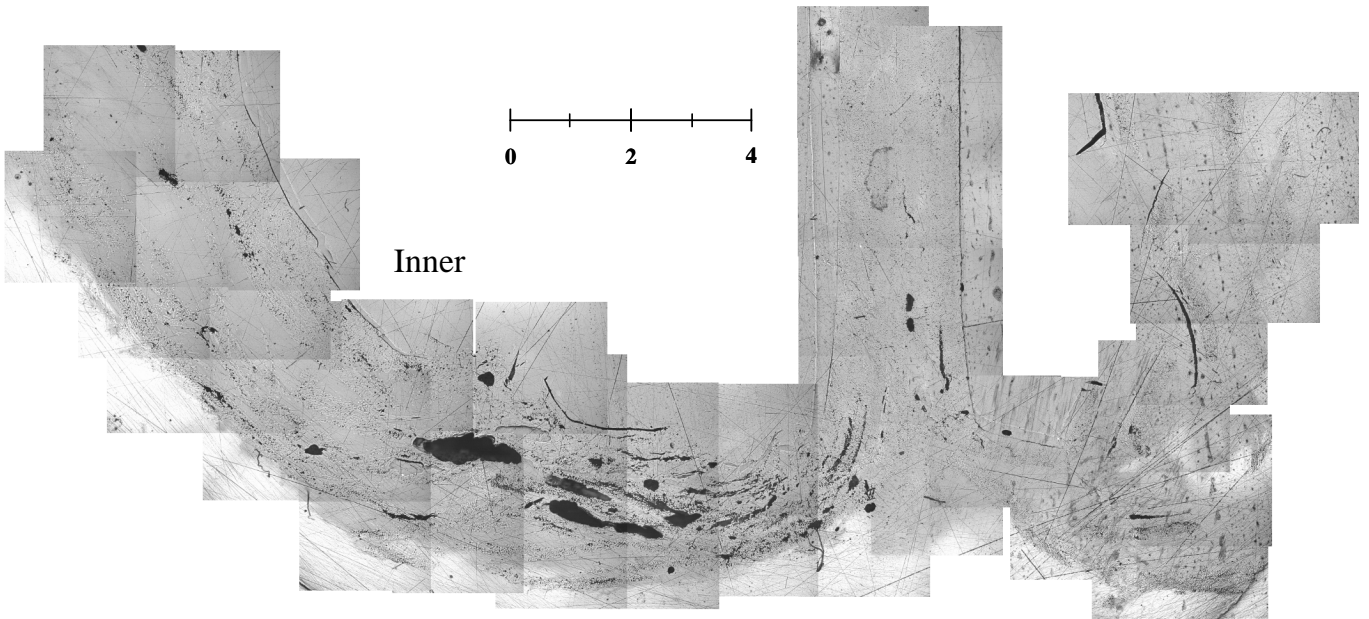


**Figure 76 Micrograph of NCF 90-0 Crush Zone under Dynamic Testing**

**NCF 45 QS**



**NCF 45 dynamic**

**Dimensions in mm**

**Outer**

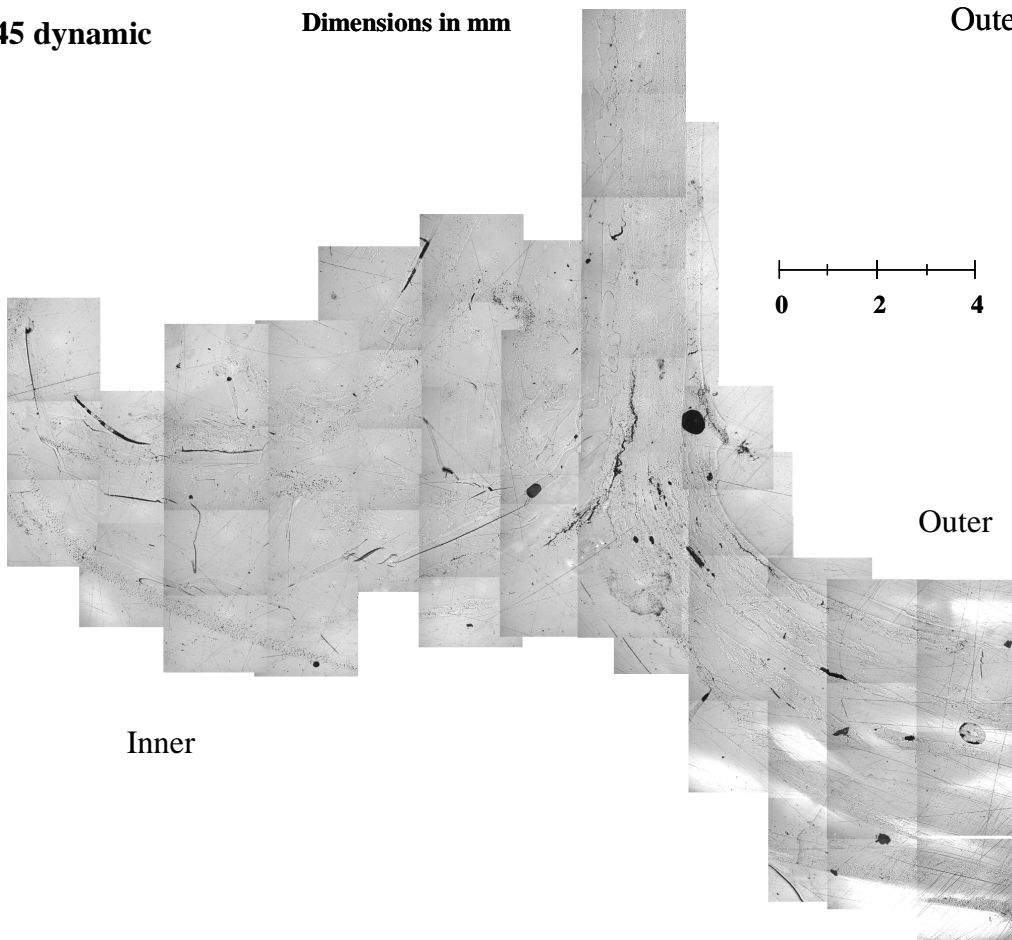


**Figure 77 Micrographs of NCF  $\pm 45$  tube at Quasi-Static and Dynamic Rates**

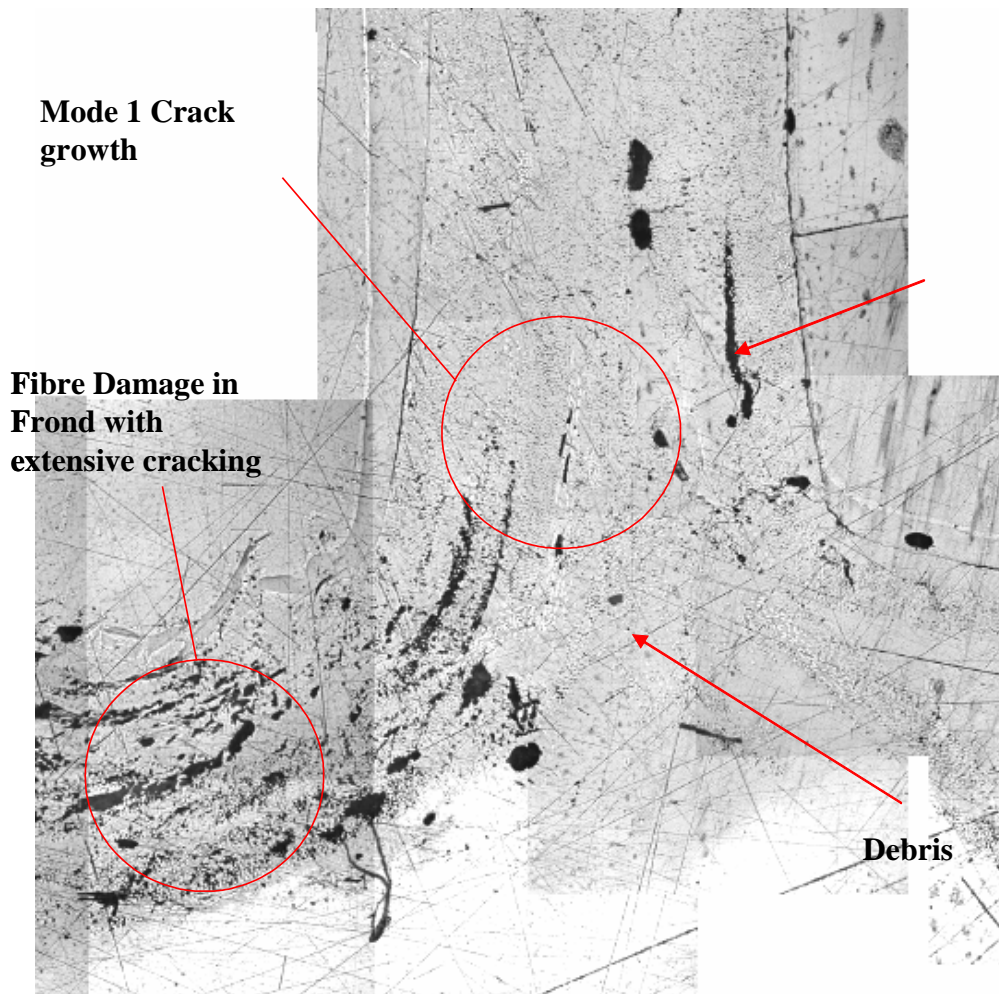


**Figure 78 Micrograph of NCF  $\pm 45$  Crush Zone under Quasi-Static Testing**

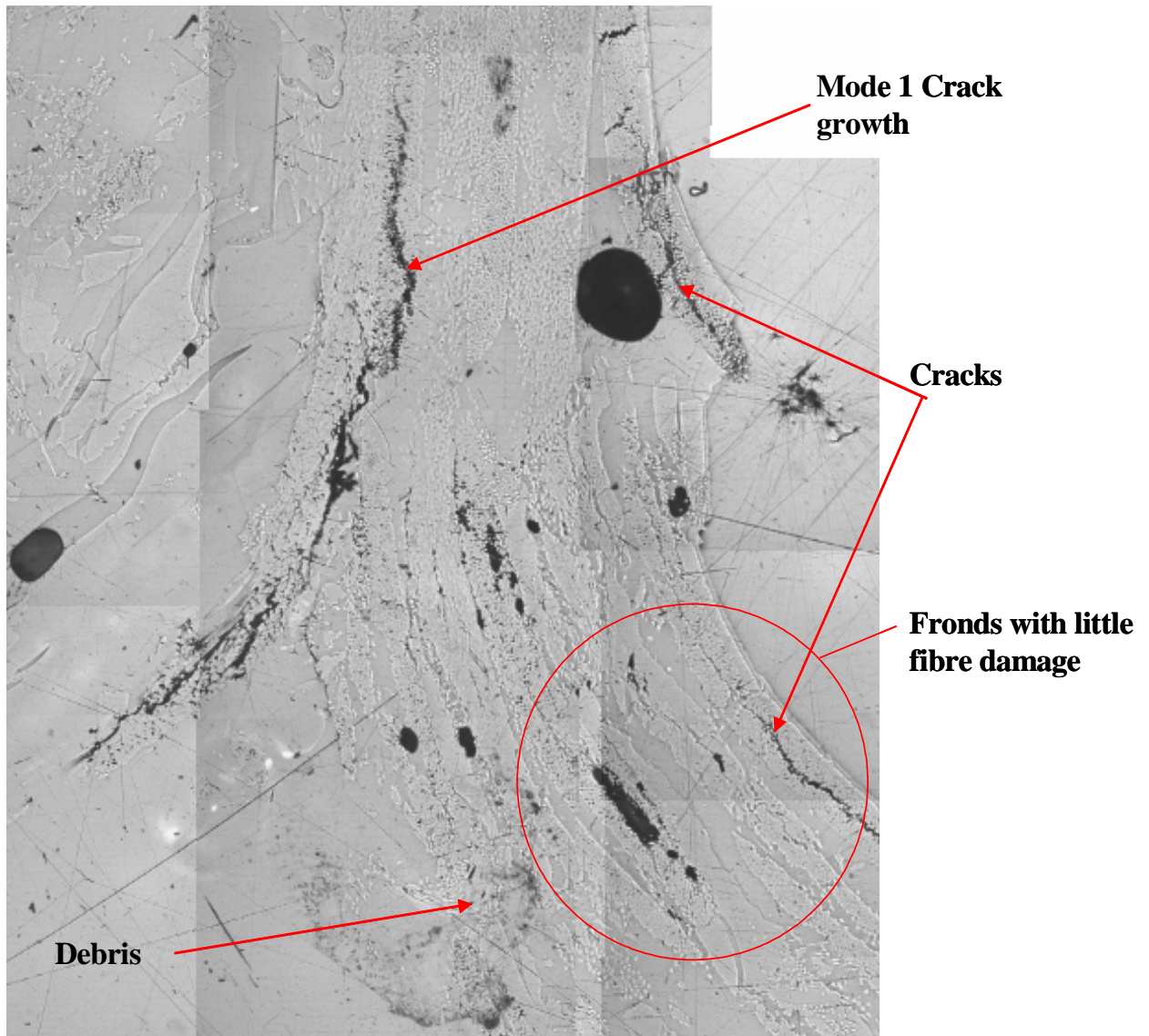
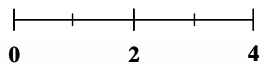
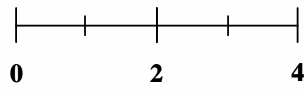


**Figure 79 Micrograph of NCF ±45 Crush Zone under Dynamic Testing**

**Damaged fibres with resin fragmentation**

**Biaxial 30 QS**

**Large cracks in damage zone**



**Biaxial 30 Dynamic**

**Intact fibres with less breakage**

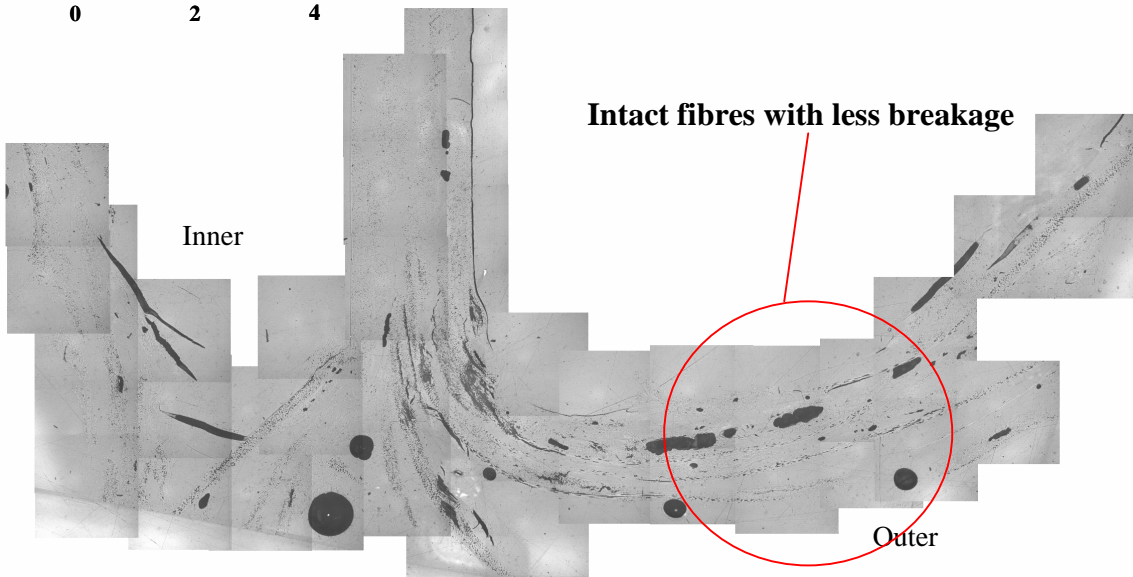


**Figure 80 Micrographs of Biaxial  $\pm 30$  tube at Quasi-Static and Dynamic Rates**

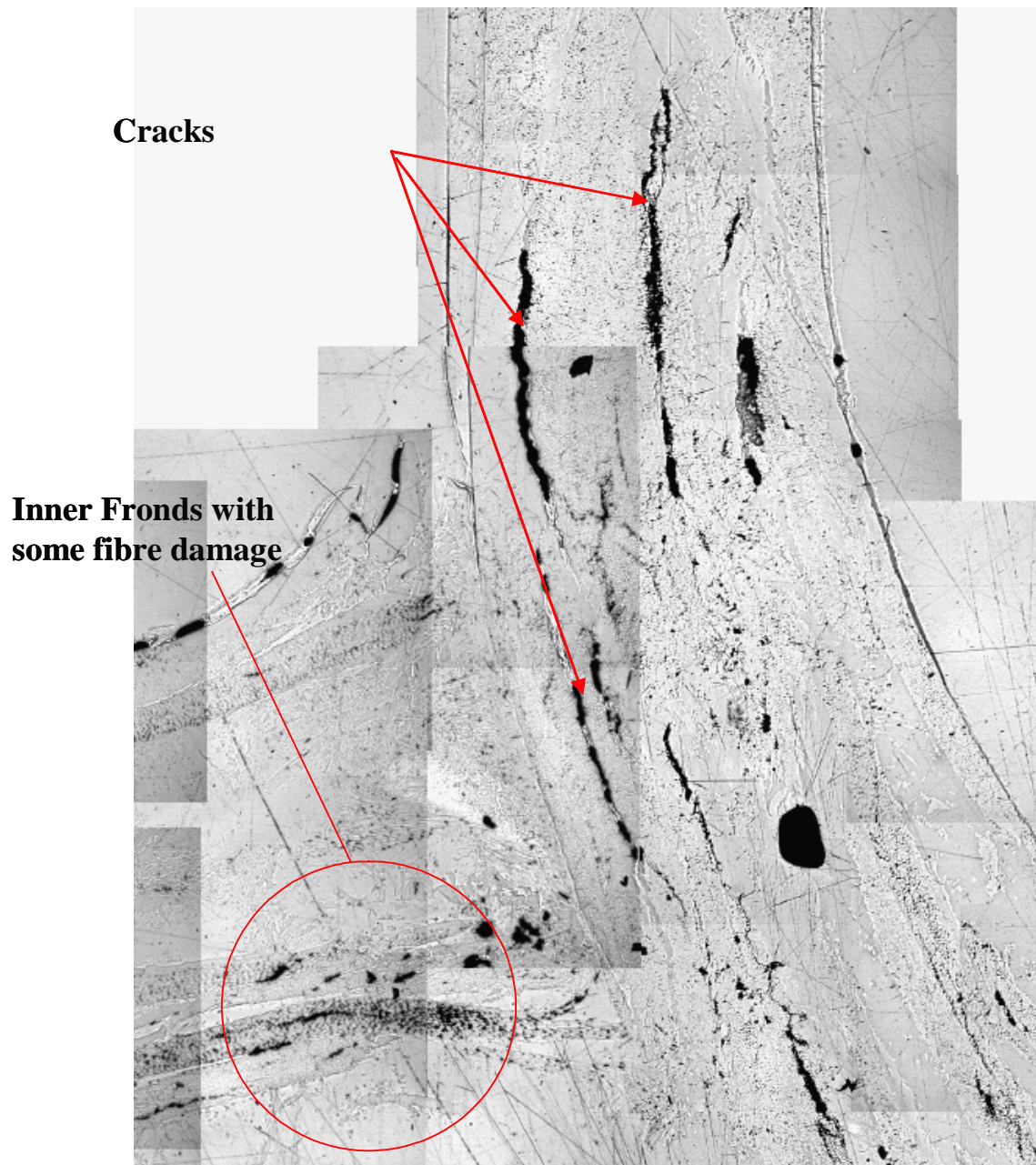


**Figure 81 Micrograph of Biaxial  $\pm 30$  Crush Zone under Quasi-Static Testing**

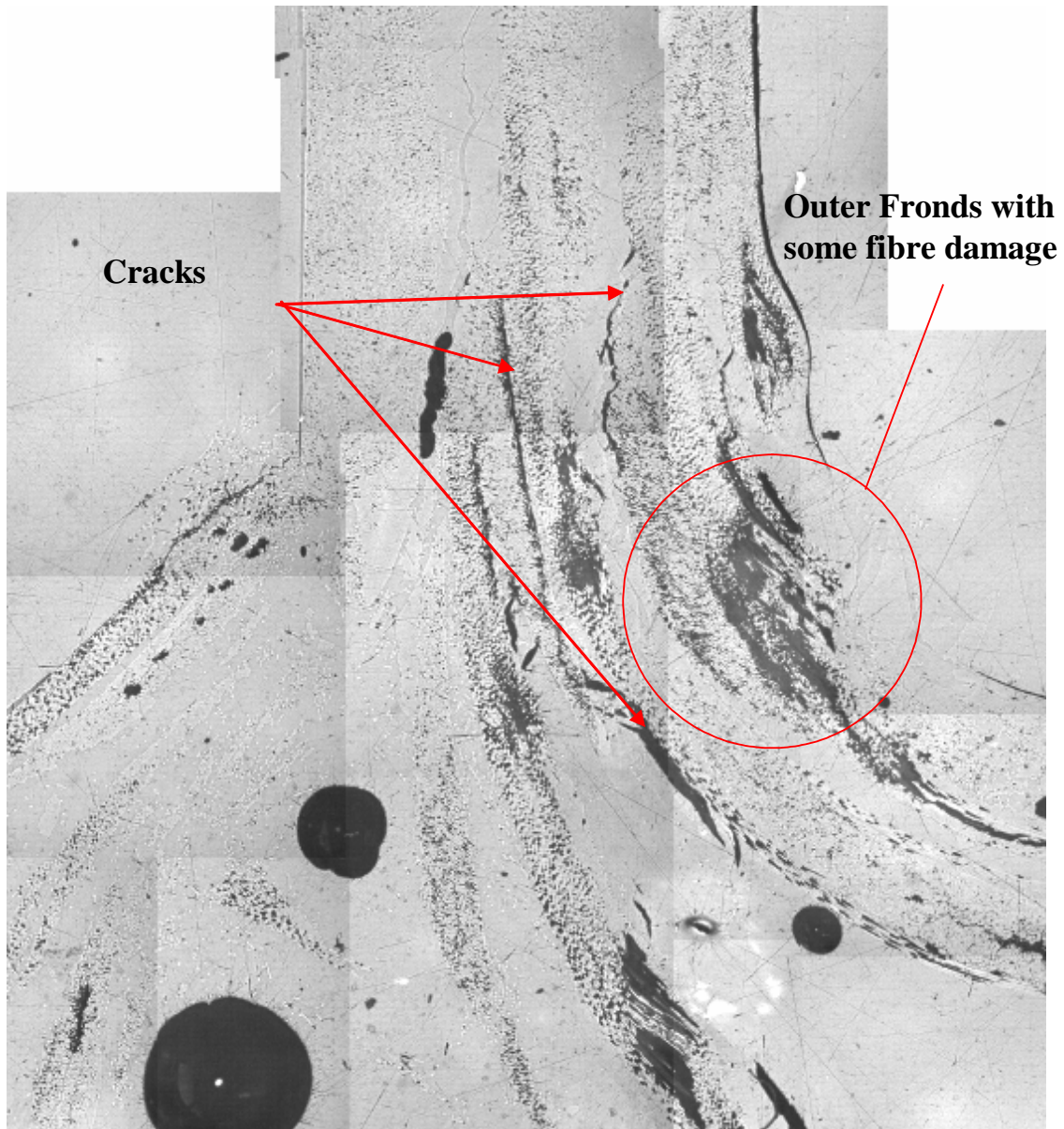


**Figure 82 Micrograph of Biaxial  $\pm 30$  Crush Zone under Dynamic Testing**

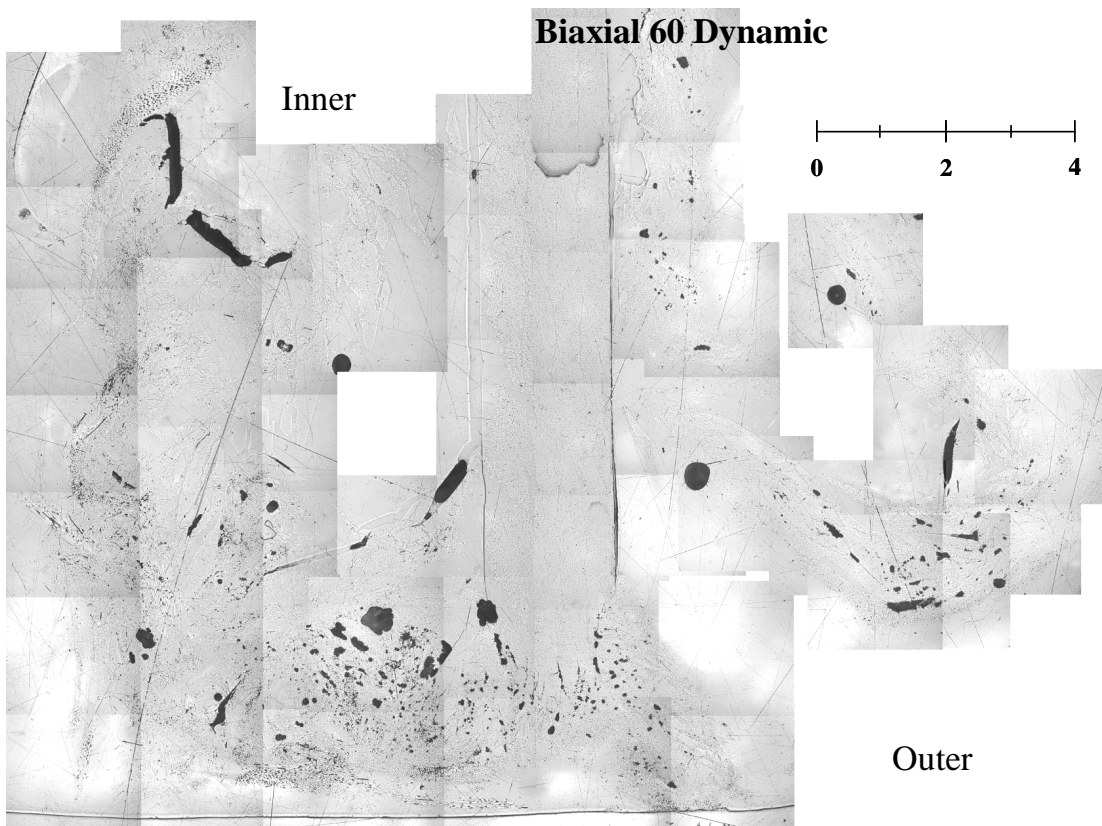
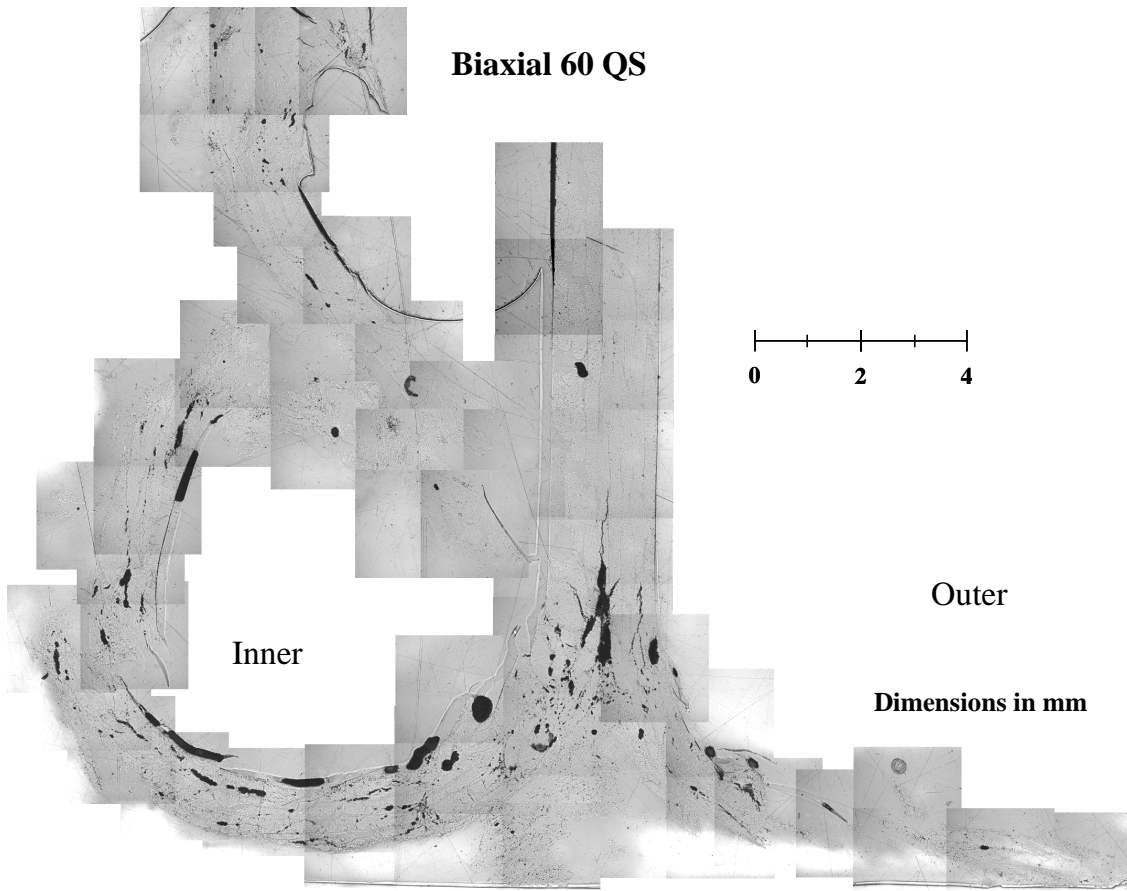


**Figure 83 Micrographs of Biaxial  $\pm 60$  tube at Quasi-Static and Dynamic Rates**

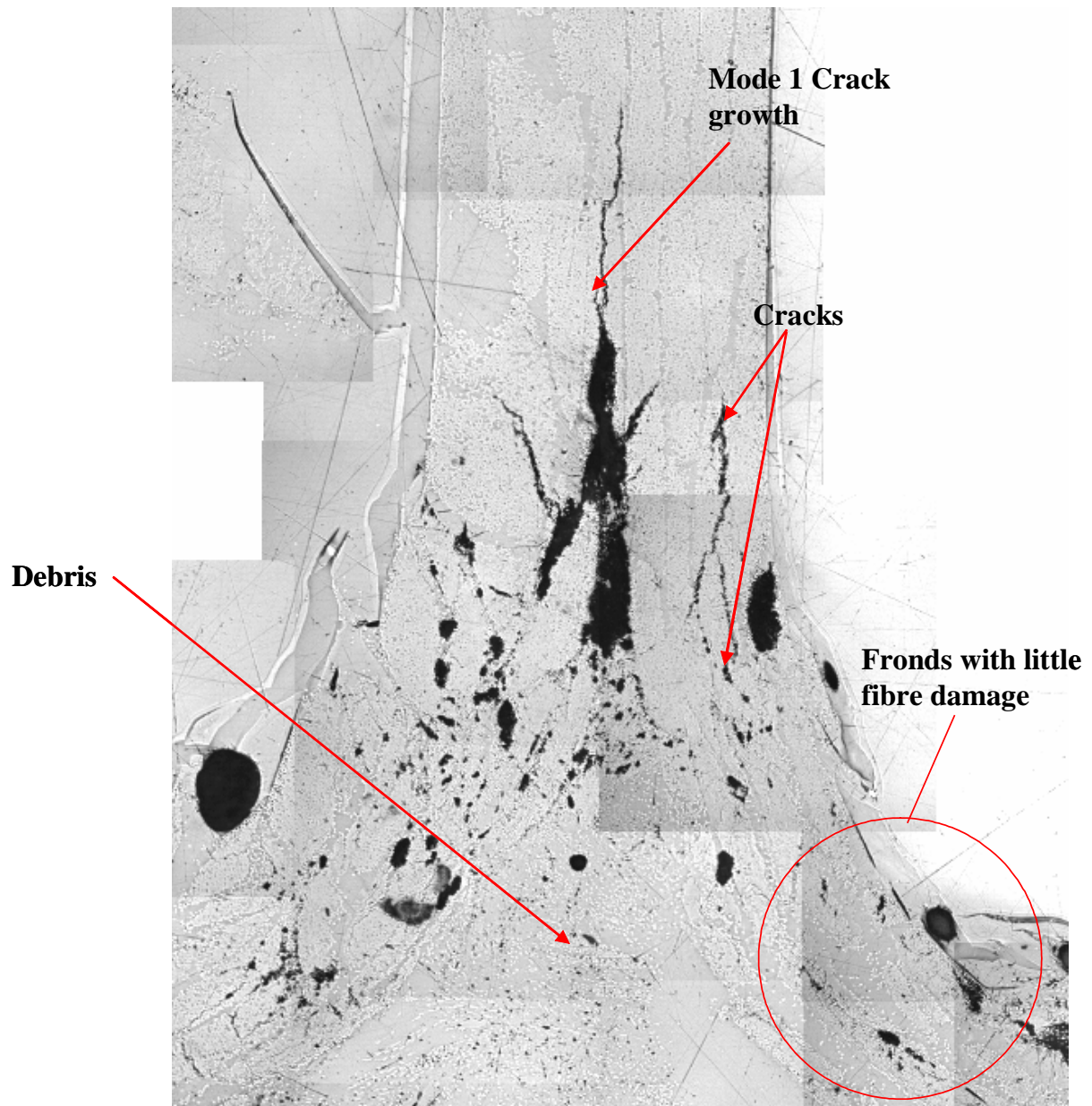


**Figure 84 Micrograph of Biaxial  $\pm 60$  Crush Zone under Quasi-Static Testing**

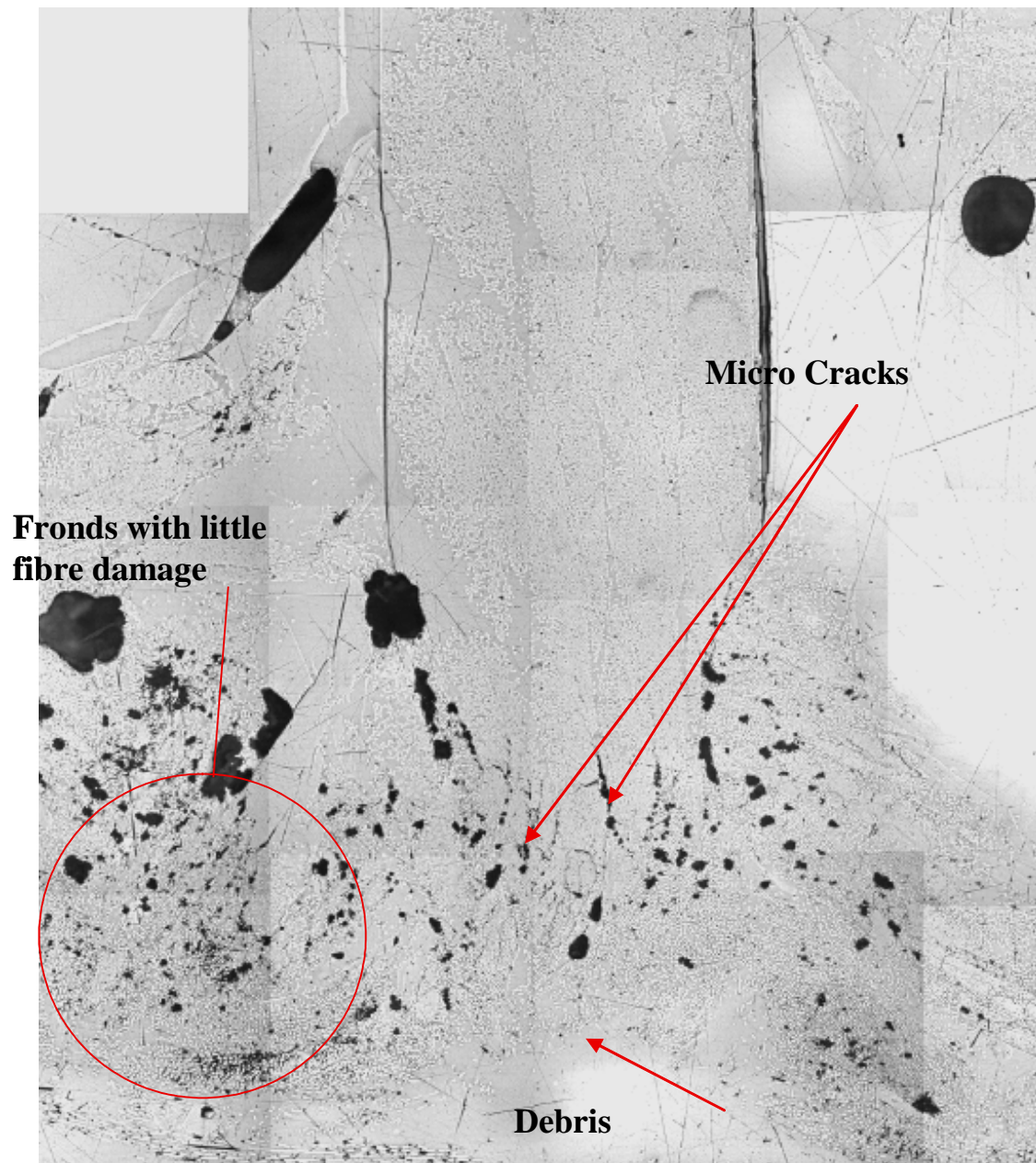
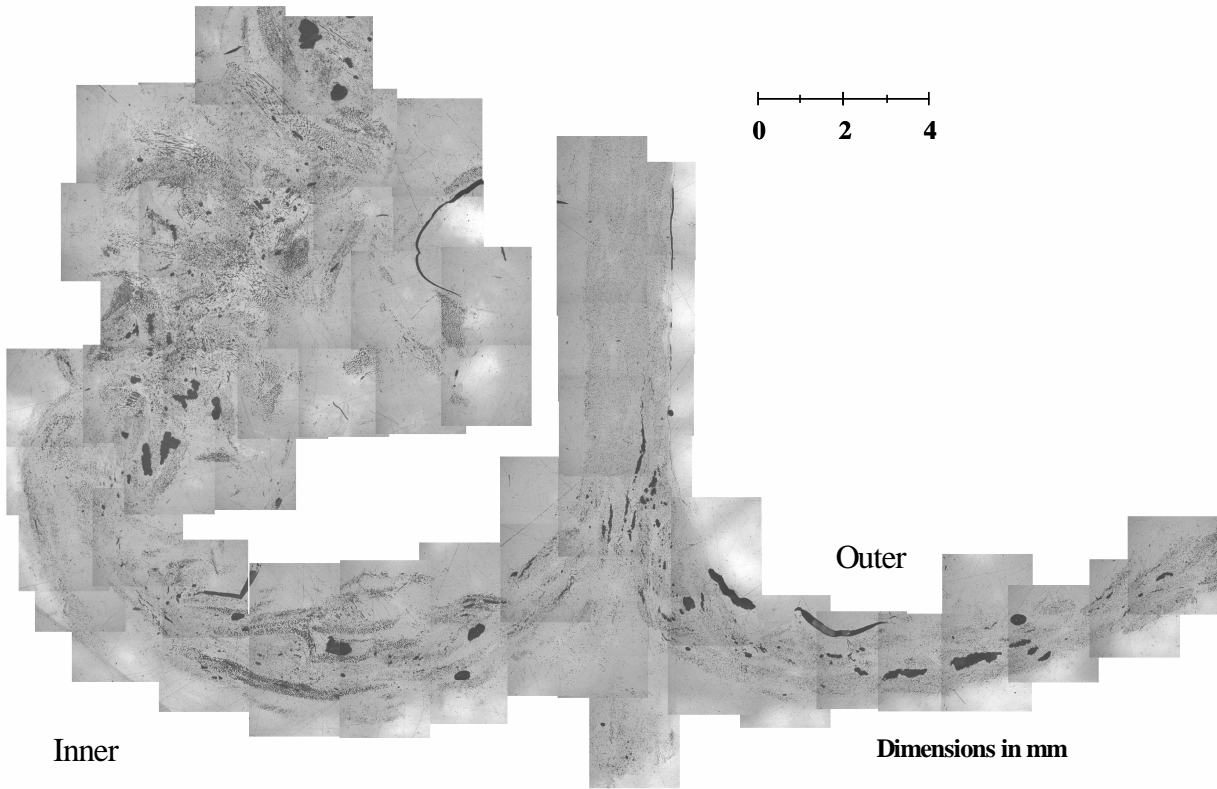


**Figure 85 Micrograph of Biaxial  $\pm 60$  Crush Zone under Dynamic Testing**

**Triaxial 60 QS**



**Triaxial 60 Dynamic**

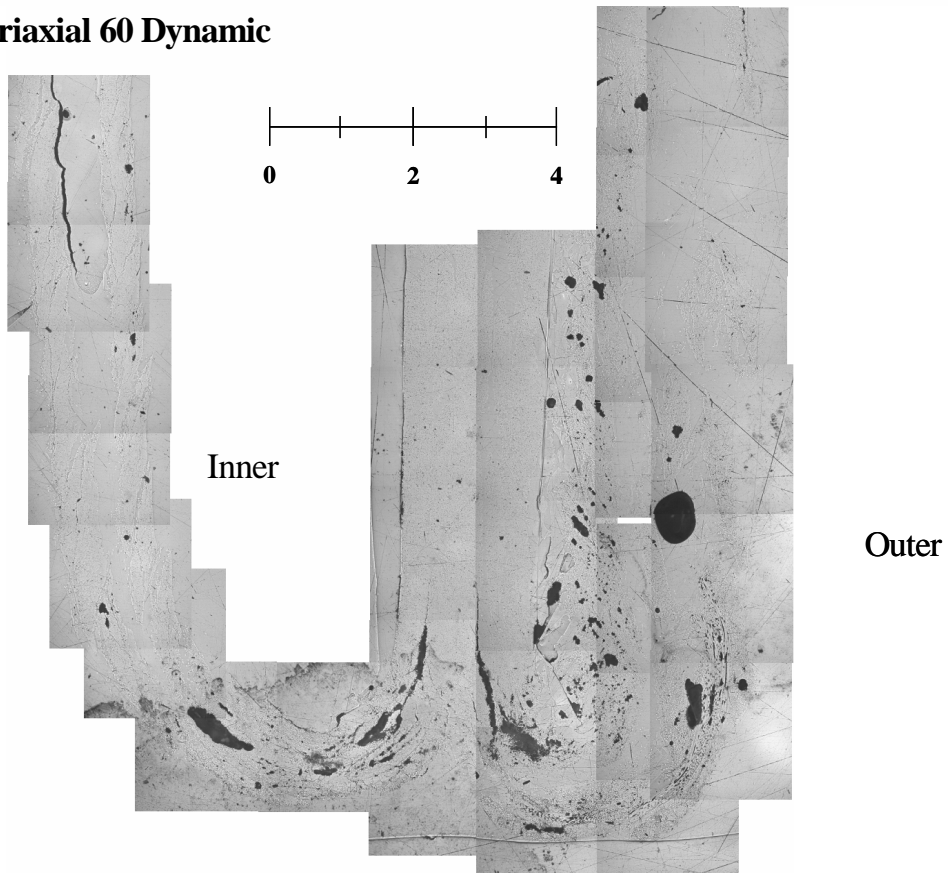


**Figure 86 Micrographs of Triaxial 0±60 tube at Quasi-Static and Dynamic Rates**

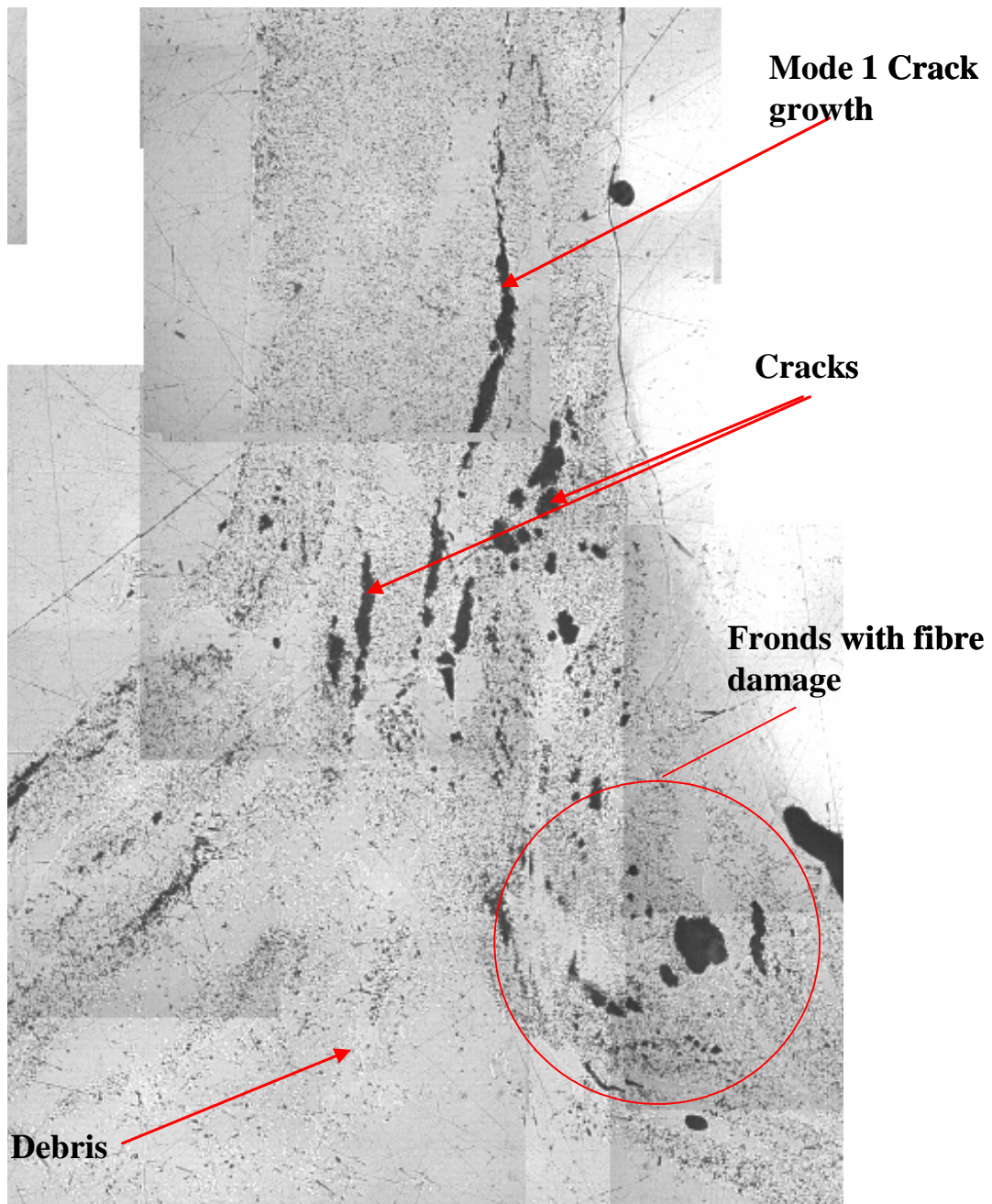


**Figure 87 Micrograph of Triaxial  $\pm 60$  Crush Zone under Quasi-Static Testing**

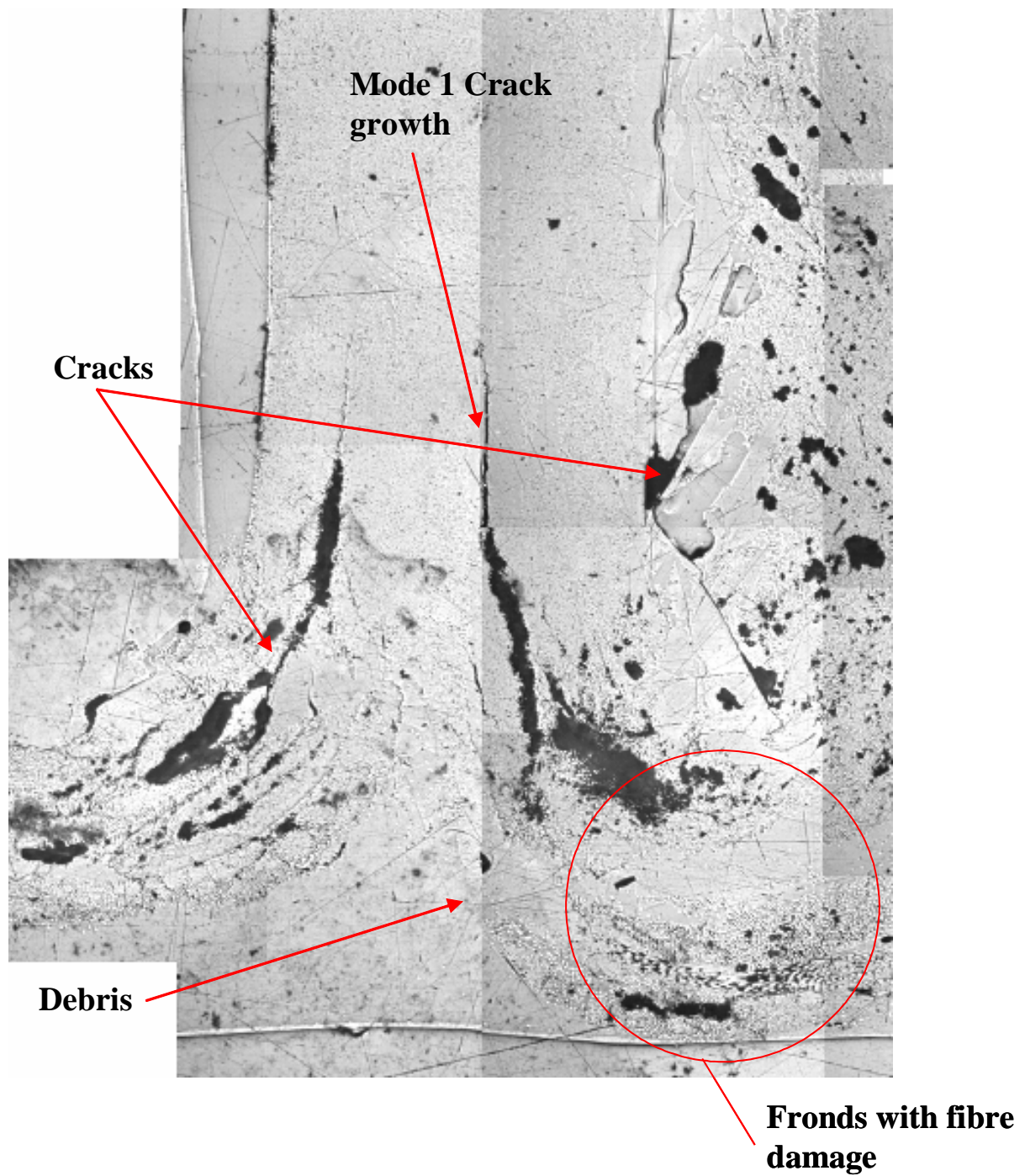


**Figure 88 Micrograph of Triaxial  $\pm 60$  Crush Zone under Dynamic Testing**

In the NCF 0-90 samples, Figure 71, it can be seen that the outer layer of the NCF fabric just splays, playing a very small part in the energy absorption process's with very small amounts of fibre damage and resin fragmentation, compared to the inner fronds that show large amounts of resin and fibre damage. Also evident is the elastic spring back in these samples with some cracking seen in the fronds.

The NCF 90-0 samples, Figure 74, show much more resin fragmentation with more fibre damage evident in the fronds. All layers of the tube participate fully in the crush process, due to the external hoop fibres restraining the axial fibres and reducing splaying, and give one reason why the energy absorption of this orientation is higher. Visually the failure mode seen in these samples is very similar in shape to that experienced by Ribeaux[7] in his CoFRM tubes. In these samples a much larger centre wall crack can be seen. This is significantly higher than any cracking associated with the NCF 0-90 samples.

The Micrographs of the dynamic NCF  $\pm 45$  sample, Figure 77, shows the lack of resin fragmentation and the intact individual tows after the crush. The quasi-static sample is similar to the NCF 90-0 sample, thus explaining why the energy absorption levels are similar.

The biaxial  $\pm 30$  samples, Figure 80, show a large number of cracks in the crush zone on the edge of the fibre tows, there is some evidence that the inner fronds show more fibre damage and resin fragmentation. Dynamically very little fibre damage is seen, and there is little evidence of buckling. This lack of fibre damage explains the lower SEA seen by these samples.

Both sets of Biaxial  $\pm 60$  tubes, Figure 83, show evidence of some buckling in the inner layers of the tube and splaying on the outer layers. There is much more resin fragmentation and fibre damage apparent than in the Biaxial  $\pm 30$  tubes. This explains the higher energy absorptions seen, especially at the higher rate. There is a much larger centre wall crack evident quasi-statically in both Biaxial  $\pm 60$  and Triaxial  $\pm 60$  samples. The Triaxial  $\pm 60$  tubes show a similar failure mode to the Biaxial  $\pm 60$  tubes quasi statically. On the inner layers there is slightly more fibre damage, a possible reason why the energy absorption is higher. Dynamically no buckling or folding can be seen and the failure mode is much closer to that seen in CoFRM and the 90-0 NCF samples.

## 4.2.6. Ultimate Compressive Stress

Data for the UCS with undamaged (virgin) tubes is presented in Table 13.

**Table 13 UCS Data For Undamaged Tubes**

Fibre Type	Chart Ref	Quasi-static UCS MPa	Quasi-static Crushing Stress MPa	Dynamic UCS MPa	Dynamic Crushing Stress MPa
NCF 0-90	0-90	139.1(5.9)	62.8(2.7)	133.7(13.5)	50.3(2.4)
NCF 90-0	90-0	207.6(5.6)	83.8(1.4)	170.2(10.8)	62.8(5.8)
NCF AO	AO	148.8(12.8)	71.2(1.6)	147.5(15.1)	71.2(9.2)
NCF HO	HO	165.4(22.9)	88.0(2.2)	160.1(36.9)	54.4(4.1)
NCF ±45	±45	102.2(18.0)	83.8(8.0)	110.3(11.2)	50.3(7.7)
Braid ±30	B30	128.9(4.7)	73.3(1.1)	143.2(9.8)	54.4(22.7)
Braid ±45	B45	118.3(0.1)	67.0(3.8)	122.5(14.8)	79.6(1.4)
Braid ±60	B60	106.2(3.4)	88.0(23.0)	125.2(9.8)	92.1(5.1)
Triaxial ±30	T30	155.1(3.5)	NA	221.7(4.3)	NA
Triaxial ±45	T45	137.1(2.3)	NA	161.6(3.0)	NA
Triaxial ±60	T60	136.4(7.7)	98.4(0.5)	114.0(5.7)	90.0(5.8)

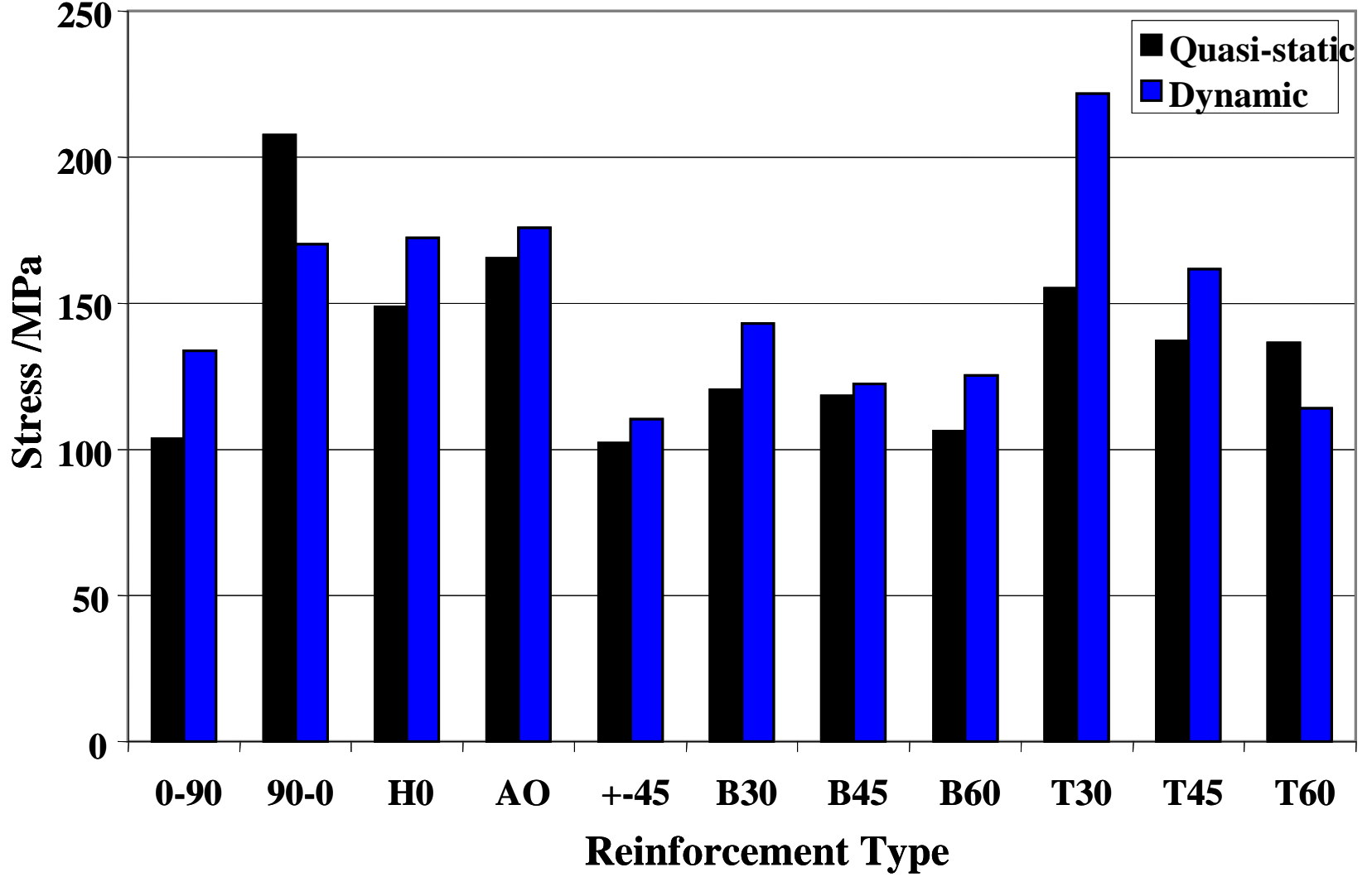
All samples were 80mm long circular Ø38.1mm glass/polyester samples.

In the table NCF AO refers to fibre orientation (c) from section 3.2, page 55 and NCF HO refers to fibre orientation (d) from section 3.2, page 55.

The UCS data can also be seen in Figure 89

See Table 13 for chart references

Figure 89 UCS for Different Fibre Architectures



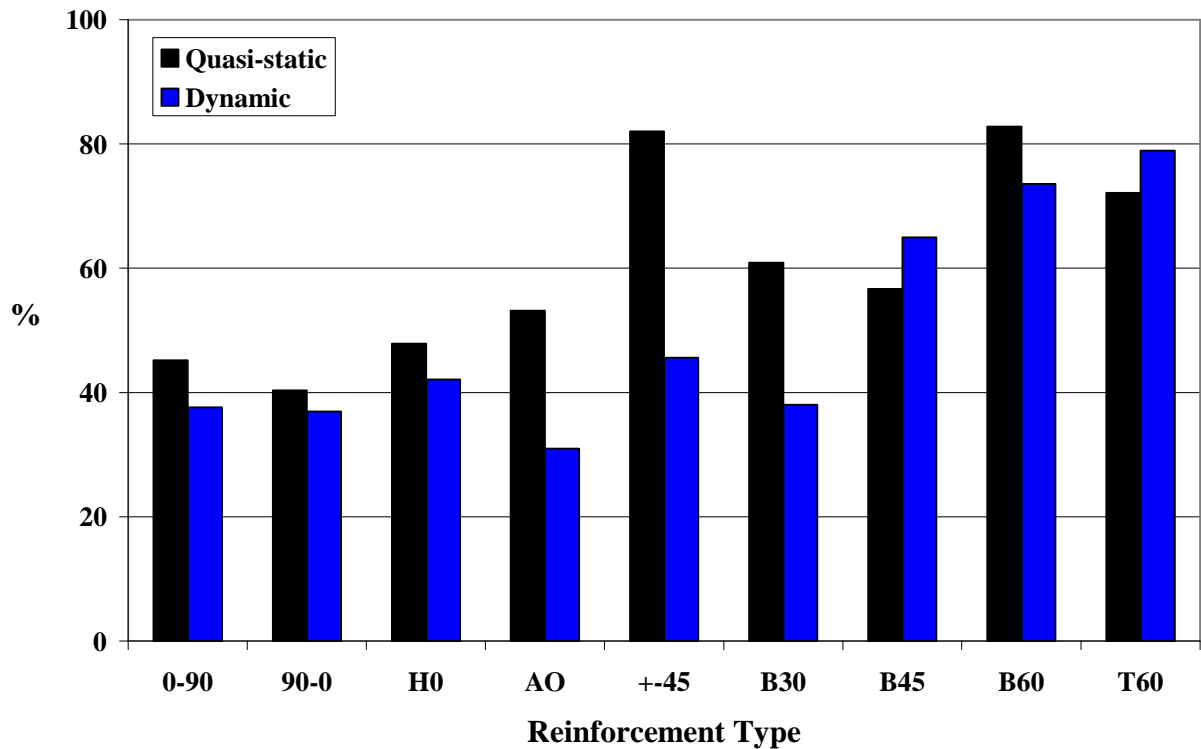


**Figure 90 Average Crushing Stress as Percentage of Ultimate Compressive Stress**

The majority of the samples exhibit an increase in UCS with rate. By looking at Figure 90 and Figure 89 it can be seen that in the most part the results obtained agree with those found by Fernie [4] and Ribeaux[7]; Fernie found increase of up to 46% in UCS with rate. Here the 0-90, 90-0 and T60 samples show a decrease in UCS with rate, which could be attributed to a change in the mode of failure.

From Figure 90 it can be seen that when the average crushing stress is divided by the UCS, the dynamically tested samples show a lower percentage than the quasi-static samples. This means that they crush at a lower load compared to the ultimate compressive load of the sample. The samples B45 and T60 appear to be an exception to this trend, with the T60 values distorted by a lower measured dynamic UCS

## **4.2.7. Stress Concentrations**

This section is split into theoretical and experimental sections. The experimental sections look at the effect of a hole drilled through the thickness of the tube upon the energy absorption capability of the tube. The theoretical sections look at the stress concentration factors associated with these holes.

In the present work, the stress concentration/damage is represented by a hole, drilled perpendicular to the axis of the tube.

### **4.2.7.1. Holes**

Hole sizes of 5mm up to 16mm diameter were tested. Initial testing by Warrior and Ribeaux [99] suggested that these levels would provide a suitable level of damage to allow the tube to fail in an unstable manner.

#### **4.2.7.1.1. Initial testing**

The results presented here are the initial testing with the NCF 0-90 orientation. Holes were drilled at positions of 15 and 45 mm from the chamfer. The testing was undertaken at 2 rates, quasi-statically at  $10\text{mm min}^{-1}$  and dynamically at  $5\text{ms}^{-1}$ . The results can be seen in Table 14.

**Table 14 SEA Data for Initial Testing with Holes**

Test Reference	Hole Location /mm	Hole Diameter /mm	Quasi-static SEA (kJ/kg) (std. Dev %)	Failure mode	Dynamic SEA (kJ/kg) (std. Dev %)	Failure mode
<b>C0m</b>	<b>NA</b>	<b>NA</b>	<b>39.0 (2.7)</b>	<b>1</b>	<b>32.7 (2.4)</b>	<b>1</b>
C10m15	15	Ø10	36.0 (1.4)	2+1	31.1 (7.6)	1+2
C16m15	15	Ø16	33.0 (8.4)	2	28.9 (3.5)	2
C10m25	25	Ø10	36.4 (6.5)	3	29.1 (5.9)	3+1
C10m45	45	Ø10	41.6 (1.3)	1+3	30.8 (9.0)	1+3

The undamaged specimens crushed progressively with a stable splaying mode of failure. Long fronds were created and a small debris wedge was formed.

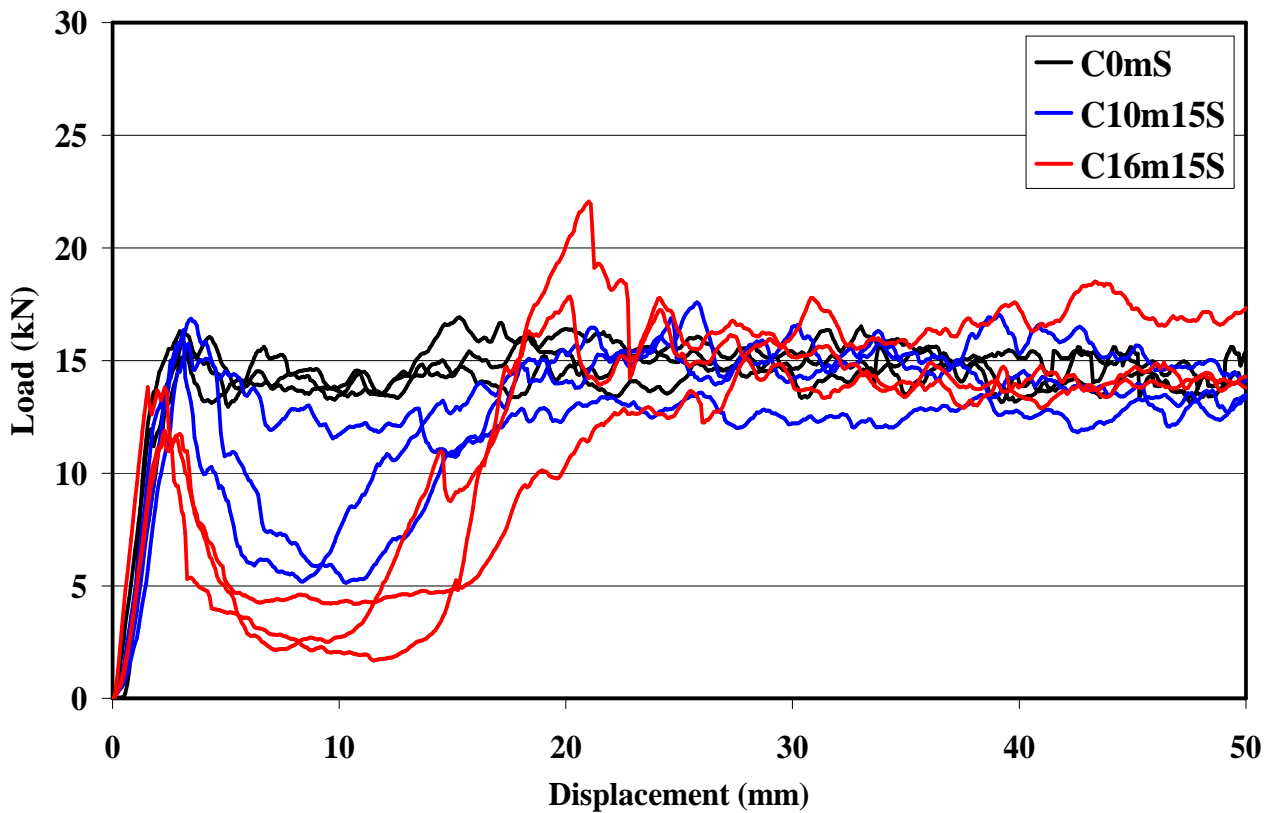


**Figure 91 Load Displacement Curve for Holes at 15mm Tested Quasi-statically**

All the specimens with holes of diameter 16mm failed with the same mode of global failure, a crack was formed at the edge of each hole where the stress was highest. This crack then propagated around the circumference of the tube in a quick and catastrophic manner. This caused the tube to split and collapse. The load fell to a small level. When the crush reached 15mm i.e. the position of the crack where the fracture surface meets the crush platen, the tube again began to absorb energy, and fronds were formed and a stable crush mode was achieved. The load displacement curve can be seen in Figure 91.

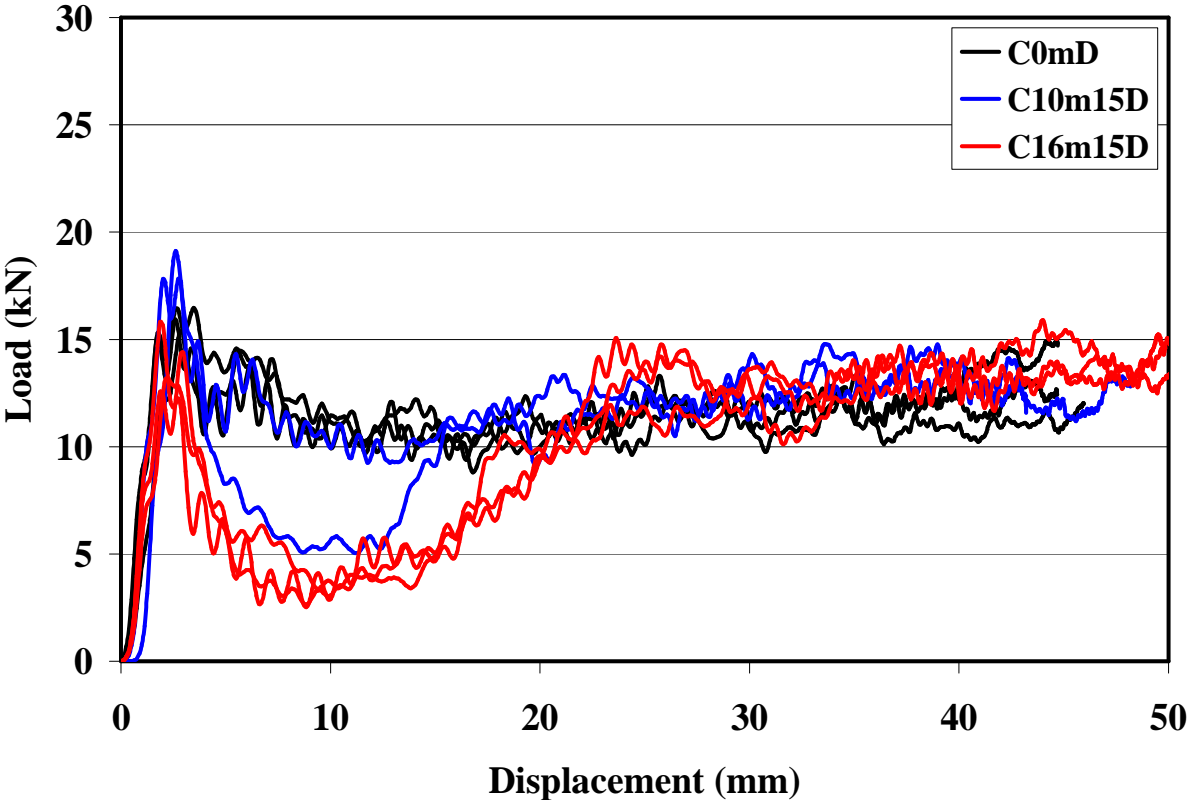


**Figure 92 Load Displacement Curve for Holes at 15mm Tested Dynamically**

Dynamically the SEA decreases by up to 21% for an undamaged specimen. This reduces 12% for the damaged specimens. The threshold levels for damage are similar between static and dynamic tests, however, only one of the tubes with a 10mm hole failed globally at dynamic rates, compared to two specimens statically. Figure 92 shows the load displacement curve for the dynamic samples.

The effects of the damage appear to be more localised during the dynamic tests, i.e. the effects of the damage are less pronounced at dynamic rates.

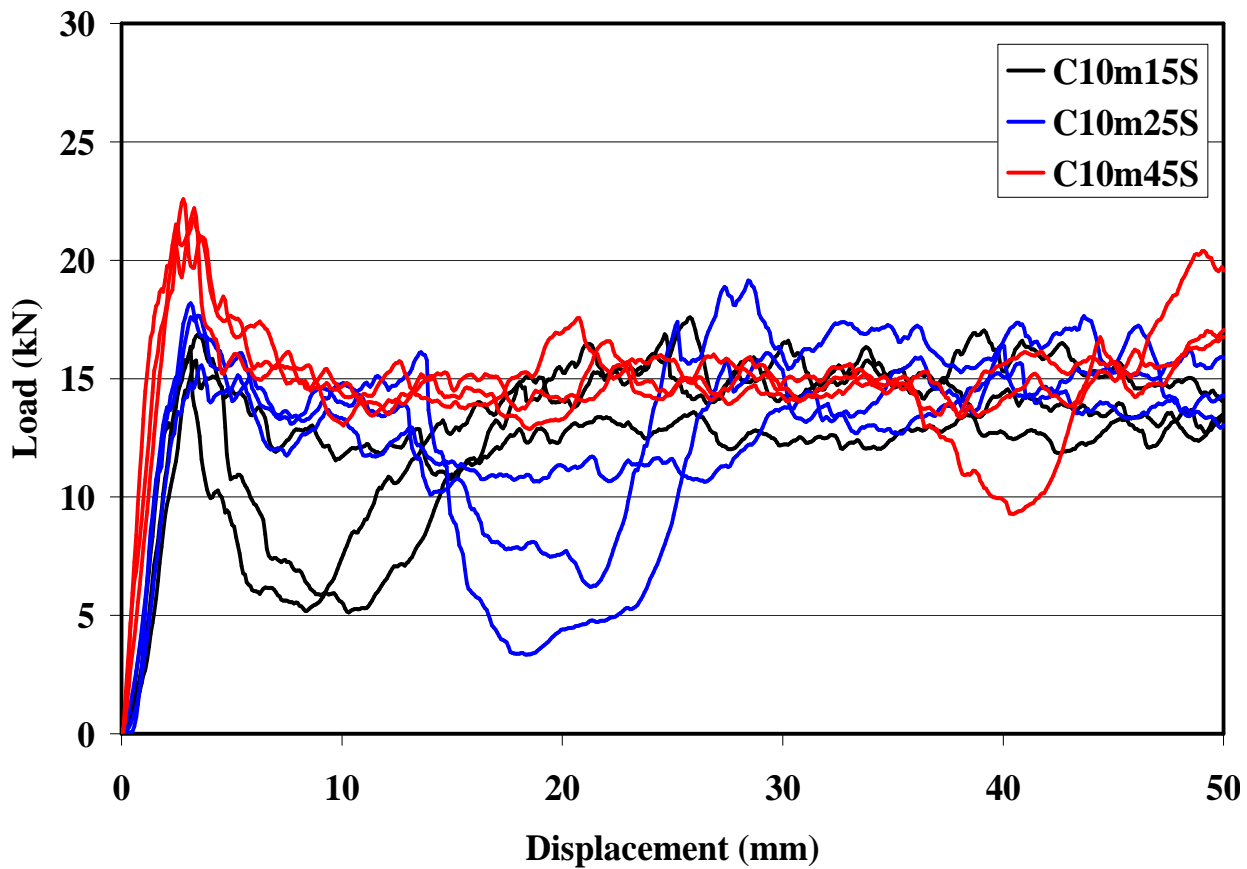


**Figure 93 Load Displacement Curve for Holes along Tube**

Only one specimen with a hole at 45mm showed any effect from the hole. In this case, there was a small drop in load 10mm before the centre of the hole. The other specimens showed no effect. The specimens failed statically and dynamically in a similar way. Again, the dynamic energy absorption was lower than the static.

These results show that holes of this size only cause a local unstable failure near the hole. This is illustrated in Figure 93.

#### 4.2.7.1.2. Holes at 25mm from Chamfer

This section shows the results of different sizes holes drilled at 25mm from the chamfered end of the tube. The majority of the data is for circular section tubes, however one set of data is present for square sectioned tubes constructed from 0-90 NCF (see Table 15).

**Table 15 Data for NCF Samples with Holes at 25mm from Chamfer**

Fibre Type	Test Reference	Hole Diameter /mm	Quasi-static SEA (kJ/kg) (Std. Dev %)	Failure mode	Dynamic SEA (kJ/kg) (Std. Dev %)	Failure mode
<b>NCF 0-90</b>	<b>C0m</b>	<b>0</b>	<b>39.0 (2.7)</b>	<b>1</b>	<b>32.7 (2.4)</b>	<b>1</b>
NCF 0-90	C5m	Ø5	40.9 (1.9)	1	31.8 (1.2)	1
NCF 0-90	C10m	Ø10	36.4 (6.5)	3&1	30.6 (5.9)	1&3
NCF 0-90	C16m	Ø16	23.2 (5.8)	2	23.9 (5.1)	2
<b>NCF 0-90</b>	<b>Q0m</b>	<b>0</b>	<b>39.8 (6.9)</b>	<b>1</b>	<b>28.9 (4.6)</b>	<b>1</b>
NCF 0-90	Q5m	Ø5	41.2 (8.4)	1	30.0 (2.9)	1
NCF 0-90	Q10m	Ø10	35.7 (12.7)	1&3	31.5 (3.9)	1
NCF 0-90	Q16m	Ø16	21.7 (7.2)	2	29.3 (9.7)	1&3
<b>NCF 90-0</b>	<b>C900m</b>	<b>0</b>	<b>50.4 (1.4)</b>	<b>1</b>	<b>39.8 (5.8)</b>	<b>1</b>
NCF 90-0	C905m	Ø5	57.1 (5.9)	1	40.3 (0.9)	1
NCF 90-0	C9010m	Ø10	28.2 (14.5)	2	39.4 (2.3)	1&3
NCF 90-0	C9016m	Ø16	31.0 (1.1)	2	27.4 (5.4)	2
<b>NCF +/-45</b>	<b>C450m</b>	<b>0</b>	<b>55.4 (8.0)</b>	<b>1</b>	<b>29.6 (7.7)</b>	<b>1</b>
NCF +/-45	C455m	Ø5	53.3 (5.0)	1	27.7 (9.2)	1
NCF +/-45	C4510m	Ø10	48.5 (1.9)	2	30.7 (4.2)	1&2
NCF +/-45	C4516m	Ø16	30.8 (42.2)	2	17.5 (25.0)	2

Where C denotes Circular cross-section and Q denotes Square cross-sectional tubes

When tested with the effects of the stress-concentration, the 0-90 tubes samples with a 5mm hole failed progressively by mode 1 failure. The samples showed a slight increase in SEA over the samples without any damage (as a result of the reduction in mass due to the hole). Dynamically, the behavior was similar. The 5mm holes caused only a small reduction in SEA and all failed progressively.

The samples with 10mm holes crushed under quasi-static loading with a mixture of failure modes. Two of the samples with holes crushed with a mode 3 failure (local load drop-off) and the other sample crushed progressively in a mode 1 (undamaged tube) failure (See Figure 94)

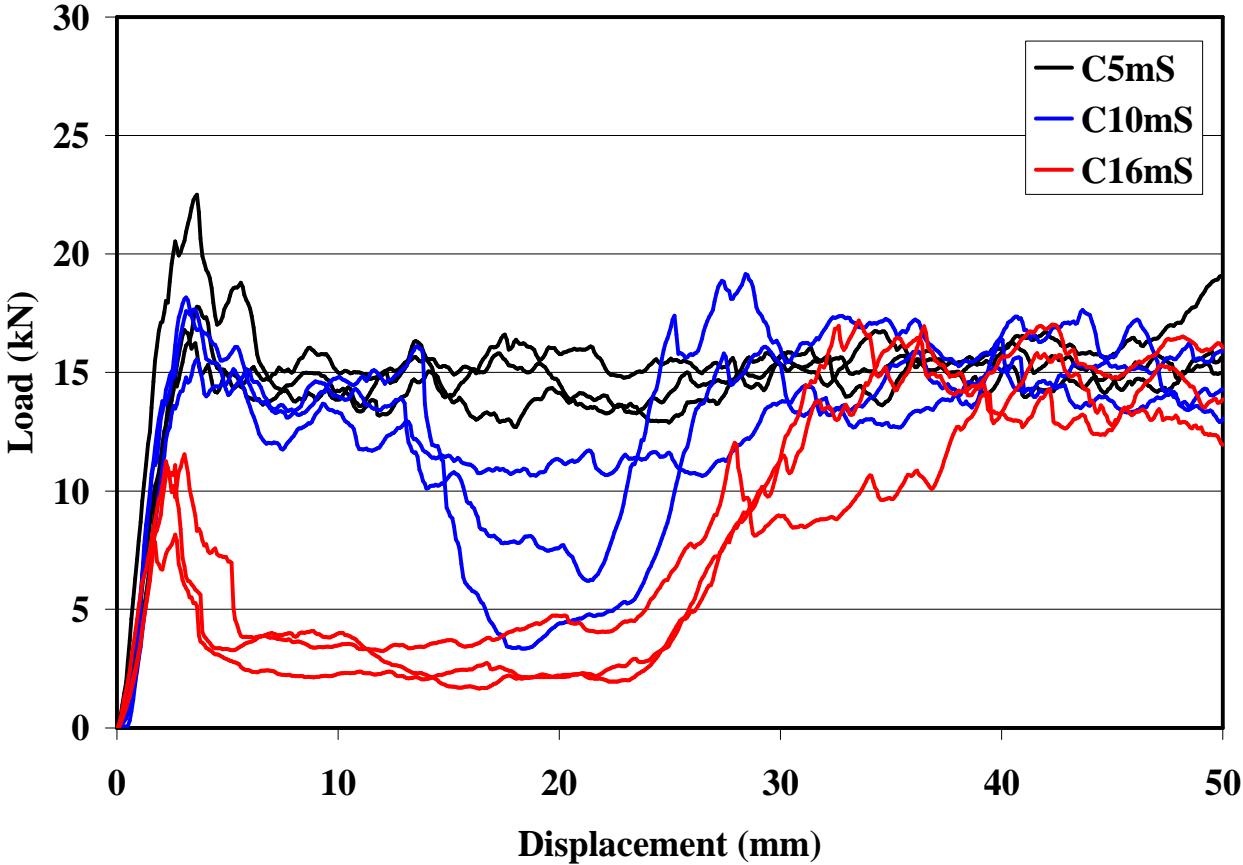


**Figure 94 Load Displacement Curve for NCF 0-90 with Holes at 25mm under Quasi-static Loading**

Dynamically, the 10mm hole samples failed predominantly through a mode 1 failure, but with 1 of the samples at 25mm failing in mode 3, however, the drop in SEA is small. In all of the samples tested the specimens with 16mm holes all failed globally (mode 2), under both static and dynamic loadings. As soon as the maximum load was reached, a crack propagated around the circumference of the tube causing global failure (see Figure 95). This is typical behaviour of a sample above the threshold level. Failure occurred at the edge of the damage zone - a stress-induced crack was formed and quickly propagated parallel to the fibre angles.

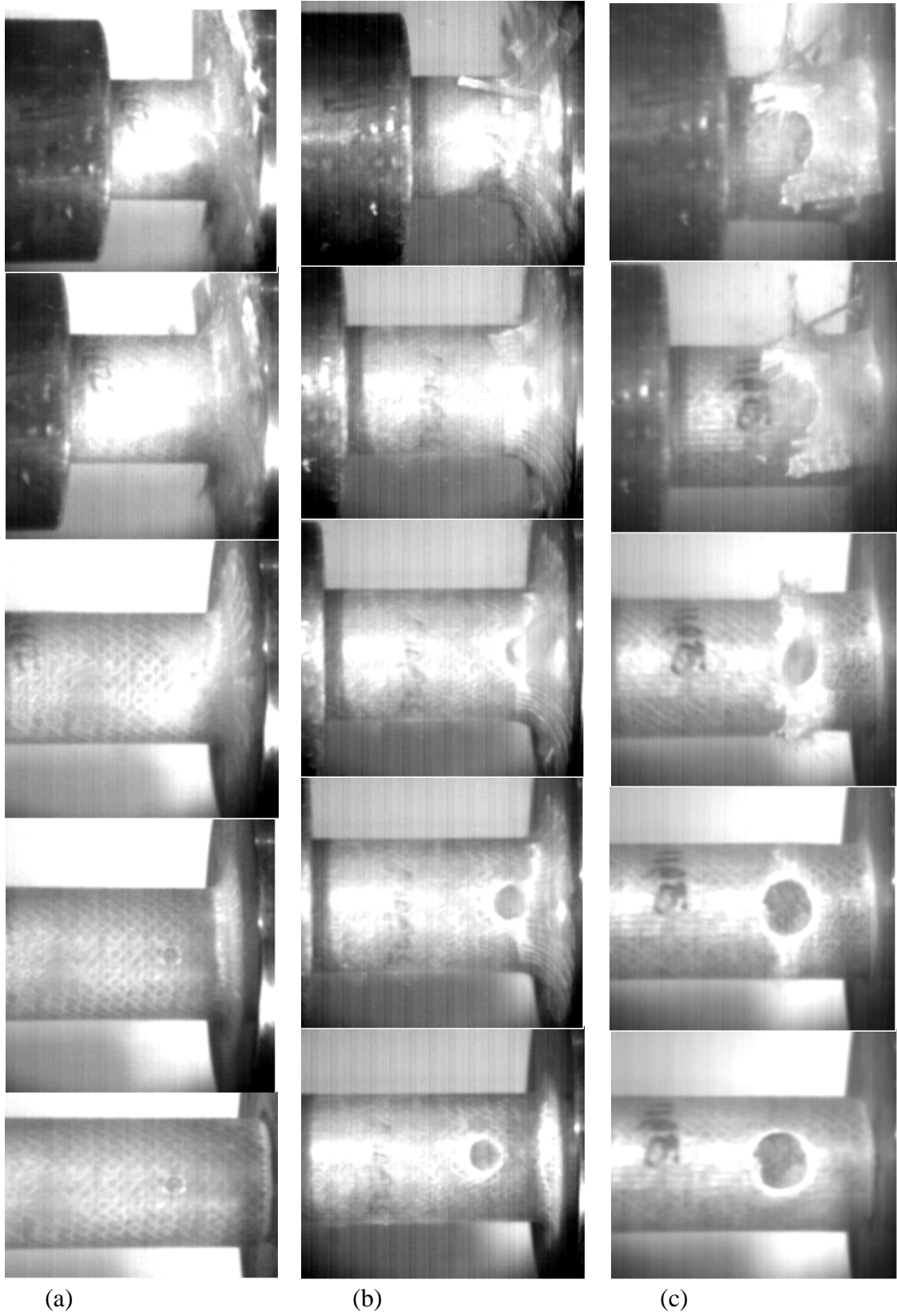


**Figure 95 NCF 0-90 Tubes with Holes, Samples C5m (a), C10m (b), and C16m (c), Under Dynamic Loading**

The 90-0 samples dynamically followed the same pattern as the 0-90 tubes. Quasi-statically the only difference was the samples with 10mm holes now failed globally in a mode 2 failure (see Figure 96). The  $\pm 45$  samples failed quasi-statically the same way as the 90-0 tubes. Samples with 5 mm holes crushed progressively and those with 10mm holes failed globally. Two of the samples with 10mm holes, dynamically, crushed progressively and the third failed globally. An illustration of the failure mode for the  $\pm 45$  NCF samples can be seen in Figure 97.

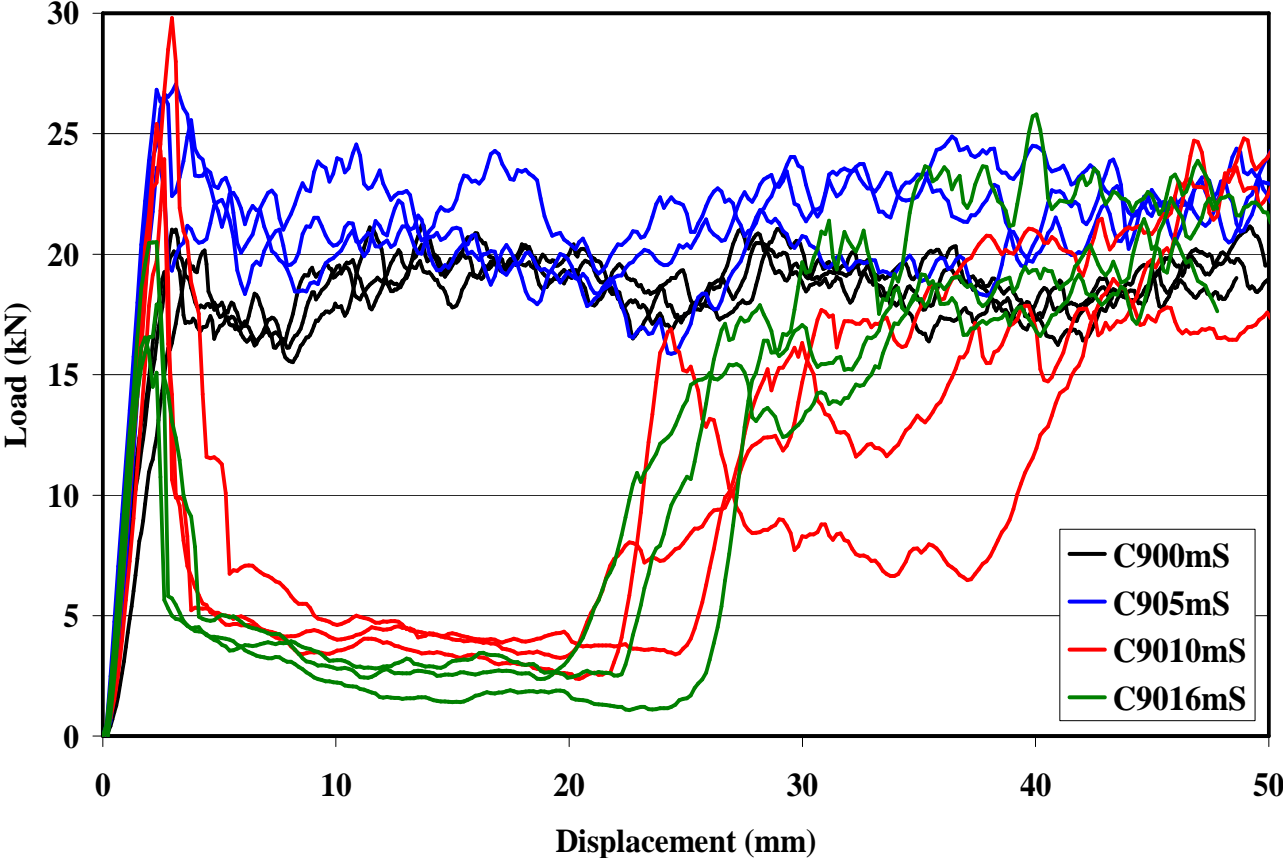


**Figure 96 Load Displacement Curve for NCF 90-0 with Holes at 25mm under Quasi-static Loading**

For a tube of this geometry, where  $D/t = 19$ , a single hole of 16mm diameter, i.e.  $D/d = 2.375$ , will cause global failure in all samples. For the NCF specimens a 5mm hole,  $D/d = 7.6$ , causes no effect on SEA quasi-statically or dynamically. A  $D/d$  of 3.8, a 10mm hole, appears to be the threshold for the NCF tubes

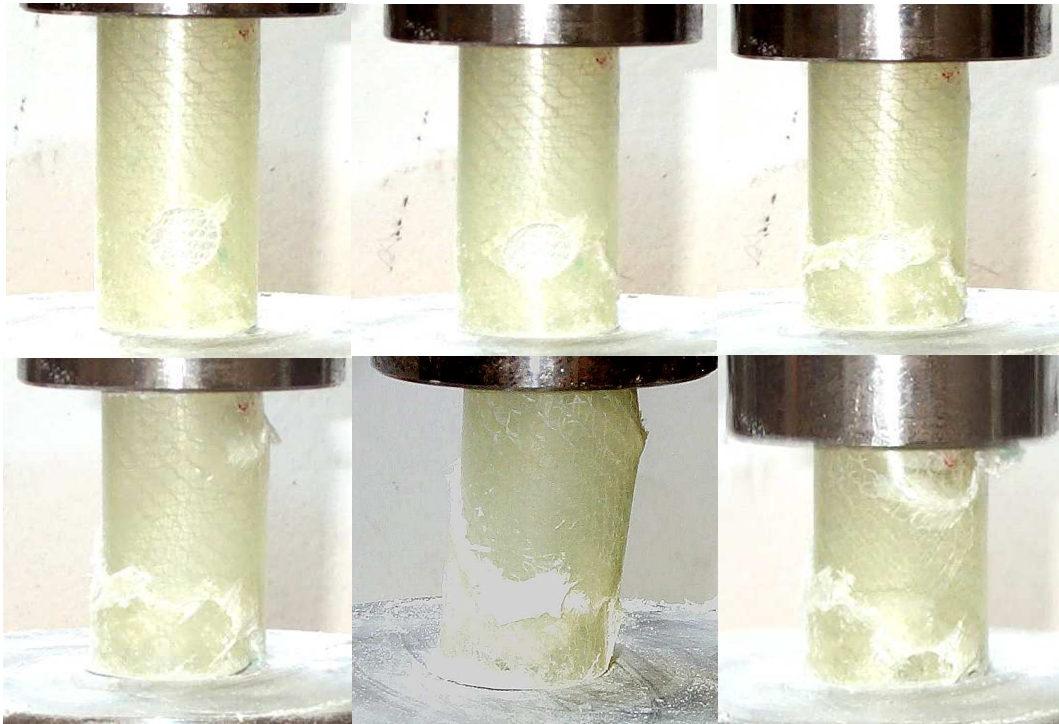


**Figure 97 NCF  $\pm 45$  Sample C4516m under Quasi-static Loading**

For the square samples, the pattern was very similar. Quasi-statically, the samples with 5mm holes all failed progressively and two of samples with 10mm holes failed progressively with only small drops in load near the hole, again due to reduction in area. In the 3<sup>rd</sup> sample there was a slightly larger decrease in load, and the sample did not recover fully. The 16mm hole samples again failed globally, with the crack progressing to the corner of the tube, then down the next side until the section broke away (Figure 98).

Under dynamic testing, the square samples performed much better. The 5mm and 10mm holes had very little effect on the mode of failure, these samples all crushed progressively with only a slight drop in load at the hole in one of the Q10m samples. With the larger sized hole, all samples failed progressively, although 1 of them failed locally in mode 3 failure. The load-displacement curve can be seen in Figure 99.

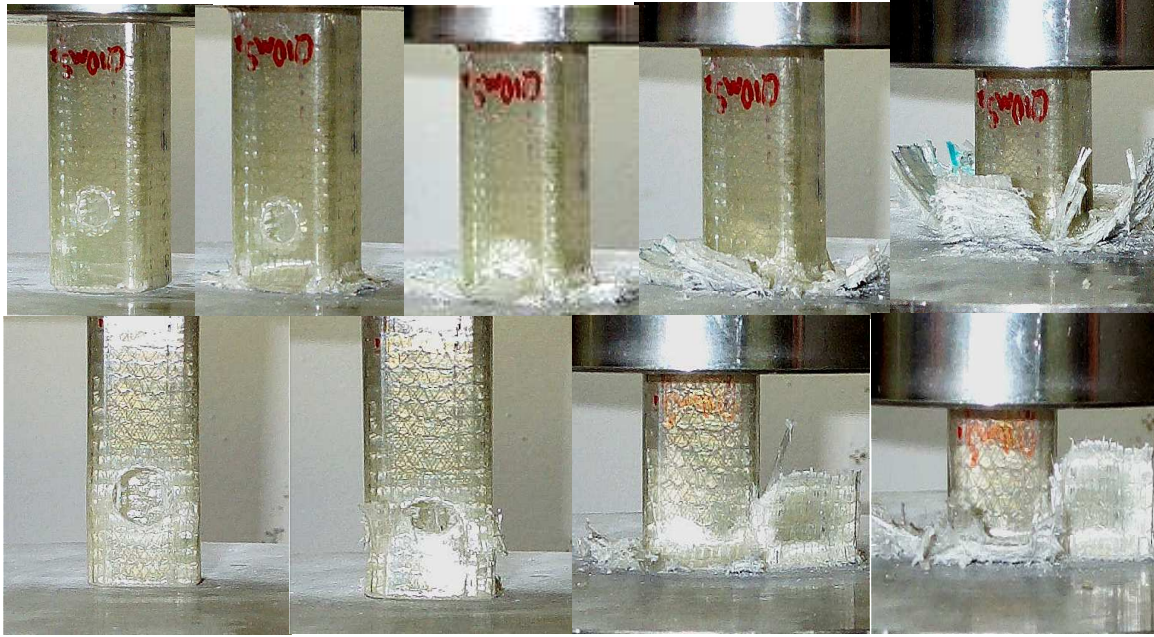


Figure 98 Samples Q10m and Q16m under Quasi-static Loading

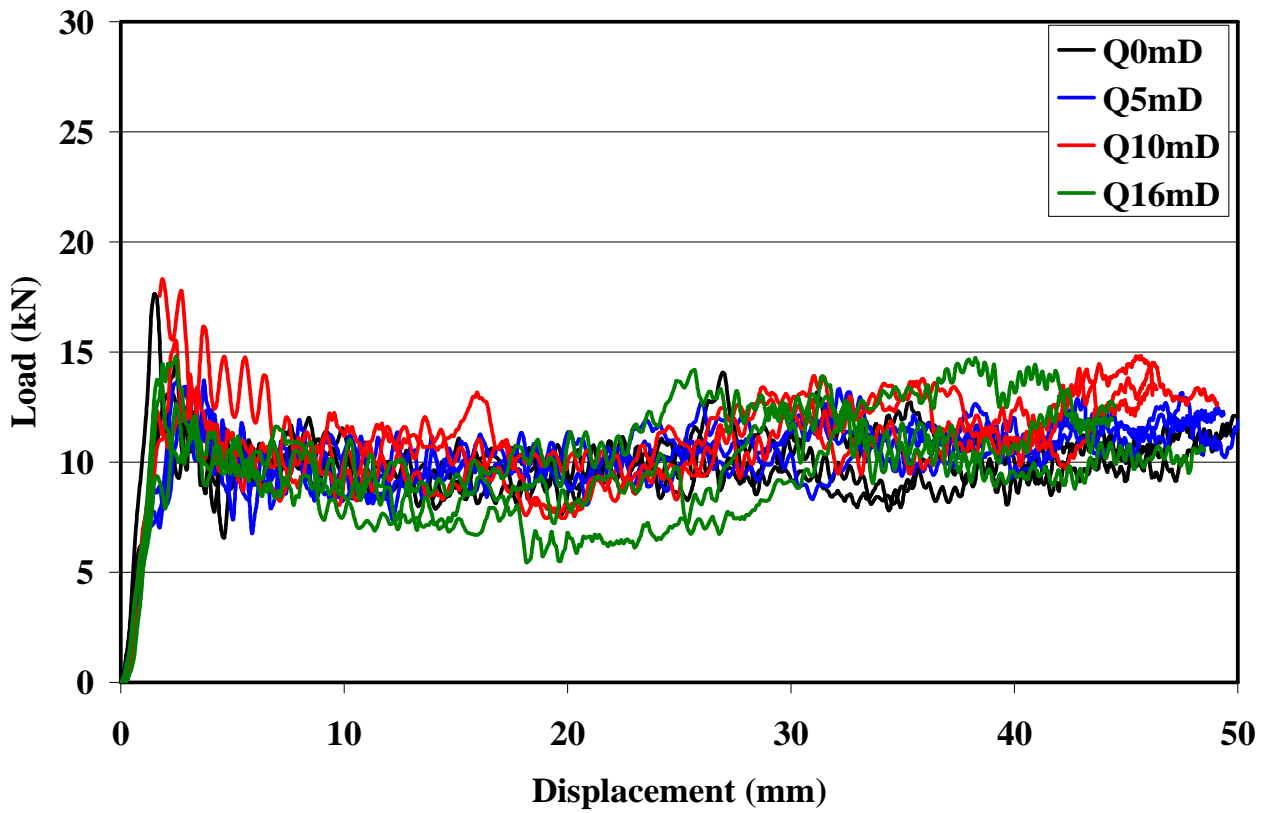


Figure 99 Load Displacement Curve for Square NCF 0-90 under Dynamic Loading

**Table 16 Data For Braided Samples With Holes at 25mm From Chamfer**

Fibre Type	Test Reference	Hole Diameter /mm	Quasi-static SEA (kJ/kg) (Std. Dev %)	Failure mode	Dynamic SEA (kJ/kg) (Std. Dev %)	Failure mode
<b>Braid ±30</b>	<b>CB30m</b>	<b>0</b>	<b>44.1 (1.1)</b>	<b>1</b>	<b>30.7 (22.7)</b>	<b>1</b>
Braid ±30	CB305m	Ø5	29.6 (12.9)	1&2	33.9 (9.1)	1
Braid ±30	CB3010m	Ø10	32.6 (12.4)	2	32.8 (8.8)	1
Braid ±30	CB3016m	Ø16	27.7 (16.4)	2	27.1 (19.1)	2&1
<b>Braid ±45</b>	<b>CB450m</b>	<b>0</b>	<b>38.8 (3.8)</b>	<b>1</b>	<b>48.4 (1.4)</b>	<b>1</b>
Braid ±45	CB455m	Ø5	32.6 (28.2)	2	46.9 (4.1)	1
Braid ±45	CB4510m	Ø10	34.5 (10.0)	2	45.7 (4.0)	1
Braid ±45	CB4516m	Ø16	27.5 (13.0)	2	31.6 (1.2)	2
<b>Braid ±60</b>	<b>CB600m</b>	<b>0</b>	<b>45.1 (23.0)</b>	<b>1&amp;3</b>	<b>52.6 (5.1)</b>	<b>1</b>
Braid ±60	CB605m	Ø5	33.8 (8.9)	3	41.9 (10.7)	3&1
Braid ±60	CB6010m	Ø10	30.8 (14.7)	2	30.3 (8.1)	2&3
Braid ±60	CB6016m	Ø16	29.1(4.6)	2	26.7 (15.1)	2
<b>Braid 0±60</b>	<b>CT600m</b>	<b>0</b>	<b>53.8 (0.5)</b>	<b>1</b>	<b>48.7 (3.9)</b>	<b>1</b>
Braid 0±60	CT605m	Ø5	48.2 (23.8)	1&3	47.7 (4.1)	1
Braid 0±60	CT6010m	Ø10	36.2 (15.8)	2	28.4 (20.1)	2&1

Quasi-statically the behaviour of the braided tubes with 10mm and 16mm holes was similar (see Table 16 for SEA data). All braided samples failed globally with cracks starting at the edge of the hole. The cracks followed fibre orientations (Figure 100) and propagated along the tows. Some cracks propagated downwards to the damage zone, others were seen to form in line with the fabric orientation with one side propagating upwards to the top crush platen.

The specimens with 5mm holes behaved differently. For the ±30 tubes, 2 samples failed progressively in a mode 1 failure, and 1 sample failed globally (Figure 101). All samples failed globally for the ±45 tubes, and all samples showed a local drop off in load for the ±60 tubes. The addition of the axial fibres into the braid (Braid 0±60) appears to have improved the damage tolerance over the ±60 tubes. Now 2 samples show no effects from the hole and the third shows only a small decrease in load. The Energy absorption is also improved over the ±60 tubes.



**Figure 100 Braided Samples CB3010m, CB605m and CB3016m Showing Mode 2 Failure**



**Figure 101 Braided Sample CB3010m, Showing Mode 2 Failure**

Dynamically all the samples with 5mm holes failed progressively, (mode 1 failure) however, 2 samples of  $\pm 60$  had a local drop off in load around the hole (mode 3 failure). When the hole size was increased to 10mm, all of the samples crushed progressively for the  $\pm 45$  tubes and the  $\pm 30$  tubes. In the case of the  $\pm 60$  tubes 2 samples failed globally and 1 sample failed progressively in mode 3. At a hole size of 16mm all the  $\pm 60$  and  $\pm 45$  samples failed globally. 2 samples failed globally and one crushed progressively with the  $\pm 30$  tubes.

Quasi-statically the threshold value for the first onset of global or undesired failure for the braided tubes is  $D/d = 7.6$ , dynamically for the  $\pm 30$  and the  $\pm 45$  the threshold has improved to a value less than  $D/d = 3.8$ .

**Table 17 Data For CoFRM Samples With Holes at 25mm From Chamfer From [7]**

Fibre Type	Test Reference	Hole Diameter /mm	Quasi-static SEA (kJ/kg) (Std. Dev %)	Failure mode	Dynamic SEA (kJ/kg) (Std. Dev %)	Failure mode
<b>CoFRM<sup>a</sup></b>	<b>Co0m</b>	<b>0</b>	<b>74.6 (3.8)</b>	<b>1</b>	<b>70.2 (4.0)</b>	<b>1</b>
CoFRM	Co5m	Ø5	58.7 (39.7)	1&2	69.7 (6.7)	1
CoFRM	Co10m	Ø10	22.0 (24.7)	2	56.7 (10.4)	3
CoFRM	Co16m	Ø16	22.3 (52.6)	2	20.1 (28.4)	2

Comparing the threshold damage levels, at which the sample begins to fail in a non-progressive manner, for the circular NCF 0-90 tube statically the threshold is a 10mm hole,  $D/d = 3.8$  this is half that seen by a similar CoFRM tube which had a  $D/d = 7.6$ . Dynamically this threshold is the same, although more samples failed progressively suggesting an improved damage tolerance at the higher rates. Statically the results are the same for the square tubes; the threshold is again 10mm with a  $W/d$  of 3.0. Dynamically however, there is no effect on the crush mode at this level. The threshold level is increased to a hole size of 16mm ( $W/d = 1.875$ ) at this level only one of the samples failed globally. This is a significant improvement over the CoFRM results of [140] which show the threshold to be a  $W/d = 6$ , although the SEA levels are lower.

#### 4.2.7.2. Failure Stress Comparison

Whilst looking at the effects of stress concentrations it is useful to ascertain the level of maximum stresses for the samples tested. The UCS for an undamaged specimen has been presented earlier, and both the peak stress and crushing stress for undamaged specimens can be estimated simply from the load displacement data. This information is presented in Table 18 for quasi-static testing and Table 19 for dynamic testing. Prediction of failure was a desired outcome so in order to investigate any trends in the data the global failure stress of a sample with a 16mm hole was measured. This enabled a stress comparison to be made between samples with a stress concentration and without. This diameter of hole was chosen because all specimens failed in a Mode 2 failure mode quasi-statically, and predominantly by a mode 2 failure type dynamically. This is presented as the Mode 2 UCS below.

**Table 18 Quasi-Static Stress Data**

Fibre Type	Ref	Quasi-static	Peak Stress	Crushing	Mode 2
		UCS MPa	MPa	Stress MPa	UCS MPa
		Undamaged	Undamaged	Undamaged	16mm hole
NCF 0-90	0-90	139.1	71.1	59.3	43.2
NCF 90-0	90-0	207.6	85.6	81.5	76.7
NCF AO	AO	148.8	111.1	88.0	71.4
NCF ±45	±45	102.2	82.5	83.8	74.0
Braid ±30	B30	128.9	94.1	73.3	64.8
Braid ±60	B60	106.2	88.0	88.0	58.1
Triaxial ±60	T60	136.4	104.8	98.4	80.3

**Table 19 Dynamic Stress Data**

Fibre Type	Ref	Dynamic UCS MPa	Peak Stress MPa	Crushing Stress MPa	Mode 2 UCS MPa
		Undamaged	Undamaged	Undamaged	16mm hole
NCF 0-90	0-90	133.7	68.2	50.3	60.0
NCF 90-0	90-0	170.2	105.1	62.8	89.6
NCF AO	AO	175.8	85.0	54.4	66.8
NCF ±45	±45	110.3	73.7	50.6	75.4
Braid ±30	B30	143.2	84.7	54.4	79.6
Braid ±60	B60	125.2	99.1	92.1	63.3
Triaxial ±60	T60	114.0	93.3	90.0	74.4

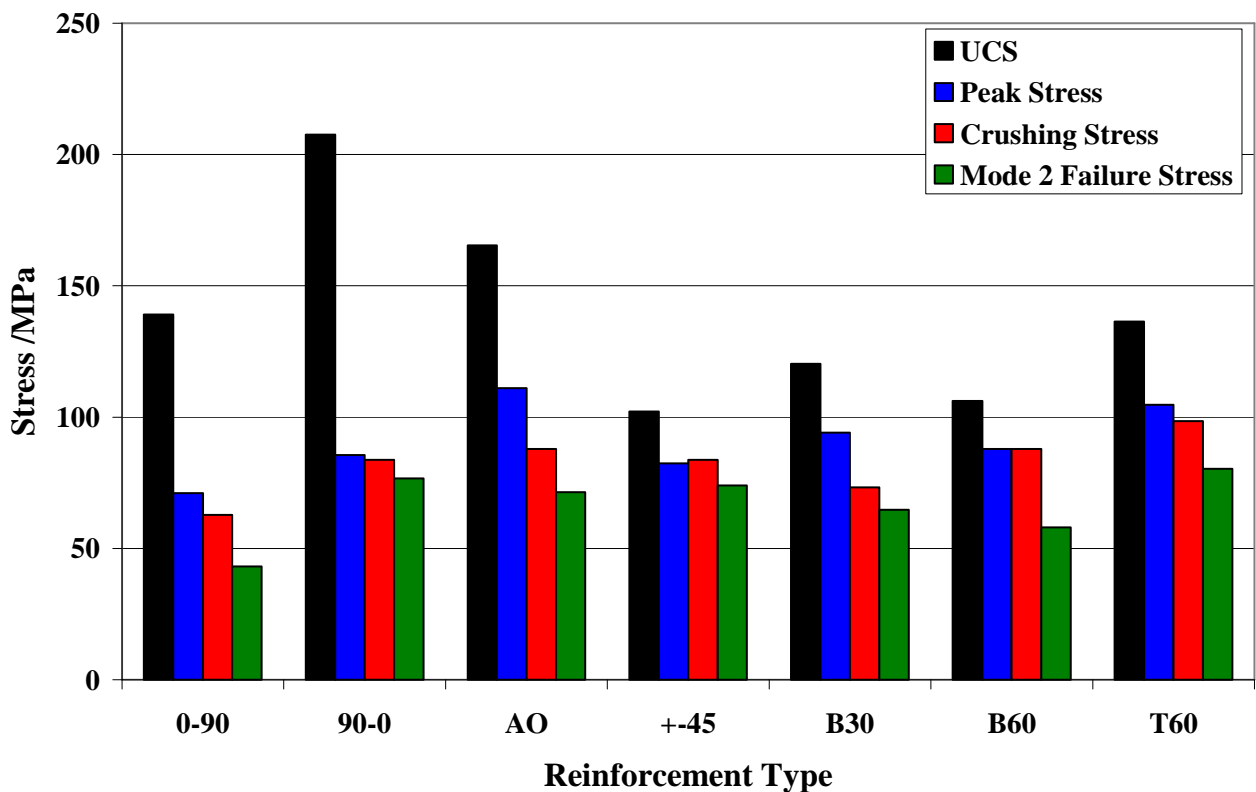


**Figure 102 Quasi-static Stress Comparison**

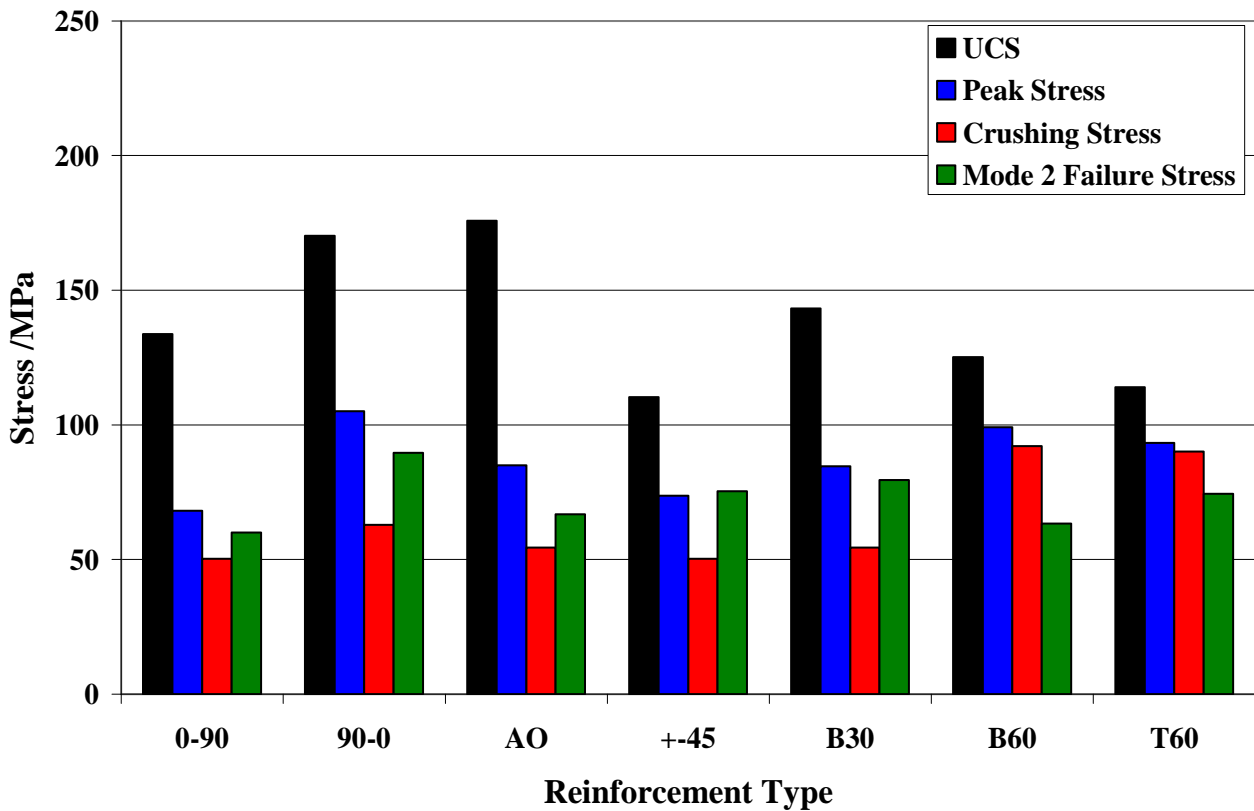


**Figure 103 Dynamic Stress Comparison**

Ribeaux [7] suggested that it was the crushing stress that gave an indication of the failure mode. In his results, for the samples that failed globally, an undamaged tube of that type crushed at a higher proportion of the UCS.

For global failure the quasi-static results presented here (Figure 102) suggest that the crushing stress is required to be higher than the Mode 2 failure stress. The results show that the crushing stress in all cases is higher than the failure stress for the samples with a 16mm hole.

This is illustrated in Figure 104, which shows a sampled undergoing progressive crush and a sample showing Mode 2 global failure. Here it can be seen that the crushing stress  $\sigma_c$  is higher than the peak failure stress  $\sigma_f$

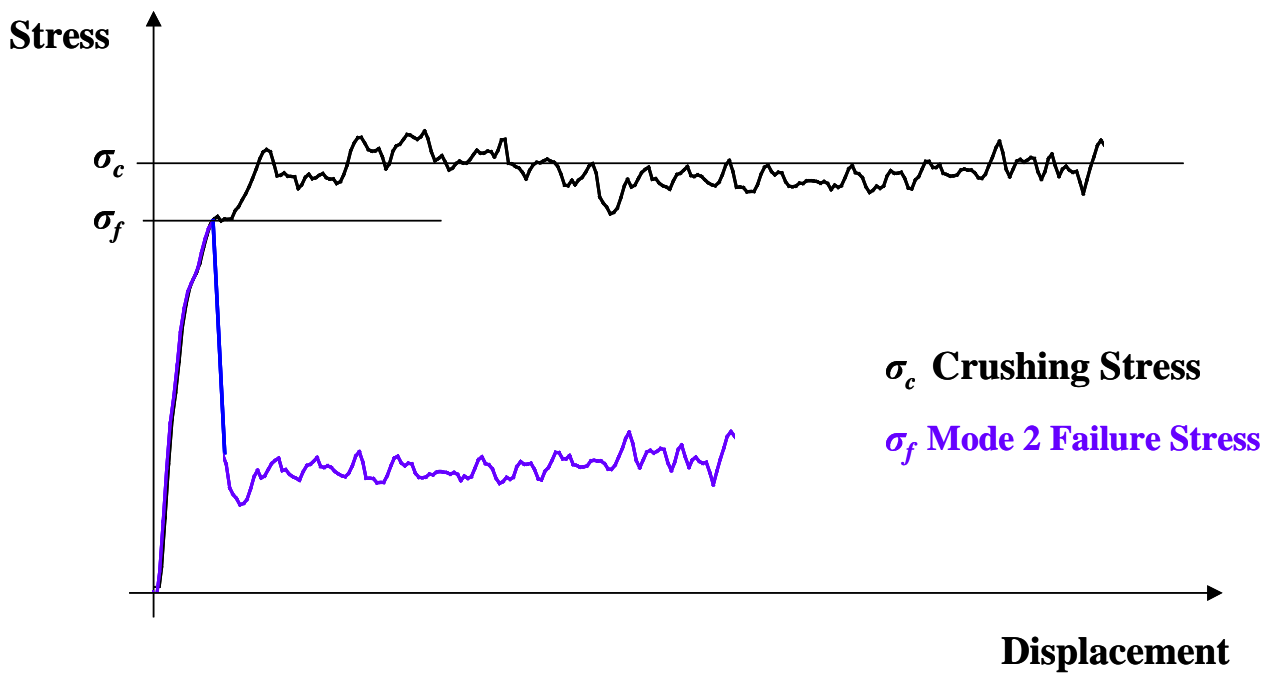


**Figure 104 Crushing Stress and Failure Stress Comparison from Quasi-static Results.**

The samples tested by Ribeaux[7] had no peak stress because of the lower in-plane strength of the CoFRM tubes, therefore peak stress = crushing stress.

This result is not valid for all the samples presented in this study. Examining the dynamic results in Figure 103 it can be seen that the crushing stress is significantly lower than the mode 2 failure stress. If Ribeaux's [7] result were to be applied then samples would not fail globally if it were the crushing stress that determined global failure. The results presented here do however show that a number samples fail globally, thus contradicting this theory.

If the peak stress is considered, then both quasi-statically and dynamically it is significantly higher than the crushing stress for the samples testing here; this can be attributed to the higher in-plane properties of the NCF and braided fabrics. As the peak stress is reached before the crushing stress it must be this that determines mode 2 failure.

Figure 103 shows the peak stress  $\sigma_p$  is higher than the mode 2 failure stress  $\sigma_f$ , also illustrated in the stress displacement curve Figure 105. From this figure, it can also be seen that as the

failure stress  $\sigma_f$  is greater than the crushing stress  $\sigma_c$ , the sample should not fail globally if we apply Ribeaux's[7] theory. As global failure occurs this must be triggered by the peak stress.

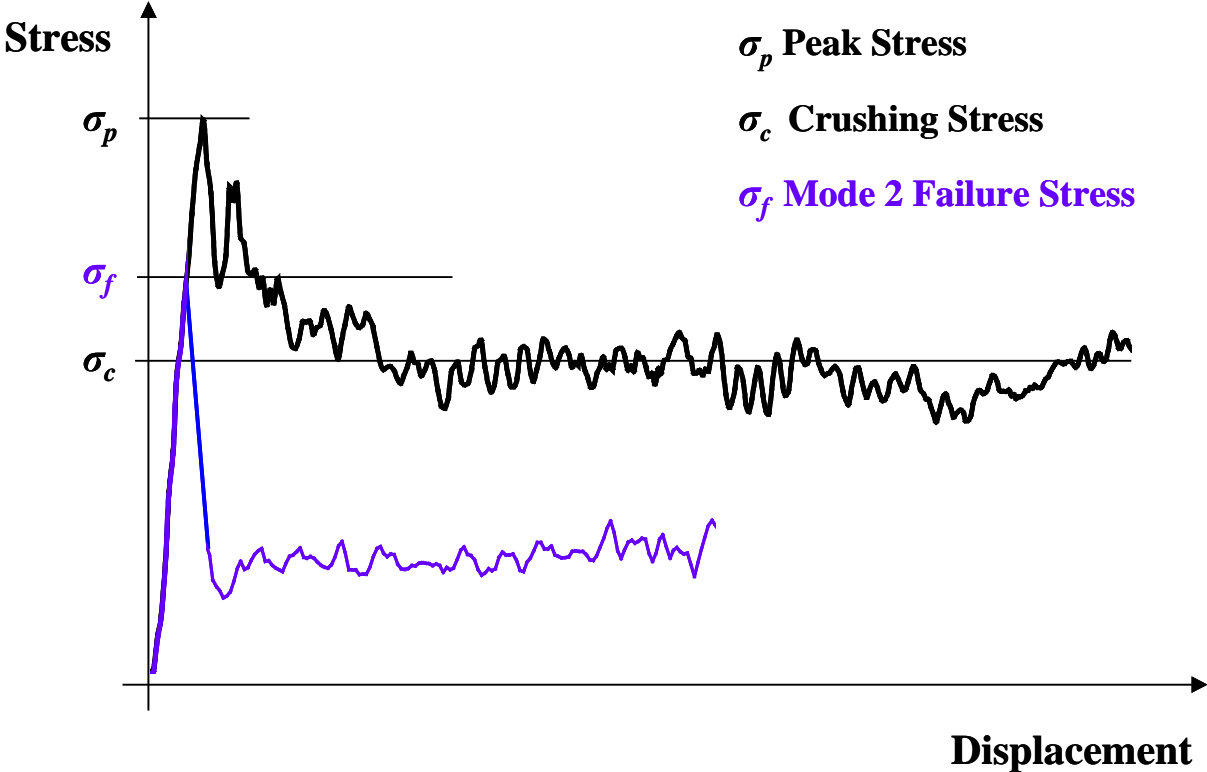


Figure 105 Stress Comparison for Samples with High In-Plane Properties

Thus for the majority of samples if the peak stress is greater than the mode 2 failure stress the sample will collapse globally in a mode 2 failure. If the peak stress is less than the mode 2 failure stress the sample will crush progressively.

### 4.2.7.3. Experimental Determination of Stress Concentration Factors

The previous section gave an indication of whether or not a tube would fail globally, but still did not show in what failure mode. Considering the SCF ( $K^1$ ) and crushing stress  $\sigma_c$  may give an answer. Multiplying the crushing stress by the stress concentration factor will give a theoretical maximum value of stress. If this is compared to the UCS, which is the maximum strength of the tube, then if it is greater the tube will fail globally, if it is less the tube will crush progressively. This is summarised by equation (15), which is proposed as the Mode 2 failure criteria.

$$\sigma_c * K^1 > UCS \quad (15)$$

Where  $\sigma_c$  is crushing stress and UCS is measured experimentally.

In determining SCF there are a number of analytical and numerical methods in existence (some of which are described in Appendix 3d). Here a novel approach used Thermal Stress Analysis (TSA) to try to establish the SCF for a cross-section of samples from this study.

Importantly, the tubes in the study are of brittle nature resulting in no redistribution of load after initial failure thus the SCF can be used as a guide to ultimate global failure. A FEA study on composites tubes (described in Appendix 3) showed that the maximum SCF lies on the outside surface of the tube and thus can be measured by an external detector. The SCFs were determined by thermal analysis using the Delta-Therm system. The camera was calibrated using a cold plate at 18°C and a hot plate at 38°C to verify that the camera sensor was reading the temperature values correctly.

The analysis was based upon the following equation [100] for Isotropic tubes :

$$\Delta(\sigma_1 + \sigma_2) = A.S \quad (16)$$

Where  $A$  = Calibration Constant and  $S$  = Output from detector.

$\sigma_1$  = Stress parallel to loading direction and  $\sigma_2$  = Stress perpendicular to loading direction

For a sample with plane stress and no hole, the calibration constant A can be found by rearranging the equation, as the applied stress and the output of the detector are known. This value of A can be used for the other samples of that type with a hole.

Importantly Quinn and Barton[80] state that on the surface of the cylinder at the rim of the hole there is only one principle stress, tangential to the hole. This means that the value of stress measured at the edge of the hole is the stress due to the presence of the hole in the direction of the applied load. Thus it is possible to determine the SCF by thermo-elastic stress analysis.

This can be applied directly to the CoFRM samples. For the NCF samples Cunningham et al [100] show for a sample with axial fibres on the outer layer  $\sigma_1 = \sigma_{app}$  and  $\sigma_2 = 0$ , for a sample with fibres at  $90^\circ$  to the applied load  $\sigma_2 = \sigma_{app}$  and  $\sigma_1 = 0$ .

For the NCF samples the Thermal Stress orthotropic equation (1) from Santulli et al [141] needs to be applied.

$$\Delta(\alpha_1\sigma_1 + \alpha_2\sigma_2) = A.S$$

Where  $\alpha_n$  is the thermal expansion coefficient parallel or perpendicular to the loading direction.

One of the unknown terms is removed when  $\sigma_2 = 0$  or  $\sigma_1 = 0$  for the NCF 0-90 and NCF 90-0 orientations respectively. Thus  $A/\alpha_n$  now becomes the constant for each material to be determined. Once this is determined from a sample with no hole, the stress for a sample with a hole can be measured. If this is divided by the applied stress, then this ratio will be the SCF for that sample

The results for SCF can be seen in Table 20.

**Table 20 SCF Values from Thermal Analysis**

Tube Type	SCF at hole size	
	5mm	10mm
CoFRM 2mm	2.77	2.83
CoFRM 4mm	2.63	2.70
NCF 0-90	2.28	2.42
NCF 90-0	2.18	2.44

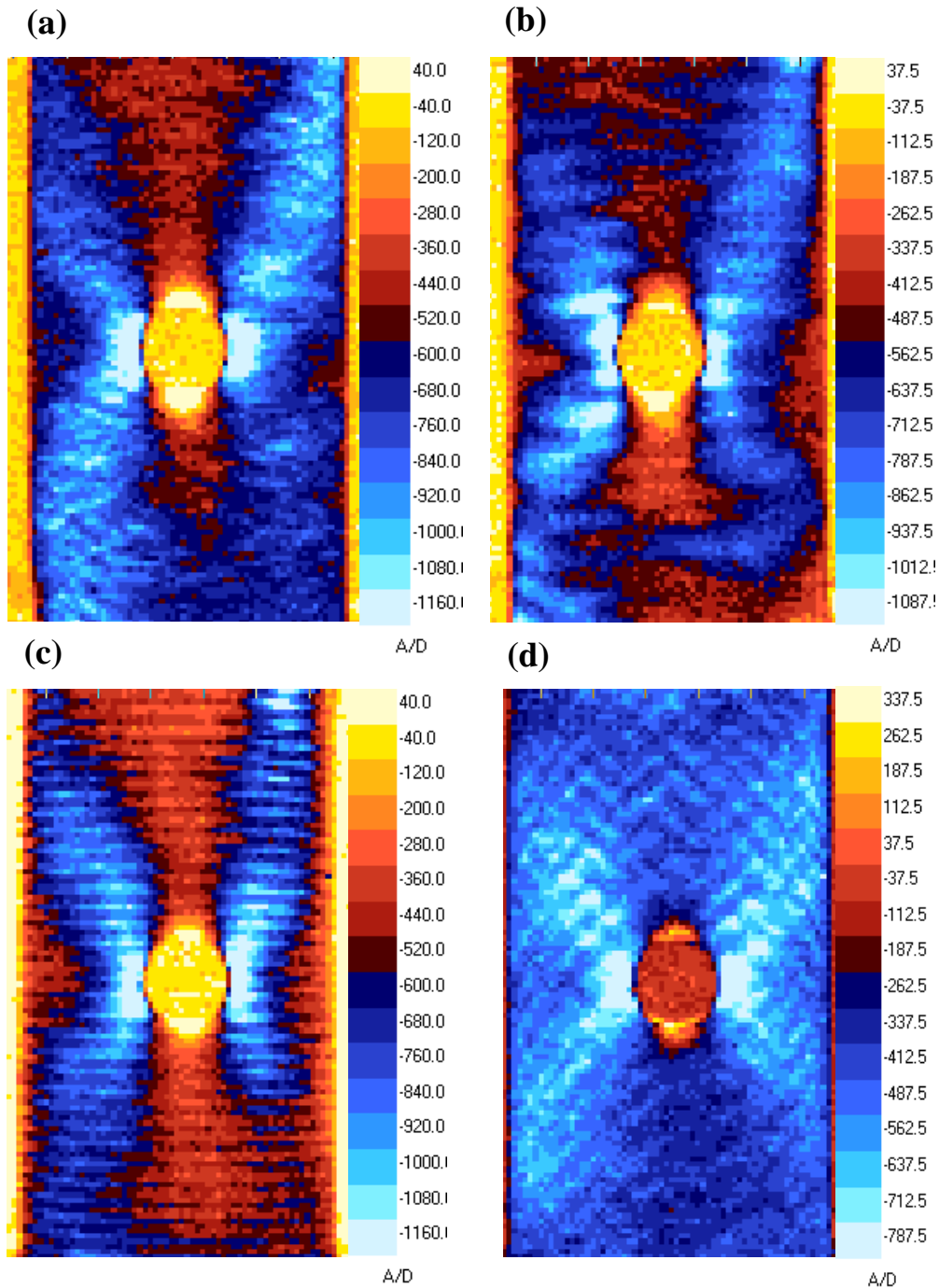


**Figure 106 Output Images ( $S$  in equation 16) from Delta-Therm Software for Samples:  
 (a) Co10m, (b) C10m, (c) C9010m, and (d) CB4510m**

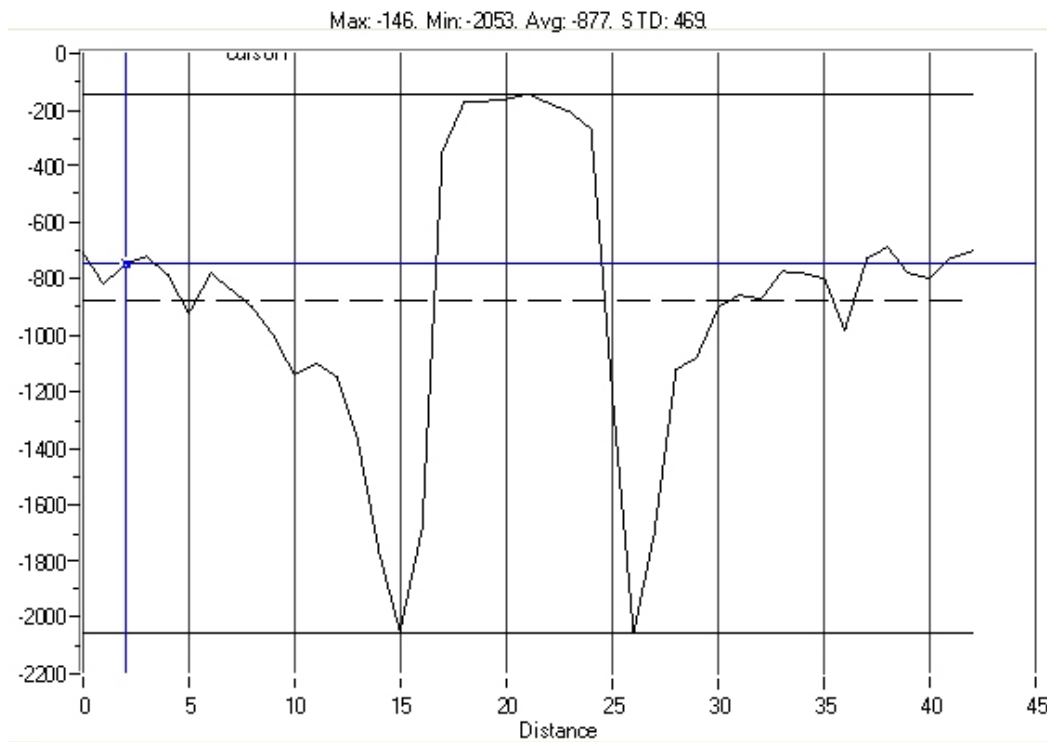


**Figure 107 Typical Plot of Output Detector Data (s) Across Tube (Where distance is in mm and distance 0 is the edge of the tube).**

The full detector outputs (Figure 106) were used to produce the plot of data (Figure 107). This plot of data is a horizontal line drawn from one edge of the tube to the other through the hole at its widest point. The Deltavision software then plots all the detector output values at each point along this line. The minimum point is where the maximum stress concentration occurs, at the edge of the hole in all cases. This value is used in the calculation to obtain a value for the stress at the edge of the hole. This can be divided by the applied stress to give the stress concentration factor.

The plots of the Delta-Therm images clearly show the position of the maximum stress concentration is at the edge of the hole at  $90^\circ$  to the tube axis. The minimum value is seen to be at the top and bottom edges of the hole along the tubes major axis. From Figure 106 the pattern of the stresses in each of the tubes is similar, although there are slight variations seen with each type of fibre architecture.

Importantly, although the resin, the fibre material, and the tube architecture are the same the SCF values vary with fibre architecture. This is in agreement with Toubal et al[142] and Kaltakci's [83] results, that stress concentration factors are highly dependant on fibre angle.

**Table 21 SCF Comparison**

Hole size	Theoretical			Thermal	
	Savin	Roark	CoFRM	NCF 0-90	NCF 90-0
5 mm	3.21	3.16	2.77	2.28	2.18
10 mm	3.85	3.50	2.83	2.42	2.44
16 mm	5.19	4.14			

From Table 21 it can be seen that the values of SCF are also significantly lower than those predicted by Savin's equation and the formula for stress concentration about a hole from Roark[143].

**Table 22 SCF and UCS Table for 5mm Hole after TSA**

Hole size	CoFRM		NCF 0-90		NCF 90-0	
	Q-S	Dynamic	Q-S	Dynamic	Q-s	Dynamic
SCF	2.77	2.77	2.28	2.28	2.18	2.18
$\sigma_c$ (MPa)	99.1	86.1	60.3	51.7	90.5	64.6
$\sigma_c \times$ SCF (MPa)	274.4	238.6	137.5	117.8	197.2	140.8
UCS (MPa)	174.9	234	139.1	133	208	170
% Difference	-56.9	-2.0	1.2	11.4	5.2	17.2

From Table 22 the difference between UCS and  $\sigma_c \times$  SCF gives negative values for CoFRM at quasi-static rates and dynamic rates. Quasi-statically the CoFRM samples fail in a mode 2 type failure, dynamically they fail in a mode 3 type failure. Quasi-statically the difference between UCS and  $\sigma_c \times$  SCF is -56.9% (the minus sign indicating global failure, as UCS is lower) and dynamically it is -2.0%. The much smaller difference at dynamic rates can be

attributed to mode 3 failure, i.e. when the difference is small and negative the sample will fail by mode 3 failure, when it is large and negative it will fail by mode 2 failure.

The NCF specimens show positive values of the difference between UCS and  $\sigma_C \times SCF$ . This implies that there are no failures at quasi-static or dynamic rates. This is close to the experimental observations seen previously. All the results are predicted correctly.

**Table 23 SCF and UCS Table for 10mm Hole after TSA**

Hole size	CoFRM		NCF 0-90		NCF 90-0	
	Q-S	Dynamic	Q-S	Dynamic	Q-S	Dynamic
SCF	2.83	2.83	2.42	2.42	2.44	2.44
$\sigma_C$ (MPa)	99.1	86.1	60.3	51.7	90.5	64.6
$\sigma_C \times SCF$ (MPa)	280.4	243.8	145.9	125.1	220.7	157.6
UCS (MPa)	174.9	234	139.1	133	208	170
%Difference (MPa)	-60.3	-4.2	-4.9	6.0	-6.1	7.3

Again, from Table 23 negative values are produced for the difference between UCS and  $\sigma_C \times SCF$  for CoFRM at quasi-static rates and dynamic rates. Quasi-statically the CoFRM samples fail in a mode 2 type failure, dynamically they fail in a mode 3 type failure. Quasi-statically the difference between UCS and  $\sigma_C \times SCF$  is -60.3% (the minus sign indicating failure, as UCS is lower) and dynamically it is -4.2%.

The NCF specimens show small negative values of the difference between UCS and  $\sigma_C \times SCF$  at quasi-static rates. The respective values are -4.9% and -6.1%. The experimental results show that the 0-90 tubes fail by mode 3 failure and the 90-0 specimens fail by mode 2 failure. The larger difference for the 90-0 tube suggests a greater mode of failure. At dynamic rates, the difference between UCS and  $\sigma_C \times SCF$  is positive and small. This implies that there are no failures at this rate. This is close to the experimental observations seen; one sample of each type fails in a mode 3 failure, although for both samples the drop in load is very small.

Thus, the majority of the results are predicted correctly. This suggests that equation (15) is valid.

Using the results above and the experimental data the following failure criteria can be created.

$$\text{If } \left(1 - \frac{\sigma_c \cdot SCF}{UCS}\right) \cdot 100 > 0 \text{ then the sample will crush progressively (mode 1 failure)} \quad (17)$$

$$\text{If } \left(1 - \frac{\sigma_c \cdot SCF}{UCS}\right) \cdot 100 > -5 \text{ but } < 0 \text{ then the sample will fail by a mode 3 failure mode} \quad (18)$$

$$\text{If } \left(1 - \frac{\sigma_c \cdot SCF}{UCS}\right) \cdot 100 < -5 \text{ then the sample will fail globally in mode 2 failure.} \quad (19)$$

The mode 1 and mode 2 failure types are predicted easily, however the bounds for mode 3 failure are small, in this case 5%. This lies within experimental errors, and errors within the TSA analysis, thus further samples are required to expand the range of data. However even taking into account the possible errors this is still a useful result.

## 4.2.8. Impact Damage

This section concerns the experimental work associated with impact damage. Impact damage is important because it simulates damage that could occur during service or during manufacturing conditions. Damage was created by an out-of-plane impact, using an impactor tup with a hemispherical end of diameter 12mm. Energy levels of 1.5J, 3J, 6J and 9J were delivered on an instrumented falling weight drop tower with a mass of 5.8kg attached. The samples were tested at  $10\text{mm}\cdot\text{min}^{-1}$  and  $5\text{ms}^{-1}$ .

### 4.2.8.1. Impact Damage at 45mm from Chamfer

The first set of data is for the NCF 0-90 tubes with an impact at 45mm from the chamfered end of the sample.

**Table 24 SEA Data for NCF 0-90 Tubes with Impact Damage at 45mm from Chamfer**

Test Reference	Impact Level	Damage Size /mm (axial x hoop)	Quasi-static SEA (kJ/kg) (Std. Dev %)	Quasi-static Failure mode	Dynamic SEA (kJ/kg) (Std. Dev %)	Dynamic Failure mode
<b>C0m</b>	<b>None</b>	<b>0</b>	<b>39.0 (2.7)</b>	<b>1</b>	<b>32.7 (2.4)</b>	<b>1</b>
C1.5J45	1.5J	20x15	41.4 (11.0)	1	31.5 (4.9)	1
C3J45	3J	32x18	25.3 (49.9)	2&1	28.1 (3.4)	1
C6J45	6J	45x25	18.7 (9.0)	2	29.6 (6.4)	1
C9J45	9J	50x30	17.2 (7.9)	2	28.0 (7.4)	3&1

The damage due to impact zone size noted in Table 24 was based on visual inspection of the damage zone and is restricted to the extent of the stress whitening – typically the damage zone shape was ellipsoidal, with the major axis aligned axially and the minor axis circumferential.

An impact of 1.5J caused a zone of delamination and in-plane matrix damage in all samples, with no visible penetration from the tup (see Figure 108). Increasing the energy to 3J caused an increase in the size of the delamination area and evidence of radial and circumferential cracking from the point of impact on the outer and inner surfaces of the tube. Impact damage

of 6J increased the damage zone and cracking size and some protrusion on the inner surface of the tube was seen. The impact of 9J caused a further increase in delamination zone with significant circular cracking around the impact zone - there was also visible penetration on the surface of the order of 1mm and a corresponding protrusion on the inner surface of the tube.

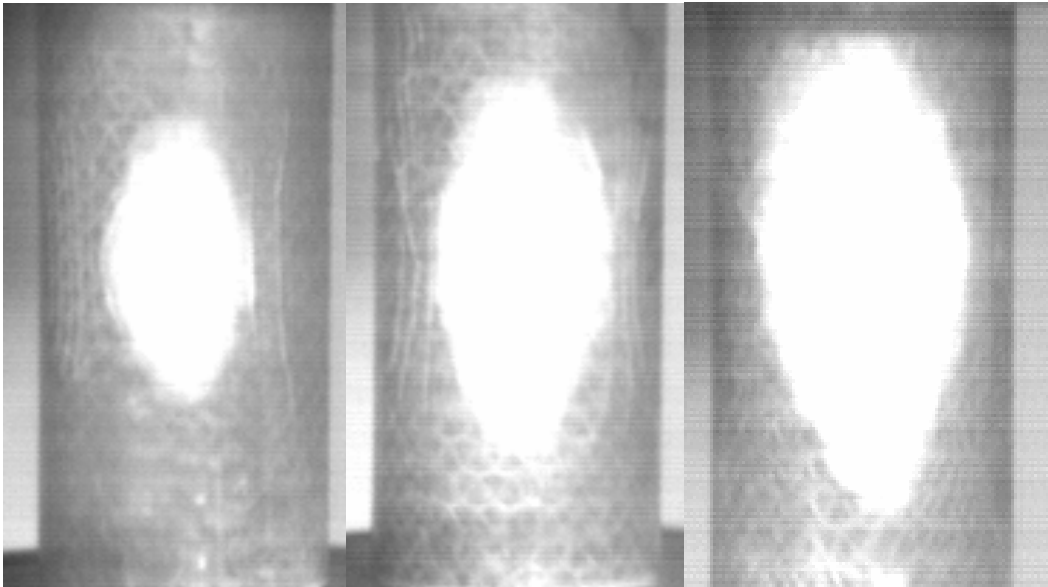


**Figure 108 Samples C3J45, C6J45 and C9J45 Showing Increasing Area of Stress Whitening.**

Quasi-statically the threshold damage level (i.e. the first sample begins to fail in an undesired manner) is 3J with 2 of the samples failing by a mode 2 type failure mode. Interestingly the samples with 1.5J of impact damage have a slightly higher SEA than the undamaged samples, it is noted that the deviation is relatively large, so this could be attributed to experimental errors or a particularly high performing sample. However, with the damage being so far away from the crush zone, samples that may fail if they were closer to the chamfer are restricted, so further positions were required to be tested.

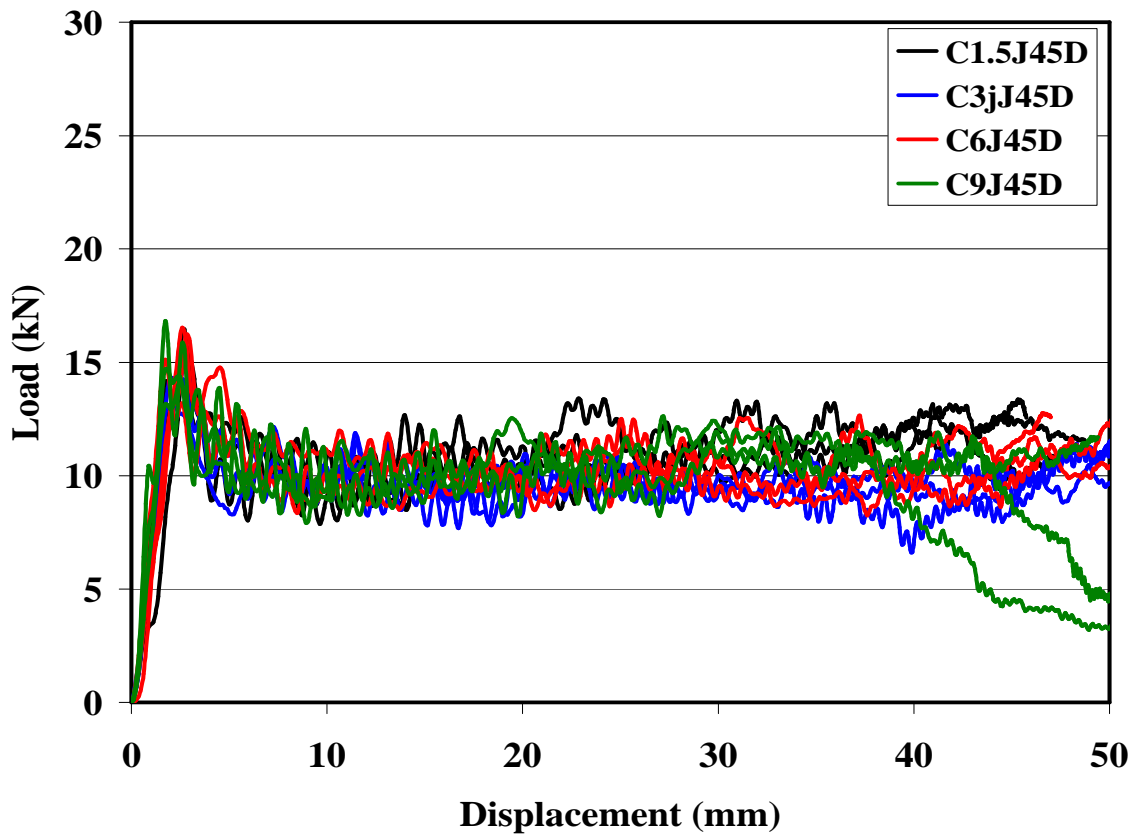
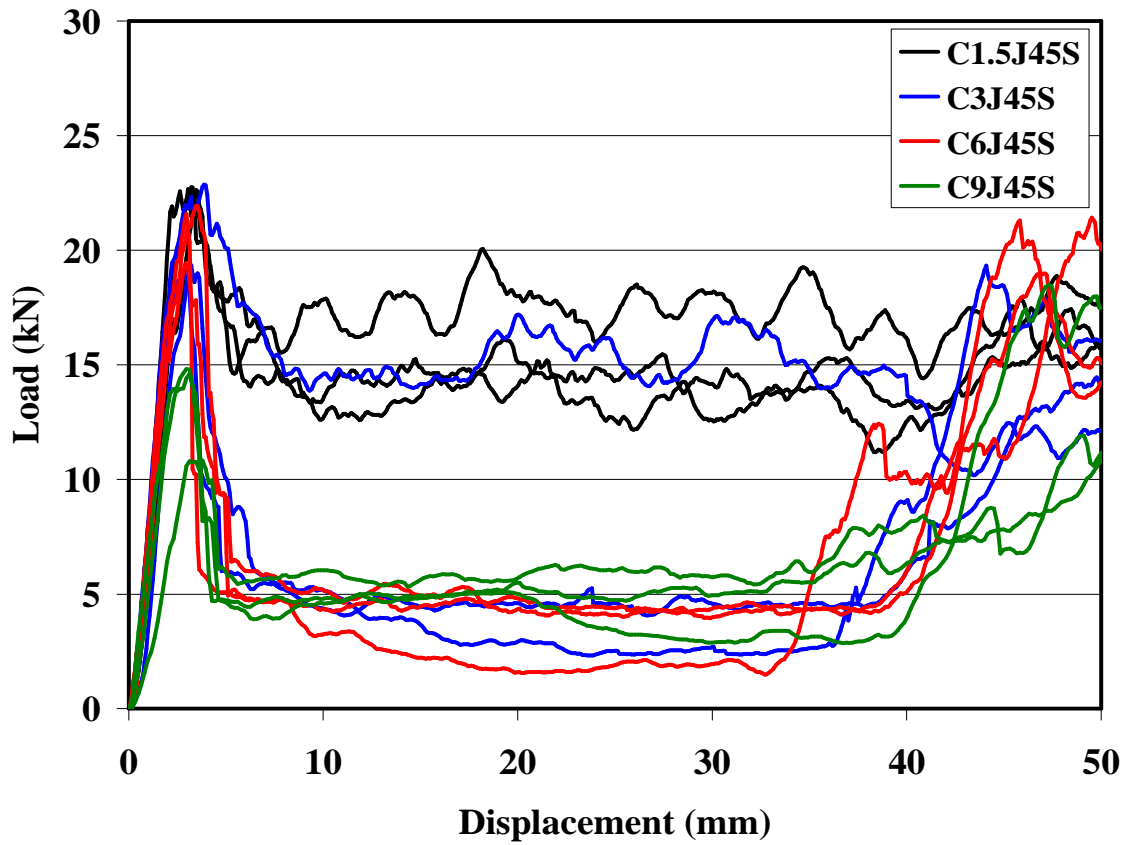
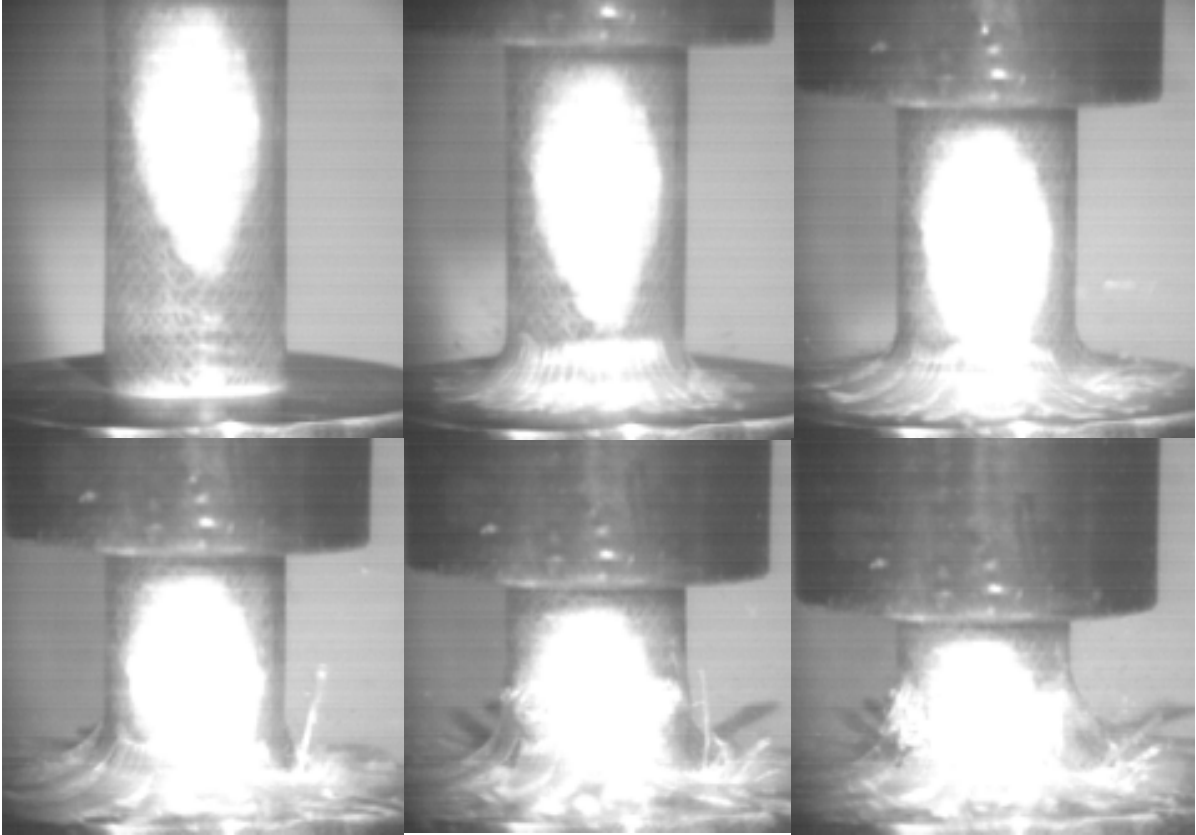


Figure 109 Load Displacement Curve for NCF Samples with Impact Damage at 45mm from Chamfer

The threshold level for damage dynamically has increased to 9J, i.e. the samples can take 3x the impact energy before failing undesirably. Looking at the load displacement curves (Figure 109) for the dynamic loading, there is a small reduction in load with the 9J samples towards the end of crush, associated with Mode 3 failure. This drop in load at 40mm suggests that these only fail when the crush zone interacts with the widest part of the damage zone. Thus if the crushing had progressed further the effects seen would be greater, or if this damage zone was located closer to the chamfer then the effects would be seen earlier on the load displacement curves.



**Figure 110 NCF Sample C9J45 under Dynamic Loading Showing Mode 3 Failure**

#### 4.2.8.2. Impact Damage at 30mm from Chamfer

In the literature impact damage is often treated and modelled as being a cut-out or hole with diameter of similar size to the damage zone [48, 93, 106]. To investigate this theory, comparisons need to be undertaken with the stress concentration/hole work in section 4.2.7.1.2 to establish its validity. The centreline of the damage was moved to 30mm to enhance interaction with crush zone effects. The dataset for the impact-damaged specimens is in Table 25.

**Table 25 SEA Data for NCF Samples with Impact Damage at 30mm from Chamfer**

Fibre Type	Test Ref	Impact Level	Damage Size /mm (axial x hoop)	Quasi-static SEA (kJ/kg) (Std. Dev %)	Quasi-static Failure mode	Dynamic SEA (kJ/kg) (Std. Dev %)	Dynamic Failure mode
<b>NCF 0-90</b>	<b>C0m</b>	<b>None</b>	<b>0</b>	<b>39.0 (2.7)</b>	<b>1</b>	<b>32.7 (2.4)</b>	<b>1</b>
NCF 0-90	C1.5J	1.5J	20x15	38.8 (9.8)	1&3	31.1 (3.0)	1
NCF 0-90	C3J	3J	32x18	21.0 (16.4)	2	31.7 (7.0)	1
NCF 0-90	C6J	6J	45x25	20.3 (11.9)	2	31.7 (0.9)	1
NCF 0-90	C9J	9J	50x30	21.4 (13.9)	2	24.1 (15.0)	2&3
<b>NCF 0-90</b>	<b>Q0m</b>	<b>None</b>	<b>0</b>	<b>39.8 (6.9)</b>	<b>1</b>	<b>28.9 (4.6)</b>	<b>1</b>
NCF 0-90	Q1.5J	1.5J	22x20	40.6 (1.5)	1	29.4 (5.6)	1
NCF 0-90	Q3J	3J	35x25	31.8 (12.2)	1&2	29.8 (6.1)	1&3
NCF 0-90	Q6J	6J	44x30	21.7 (9.1)	2	27.3 (6.9)	3&1
NCF 0-90	Q9J	9J	48x30	26.3 (23.5)	2	29.9 (4.0)	1&3
<b>NCF 90-0</b>	<b>C900m</b>	<b>None</b>	<b>0</b>	<b>50.4 (1.4)</b>	<b>1</b>	<b>39.8 (5.8)</b>	<b>1</b>
NCF 90-0	C901.5J	1.5J	22x20	44.7 (34.1)	1&2	44.3 (16.5)	1
NCF 90-0	C903J	3J	33x21	46.1 (25.0)	1&2	40.2 (1.0)	1
NCF 90-0	C906J	6J	52x28	34.8 (44.5)	2&1	37.5 (8.8)	1&3
NCF 90-0	C909J	9J	57x30	39.5 (22.2)	2&1	36.5 (9.1)	3&1
<b>NCF +/-45</b>	<b>C450m</b>	<b>None</b>	<b>0</b>	<b>55.4 (8.0)</b>	<b>1</b>	<b>29.6 (7.7)</b>	<b>1</b>
NCF +/-45	C451.5J	1.5J	20x15	43.7 (15.8)	1,2,3	30.1 (3.8)	1
NCF +/-45	C453J	3J	28x20	28.8 (39.7)	2	27.6 (4.5)	1
NCF +/-45	C456J	6J	36x26	19.8 (21.5)	2	28.7 (21.7)	1&2
NCF +/-45	C459J	9J	45x28	27.1 (12.0)	2	29.1 (9.4)	2d

Where C denotes Circular cross-section and Q denotes Square cross-section

When tested with the impact-damage, the 0-90 tubes showed a threshold damage level of 3J quasi-statically and 9J dynamically, although one sample at 1.5J appeared to show a decrease in load around the damage zone and was classed as mode 3 failure - this lowered the SEA measured slightly. Typically, above the threshold level, failure occurred at the edge of the damage zone - a stress-induced crack was formed and quickly propagated parallel to the fibres.

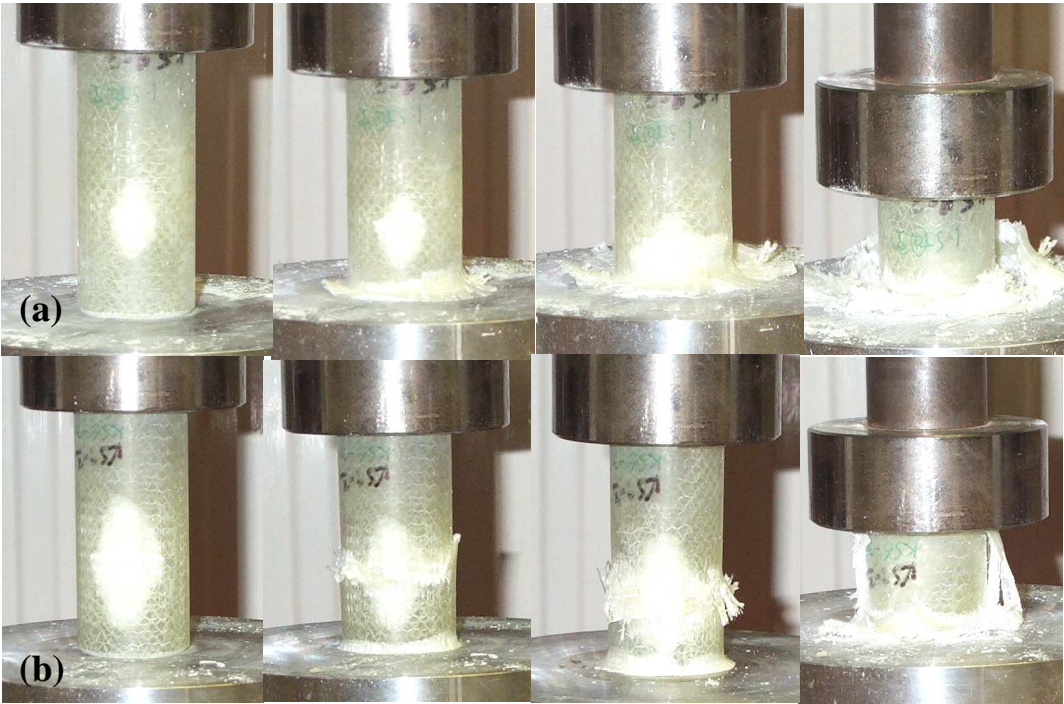


**Figure 111 Circular NCF Samples C1.5J (a) and C6J (b) under Quasi-Static Loading**

Comparing the samples with impact damage at 45mm and 30mm, it can be seen that similar patterns occur dynamically and quasi-statically. The samples with damage at 30mm seem to perform marginally worse under both loading conditions. This can be attributed to the position of the damage zone. Under mode 3 failure, the effect of damage on SEA appears to be greater closer to the chamfer. Conversely, for mode 2 failure the effect on SEA is greater the further away from the chamfer, partially due to the load having less time to recover after the crush zone passes through the damage zone.

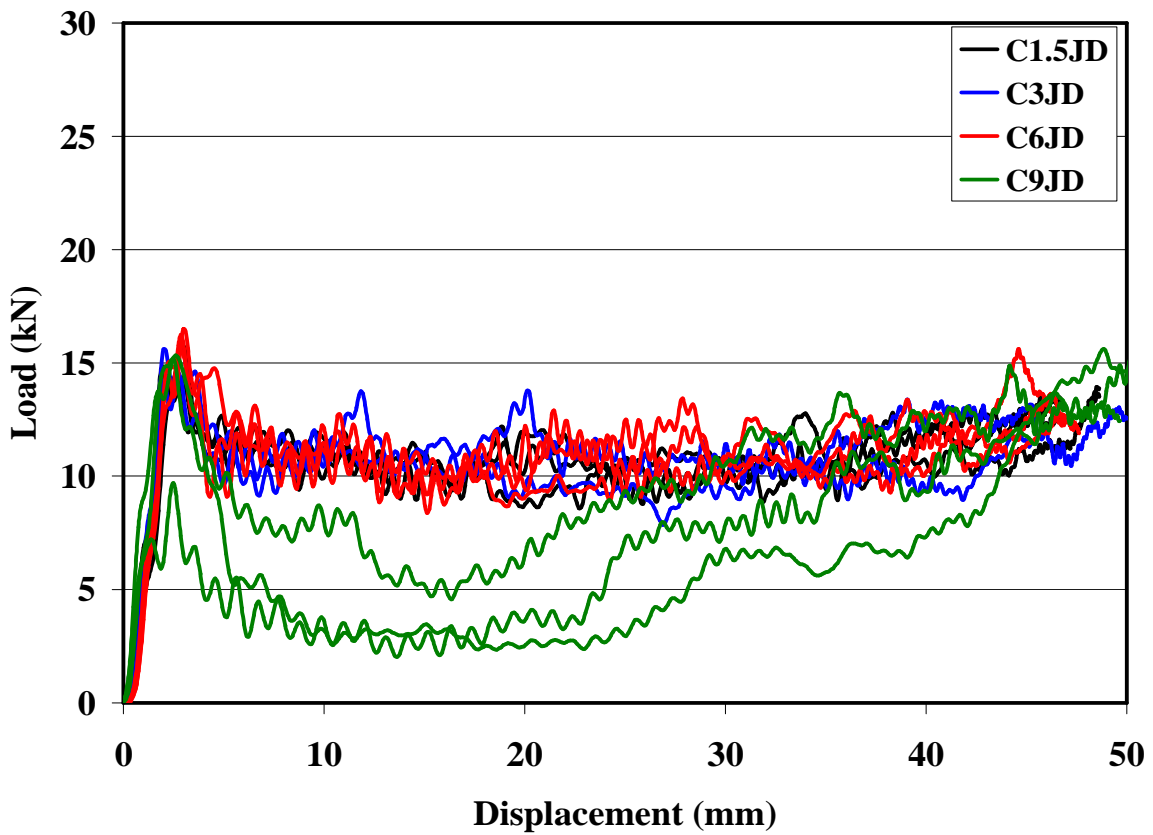
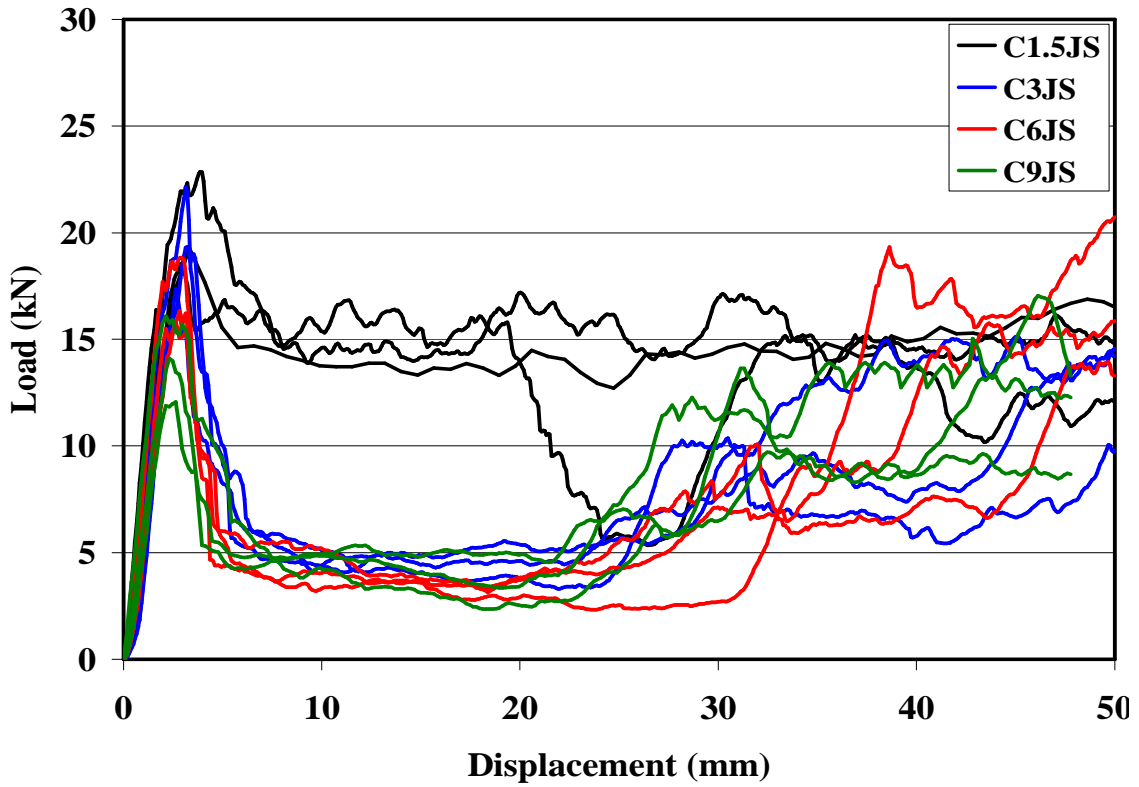


Figure 112 NCF 0-90 Tubes with Impact Damage at 30mm from Chamfer for Quasi-static and Dynamic Testing

The 90-0 tubes showed a threshold level of 1.5J quasi-statically and 6J dynamically, (although at this level the failure was only local (failure mode 3), and only in one of the three samples). Comparing the load displacement curve for NCF 0-90 (Figure 112) and NCF 90-0 (Figure 113), the peak load for the undamaged 90-0 sample is much greater (30MPa vs. 22MPa) and the steady-state crushing load is higher (~18MPa vs. 15MPa)

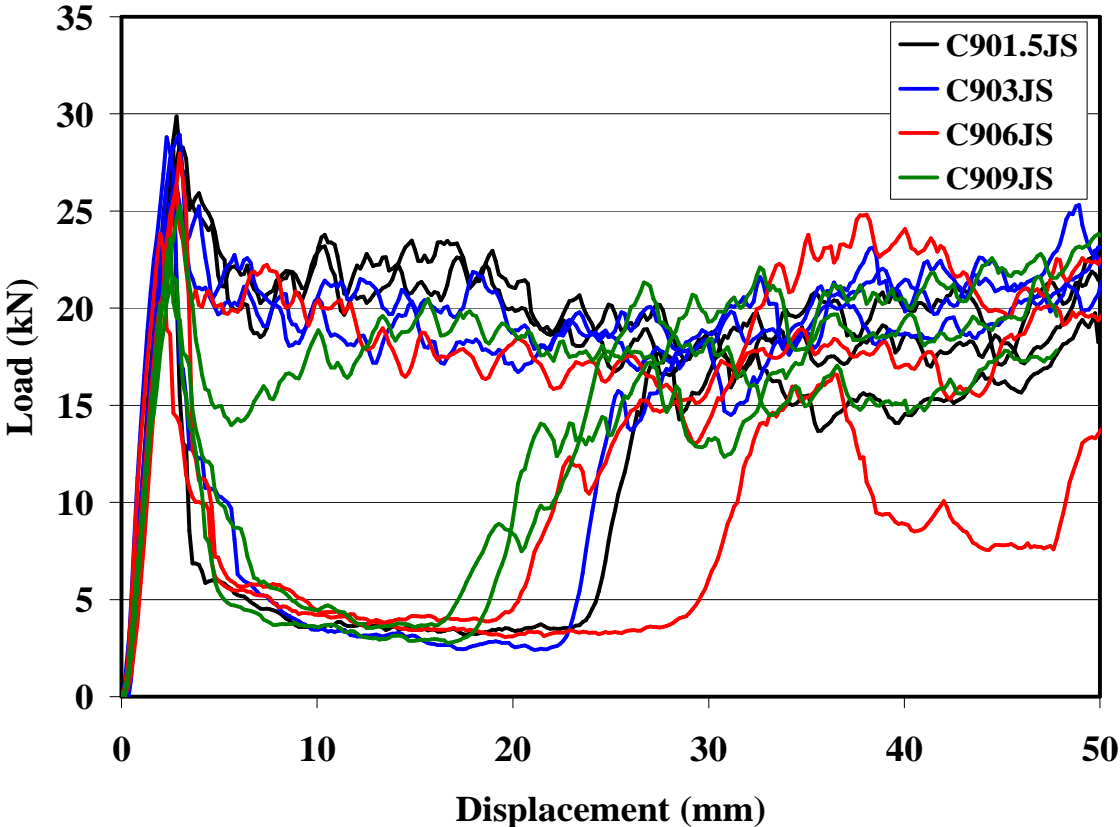
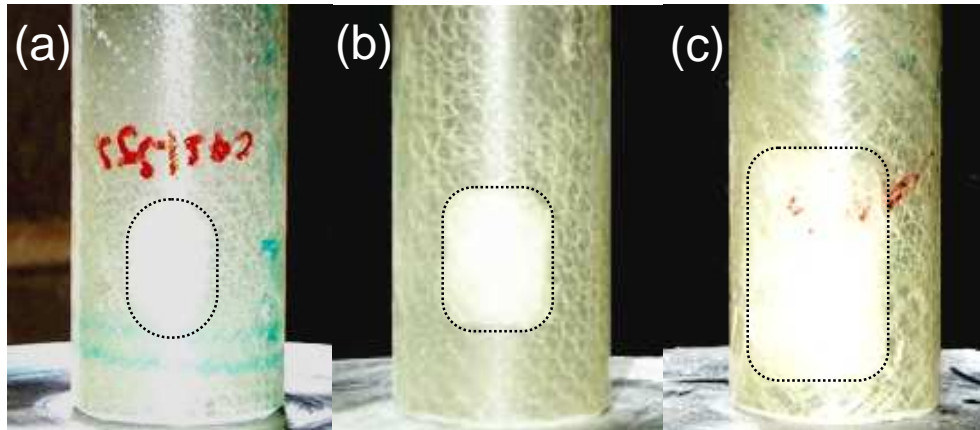


Figure 113 Load Displacement Curve for NCF 90-0

The shape of the damage zone/area of stress whitening was different for the NCF  $\pm 45$  tubes. The shape was less elliptical and more rectangular, especially at the higher impact values (see Figure 114). The NCF  $\pm 45$  tubes had threshold levels of 1.5J quasi-statically and 6J dynamically.



**Figure 114  $\pm 45$  NCF tube with a) 1.5J, b) 3J, and c) 9J of damage**

Under quasi-static loading, the square tubes showed a very similar pattern to the circular tubes. The samples with 1.5J damage crushed progressively and showed no effects from the damage zone and crush zone interacting. The samples with 6J and 9J damage all failed globally by mode 2. At the damage level of 3J one of the samples crushed progressively and the others failed globally.

Dynamically the samples with 1.5J damage failed progressively. At 3J one of the samples failed in the vicinity of the damage zone (mode 3). The other 2 failed progressively. Increasing the damage level to 6J caused 2 of the samples to fail in the vicinity of the damage whilst the 3<sup>rd</sup> failed progressively. At 9J damage the reverse occurred. Two of the samples failed progressively with the 3<sup>rd</sup> failing globally near the damage zone.

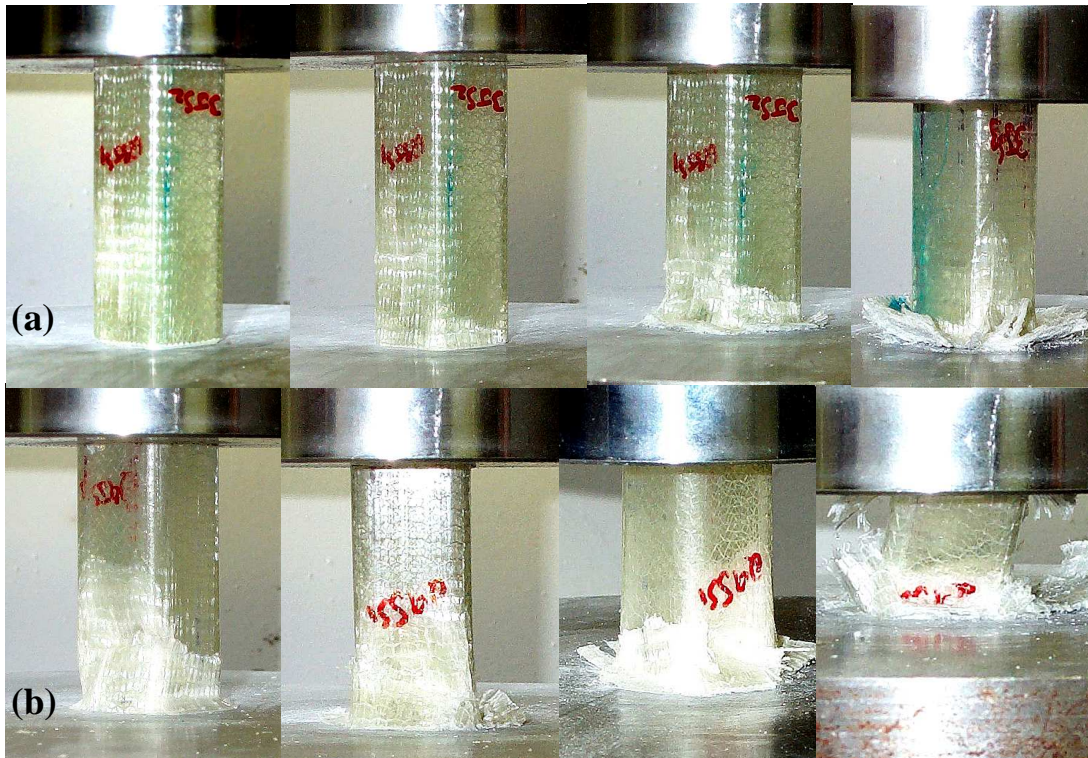


**Figure 115 NCF Samples Q3J (a) and Q9J (b) under Quasi-static Loading**

At levels of 6J and above, the square samples appeared to split normally at the corners into fronds with the faces splaying. However, in some samples the damaged face appeared to buckle with one of the folds occurring across the minor axis of the damage zone (see Figure 115).

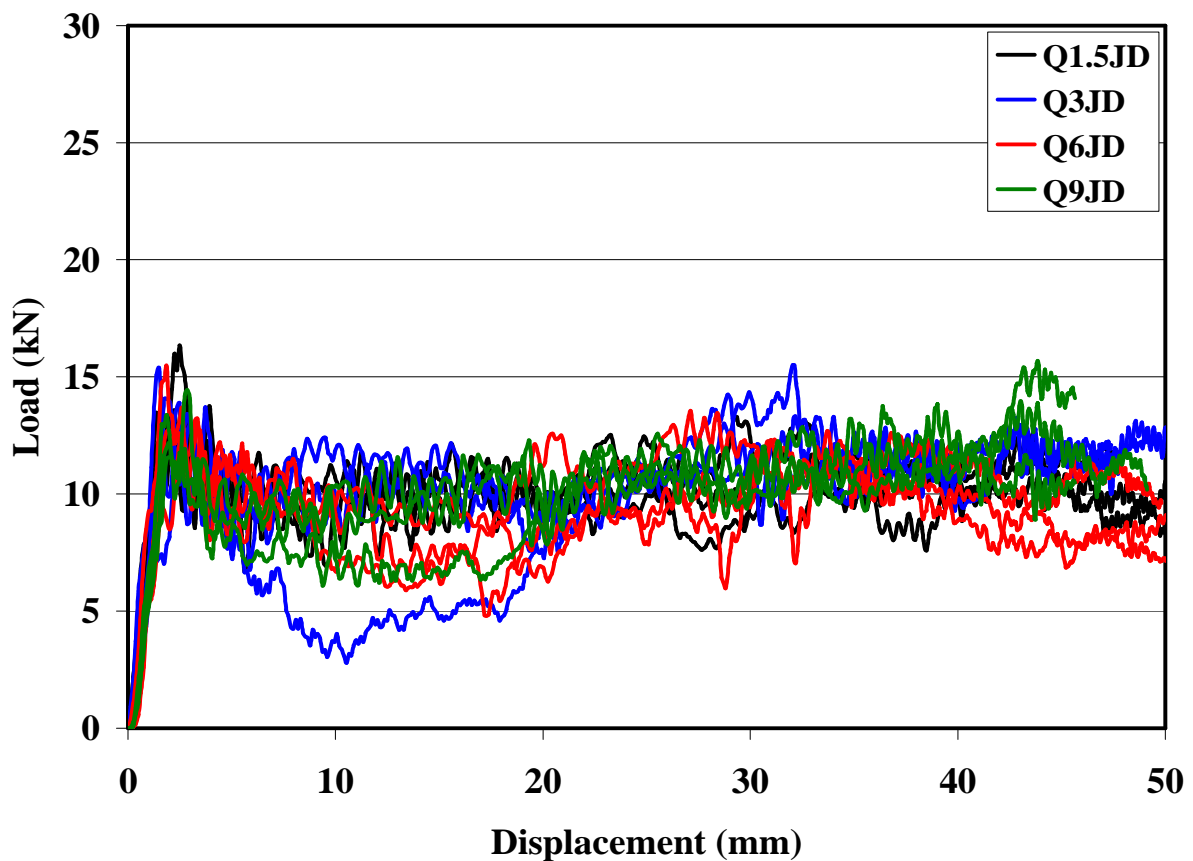


**Figure 116 Square NCF Sample with Impact Damage under Dynamic Loading**

The square samples perform slightly better than the circular section samples under these conditions. No samples failed at 1.5J, compared to 1 failing in a mode 3 type failure for the circular section. This is attributed to the corners of the square tube providing a discontinuity causing cracks to be constrained to the face. Unlike the CoFRM tubes, the higher in-plane strength of the NCF means that the geometric stress raiser of the corner does not influence the mode of failure. The load displacement curve is shown in Figure 116

The next set of samples used braided architectures impacted in the same manner as the NCF samples. This data is presented in Table 26.

**Table 26 Impact Data for Braided Tubes**

Fibre Type	Test Reference	Impact Level	Damage Size /mm (axial x hoop)	Quasi-static SEA (kJ/kg) (Std. Dev %)	Quasi-static Failure mode	Dynamic SEA (kJ/kg) (Std. Dev %)	Dynamic Failure mode
<b>Braid ±30</b>	<b>CB300m</b>	<b>None</b>	<b>0</b>	<b>44.1 (1.1)</b>	<b>1</b>	<b>30.7 (16.7)</b>	<b>1</b>
Braid ±30	CB301.5J	1.5J	22x13	37.7 (17.5)	1&2	30.1 (7.8)	1
Braid ±30	CB303J	3J	28x16	36.3 (5.4)	1&2	29.6 (7.1)	1
Braid ±30	CB306J	6J	43x24	31.0 (19.9)	2	31.5 (6.1)	1&3
Braid ±30	CB309J	9J	49x26	38.6 (5.7)	2	31.6 (5.4)	1&3
<b>Braid ±45*</b>	<b>CB450m</b>	<b>None</b>	<b>0</b>	<b>38.8 (3.8)</b>	<b>1</b>	<b>48.4 (1.4)</b>	<b>1</b>
Braid ±45*	CB451.5J	1.5J	24x18	32.6 (28.2)	2	46.5 (7.8)	1
Braid ±45*	CB453J	3J	33x23	34.5 (10.0)	2	47.9 (2.0)	1
Braid ±45*	CB456J	6J	40x24	27.5 (13.0)	2	38.9 (8.6)	2
Braid ±45*	CB459J	9J	49x27	28.0 (29.0)	2	39.4 (18.5)	2
<b>Braid ±60</b>	<b>CB600m</b>	<b>None</b>	<b>0</b>	<b>45.1 (23.0)</b>	<b>1&amp;3</b>	<b>52.6 (5.1)</b>	<b>1</b>
Braid ±60	CB601.5J	1.5J	12x16	35.7 (4.8)	2	39.6 (29.9)	1&3
Braid ±60	CB603J	3J	19x22	24.7 (11.5)	2	35.8 (4.6)	2&3
Braid ±60	CB606J	6J	21x27	29.1 (14.0)	2	31.4 (11.8)	2
Braid ±60	CB609J	9J	24x30	27.4 (9.1)	2	32.2 (6.7)	2&3
<b>Braid 0±60</b>	<b>CT600m</b>	<b>None</b>	<b>0</b>	53.8 (0.5)	1	48.7 (3.9)	1
Braid 0±60	CT601.5J	1.5J	17x16	37.5 (9.5)	2&3	45.2 (3.7)	1
Braid 0±60	CT603J	3J	26x20	36.2 (29.2)	2	42.2 (11.1)	3&1
Braid 0±60	CT606J	6J	35x25	35.0 (11.5)	2	30.3 (8.4)	2&3
Braid 0±60	CT609J	9J	43x27	36.0 (17.7)	2	29.1 (17.8)	2

\* Data taken from [98]

The area of stress whitening again varied with the fibre angles for the braided glass tubes. The ±30 tubes showed an elliptical shape with the major axis parallel to the major axis of the tube. The biaxial ±45 tubes have been reported as showing a more rectangular shape with the major axis axially and the minor axis circumferential. The damage zone for the braided ±60 tubes was rectangular in shape with the major axis circumferential and the area of damage was smaller than in all other tubes (Figure 117).



**Figure 117 Impacted samples with (a)  $\pm 30$  with 1.5J damage, (b)  $\pm 60$  with 6J damage and (c)  $0\pm 60$  with 3J damage**

Quasi-statically the braided samples all failed with a low threshold level of 1.5J. For the  $\pm 45$  tubes this represented a decrease in SEA over an undamaged tube of approximately 29%. For the  $\pm 60$  tube, this reduction was 45%. Dynamically the threshold level was significantly increased - the  $\pm 30$  and  $\pm 45$  tubes displayed the same threshold value, 6J, although the  $\pm 30$  tube was more robust at damage levels above the threshold (see load displacement curves Figure 118 - Figure 120). Only one sample at each level failed globally for the  $\pm 30$  tubes, whereas all samples fail for the  $\pm 45$  tubes. At an angle of  $\pm 60$ , the samples showed a threshold damage level of 1.5J, with an SEA of 39.6kJ/kg. Although the threshold levels were the same for the biaxial  $\pm 60$  and the triaxial  $0\pm 60$  tube, the latter again showed an improvement in damage tolerance with fewer samples failing globally at each level.

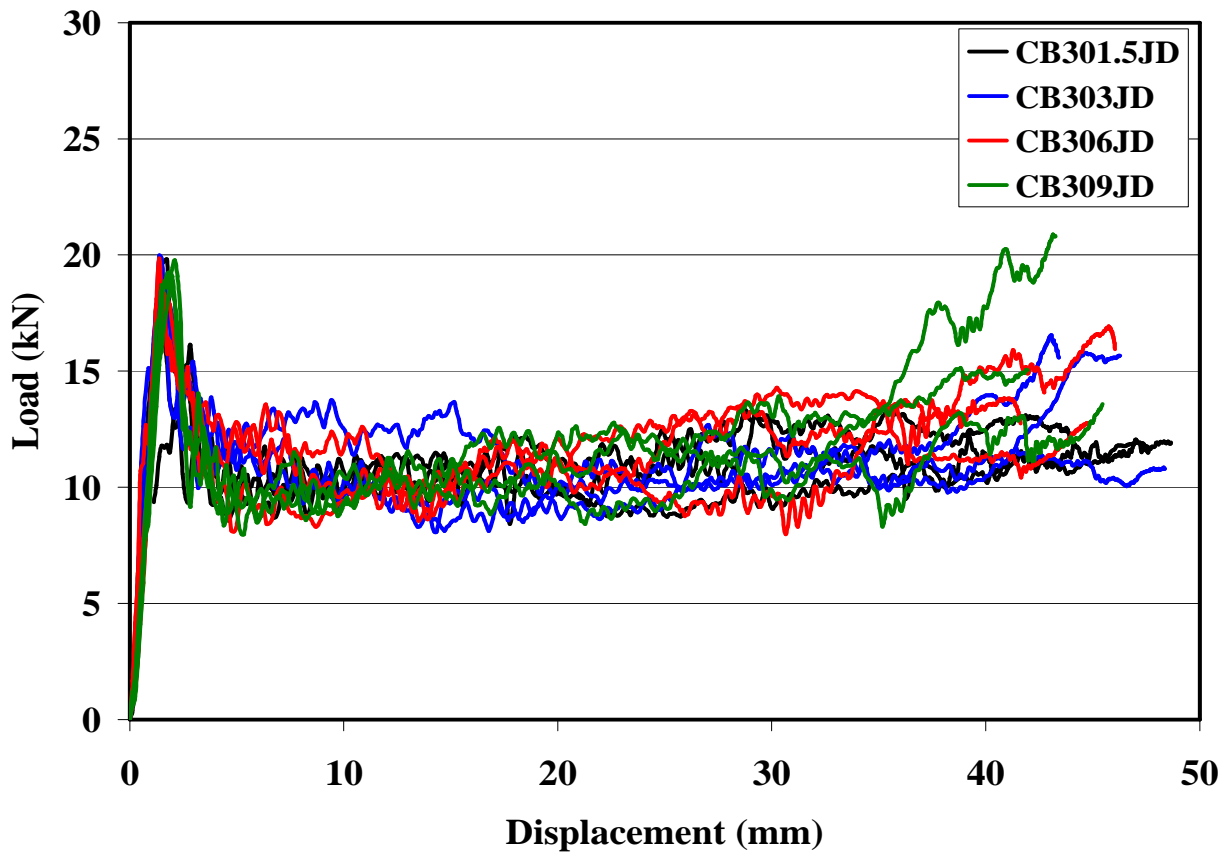
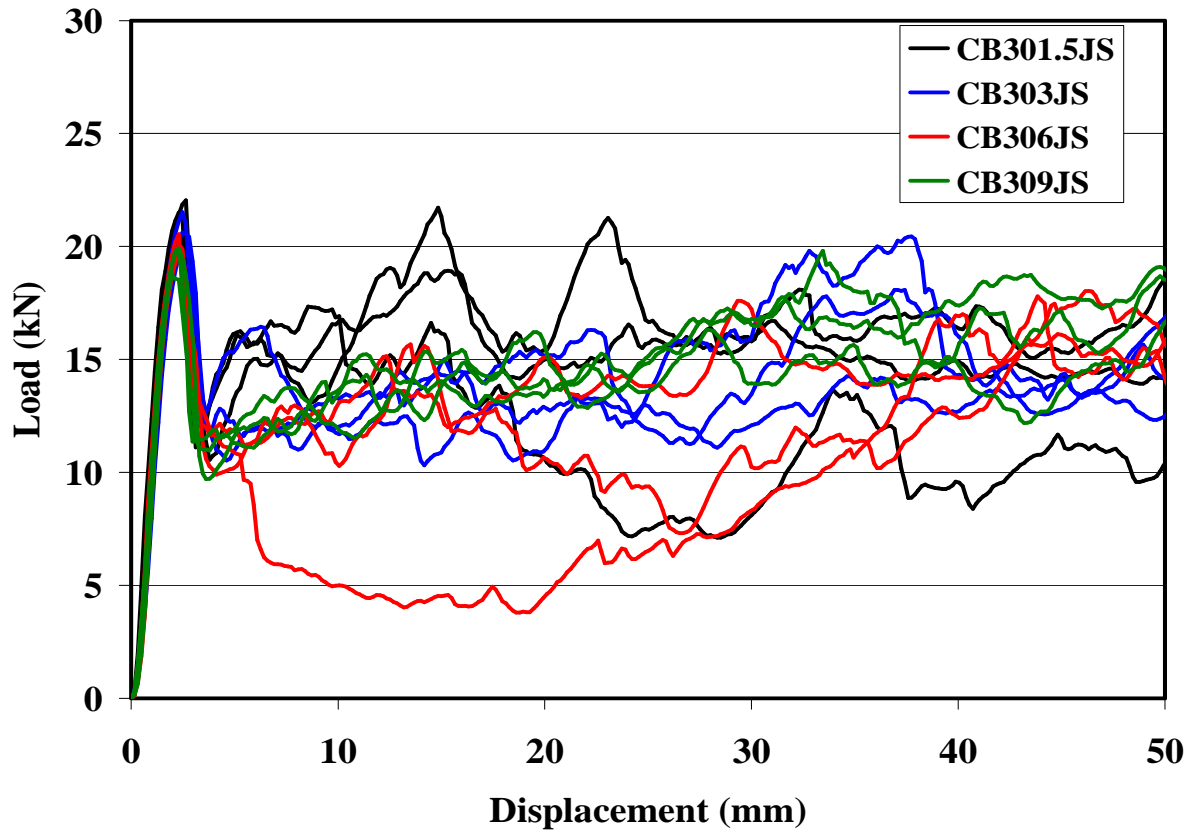


Figure 118 Biaxial  $\pm 30$  Samples with Impact Damage

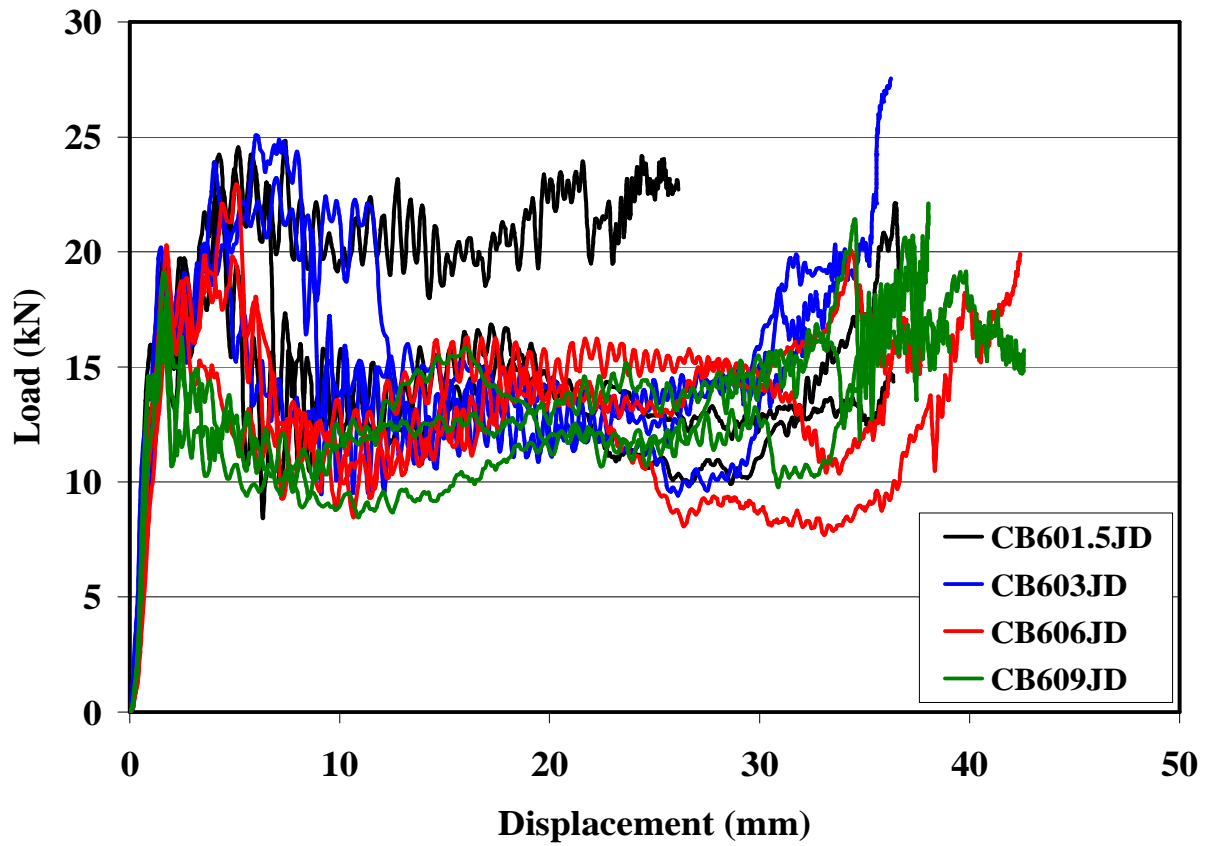
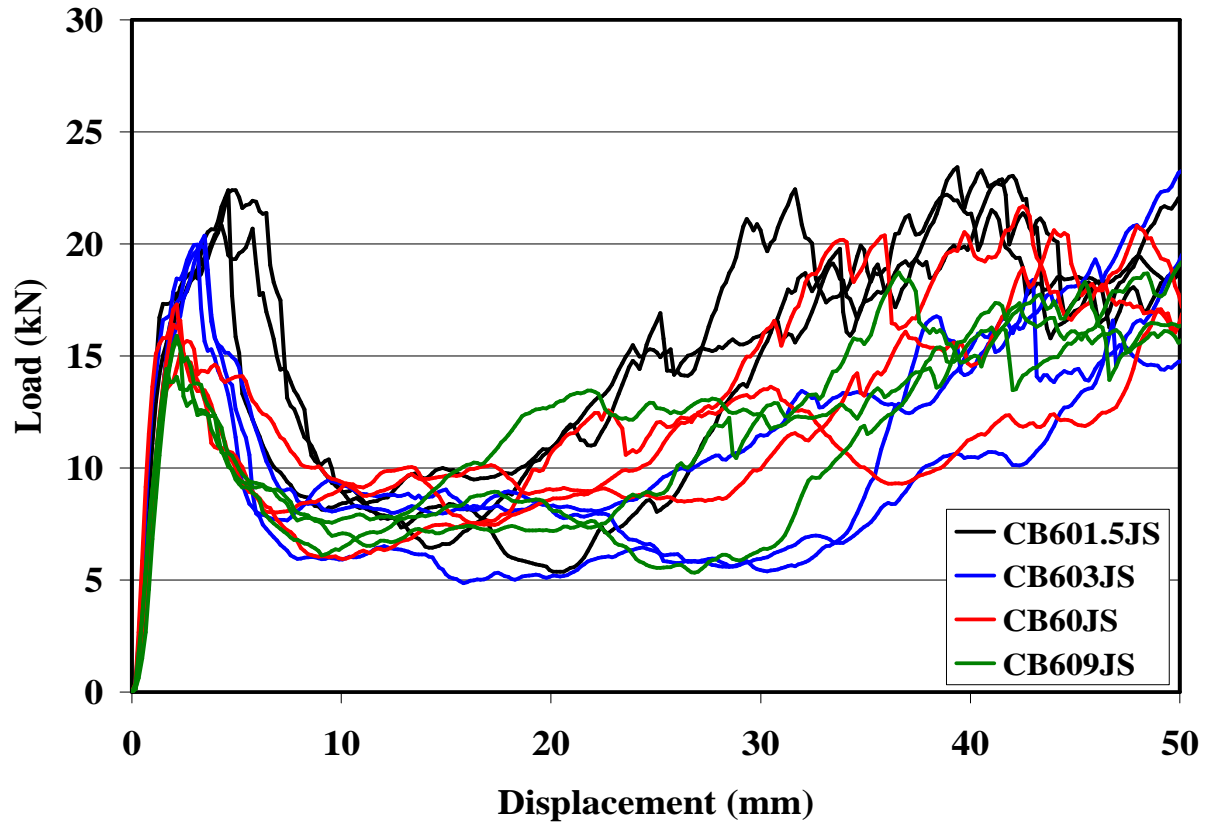


Figure 119 Biaxial  $\pm 60$  Samples with Impact Damage

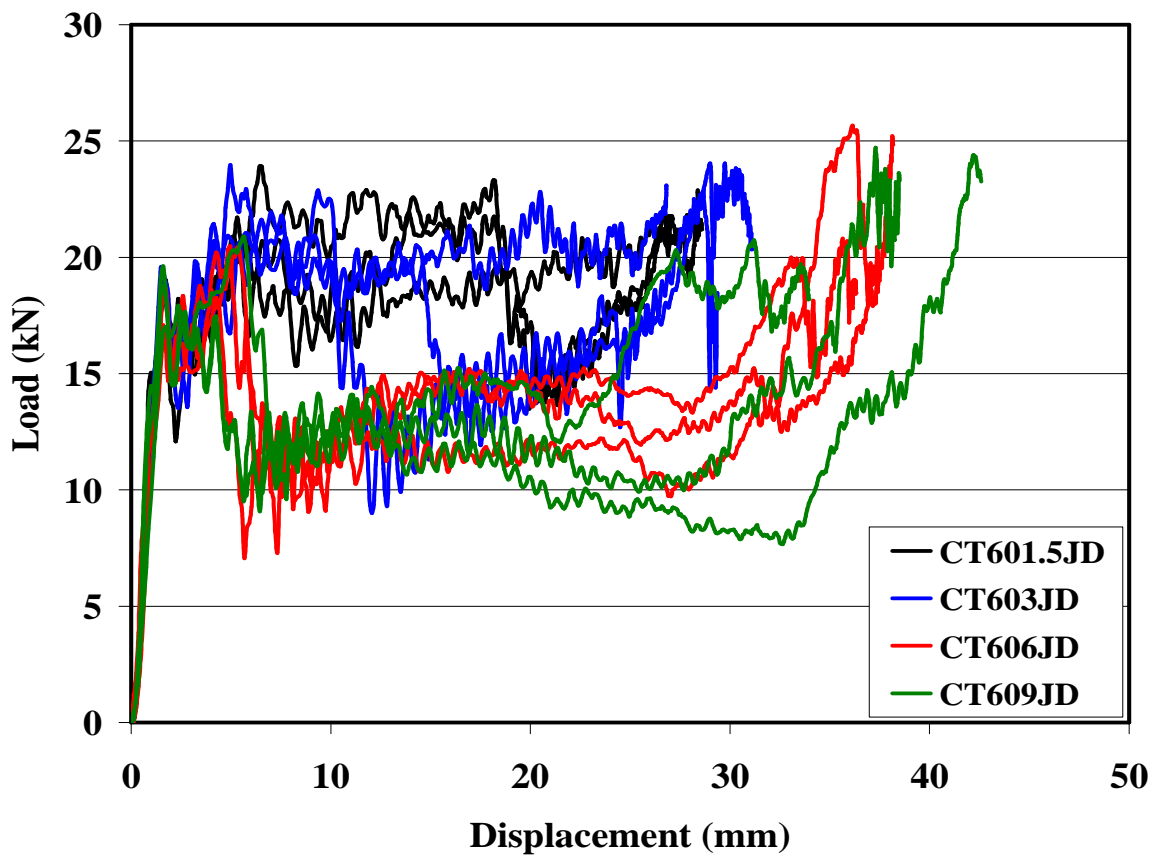
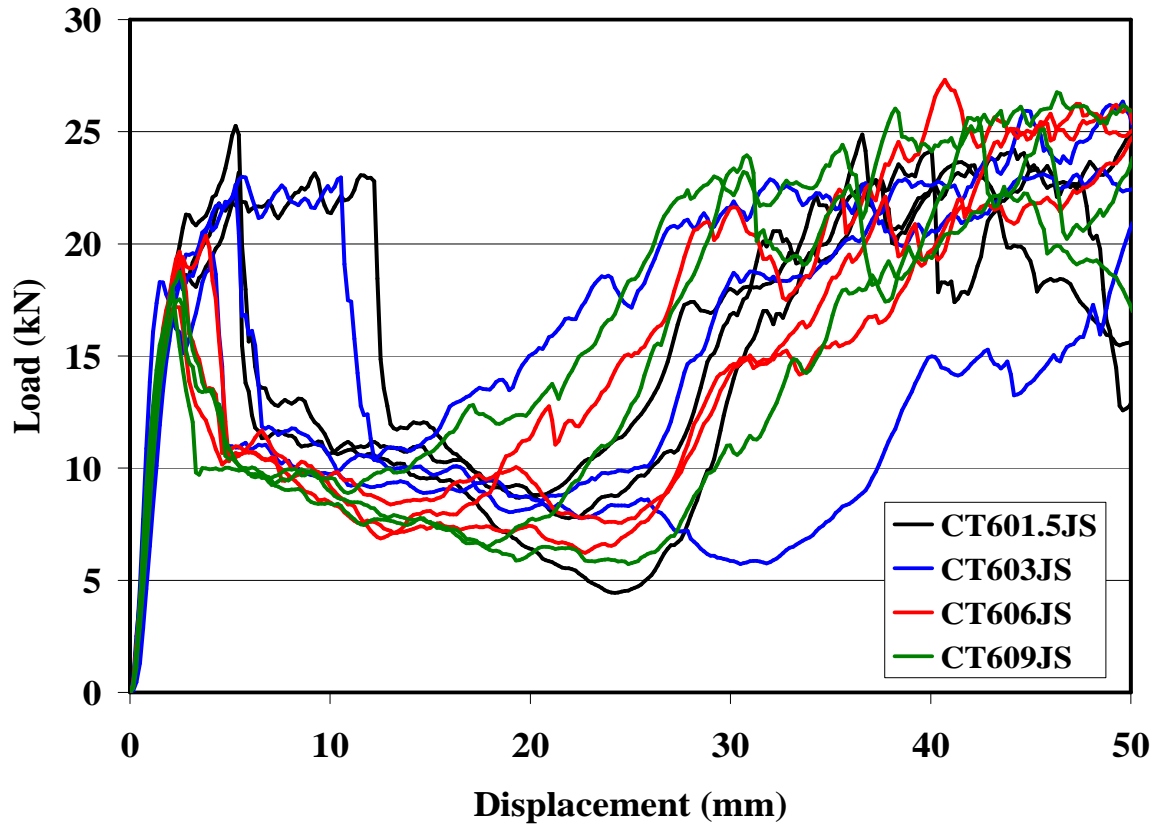


Figure 120 Triaxial  $\pm 60$  Samples with Impact Damage

Literature [48, 93, 106] has proposed that an area of damage can be treated as a cut-out or hole of the same size, here taking our results with a NCF 0-90 tube, 1.5J of damage cause a similar mode of failure (i.e. progressive crush) to a 5-10mm hole depending upon the sample architecture and 3J can be considered the equivalent of a 10-16mm hole. Using the dimensions of the area of the stress whitening, the formula for the area of an ellipse is:

$$\frac{\pi \cdot (a \cdot b)}{4}, \text{ where } a \text{ and } b \text{ are the major and minor axes of the damage zone.}$$

For a 1.5J impact Area =  $\pi \cdot (25 \times 15) / 4 = 294.5 \text{ mm}^2$ , for a 5mm hole the area is  $19.6 \text{ mm}^2$ , the area of the stress whitening is approximately 15 times greater than that of the equivalent hole. Equating this to a 10mm hole gives an area of  $78.5 \text{ mm}^2$ , meaning the area of stress whitening is at least 3.8 times the area of the equivalent hole. For a 3J impact Area =  $\pi \cdot (32 \times 18) / 4 = 452.4 \text{ mm}^2$ , for a 10mm hole the area is  $78.5 \text{ mm}^2$ , the area of the stress whitening here is 5.8 times larger than the 10mm hole. For a 16mm hole, the area is  $201.6 \text{ mm}^2$ , which is 2.2 times smaller than the area of stress whitening. Looking at the 6J impact Area =  $\pi \cdot (45 \times 25) / 4 = 883.6$  comparing to a 16 mm hole the area of stress whitening is 4.4 times larger.

Taking the smallest ratio between areas of holes and impact damage, the area of the stress whitening is at least 2.2 times greater than the area of the equivalent hole; in reality this is probably conservative as this is the upper boundary and the actual equivalent ratio could possibly lie between 2.2 and 5.8 depending upon the fibre architecture. This suggests that using a hole the same area as the damaged zone in calculations will produce a very conservative estimate for failure levels and damage effects predictions.

Dividing the area of the damage zone by a factor of 2.2 could produce improved estimates, which could be used to calculate an equivalent hole size. This equivalent hole size can be used in calculations for stress concentrations, and to help give an indication as to whether or not the damaged sample will fail. It should be noted however that this value is dependant upon the sample architecture. Even in this study for many of the samples the factor of 2.2 is still very conservative.

#### 4.2.9. Compression After Impact Strength (CAI)

Compression After Impact strength (CAI) has been studied in the literature [106, 107] modelling the damage as firstly a circular area of damage, and secondly as an elliptical area of damage. The formulae presented in these papers can be used to estimate the CAI strength for the tubes in this study.

$$\frac{\sigma_{CAI}}{\sigma_o} = \frac{2}{2 + \xi_1^2 + 3.\xi_1^4 - (K_T^\infty - 3).(5.\xi_1^6 - 7.\xi_1^8)} \quad (20)$$

Where,

$$\xi_1 = \frac{r}{(r + a_o)} \quad (21)$$

and

$$K_T^\infty = 1 + \sqrt{2 \left( \sqrt{\frac{E_y}{E_x}} - \nu_{yx} + \frac{E_y}{2.G_{yx}} \right)} \quad (22)$$

$\sigma_o$  = Undamaged Compressive Strength,  $r$  = radius of circular damage,  $a_o$  = characteristic distance, where subscripts x and y refer to perpendicular and parallel to the loading directions in the composite.

Equations (20) – (22) are for the CAI Strength to Undamaged Compressive Strength Ratio for tubes with a circular area of damage from [107]

The corresponding equations for an elliptical area of damage from [106] are:

$$\sigma_{CAI} = \sigma_0 \cdot \left[ 1 + \frac{1}{\sqrt{\xi^{-2} - 1 + \lambda^2} \cdot (\xi^{-2} + \sqrt{\xi^{-2} - 1 + \lambda^2})} \right] + \frac{(\lambda^2) \cdot (\lambda + 1) \cdot (\xi^{-2} + 2 \cdot \sqrt{\xi^{-2} - 1 + \lambda^2})}{\left[ ((\xi^{-2} - 1) + \lambda^2)^{\frac{3}{2}} \cdot \left[ (\xi^{-2} + \sqrt{\xi^{-2} - 1 + \lambda^2})^2 \right] \right]} - \left[ \left( \frac{\lambda^7}{2} \right) \cdot \left( K_T - 1 - \frac{2}{\lambda} \right) \right] \cdot \left[ \left[ \frac{5 \cdot \xi^{-1}}{\left( (\xi^{-2} - 1) + \lambda^2 \right)^{\frac{7}{2}}} \right] - \left[ \frac{7 \cdot \lambda^2 \cdot \xi^{-1}}{\left( (\xi^{-2} - 1) + \lambda^2 \right)^{\frac{4}{2}}} \right] \right]$$

(23)

where,

$$\lambda := \frac{b}{a}$$

(24)

$$\xi := \frac{a}{a + b_0}$$

(25)

$$K_T = (K_T)^\infty / \left[ \left[ \frac{\lambda^2}{(1 - \lambda)^2} \right] + \left[ \frac{(1 - 2 \cdot \lambda)}{(1 - \lambda)^2} \cdot \sqrt{1 + (\lambda^2 - 1) \cdot \left( \frac{2 \cdot a}{W} \right)^2} \right] \right] - \frac{(\lambda^2)}{(1 - \lambda)} \cdot \frac{\left( \frac{2 \cdot a}{W} \right)^2}{\sqrt{1 + (\lambda^2 - 1) \cdot \left( \frac{2 \cdot a}{W} \right)^2}} + \frac{\left[ \lambda^7 \cdot \left( \frac{2 \cdot a}{W} \right)^6 \cdot \left[ (K_T)^\infty - 1 - \frac{2}{\lambda} \right] \cdot \left[ \left[ 1 + (\lambda^2 - 1) \cdot \left( \frac{2 \cdot a}{W} \right)^2 \right]^{\frac{-5}{2}} - \left[ \left( \frac{2 \cdot a}{W} \right)^2 \cdot \left[ 1 + (\lambda^2 - 1) \cdot \left( \frac{2 \cdot a}{W} \right)^2 \right]^{\frac{-7}{2}} \right] \right] \right]}{2}$$

(26)

Where  $\lambda$  denotes the hole aspect ratio of the major and minor diameters,  $2a$  and  $2b$  respectively;  $b_0$  is a characteristic length to be determined empirically;  $W$  is the width of the panel;  $K_T$  is the stress concentration factor for a finite width panel;  $K_T^\infty$  is the stress concentration factor for an infinitely wide panel which is expressed in equation (22)

Using the observed measurements of damage, and taking the characteristic length of 5.91mm for the braided samples in [106], the ratios can be calculated, modelling the tubes as a flat plate of width 119.69mm.

In order to calculate the value of in-plane shear modulus,  $G_{xy}$  in equation 22, two methods have been used to calculate  $G_{12}$ , firstly a simple micro mechanics approach (equations (27) – (29)) and a semi empirical method based upon a Halphin-Tsai equations in (30) & (31) as described from [144] and material data produced by Turner [145]. The value for  $G_{12}$  is used for  $G_{xy}$  assuming that the fibres parallel to the loading direction do not play a significant part in contributing to shear modulus. It should be noted that this will only give an approximation of the true value of  $G_{xy}$ , as the  $90^\circ$  fibres will contribute to any stiffness or strength values and  $G_{12}$  value used will only be truly accurate for unidirectional composites.

$$\frac{1}{G_{12}} = \frac{V_f}{G_f} + \frac{V_m}{G_m} \quad (27)$$

$$G_f = \frac{E_f}{2 \cdot (1 + \nu_f)} \quad G_m = \frac{E_m}{2 \cdot (1 + \nu_m)} \quad (28) \quad (29)$$

Where subscripts  $f$  refers to fibre,  $m$  to matrix and  $12$  refers to the composite

$$\frac{G_{12}}{G_m} = \frac{(1 + \xi \cdot \eta \cdot V_f)}{(1 - \eta \cdot V_f)} \quad (30)$$

Where reinforcing factor  $\xi = 1$  and

$$\eta = \frac{\left(\frac{G_f}{G_m}\right) - 1}{\frac{G_f}{G_m} + \xi} \quad (31)$$

Table 27 shows the calculated values of In-plane Shear Modulus using data from Table 28 and equations 27-31.

**Table 27 In-Plane Shear Modulus**

Fibre Type	$G_{xy}$ /GPa Mechanics of materials	$G_{xy}$ /GPa Halphin-Tsai
CoFRM <sup>*</sup>	3.27	
NCF 0-90	1.92	2.47
NCF 90-0	1.87	2.38

\*Measured experimentally by [111]

**Table 28 Values used in Calculating In-Plane Shear Modulus**

Property	NCF 0-90	NCF 90-0
$V_f$	0.331	0.313
$E_y$ (GPa) <sup>1</sup>	24.4	24.6
$E_x$ (GPa) <sup>1</sup>	24.6	24.4
$E_f$ (GPa) <sup>2</sup>	85	85
$E_m$ (GPa) <sup>2</sup>	3.4	3.4
$\nu_{xy}$ <sup>3</sup>	0.3	0.3
$\nu_f$ <sup>2</sup>	0.2	0.2
$\nu_m$ <sup>2</sup>	0.3	0.3

<sup>1</sup> measured experimentally by [145] for samples with identical fibre types and  $V_f = 0.39$

<sup>2</sup> Values from Table 3.1 [144], <sup>3</sup> assumed value

Table 29 shows the data for the calculated CAI ratio for CoFRM samples.

**Table 29 Compression After Impact Strength Ratio for CoFRM**

Fibre Type	Impact Level/J	Damage Size /mm (axial x hoop)	$\sigma_{CAI}/\sigma_o$	
			Circular	Elliptical
CoFRM	1.5	15x13	0.77	0.65
CoFRM	3	24x18	0.68	0.53
CoFRM	6	38x22	0.60	0.45
CoFRM	9	39x26	0.58	0.41

$\sigma_{CAI}/\sigma_o$  Elliptical in Table 29 and Table 30 was calculated for the data in this study using equations 1 through 5 from Falzon and Herzberg [106].  $\sigma_{CAI}/\sigma_o$  was calculated using the equations presented earlier in this section. Table 30 shows the corresponding data for the calculated CAI ratio for NCF samples.

**Table 30 Compression After Impact Strength Ratio for NCF**

Fibre Type	Impact	Damage Size /mm (axial x hoop)	$\sigma_{CAI}/\sigma_o$	$\sigma_{CAI}/\sigma_o$	$\sigma_{CAI}/\sigma_o$	$\sigma_{CAI}/\sigma_o$
	Level		Circular	Elliptical	Circular	Elliptical
	/J				Halphin-Tsai	Halphin-Tsai
NCF 0-90	1.5	20x15	0.74	0.60	0.73	0.59
NCF 0-90	3	32x18	0.66	0.50	0.65	0.50
NCF 0-90	6	45x25	0.58	0.41	0.58	0.41
NCF 0-90	9	50x30	0.55	0.39	0.54	0.38
NCF 90-0	1.5	22x20	0.70	0.56	0.69	0.55
NCF 90-0	3	33x21	0.64	0.48	0.63	0.47
NCF 90-0	6	52x28	0.55	0.39	0.55	0.38
NCF 90-0	9	57x30	0.54	0.37	0.53	0.37

The values for  $\sigma_{CAI}/\sigma_o$  circular and  $\sigma_{CAI}/\sigma_o$  elliptical used the mechanics of material data for  $G_{xy}$  (equations 27-29) and the values for  $\sigma_{CAI}/\sigma_o$  circular Halphin-Tsai and  $\sigma_{CAI}/\sigma_o$  elliptical Halphin-Tsai used the Halphin-Tsai data for  $G_{xy}$ . (equations 30 & 31). Circular refers to equations 20-22 modelling the damage as a circular area, and elliptical refers to equations 23-26 modelling the damage as an elliptical area

The ratios presented here suggest that CoFRM will perform better after impact than NCF samples. Using the Halphin-Tsai equation to produce values for  $G_{xy}$  had the effect of decreasing the  $\sigma_{CAI}/\sigma_o$  ratio.

Thus if shear modulus is increased the  $\sigma_{CAI}/\sigma_o$  ratio decreases. Looking at the values for NCF 0-90 with 1.5J of damage (Table 30), a 28% increase in the value used for  $G_{xy}$  between  $\sigma_{CAI}/\sigma_o$  circular and  $\sigma_{CAI}/\sigma_o$  circular Halphin-Tsai, results in a maximum of a 1.4% decrease in  $\sigma_{CAI}/\sigma_o$  for a circular area of damage. This suggests that the in-plane shear modulus does not have a major effect upon the values for  $\sigma_{CAI}/\sigma_o$ .

Table 31 shows the experimental data for  $\sigma_{CAI}$  and  $\sigma_o$  as measured in this study.  $\sigma_{CAI}$  is taken as the maximum strength of an impacted sample under quasi-static crush and  $\sigma_o$  is for the undamaged samples. The CoFRM data is extrapolated from results produced by Ribeaux [7]

**Table 31 Measured Compression After Impact Strength Ratios**

Fibre Type	Impact Level	Damage Size /mm (axial x hoop)	$\sigma_{CAI}$ /MPa	$\sigma_o$ /MPa	$\sigma_{CAI}/\sigma_o$ i
CoFRM	1.5	15x13	108.31	174.9	0.62
CoFRM	3	24x18	97.26	174.9	0.56
CoFRM	6	38x22	79.58	174.9	0.45
CoFRM	9	39x26	75.16	174.9	0.43
NCF 0-90	1.5	20x15	101.69	139.1	0.73
NCF 0-90	3	32x18	86.68	139.1	0.62
NCF 0-90	6	45x25	75.11	139.1	0.54
NCF 0-90	9	50x30	62.27	139.1	0.45
NCF 90-0	1.5	22x20	127.24	207.6	0.61
NCF 90-0	3	33x21	123.87	207.6	0.60
NCF 90-0	6	52x28	114.80	207.6	0.55
NCF 90-0	9	57x30	103.82	207.6	0.50

Comparing Table 29 -Table 31 it can be seen that a good agreement is reached between the experimental and the elliptical calculated values for the CoFRM tubes. The 0-90 NCF tubes show good agreement with circular Halphin-Tsai values at low damage sizes, but appear to overestimate CAI slightly at higher impact levels. The NCF 90-0 tubes show closest agreement with the circular calculated values using the Halphin-Tsai equation to calculate in-plane shear modulus, especially at higher impact levels.

There is still a significant error between the calculated and experimental values for the NCF materials at certain damage levels. This error could possibly be reduced using a measured in-plane shear modulus or one calculated by other means, or perhaps by using a characteristic length unique to each fibre type and architecture.

If the failure modes for each tube type are examined; the quasi-statically crushed CoFRM samples had a threshold of 1.5J, the NCF samples had a threshold of 3J.

Thus the values of the  $\sigma_{CAI}/\sigma_o$  ratio corresponding to the threshold level of failure are at 65 for the CoFRM, 0.65 for the NCF 0-90 and 0.63 for NCF 90-0 from the theoretical values. Using the experimental values then these become 0.62, 0.62 and 0.60 respectively.

If these levels are matched to the failure modes of the specimens the following criteria can be determined from the theoretical data.

$$\sigma_{CAI}/\sigma_o > 0.65 \quad \text{no failure will occur} \quad (32)$$

$$0.55 < \sigma_{CAI}/\sigma_o < 0.65 \quad \text{First onset of failure, mixture of modes 1, 2 \& 3} \quad (33)$$

$$\sigma_{CAI}/\sigma_o < 0.55 \quad \text{Mode 2 failure} \quad (34)$$

Looking at the experimental data these bounds become

$$\sigma_{CAI}/\sigma_o > 0.62 \quad \text{no failure will occur} \quad (35)$$

$$0.55 < \sigma_{CAI}/\sigma_o < 0.62 \quad \text{First onset of failure, mixture of modes 1, 2 \& 3} \quad (36)$$

$$\sigma_{CAI}/\sigma_o < 0.55 \quad \text{Mode 2 failure} \quad (37)$$

It should be noted that the NCF 90-0 1.5J samples disagree with this boundary as they show no failure, but they have a ratio of 0.61.

### 4.2.10. Interlaminar Shear Strength

The interlaminar shear strength was calculated using the data from ILSS rig, and SEA was plotted against this for each sample (Figure 121). The data presented here was obtained under quasi-static conditions

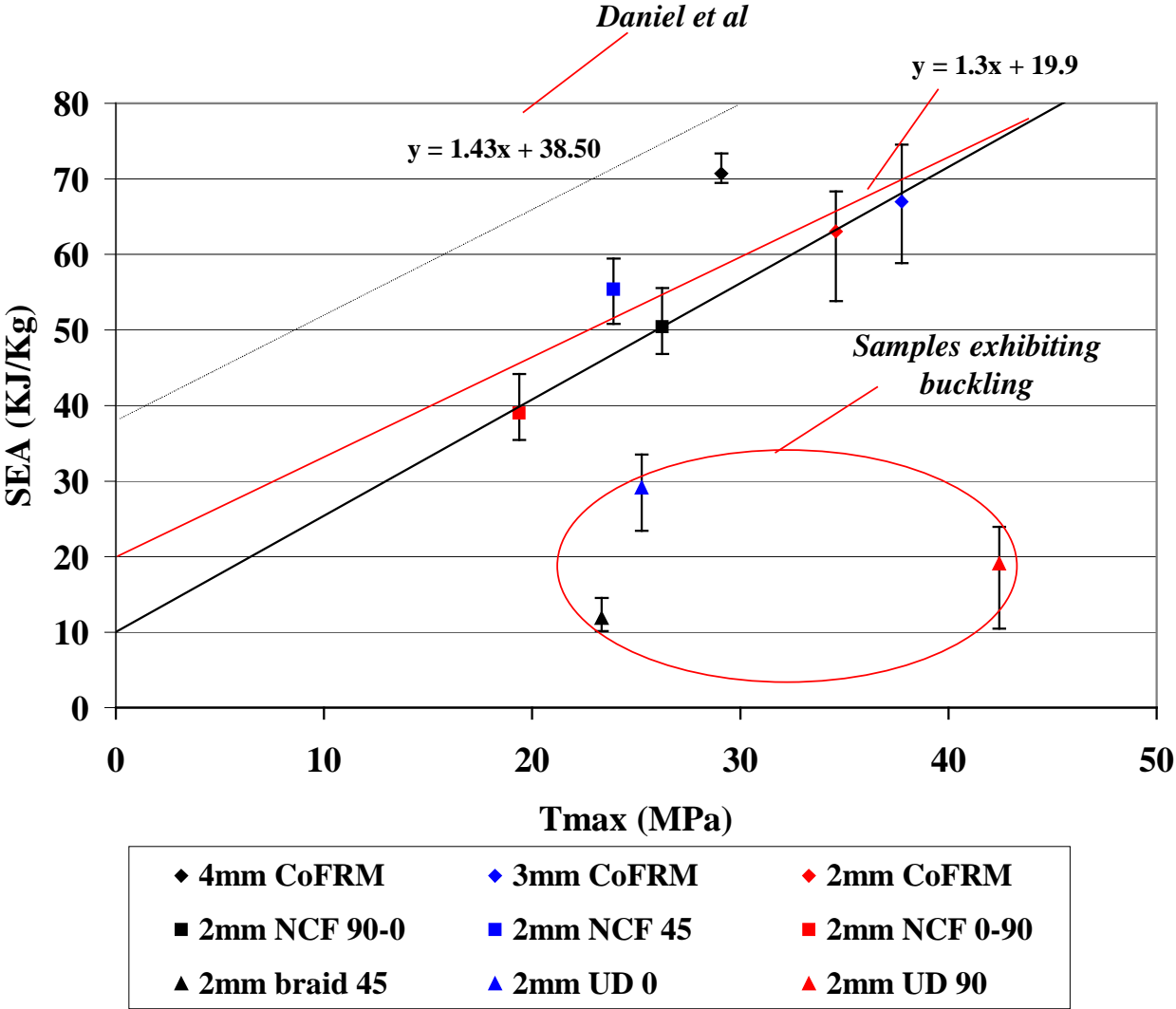


Figure 121 SEA vs Interlaminar Shear Strength

In Figure 121 the error bars refer to max and min SEA values, with the plotted points showing the average. From the above figure, it can be seen that 4 of the points that fail in a splaying

mode lie on a line. However, if all the points that do not buckle are considered then these lie near to a trend line, produced by using a least squares fit, of

$$y = 1.3x + 19.9. \quad (38)$$

The theory proposed by Daniel et al [73] stated that ILSS is the important factor in determining energy absorption. However, their testing method ensured that all samples failed by the same mode, whereas here the mode of failure is dependant upon the sample orientation. As the SEA data was obtained by crushing tubes (a more realistic way of obtaining energy absorption when comparing to real life automotive crash applications) the failure mode, as documented earlier, has a significant effect on energy absorption.

The samples lying close to the line are those that splay and crush in a progressive fragmentation mode e.g. NCF fabrics and CoFRM samples. Those that buckle, the pure axial unidirectional and the biaxially braided  $\pm 45$  tube, lie away from the line. The unidirectional hoop tube lies away from the line also. Here there is no axial reinforcement so the tube splits into rings, which absorb little energy in a stacking style of failure. The only real energy absorption is through the fragmentation of the matrix between each ring.

Looking at Daniel et al and their theory, it cannot explain the square CoFRM tube that has a similar ILSS to the CoFRM 2mm tube on the graph, but a significantly lower SEA. This would create another point significantly distant from the others. The equation of the line that their points lie upon is  $y = 1.43x + 38.5$ . Figure 121 suggests that this equation will overestimate the SEA significantly when compared o the results for the tubes under test here.

Thus it can be concluded that ILSS is only a significant factor in determining the SEA for tubes that fail by splaying or fragmentation. It does not apply to those that fail through other failure modes.

Using the equation of the line,  $y = 1.3x + 19.9$ , if the ILSS is a known value, then for a sample that crushes progressively the SEA can be simply calculated from:

$$SEA (\text{kJ.kg}^{-1}) = 1.3 \times \text{ILSS (MPa)} + 19.9 \quad (39)$$

In investigating SEA, mass per unit length of sample and crush strength a pattern emerges. If SEA is multiplied by mass per unit length of sample the crush load is obtained.

$$F_c \text{ (N)} = \text{SEA (kJ.kg}^{-1}\text{)}. M_l \text{ (kgm}^{-1}\text{)} \quad (40)$$

The crushing load can simply be divided by the area of the tube in order to calculate the crushing stress.

$$\sigma_c = F_c / a_c \quad (41)$$

#### 4.2.11. Interleaf

A thermo-plastic interleaf was added in order to improve the damage tolerance of the composite tubes. The addition of a thermoplastic interleaf has been shown to increase interlaminar fracture toughness and thus affect performance. To investigate this, the interleaf was added during the performing process between each ply in the test specimens, and holes were drilled at 25mm from the chamfered end to investigate the threshold failure levels..

**Table 32 SEA Data for NCF 0-90 with Interleaf and Holes**

Fibre Type	Test Reference	Hole Diameter /mm	Quasi-static SEA (kJ/kg) (Std. Dev %)	Failure mode	Dynamic SEA (kJ/kg) (Std. Dev %)	Failure mode
<b>NCF 0-90</b>	<b>C0mil</b>	<b>0</b>	<b>32.7 (3.7)</b>	<b>1</b>	<b>31.6 (2.1)</b>	<b>1</b>
NCF 0-90	C5mil	Ø5	34.4 (4.2)	1	32.6 (3.1)	1
NCF 0-90	C10mil	Ø10	21.9 (1.1)	2	30.4 (7.3)	3+1
NCF 0-90	C16mil	Ø16	21.7 (8.1)	2	25.9 (8.2)	2

The results for the quasi-statically crushed tubes with interleaf form a similar pattern to those tubes without (Table 32).. The threshold level for holes is again 10mm, above this value all specimens fail.

Dynamically the threshold level is still 10mm, however, only one of the three samples failed in testing. This shows an improvement over static tubes and the tubes without interleaf. From the load displacement curve (Figure 122) it can be seen that the samples with a 5mm hole fail in a mode 1 mode, the samples with 10mm fail progressively in mode 3 and the samples with 16mm fail globally in mode 2.

There is a drop in load between the static samples without interleaf and the samples with interleaf. This is in the region of 10%. For the results presented by Ribeaux [7] the drop in load seen with the addition of an interleaf results in a reduction in SEA of 28.6%. Ribeaux attributed this reduction in SEA to the presence of the interleaf reducing the coefficient of friction between the sample and the crush platen from 0.36 to 0.22.

This effect is not seen dynamically in the NCF tubes as both samples with and without an interleaf crush at the same load, the samples with an interleaf show a lower peak load and the load displacement curve is smoother (Figure 122), however, dynamically the CoFRM samples still show a decrease of ~21% in SEA with the addition of an interleaf.

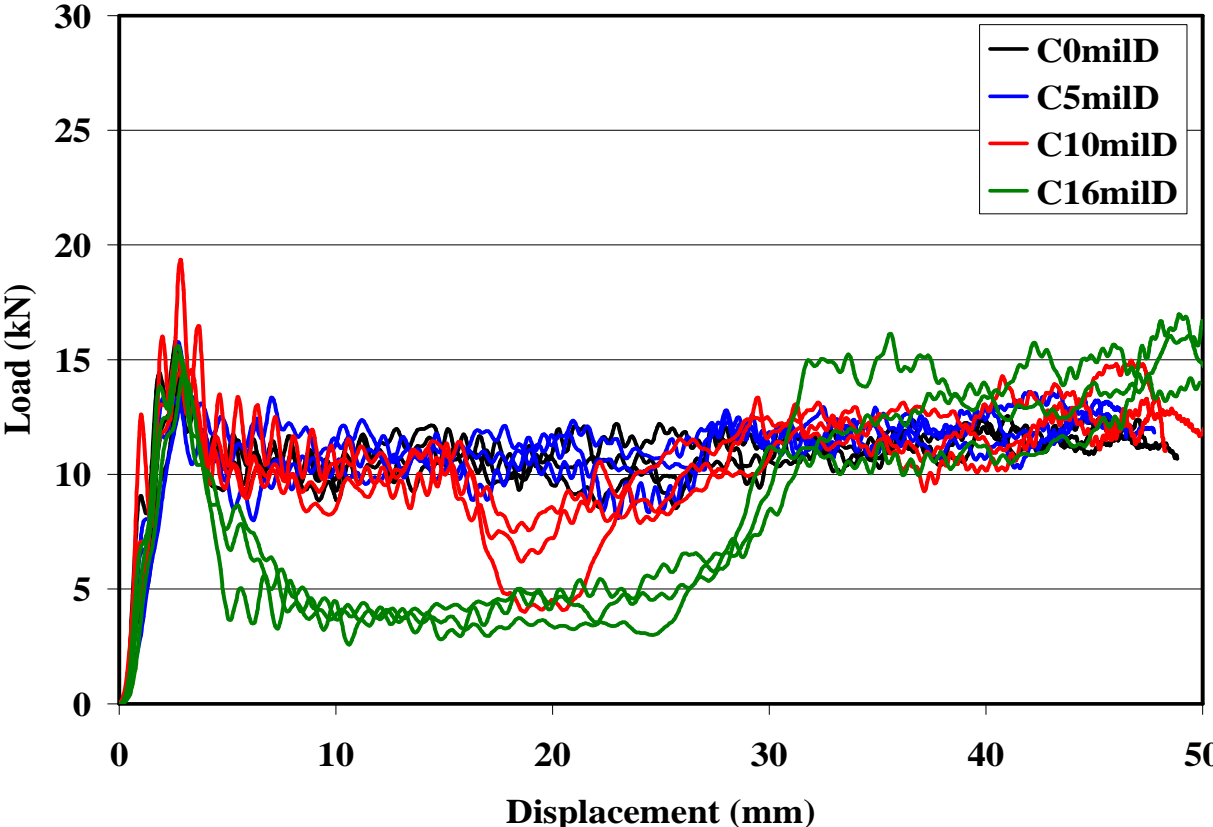


**Figure 122 Load Displacement Curve for Samples with Interleaf under Dynamic Loading**

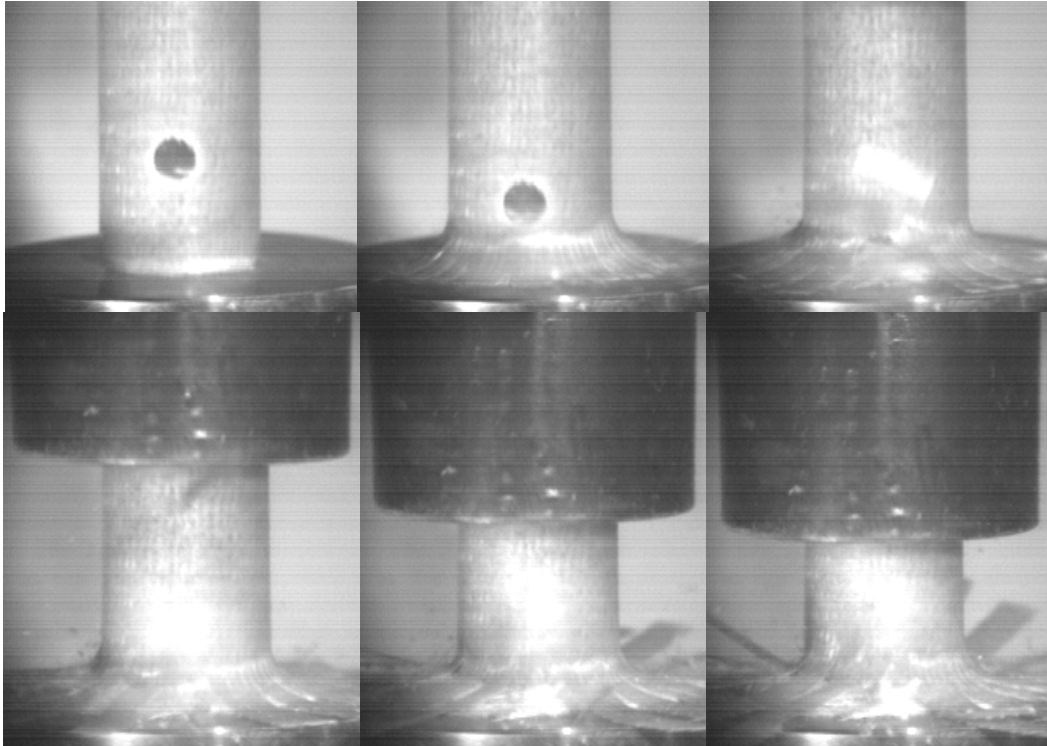


**Figure 123 Interleaf sample C10mil under Dynamic Loading**

The results for the quasi-statically crushed tubes with an interleaf and impact damage form a similar pattern to those tubes without (Table 33).

**Table 33 SEA Data for NCF 0-90 with Interleaf and Impact Damage**

Fibre Type	Test Reference	Damage size /mm	Quasi-static SEA (kJ/kg) (Std. Dev %)	Failure mode	Dynamic SEA (kJ/kg) (Std. Dev %)	Failure mode
<b>NCF 0-90</b>	<b>C0mil</b>	<b>0</b>	<b>32.7 (3.7)</b>	<b>1</b>	<b>31.6 (2.1)</b>	<b>1</b>
NCF 0-90	C3Jil	22x18	33.3 (1.1)	1	30.26 (3.0)	1
NCF 0-90	C6Jil	26x24	31.1 (24.3)	1+2	31.6 (3.8)	1
NCF 0-90	C9Jil	48x28	19.5 (10.5)	2	32.2 (3.6)	1
NCF 0-90	C12Jil	50x30	20.4 (5.7)	2	29.3 (19.6)	1+2
NCF 0-90	C15Jil	56x36	19.2 (14.3)	2	27.7 (2.1)	2

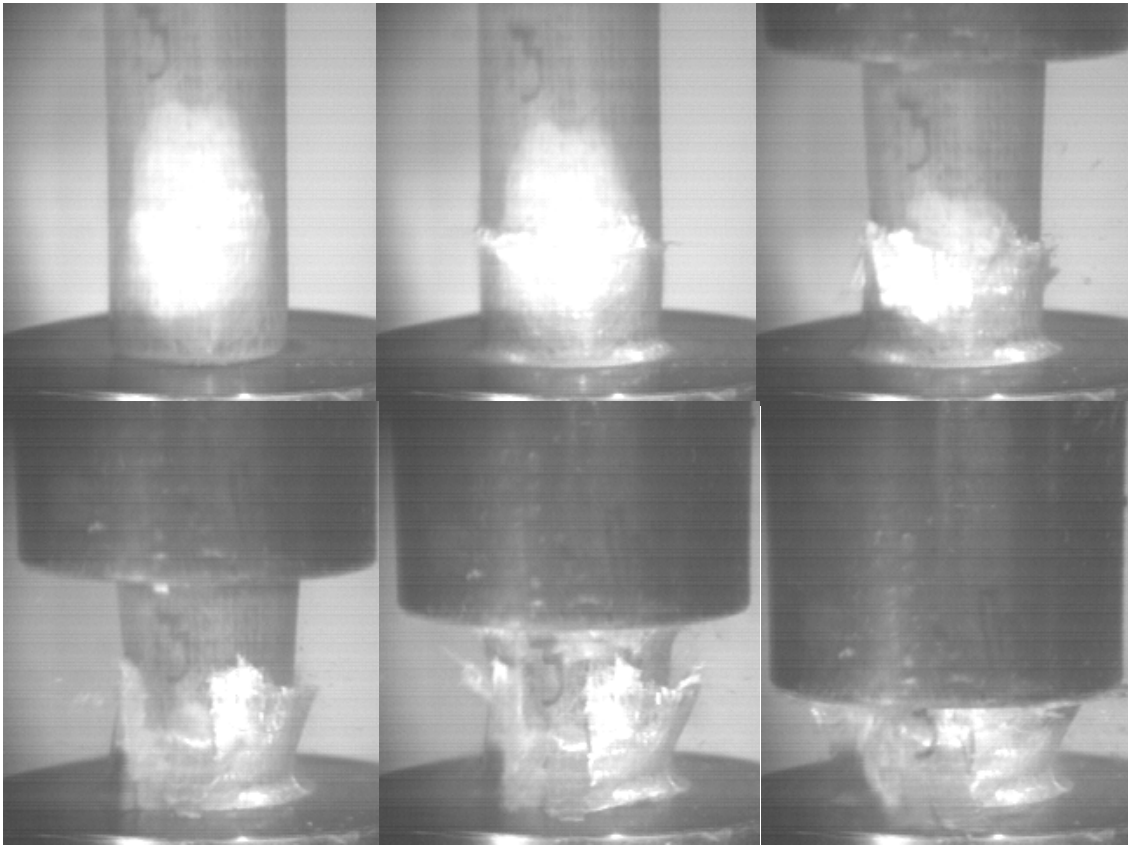


**Figure 124 Interleaf sample C12Jil under Dynamic Loading**

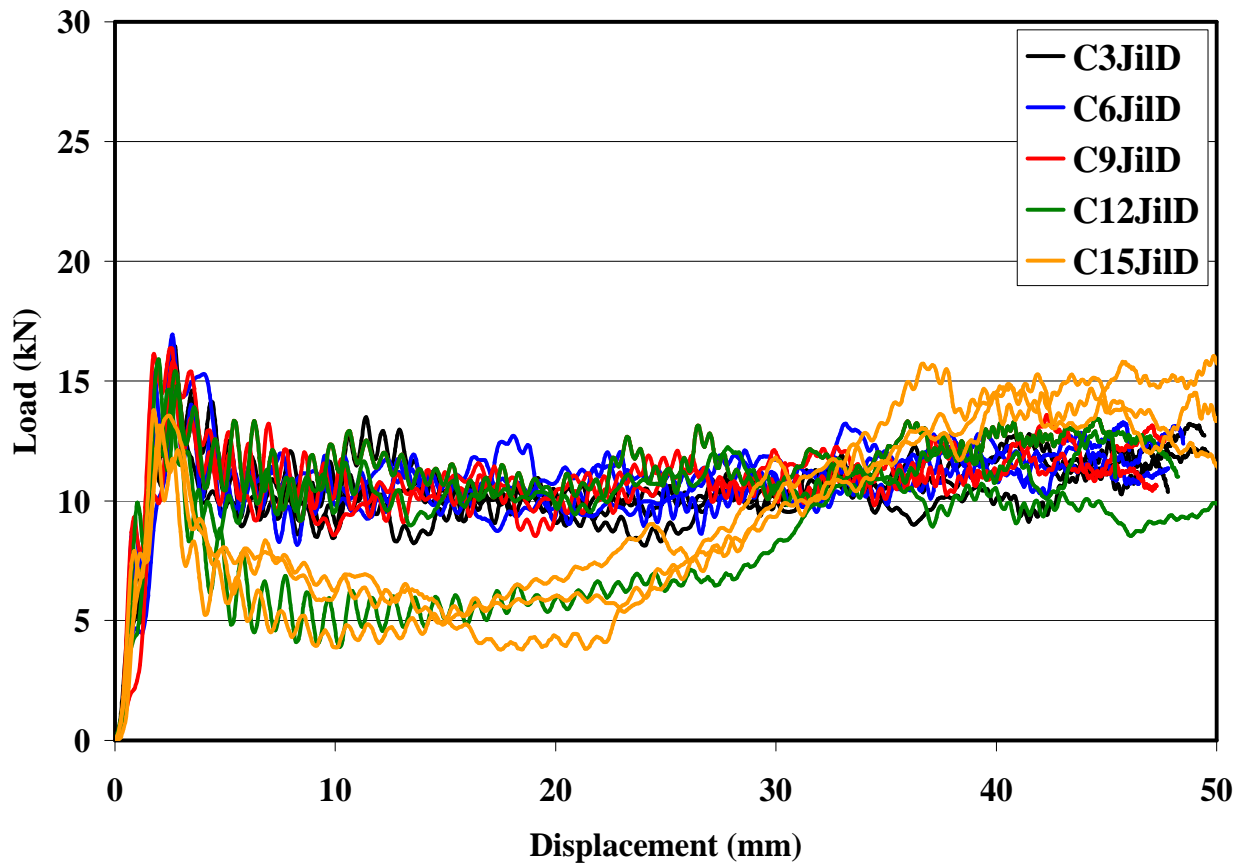


**Figure 125 Load Displacement Curve for Samples with Interleaf and Impact Damage**

The size of the damaged area caused by the impact with the tup was visually reduced in size with addition of the interleaf (Table 33). A 9J impact in the tube with interleaf caused a similar damage size in a tube without interleaf as an impact of 6J. This effect has been noted before in literature [109, 113].

The tubes with interleaf crush in a similar mode to the tubes without. The threshold level for impact statically is increased from 3J to 6J over the samples without interleaf. An example of a sample crushing can be seen in Figure 124.

Dynamically the threshold level is increased, from 9J for a tube without interleaf to 12J to a sample with interleaf. This is illustrated in Figure 125.

Again, there is a drop in load between the static samples without interleaf and the samples with interleaf. This is in the region of 10% and is still not seen dynamically.

The addition of interleaf reduces the SEA seen for the tubes both statically and dynamically. This was seen by Ribeaux [7] and Sohn et al [146] who observed a reduction in compressive strength of the composite samples tested with interleaf. This effect has also been reported by Warrior et al[111] who note that the mode I fracture toughness is increased with the addition of thermoplastic interleaf. This information suggests that interleaf is not a suitable for in crashworthiness applications where energy absorption is of paramount importance, but is suited to applications where damage tolerance is more critical.

## 5.0 Conclusions

The first major conclusion to be drawn from this work was that the resin system was the most significant factor affecting energy absorption for the large carbon tubes. The variations in SEA were all small between different fibre angles and architectures, but large between the polyester, vinyl-ester and epoxy resins tested here. A similar trend was observed for the glass NCF tubes, suggesting for maximum performance, epoxy resins need to be used.

Clearly fibre orientation and architecture still have a significant effect on failure mode and hence energy absorption, but in previous work by Daniel et al [147] they were suggested to be less important than through thickness properties in determining SEA. Daniel et al [147] stated that the orientation of the structure can be ignored in determining energy absorption if fibre volume fraction and coupon width are similar. The results presented here suggest that failure mode is still the dominant factor in controlling SEA. Daniel et al's results are only valid for samples that crush progressively and the nature of their test equipment ensured this. The predictive method for obtaining SEA from ILSS, originally proposed by Daniel et al [73], has been refined and its validity to tubular geometries and specimens has been established.

In this study, it has been shown that samples fail in a number of different failure modes. When a graph of SEA vs ILSS was plotted the samples that crushed progressively all fell close to a linear relationship. The samples that buckled, globally or locally, displayed a low SEA but a high ILSS (the ILSS has little effect upon SEA during buckling). This implies that orientation is a factor that influences crushing mode, which in turn has an effect upon energy absorption. However it is useful to reiterate that a linear relationship appears to apply for samples that do not buckle, in agreement with Daniel et al [73].

Significantly this study has shown that the NCF and biaxially braided reinforcements tested have offered relatively low SEA levels – notably lower than those seen for the CoFRM samples in [7] and slightly lower than the accepted SEA values for steel and aluminium tubes of similar geometry. This could be attributed to the relatively low fibre volume fractions of the tubes tested here (NCF ~30%). It has been well established that there is a link between fibre volume fraction and SEA, noting that in this study generally the samples with the higher fibre volume fractions had the higher SEA value whilst the reduction in SEA between

CoFRM and NCF was attributed to higher in-plane strengths and lower through thickness properties of the NCF allowing the crushing process to occur at a lower load.

The fibre orientation or stacking sequences, in this study, has been shown to affect the failure mode and SEA dramatically. Due to the stitching process of the NCF fabric, a number of possible orientations could be tested using the same material.

When investigating tube architecture with the same fibre architecture, little difference was seen between SEA's for the circular and square architectures presented here (39.0kJ/kg versus 39.8kJ/kg); both failed in a similar manner at a similar load. Ribeaux and Warrior [140] recorded a different result. In their testing SEA decreased when changing from a circular section to a square section - a decrease of 21% was recorded. They attributed this drop to geometric stress raisers at the corners and a reduction in composite material properties. Here the geometric stress raiser has less of an effect due to the discontinuous nature of the NCF fabric, where the gaps between the fibre tows create a complex stress distribution not seen in the CoFRM fabrics. This complex distribution of stresses negates the effects of the corner.

Testing rate results showed that there was an initial drop in SEA for all samples in the range of  $0-1\text{ms}^{-1}$  (The NCF 90-0 orientation showed the largest decrease in SEA with rate and the triaxial braided  $0\pm 60$  showed the smallest drop). After the initial decrease in SEA, the level then remained steady for all samples up to the limit of the test equipment,  $7\text{ms}^{-1}$ . No downward trends were seen during this section of testing, suggesting this pattern would continue at higher rates. This result is important as it establishes that testing at  $5\text{ms}^{-1}$  has the potential to simulate testing at higher rates; i.e. results obtained at this rate are valid for higher velocities and the complexity/cost of equipment required can be reduced (although this needs to be treated with caution as the response cannot safely be predicted for ballistic rates, and possibly even at automotive rates, so further testing at is required to verify this result).

A second predictive technique for identifying the failure mode of a sample with a SCF or area of damage has been introduced. The introduction of a stress concentration was found to have a significant effect on the failure mode. The previously reported threshold level effect was observed, where a change in the mode of failure occurred, from progressive crush to global fracture, initiated at the stress concentration and was seen to apply to NCF at both static and impact rates and in braids at impact rates. Quasi-statically, the circular NCF 0-90 tubes had a

threshold level of 10mm ( $D/d = 3.8$ ); this is twice the size of that seen by a similar CoFRM tube which had a  $D/d = 7.6$  [139]. The step sizes in this study were large, and a smaller step-size may provide a more representative value of the threshold level.

The NCF  $\pm 45$  and NCF 90-0 both showed a reduced tolerance to damage than the 0-90 tubes and the braided tubes showed a further reduction in tolerance than the NCF samples. Quasi-statically, the braided circular tubes had a threshold level of 5mm, although the biaxial  $\pm 30$  tubes however did appear to show a small improvement in damage tolerance.

The square NCF tubes behaved in a similar manner to the circular specimens; the threshold was again 10mm with a  $W/d$  of 3.0. Dynamically there was no effect on the crush mode at this level - the threshold level was increased to a hole size of 16mm ( $W/d = 1.875$ ), and at this level only one of the samples failed globally. This was a significant improvement over the CoFRM results of [140] which show the threshold to be a  $W/d = 6$ . This result is important for automotive applications as it shows that a square geometry will perform as well as a circular geometry when damaged, and shows a significant improvement in damage tolerance over the CoFRM samples from [7].

At dynamic rates, the damage tolerance of all tubes was increased. Although the threshold levels for NCF tubes remained the same, fewer samples of each type were failing. The braided tubes showed a significant improvement dynamically. The  $\pm 30$  and  $\pm 45$  tubes exhibited the highest tolerance to damage of the braided tubes with a threshold hole size of 16mm. This data indicated that higher axial fibre content limited damage progression around the circumference of the tube, increasing stability.

Out-of-plane impact was seen to have a significant effect on the crush mode, in a similar manner to that reported for a stress concentration. The previously reported threshold damage size effect was seen to apply to NCF tubes at both static and impact rates and in braids at impact rates. Quasi-statically, the circular NCF 0-90 tubes had a threshold level of 3J - an increase in tolerance over the previously reported CoFRM value of 1.5J [139]. The 90-0 and  $\pm 45$  NCF tubes showed a static threshold level similar to the CoFRM. Quasi-statically, the braided circular tubes had a threshold level of 1.5J, although the biaxial  $\pm 30$  tubes appeared to show a small improvement in damage tolerance.

Dynamically, the threshold value for a circular 0-90 tube was increased to 9J. For the square tubes, the threshold was more difficult to ascertain because of the local buckling observed, This occurred at 6J and above but only had a slight effect on the SEA level. At a level of 9J the tubes show a greater reduction in SEA. The threshold values in all other samples were seen to improve with rate, agreeing with previously reported results.

In order to try and predict undesirable failure of samples previous work[7] suggested crushing stress as the factor determining. If the crushing stress of the sample was lower than the mode 2 failure stress then progressive crush would occur (observed in many samples in this study).

Importantly in this study it was noted that a number of samples still failed even though the crushing stress was lower than the failure stress. In comparing the crush response traces, the high in-plane strengths of the NCF and braided fabrics gave a different looking load-displacement curve to that associated with the CoFRM fabric. The load rises steadily, initiated by the chamfer, to a peak value, where the structure is taking the maximum load. The sample then fails and the load relaxes to the steady-state crushing stress - this peak stress in most cases was significantly higher than the crushing stress, clearly seen in the dynamic samples. (The samples tested by Ribeaux[7] had no peak stress, so peak stress = crushing stress).

It was observed that if the peak stress was greater than the level of stress required to cause global or mode 2 failure, then the sample would collapse globally in a mode 2 failure. If the peak stress was less than this failure stress level the sample would crush progressively.

Thus a novel approach in predicting the failure mode of a sample with a SCF was suggested in this study, it was proposed that the crushing stress multiplied by the SCF would give a factored value of stress. If this number were compared to the UCS, it would give an indication of when the tube would fail. If the calculated stress value is greater than the UCS the tube will fail globally, and if it is less the tube will crush progressively. This gave us the Mode 2 failure criteria (equation (15)):

$$\sigma_c * K^1 > UCS$$

The results of this equation give a good indication to the failure mode of a sample under crush, and will indicate when a sample will fail globally due to the crushing stress.

Existing formulae for stress concentration factors have been investigated and found to be conservative when compared to experimental results, whilst not taking into account the tube and fibre architectures of the composites (many of the formulae were originally derived for use with metallic tubes). The complex architecture of a composite tube means that an experimental method of establishing the stress concentration, such as the thermal method described gives suitable results.

Using thermal analysis to establish the SCF is a technique previously unused with composite tubes. Whilst it has its drawbacks in terms of temperature effects due to the detector array, and testing conditions [80], it nevertheless offers a quick and easy method for establishing the SCF of hole or notch in a composite specimen. Using this new approach to obtain the SCF from the thermal analysis and evaluating this SCF against experimental observations from earlier in the study along with the failure criteria equation, the following failure criteria were established (equations (17)-(19)):

If  $\left(1 - \frac{\sigma_c \cdot SCF}{UCS}\right) \cdot 100 > 0$  then the sample will crush progressively (mode 1 failure)

If  $\left(1 - \frac{\sigma_c \cdot SCF}{UCS}\right) \cdot 100 > -5$  then the sample will fail by a mode 3 failure mode

If  $\left(1 - \frac{\sigma_c \cdot SCF}{UCS}\right) \cdot 100 < -5$  then the sample will fail globally in mode 2 failure.

The mode 1 and mode 2 failure types are predicted easily, however the bounds for mode 3 failure are small, in this case 5%. This lies within experimental errors, and errors within the TSA analysis, thus further samples are required to expand the range of data. However even taking into account the possible errors this provides a useful and powerful result.

Whilst Literature [48, 93, 106] has proposed that an area of damage can be treated as a cut-out or hole of the same size, the results presented here have shown that this is a conservative estimate, and that a tube with damage can still perform in a similar way to a tube with no damage. A better estimate will be produced by dividing the area of the damage zone by a factor (proposed here to be a minimum of 2.2) and then simply calculating the new hole size

this equates to. This equivalent hole size can be used in calculations for stress concentrations, and will give a quick indication as to whether or not the damaged sample will fail, crucial in a workshop strip where the part cannot be removed from a complex structure.

Applying the CAI strength equations to the samples in this study gave a more accurate method for prediction of failure of a sample with impact damage. This CAI strength gives the failure strength of the sample. So for a damaged area the failure load can be predicted. The large volume of data collected in this study allows a useful comparison between experimental and theoretical results to be made. Importantly, in a similar way to the criteria produced for failure modes with a stress concentration factor, comparing the experimental results and the CAI data, failure criteria could be produced using the values for the  $\sigma_{CAI}/\sigma_o$  ratio.(equations (32)-(34)

$\sigma_{CAI}/\sigma_o > 0.65$	no failure will occur
$0.55 < \sigma_{CAI}/\sigma_o < 0.65$	First onset of failure, mixture of modes 1, 2 & 3
$\sigma_{CAI}/\sigma_o < 0.55$	Mode 2 failure

Although these are useful and important results for prediction of the response of a damaged tube, they must be used with some caution. Due to time constraints, some of the data for these equations was calculated from material properties using assumptions based upon the makeup of the structure in order to calculate values for the in-plane shear strength. Whilst the characteristic length was taken from the literature, this value does not vary significantly from the number used and the material properties calculated were conservative. Based upon these values, the results from the above equations will not be completely accurate although they do show a reasonable agreement with the experimental results obtained in this study. Using measured values for all the parameters will increase the accuracy of the predictions, and possibly increase the failure bounds, importantly for each material/specimen type they need to be calculated only once.

There are a number of directions the work in this study could be extended and built upon. Testing at automotive rates would allow an improved understanding of the effects of damage upon automotive impacts and to validate testing at  $5\text{ms}^{-1}$  and establish if this gives a true representation of testing at higher rates.

Further crash testing upon automotive style structural rails would fully establish a correlation between these and the large existing data set based upon simple structures.

The TSA work could be extended to encompass a wider sample range including different geometries, resins and architectures that would improve the accuracy of any conclusions.

Further testing of carbon tubes would allow the effects of fibre architecture to be investigated with different sized tubes and validate the results presented here suggesting that fibre architecture has little affect upon energy absorption when compared to resin type.

## 6.0 References

1. Lie, A. and C. Tingvall. *How Does Euro NCAP Results Correlate to Real Life Injury Risks - A Paired Comparison to Car Crashes*. in *International Research Council On The Biomechanics of Impact (IRCOBI)*. 2000. Montpellier.
2. Farley, G. and R. Jones, *Crushing Characteristics of Continuous Fibre-Reinforced Composite Tubes*. *Journal of Composite Materials*, 1992. **26**(1): p. 37-50.
3. Jones, N., *Structural Impact*. 1989, Cambridge: Cambridge University Press.
4. Fernie, R., *Loading Rate Effects on the Energy Absorption of Lightweight Tubular Crash Structures*, *PhD Thesis*, in *Mechanical, Materials, Manufacturing Engineering and Management*. 2002, University of Nottingham: Nottingham.
5. Thornton, P.H. *Metal and FRP composite energy absorbing structures*. in *Advanced Composites Conference*. 1985. Dearborn, MI, USA.
6. Ramakrishna, S., *Microstructural Design of Composite Materials for Crashworthy Structural Applications*. *Materials and Design*, 1998. **18**(3): p. 167-173.
7. Ribeaux, M., *The Effect of Existing Damage on the Energy Absorption Potential of Bonded Polymer Composite Structures*, *PhD Thesis*, in *School of Mechanical, Materials and Manufacturing Engineering*. 2003, University of Nottingham.
8. Hull, D., *Axial Crushing of Fibre Reinforced Composite Tubes*. *Structural Crashworthiness*. Lectures Presented at the First International Symposium on Structural Crashworthiness, 1983: p. 118-135.
9. Daniel, L., P.J. Hogg, and P.T. Curtis, *The relative effects of through-thickness properties and fibre orientation on energy absorption by continuous fibre composites*. *Composites Part B: Engineering*, 1999. **30**(3): p. 257-266.
10. Harte, A.-M., N.A. Fleck, and M.F. Ashby, *Energy absorption of foam-filled circular tubes with braided composite walls*. *Eur. J. Mech A/Solids*, 2000. **19**: p. 31-50.
11. Mamalis, A.G., D.E. Manolakos, G.A. Demosthenous, and M.B. Ioannidis, *The Static and Dynamic Collapse of Fibreglass Composite Automotive Frame Rails*. *Composite Structures*, 1996. **34**: p. 77-90.
12. Gupta, Y.M. and R. Velmurugan, *Analysis of Polyester and Epoxy Composite Shells Subjected to Axial Crushing*. *International Journal of Crashworthiness*, 2000. **5**(3): p. 333-344.
13. Mamalis, A.G., D.E. Manolakos, M.B. Ioannidis, P.K. Kostazos, and E.C. Chirwa, *Static and Dynamic Axial Collapse of Fibreglass Composite Thin-Walled Tubes: Finite Element Modelling of The Crush Zone*. *International Journal of Crashworthiness*, 2003. **8**(3): p. 247-254.
14. Laananen, D.H. and A.O. Bolukbasi, *Prediction of Energy Absorption in Composite Stiffeners*. *Composite Structures*, 1995. **32**: p. 173-186.
15. Fairfull, A. and D. Hull, *Energy Absorption of Polymer Matrix Composite Structures : Frictional Effects*. "Symposium on Structural Failure, Chapter 8", 1988: p. 255-279.
16. Quek, S.C., A.M. Waas, J. Hoffman, and V. Agaram, *The crushing response of braided and CSM glass reinforced composite tubes*. *Composite Structures*, 2001. **52**: p. 103-112.
17. Belingardi, G., A. Gugliotta, and R. Vadori, *Numerical Simulation of Fragmentation of Composite Material Plates due to Impact*. *International Journal of Impact Engineering*, 1998. **21**(5): p. 335-347.
18. Lee, H.K., S. Simunovic, and D.K. Shin, *A Computational Approach for Prediction of the Damage Evolution and Crushing Behaviour of Chopped Random Fiber Composites*. *Computational Materials Science*, 2004. **29**: p. 459-474.

19. Mamalis, A.G., D.E. Manolakos, M.B. Ioannidis, and D.P. Papapostolou, *Crashworthy Characteristics of Axially Statically Compressed Thin-Walled Square CFRP Composite Tubes: Experimental*. Composite Structures, 2004. **63**: p. 347-360.
20. Pereira, A.B. and A.B. de Morais, *Mode I Interlaminar Fracture of Carbon/Epoxy Multidirectional Laminates*. Composites Science and Technology, 2004. **64**: p. 2261-2270.
21. Farley, G.L. and R.M. Jones, *Prediction of the Energy-Absorption Capability of Composite Tubes*. Composite Materials, 1992. **26**(3): p. 388-404.
22. Thornton, P.H., *Energy Absorption in Composite Structures*. Composite Materials, 1979. **13**: p. 247-262.
23. Mamalis, A.G., D.E. Manolakos, G.A. Demosthenous, and M.B. Ioannidis, *Analytical and Experimental Approach to Damage and Residual Strength of Fibreglass Composite Automotive Frame Rails During Manufacture*. Composite Structures, 1995. **32**: p. 325-330.
24. Hull, D., *A Unified Approach to Progressive Crushing of Fibre-Reinforced Composite Tubes*. Composites Science and Technology, 1991. **44**: p. 376-421.
25. Berry, J., *Energy Absorption and Failure Mechanisms of Axially Crushed GRP Tubes*. 1984, University of Liverpool: Liverpool.
26. Keal, R., *Post Failure Energy Absorbing Mechanisms of Filament Wound Composite Tubes*. 1983, University of Liverpool: Liverpool.
27. Farley, G., *Crushing Response of Energy Absorbing Composite Structure*. Engineering Mechanics, 1992: p. 876-879.
28. Farley, G.L. *Energy absorption in composite materials for crashworthy structures*. in *International Conference of Composite Materials VI*. 1987.
29. Farley, G.L., *Analogy for the Effect of Material and Geometrical Variables on Energy-Absorption Capability of Composite Tubes*. Composite Materials, 1992. **26**(1): p. 78-89.
30. Thornton, P.H., *The Crush Behaviour of Glass Fiber Reinforced Plastic Sections*. Composites Science and Technology, 1986. **27**: p. 199-223.
31. Czaplicki, M., R. Robertson, and P. Thornton, *Comparison of Bevel and Tulip Triggered Pultruded Tubes for Energy Absorption*. Composites Science and Technology, 1991. **40**: p. 31-46.
32. Jimenez, M.A., A. Miravete, E. Larrode, and D. Revuelta, *Effect of trigger geometry on energy absorption in composite profiles*. Composite Structures, 2000. **48**(1-3): p. 107-111.
33. Hull, D. and J.C. Coppola. *Performance of Glass Fibre-Vinyl Ester Composite Tubes Crushed Using Internal Mandrels*. in *International Conference on Composite Structures*. 1991.
34. Hull, D. and J.C. Coppola, *Effect of Trigger Geometry on Crushing of Composite Tubes*. Materials and Processing - Move into the 90s. 1989, Amsterdam: Elsevier Science Publishers B.V.
35. Cooper, E., *An Elastic-Plastic Finite Element Model for Composite Crash Structures*. 2002, University of Nottingham.
36. Rahman, M.T. and G.M. Newaz, *Effect of Impact Damage on Energy Absorption in Cylindrical PMC Tubes*. 2000.
37. Mills, A., *Automation of Carbon Fibre Preform Manufacture for Affordable Aerospace Applications*. Composites: Part A, 2001. **32**: p. 955-962.
38. Swanson, S.R. and L.V. Smith, *Comparison of the biaxial strength of braided and laminated carbon fiber composites*. Composites Part B, 1995. **27**: p. 71-77.

39. Bibo, G.A., P.J. Hogg, and M. Kemp, *Mechanical Characterisation of Glass and Carbon Fibre Reinforced Composites Made with Non-Crimp Fabrics*. Composite Science and Technology, 1997. **57**: p. 1221-1241.
40. Drapier, S. and M.R. Wisnom, *Finite-element investigation of the compressive strength of non-crimp-fabric-based composites*. Composites Science and Technology, 1999. **59**: p. 1287-1297.
41. Bibo, G.A., P.J. Hogg, R. Backhouse, and A. Mills, *Carbon-fibre Non-Crimp Fabric laminates for cost-effective damage-tolerant structures*. Composites Science and Technology, 1998. **58**: p. 129-143.
42. Bibo, G.A. and P.J. Hogg, *Influence of Reinforcement Architecture on Damage Mechanisms and Residual Strength of Glass-Fibre/Epoxy Composite Systems*. Composites Science and Technology, 1998. **58**: p. 803-813.
43. Yang, B., V. Kozey, S. Adanur, and S. Kumar, *Bending, compression, and shear behavior of woven glass fiber-epoxy composites*. Composites: Part B, 2000. **31**: p. 715-721.
44. Leif, E.A., F. Edgren, and A. Sjogren. *Effects of Stitch Pattern on the Mechanical Properties of Non-Crimp Fabric Composites*. in *European Conference for Composite Materials 11*. 2004. Rhodes, Greece.
45. Lundstrom, T.S., *The permeability of non-crimp stitched fabrics*. Composites Part A, 2000. **31**: p. 1345-1353.
46. Drapier, S., A. Pagot, A. Vautrin, and P. Henrat, *Influence of the Stitching Density on the Transverse Permeability of Non-Crimped New Concept (NC2) Multiaxial Reinforcements: Measurements and Predictions*. Composites Science and Technology, 2002. **62**: p. 1979-1991.
47. TECABS, *Technologies for Carbon-fibre Reinforced Modular Automotive Body Structures*. [www.tecabs.org](http://www.tecabs.org), 2004.
48. Falzon, P.J. and I. Herzberg, *Mechanical Performance of 2-D Braided Carbon/Epoxy Composites*. Composites Science and Technology, 1998. **58**: p. 253-265.
49. Mouritz, A.P., M.K. Bannister, P.J. Falzon, and K.H. Leong, *Review of applications for advanced three-dimensional fibre textile composites*. Composites: Part A, 1999. **30**: p. 1445-1461.
50. Mouritz, A.P., C. Baines, and I. Herzberg, *Mode I interlaminar fracture toughness properties of advanced textile fibreglass composites*. Composites: Part A, 1999. **30**: p. 859-870.
51. Toore, L. and J.M. Kenny, *Impact Testing and Simulation of Composite Sandwich Structures for Civil Transportation*. Composite Structures, 2000. **50**: p. 257-267.
52. Sun, H.-Y. and X. Qiao, *Prediction of the Mechanical Properties of Three-Dimensionally Braided Composites*. Composites Science and Technology, 1997. **57**: p. 623-629.
53. Neumeister, J., S. Jansson, and F. Leickie, *The effect of fibre architecture on the mechanical properties of carbon/carbon fiber composites*. Acta Materialia, 1996. **44**(2): p. 573-585.
54. Tang, Z.X. and R. Postle, *Mechanics of three-dimensional braided structures for composite materials - part I: fabric and fibre volume fraction*. Composite Structures, 2000. **49**: p. 451-459.
55. Kuo, W.-S., T.-H. Ko, and H.-I. Chen, *Elastic moduli and damage mechanisms in 3D braided composites incorporating pultruded rods*. Composites Part A, 1998. **29A**: p. 681-692.
56. Smith, L.V. and S.R. Swanson, *Micro-Mechanic Parameters Controlling the Strength of Braided Composites*. Composites Science and Technology, 1995. **54**: p. 177-184.

57. Karbhari, V.M. and J.E. Haller, *Rate and architecture effects on progressive crush of braided tubes*. *Composite Structures*, 1998. **43**: p. 93-108.
58. Wu, D.L., *Three-cell model and 5D braided structural composites*. *Composites Science and Technology*, 1996. **56**: p. 225-233.
59. Pandey, R. and H.T. Hahn, *Designing with 4-Step Braided Fabric Composites*. *Composites Science and Technology*, 1996. **56**: p. 623-634.
60. Pandey, R. and H.T. Hahn, *Visualization of a Representative Volume Element for Three-Dimensional Four-Step Braided Composites*. *Composites Science and Technology*, 1996. **56**(3): p. 161-170.
61. Wang, Y.-Q. and A.S.D. Wang, *Microstructure/Property Relationships on Three-Dimensionally Braided Fiber Composites*. *Composites Science and Technology*, 1995. **53**: p. 213-222.
62. Karbhari, V.M., P.J. Falzon, and I. Herzberg. *Effect of Braid Architecture on Progressive Crush of Composite Tubes*. in *41st International SAMPE Symposium*. 1996.
63. Karbhari, V.M., P.J. Falzon, and I. Herzberg, *Energy Absorption Characteristics of Hybrid Braided Tubes*. *Journal of Composite Materials*, 1997. **31**(12).
64. Chiu, C.H., C.K. Lu, and C.M. Wu, *Crushing characteristics of 3-D braided composite square tubes*. *Journal of Composite Materials*, 1997. **31**(22): p. 2309-2327.
65. Chiu, C.H., K.-H. Tsai, and W. Huang, *Crush-failure modes of 2D triaxially braided hybrid composite tubes*. *Composites Science and Technology*, 1999. **59**: p. 1713-1723.
66. Harte, A.-M. and N.A. Fleck, *Deformation and failure mechanisms of braided composite tubes in compression and torsion*. *Acta Materialia*, 2000. **48**: p. 1259-1271.
67. Harte, A.-M. and N.A. Fleck, *On the mechanics of braided composites in Tension*. *Eur. J. Mech A/Solids*, 2000. **19**: p. 259-275.
68. Subhash, G., S. Sulibhavi, and M.A. Zikry, *Influence of strain-rate on the uniaxial behavior of 2D braided textile composites*. *Composites: Part A*, 2001. **32**: p. 1583-1591.
69. Smith, L.V. and S.R. Swanson, *Strength Design with 2-D Triaxial Braid Textile Composites*. *Composites Science and Technology*, 1996. **56**: p. 359-365.
70. Farley, G., *Relationship Between Mechanical-Property and Energy-Absorption Trends for Composite Tubes*, in *NASA Technical paper 3284*. 1992, ARL Technical Report 29.
71. Feraboli, P. and A. Masini, *Development of Carbon/Epoxy Structural Components for a High Performance Vehicle*. *Composites Part B*, 2004. **35**: p. 323-330.
72. Rosseli, F. and M.H. Santare, *Comparison of the Short Beam Shear (SBS) and Interlaminar Shear Device (ISD) tests*. *Composites Part A*, 1997. **28A**: p. 587-594.
73. Daniel, L., P.J. Hogg, and P.T. Curtis, *The crush behaviour of carbon fibre angle-ply reinforcement and the effect of interlaminar shear strength on energy absorption capability*. *Composites: Part B*, 2000. **31**: p. 435-440.
74. Persson, E., I. Eriksson, and L. Zackrisson, *Effect of hole machining defects on strength and fatigue life of composite laminates*. *Composites Part A*, 1997. **28A**: p. 141-151.
75. Saha, M., R. Prabhakaran, and W.A. Waters, *Compressive Behaviour of Pultruded Composite Plates with Circular Holes*. *Composite Structures*, 2004. **65**: p. 29-36.
76. Lekkerkerker, J.G. *Stress concentration around circular holes in cylindrical shells*. in *Eleventh Int. Cong. Appl. Mech.* 1964. Munich.
77. Bull, J.W., *Stresses around large circular holes in uniform cylindrical shells*. *Journal of Strain Analysis*, 1982. **17**(1): p. 9-12.

78. Houghton, D.S. and A. Rothwell, *The Effects of Curvature on the Stress Concentration Around Holes in Shells*. College of Aeronautics Report No.156, 1962.
79. Van Tooren, M.J.L., I.P.M. Van Stijn, and A. Beukers, *Curvature Effects on the Stress Distribution in Sandwich Cylinders with a Circular Cut-Out*. *Composites Part A*, 2002. **33**: p. 1557-1572.
80. Quinn, S. and J.M. Dulieu-Barton, *Determination of Stress Concentration Factors for holes in cylinders using thermoelastic stress analysis*. *Strain*, 2002. **38**: p. 105-118.
81. Wu, H.-C. and B. Mu, *On stress concentrations for isotropic/orthotropic plates and cylinders with a circular hole*. *Composites Part B*, 2002. **34**: p. 127-134.
82. Jones, R. and D. Peng, *Composite Repairs to Cracked Holes Under Bi-Axial Loading*. *Composite Structures*, 2002. **57**: p. 459-464.
83. Kaltakci, M.Y., *Stress Concentrations and Failure Criteria In Anisotropic Plates with Circular Holes Subject to Tension or Compression*. *Computers and Structures*, 1996. **61**(1): p. 67-78.
84. Pandita, S.D., K. Nishiyabu, and I. Verpoest, *Strain Concentrations in Woven Fabric Composites with Holes*. *Composite Structures*, 2003. **59**: p. 361-368.
85. Yao, X.F., M.H. Kolstein, F.S.K. Bijlaard, W. Xu, and M. Xu, *Tensile Strength and Fracture of Glass Fibre-Reinforced Plastic (GFRP) Plate with an Eccentrically Located Circular Hole*. *Polymer Testing*, 2003. **22**: p. 955-963.
86. Cowley, K.D. and W.R. Beaumont, *Damage Accumulation at Notches and the Fracture Stress of Carbon-Fibre/Polymer Composites: Combined Effects of Stress and Temperature*. *Composite Science and Technology*, 1997. **57**: p. 1211-1219.
87. Williamson, C., J. Cook, and A.B. Clarke. *Investigation into the Failure of Open and Filled Holes in CFRP Laminates Under Biaxial Loading Conditions*. in *European Conference for Composite Materials 11*. 2004. Rhodes, Greece.
88. Richardson, M.O.W. and M.J. Wisheart, *Review of Low-Velocity Impact Properties of Composite Materials*. *Composites Part A*, 1996. **27A**: p. 1123-1131.
89. Lee, D.G., T.S. Lim, and S.S. Cheon, *Impact energy absorption characteristics of composite structures*. *Composite Structures*, 2000. **50**: p. 381-390.
90. Choi, H.Y., R.J. Downs, and F.-K. Chang, *A New Approach Toward Understanding Damage Mechanisms and Mechanics of Laminated Composites Due to Low-Velocity Impact: Part-I Experiments*. *Journal of Composite Materials*, 1991. **25**: p. 992-1011.
91. Cantwell, W.J. and J. Morton, *The impact resistance of composite materials - a review*. *Composites*, 1991. **22**(5): p. 347-362.
92. Liu, D., B.B. Raju, and X. Dang, *Size Effects on Impact Response of Composite Laminates*. *International Journal of Impact Engineering*, 1998. **21**(10): p. 837-854.
93. Corum, J.M., R.L. Battiste, and M.B. Ruggles-Wrenn, *Low-Energy Impact Effects on Candidate Automotive Structural Composites*. *Composites Science and Technology*, 2003. **63**: p. 755-769.
94. Naik, N.K. and S. Meduri, *Polymer-Matrix Composites Subjected to Low-Velocity Impact: Effect of Laminate Configuration*. *Composites Science and Technology*, 2001. **61**: p. 1429-1436.
95. Naik, N.K., R. Ramasimha, H. Arya, S.V. Prabhu, and N. ShamaRao, *Impact Response and Damage Tolerance Characteristics of Glass-Carbon/Epoxy Hybrid Composite Plates*. *Composites Part B*, 2001. **32**: p. 565-574.
96. Brewer, J.C. and P.A. Lagace, *Quadratic Stress Criterion for Initiation of Delamination*. *Journal of Composite Materials*, 1988. **22**: p. 1141-1155.
97. Karbhari, V.M., J.E. Haller, P.K. Falzon, and I. Herszberg, *Post-Impact crush of hybrid braided composite tubes*. *International Journal of Impact Engineering*, 1999. **22**: p. 419-433.

98. Warrior, N.A., K.J. Bottome, M. Ribeaux, and D.A. Bailey. *The Effects of Pre-Existing Damage on the Energy Absorption of Braided and Non-Crimp Fabric Composite Tubes*. in *ICrash 2004*. 2004. San Francisco, CA, USA.
99. Warrior, N.A. and M. Ribeaux, *Effect of Damage on the Energy Absorption of Prismatic Thin-Walled Polymer Composite Structures*. Key Engineering Materials, 2002.
100. Cunningham, P.R., J.M. Dulieu-Barton, A.G. Dutton, and R.A. Shenoi, *The Effect of Ply Lay-up upon the Thermoelastic Response of Laminated Composites*. Key Engineering Materials, 2002. **221-222**: p. 325-336.
101. Clarke, M.P. and M.J. Pavier, *Artificial damage techniques for low velocity impact in carbon fibre composites*. Composite Structures, 1993. **25**: p. 113-120.
102. Olsson, R., J. Iwarsson, L.G. Melin, A. Sjogren, and J. Solti, *Experiments and Analysis of Laminates with Artificial Damage*. Composites Science and Technology, 2003. **63**: p. 199-209.
103. Swanson, S.R., *Scaling of Impact Damage in Fiber Composites from Laboratory Specimens to Structures*. Composite Structures, 1993. **25**: p. 249-255.
104. Edgren, F., D. Mattsson, E.A. Leif, and J. Varna, *Formation of Damage and its Effects on Non-Crimp Fabric Reinforced Composites Loaded in Tension*. Composites Science and Technology, 2004. **64**: p. 675-692.
105. Xiaoping, H., H. Shenliang, and Y. Liang, *A Study On Dynamic Fracture Toughness of Composite Laminates at Different Temperatures*. Composites Science and Technology, 2003. **63**: p. 155-159.
106. Falzon, P.J. and I. Herzberg. *Prediction of the Compression-After\_Impact Strength of 2-D Braided Composites*. in *ICCM-11*. 1997. Gold Coast, Australia.
107. Khondker, O.A., I. Herszberg, and H. Hamada, *Measurements and Prediction of the Compression-After-Impact Strength of Glass Knitted Textile Composites*. Composites Part A, 2003. **35**: p. 145-157.
108. Walker, L., M.S. Sohn, and H. Xiao-Zhi, *Improving Impact Resistance of Carbon-Fibre Composites through Interlaminar Reinforcement*. Composites Part A, 2002. **33**: p. 893-902.
109. Masters, J.E., *Improved Impact and Delamination Resistance Through Interleafing*. Key Engineering Materials, 1989. **37**: p. 317-348.
110. Larsson, F., *Damage Tolerance of a Stitched Carbon/Epoxy Laminate*. Composites Part A, 1997. **28A**: p. 923-934.
111. Warrior, N.A., T.A. Turner, F. Robitaille, and C.D. Rudd, *The Effect of Interlaminar Toughening Strategies on the Energy Absorption of Composite Tubes*. Composites Part A, 2004. **35**: p. 431-437.
112. Zhong, W. and B.Z. Jang, *Material Design Approaches for Improving Impact Resistance of Composites*. Key Engineering Materials, 1998. **141-143**: p. 169-186.
113. Kim, J.-K., *Methods for Improving Impact Damage Resistance of CFRPs*. Key Engineering Materials, 1998. **141-143**: p. 149-168.
114. Tang, G., Y. Yan, X. Chen, J. Zhang, B. Xu, and Z. Feng, *Dynamic Damage and fracture mechanism of three-dimensional braided carbon fiber/epoxy resin composites*. Materials and Design, 2000. **22**: p. 21-25.
115. Findik, F. and N. Tarim, *Ballistic Impact Efficiency of Polymer Composites*. Composite Structures, 2003. **61**: p. 187-192.
116. Ulven, C., U.K. Vaidya, and M.V. Hosur, *Effect of Projectile Shape During Ballistic Perforation of VARTM Carbon/Epoxy Composite Panels*. Composite Structures, 2003. **61**: p. 143-150.

117. Savage, G., I. Bomphray, and M. Oxley, *Exploiting the Fracture Properties of Carbon Fibre Composites to Design Lightweight Energy Absorbing Structures*. Engineering Failure Analysis, 2004. **11**: p. 677-694.
118. Naik, N.K. and P. Shirirao, *Composite Structures Under Ballistic Impact*. Composite Structures, 2004. **66**: p. 579-590.
119. Hosur, M.V., J. Alexander, U.K. Vaidya, and S. Jeelani, *High strain rate compressive response of Carbon/Epoxy laminate composites*. Composite Structures, 2001. **52**: p. 405-417.
120. Hosur, M.V., M. Adya, U.K. Vaidya, A. Mayer, and S. Jeelani, *Effect of Stitching and Weave Architecture on the High Strain Rate Compression Response of Affordable Woven Carbon/Epoxy Composites*. Composite Structures, 2003. **59**: p. 507-523.
121. Akil, O., U. Yildirim, M. Guden, and I.W. Hall, *Effect of strain rate on the compression behaviour of a woven fabric S2-glass fiber reinforced vinyl ester composite*. Polymer Testing, 2003.
122. Ochola, R.O., K. Marcus, G.N. Nurick, and T. Franz, *Mechanical Behaviour of Glass and Carbon Fibre Reinforced Composites at Varying Strain Rates*. Composite Structures, 2004. **63**: p. 455-467.
123. Fernie, R. and N.A. Warrior, *Impact test rigs for high strain rate tensile and compressive testing of composite materials*. Strain, 2002. **38**(2): p. 69-73.
124. Khan, M.Z.S., G. Simpson, and C.R. Townshend, *A Comparison of the Mechanical Properties in Compression of Two Resin Systems*. Materials Letters, 2002. **52**: p. 173-179.
125. Hamada, H. *Can braided composites be used for crushing elements in cars?* in *The 11th ICCM, Gold Coast, Australia*. 1997.
126. Hamada, H., N. Nakatani, A. Nakai, and K. Kameo, *The Crushing Performance of a Braided I-Beam*. Composites Science and Technology, 1999. **59**: p. 1881-1890.
127. McCarthy, M.A. and J.F.M. Wiggeraad, *Numerical Investigation of a Crash Test of a Composite Helicopter Subfloor Structure*. Composite Structures, 2001. **51**: p. 345-359.
128. Deletombe, E., D. Delsart, D. Kohlgruber, and A.F. Johnson, *Improvement of Numerical Methods for Crash Analysis in Future Composite Aircraft Design*. Aerospace Science and Technology, 1999. **4**: p. 189-199.
129. Drechsler, K. *Advanced Composites: The Balance Between Performance and Cost*. in *24th International SAMPE Europe Conference*. 2003. Paris.
130. Browne, A.L. and S.A. Iobst, *Dynamic Axial Crush of Automotive Rail-Sized Composite Tubes Part 1: Tubes with Woven Reinforcements and Non-Plug Crush Initiators*.
131. Zealand, A.M.N., *Vanquish-composites*. 2003.
132. Farley, G., *The Effects of Crushing Speed on the Energy-Absorption Capability of Composite Tubes*. Journal of Composite Materials, 1991. **25**: p. 1314-1329.
133. Boeman, R.G. and A. Caliskan, *A Novel Capability for Crush Testing Crash Energy Management Structures at Intermediate Rates*. Society of Automotive Engineers, Inc, 2002.
134. Curtis, C.D., *Energy Absorption and Crush Behaviour of Composite Tubes*, in *School of Mechanical, Materials, Manufacturing Engineering and Management*. 2000, University of Nottingham, UK: Nottingham.
135. Duckett, M.J., *The Effect of Loading Rate on the Crush Zone Morphology of Composite Tubes*, in *School of Mechanical, Materials, Manufacturing Engineering and Management*. 2002, University of Nottingham: Nottingham.
136. Corden, T., *Development of Design and Manufacturing Techniques for Glass Reinforced Plastic Waste Water Treatment Equipment*, in *School of Mechanical,*

- Materials, Manufacturing Engineering and Management*. 1996, University of Nottingham, UK: Nottingham.
137. McMillan, A.R., *Environmental Degradation of Glass Reinforced Polyesters in the Wastewater Treatment Industry*, in *School of Mechanical, Materials, Manufacturing Engineering and Management*. 1997, University of Nottingham, UK: Nottingham.
  138. Warrior, N.A., M. Ribeaux, and D.A. Bailey. *Effect of Stress Concentrations on The Energy Absorption of Thin-Walled Random Composite Tubes*. in *Third International Conference of Thin Walled Structures*. 2003. UK.
  139. Warrior, N.A. and M. Ribeaux. *Effect of Impact Damage on the Specific Energy Absorption of Glass/Polyester*. in *American Society for Composites 17th Technical Conference*. 2002. Purdue University, Indiana, USA.
  140. Ribeaux, M. and N.A. Warrior. *Effect of Damage on the Energy Absorption of Prismatic Thin-walled Polymer Composite Structures*. in *DAMAS 2003*. 2003. University of Southampton.
  141. Santulli, C., J.M. Dulieu-Barton, and W.J. Cantwell. *Thermoelastic Investigation of Impact Damaged Woven GRP Composites*. in *4th International Conference on Modern Practices in Stress and Vibration Analysis*. 2000. Nottingham.
  142. Toubal, L., M. Karama, and B. Lorrain, *Stress Concentration in a Circular Hole in a Composite Plate*. *Composite Structures*, 2004.
  143. Young, W.C., *Roark's Formulas for Stress and Strain*. 7th ed: McGraw-Hill. p372.
  144. Kaw, A.K., *Mechanics of Composite Materials*. 1997, CRC Press: Florida. p. 154-185.
  145. Turner, T.A., *The Effects of Processing Variables on the Energy Absorption of Composite Crash Structures*, in *School of Mechanical, Materials and Manufacturing Engineering*. 2004, University of Nottingham: Nottingham.
  146. Sohn, M.S., X.Z. Hu, J.K. Kim, and L. Walker, *Impact damage characterisation of carbon fibre/epoxy composites with multi-layer reinforcement*. *Composites Part B*, 2000. **31**: p. 681-691.
  147. Daniel, I.M., I. Shareef, A.A. Aliyu, and A. Abdu. *Rate effects on delamination fracture toughness of a toughened graphite/epoxy*. in *Toughened Composites*. 1987. Houston, TX, USA: ASTM Special Technical Publication.
  148. Browne, A., N. Johnson, D. Houston, and L. Lalik. *Automotive Composites Consortium Generic Tube Crush Program: Processing and Molding Effects on the Axial Crush of RTM and SRIM Tubes*. in *SAMPE-ACCE-DOE Advanced Composites Conference*. 1999.
  149. Zywicz, E. and T. Nguyen, *On the Flexural and Extensional Behaviour of a Large-Tow Triaxial Braided Composite*. *Composites Science and Technology*, 2000. **60**: p. 2989-2999.
  150. Hamada, H., K. Kameo, M. Sakaguchi, H. Saito, and M. Iwamoto, *Energy Absorption Properties of Braided Composite Rods*. *Composites Science and Technology*, 2000. **60**: p. 723-729.
  151. Michaeli, W. and D. Jurss, *Thermoplastic pull-braiding: pultrusion of profiles with braided fibre lay-up and thermoplastic matrix system (PP)*. *Composites Part A*, 1996. **27A**(1): p. 3-7.
  152. Kuo, W.-S. and H.-I. Chen, *Fabrication and Microgeometry of Two-Step Braided Composites Incorporating Pultruded Rods*. *Composites Science and Technology*, 1997. **57**: p. 1457-1467.
  153. Nakai, A., M. Masui, and H. Hamada. *Fabrication of Large Scale Braided Composite with I-Shaped Structure*. in *ICCM-11*. 1997. Gold Coast, Australia.

154. Tada, M., T. Uozumi, A. Nakai, and H. Hamada, *Structure and Machine Braiding Procedure of Coupled Square Braids with Various Cross Sections*. Composites Part A, 2001. **32**: p. 1485-1489.
155. Grenville-Jones, K., *FEA Analysis upon Holes in Composite Cylinders*. 2004, University Of Nottingham.

## Appendix

### Appendix 1: Braided Composite Manufacturing

Problems still exist with the manufacture of braided composites. The maximum size of preform depends on the size of the braiding machine, and for large structures such as aircraft components, these are very large, complex and expensive. The machines themselves require long set-up times, and production runs are short due to the small size of the spools.

The method of manufacturing the tubes also affects the tube quality. Braided tubes require a form of shaped inner mandrel to braid upon. The quality of tube was found to increase, by Browne et al [148], using steel rather than foam cores.

For large composites for use in automotive applications, there is a reduction in fibre cost with increasing tow size. When used in conjunction with automated braiding machines and efficient moulding techniques the material becomes more economically feasible. However in order to meet the same thickness criteria, the laminates must have fewer laminae. This could cause problems with delamination effects[149]

A further method of manufacturing rods and tubes is the pultrusion process described by Hamada et al[150]. The system consists of a resin impregnator, braider, heated die, puller and cutter. The fibres are pulled through and impregnated with resin. They are then tightly woven into the preform shape and cured. Few voids are formed, and a high fibre volume fraction can be achieved. The process produces parts continuously and automatically and, they claim, cheaply.

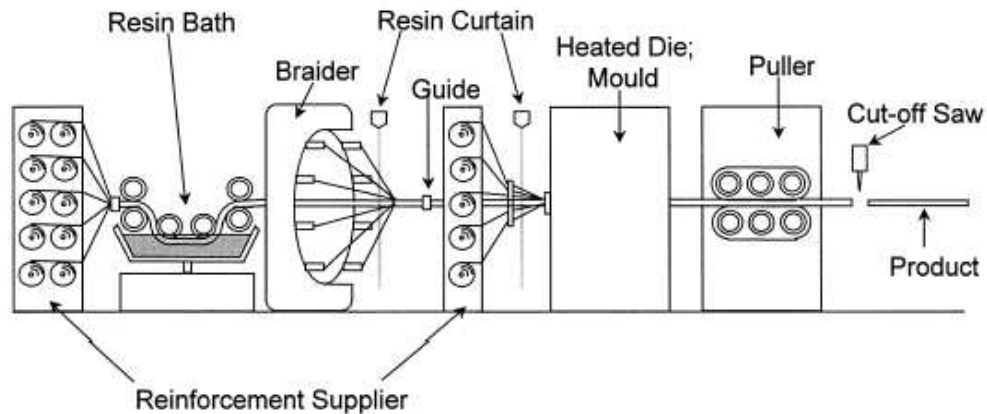


**Figure 126: Schematic drawing of the braiding pultrusion system.[150]**

This system has also been investigated for producing rods, and more recently thermoplastics.[151](see Figure 126). In this application, a sheath of thermoplastic matrix material, which protects the fibres from mechanical damage, covers the dry hybrid fibre used. The main source of the wear on the fibres comes from the braiding process; damage to the fibres occurs due to mechanical friction in the bobbins and rolls. For pressure tubes or pipe applications, the braiding angle is set to  $53^\circ$ . The fibre angle is set by the ratio of the rotation speed of the bobbins and the pull speed through the system, as well as the diameter of the core.

Kuo and Chen[152] suggested an innovative way of improving the braiding or preforms, by introducing pultruded rods as axial reinforcements. The advantages of this process are: crimp in the axial and braid in the interior of the composite is almost eliminated, the fabric is more consistent, the fabrics are rigid and there is increased resin infiltration in RTM moulding. They note that the rods must be stiff in order to resist distortion in the fabric interior, but flexible enough to allow the yarn carriers to travel between them. They suggest that smaller rods are preferable as long as they meet the minimum required rigidity. However, they note a few limitations; bending of the rods is required in braiding, so large rods cannot be used reducing the practicality of this process. They also say non prismatic parts are impossible to produce with this set-up. Although the orientation allows for favourable features regarding resin infiltration, resin pockets may appear that are weak in resisting cracks and damage. The drawbacks here suggest that this process has too many limitations for mainstream application.

Furthermore complicated braid structures have been investigated by Nakai et al[153] and Tada et al [154]. They note that a large braiding machine is required which will be ineffective for braiding small composite parts.

## **Appendix 2: Predicted In-Plane Axial and Transverse Tensile Stiffness of $\pm 45^\circ$ Braided Carbon/Vinyl Ester Using Rule of Mixtures and Laminate Theory.**

In order to establish the quality of samples produced by the braiding and moulding process a theoretical calculation was chosen to enable a comparison to be made.

### **Assumptions:**

- Fibres are straight containing no kinks
- Laminate is made up of separate layers containing unidirectional fibres not intertwined braided layers
- There are no fibres in the on axis direction

### **Data:**

Laminate properties:

$V_f$	= Fibre Volume Fraction	= 27.64%
$T$	= Laminate Thickness	= 4mm
$\theta$	= Braid Angle	= $50^\circ$

Fibre properties:

$E_{1f}$	= Axial Modulus	= 240GPa
$E_{2f}$	= Transverse Modulus	= 8.2GPa
$G_f$	= Shear Modulus	= 4.8GPa
$\nu_f$	= Poisson's Ratio	= 0.3

Matrix properties:

$$E_m = \text{Elastic Modulus} = 4.6\text{GPa}$$

$$\nu_m = \text{Poisson's Ratio} = 0.35$$

$$G_m = \text{Shear Modulus} = \frac{E_m}{2(1+\nu_m)} = 1.7\text{GPa}$$

### Calculation:

As fibre tows are all the same size, therefore the thickness of each layer does not need to be calculated

Now calculate lamina properties based on the Rule of Mixtures:

$$\begin{aligned} E_{11} &= E_f V_f + E_m (1 - V_f) = (240 \times 10^9 \times 0.2764) + [4.6 \times 10^9 \times (1 - 0.2764)] \\ &= 66.336 \times 10^9 + 3.33 \times 10^9 = \mathbf{69.66\text{Gpa}} \end{aligned}$$

$$E_{22} = \left[ \frac{V_f}{E_f} + \frac{(1 - V_f)}{E_m} \right]^{-1} = \left[ \frac{0.2764}{8.2 \times 10^9} + \frac{(1 - 0.2764)}{4.6 \times 10^9} \right]^{-1} = \mathbf{5.24\text{Gpa}}$$

$$G_{12} = \left[ \frac{V_f}{G_f} + \frac{(1 - V_f)}{G_m} \right]^{-1} = \left[ \frac{0.2764}{4.8 \times 10^9} + \frac{(1 - 0.2764)}{3.1 \times 10^9} \right]^{-1} = \mathbf{2.07\text{Gpa}}$$

$$\nu_{12} = V_f \nu_f + \nu_m (1 - V_f) = 0.2764 \times 0.3 + (1 - 0.2764) \times 0.35 = \mathbf{0.336}$$

$$\nu_{21} = \frac{E_{22} \nu_{12}}{E_{11}} = \frac{(5.24 \times 10^9 \times 0.336)}{69.66 \times 10^9} = \mathbf{0.0253}$$

Using the Laminate Theory's stiffness matrix:

$$\begin{Bmatrix} \sigma_1 \\ \sigma_2 \\ \sigma_3 \end{Bmatrix} = \begin{bmatrix} \bar{C}_{11} & \bar{C}_{12} & \bar{C}_{16} \\ \bar{C}_{12} & \bar{C}_{22} & \bar{C}_{26} \\ \bar{C}_{16} & \bar{C}_{26} & \bar{C}_{66} \end{bmatrix} \begin{Bmatrix} \epsilon_1 \\ \epsilon_2 \\ \epsilon_3 \end{Bmatrix}$$

For the lamina containing axial fibres (although there are no axial fibres these values are required to calculate the off axis values)

$$\bar{C}_{11} = \frac{E_{11}}{1 - \frac{\nu_{21}}{\nu_{12}}} = \mathbf{70.26GPa} \quad \bar{C}_{66} = G_{12} = \mathbf{2.07GPa}$$

$$\bar{C}_{22} = \frac{E_{22}}{1 - \frac{\nu_{21}}{\nu_{12}}} = \mathbf{5.28GPa} \quad \bar{C}_{61} = \mathbf{0}$$

$$\bar{C}_{12} = \frac{\nu_{21}E_{11}}{1 - \frac{\nu_{21}}{\nu_{12}}} = \mathbf{1.78GPa} \quad \bar{C}_{62} = \mathbf{0}$$

For the laminae containing the off-axis ( $\theta = 50^\circ$ ) fibres

$$OffC_{11} = C_{11} \cos^4 \vartheta + [2(C_{12} + 2C_{66}) \sin^2 \vartheta \cos^2 \vartheta] + C_{22} \sin^4 \vartheta = \mathbf{16.7Gpa}$$

$$OffC_{12} = (C_{11} + C_{22} - 4C_{66}) \cos^2 \vartheta \sin^2 \vartheta + C_{12} (\cos^4 \vartheta \sin^4 \vartheta) = \mathbf{28.0Gpa}$$

$$OffC_{22} = C_{11} \sin^4 \vartheta + [2(C_{12} + 2C_{66}) \sin^2 \vartheta \cos^2 \vartheta] + C_{22} \cos^4 \vartheta = \mathbf{17.2Gpa}$$

$$OffC_{66} = (C_{11} + C_{22} - 2C_{12} - 2C_{66}) \sin^2 \vartheta \cos^2 \vartheta + C_{66} (\sin^4 \vartheta + \cos^4 \vartheta) = \mathbf{17.5GPa}$$

$$OffC_{16} = (C_{11} - C_{22} - 2C_{66}) \sin \vartheta \cos^3 \vartheta + (C_{12} - C_{22} + 2C_{66}) (\sin^3 \vartheta \cos \vartheta) = \mathbf{14.3GPa}$$

$$OffC_{26} = (C_{11} - C_{22} - 2C_{66}) \cos \vartheta \sin^3 \vartheta + (C_{12} - C_{22} + 2C_{66}) (\cos^3 \vartheta \sin \vartheta) = \mathbf{18.7GPa}$$

Adding the contributions from the different laminae gives:

$$A_{11} = \text{Off}C_{11}T = 16.67 \times 4 = \mathbf{66.74 \times 10^6}$$

$$A_{22} = \text{Off}C_{22}T = 27.97 \times 4 = \mathbf{111.87 \times 10^6}$$

$$A_{12} = \text{Off}C_{12}T = 17.22 \times 4 = \mathbf{68.88 \times 10^6}$$

$$A_{66} = \text{Off}C_{66}T = 17.52 \times 4 = \mathbf{70.07 \times 10^6}$$

$$A_{61} = \text{Off}C_{61}T = 14.32 \times 4 = \mathbf{57.15 \times 10^6}$$

$$A_{62} = \text{Off}C_{62}T = 18.72 \times 4 = \mathbf{74.89 \times 10^6}$$

Therefore:

Axial stiffness of Specimen

$$E_{11} = \frac{A_{11}A_{22} - A_{12}^2}{A_{22}t} = \mathbf{\underline{6.08 \text{ GPa}}}$$

Transverse stiffness of Specimen

$$E_{22} = \frac{A_{11}A_{22} - A_{12}^2}{A_{11}t} = \mathbf{\underline{10.2 \text{ GPa}}}$$

The experimental value of axial stiffness obtained varies from 5.8 to 6.2 GPa depending on the exact point used to calculate the value of E from the stress/strain curve (Figure 127). This is a minimum of 17.4% decrease over the theoretical specimens.

Therefore the experimental and the theoretical values agree the theoretical lies, mid way between the upper and lower possible values taken from the graph.

This suggests that the samples produced are of suitable quality.

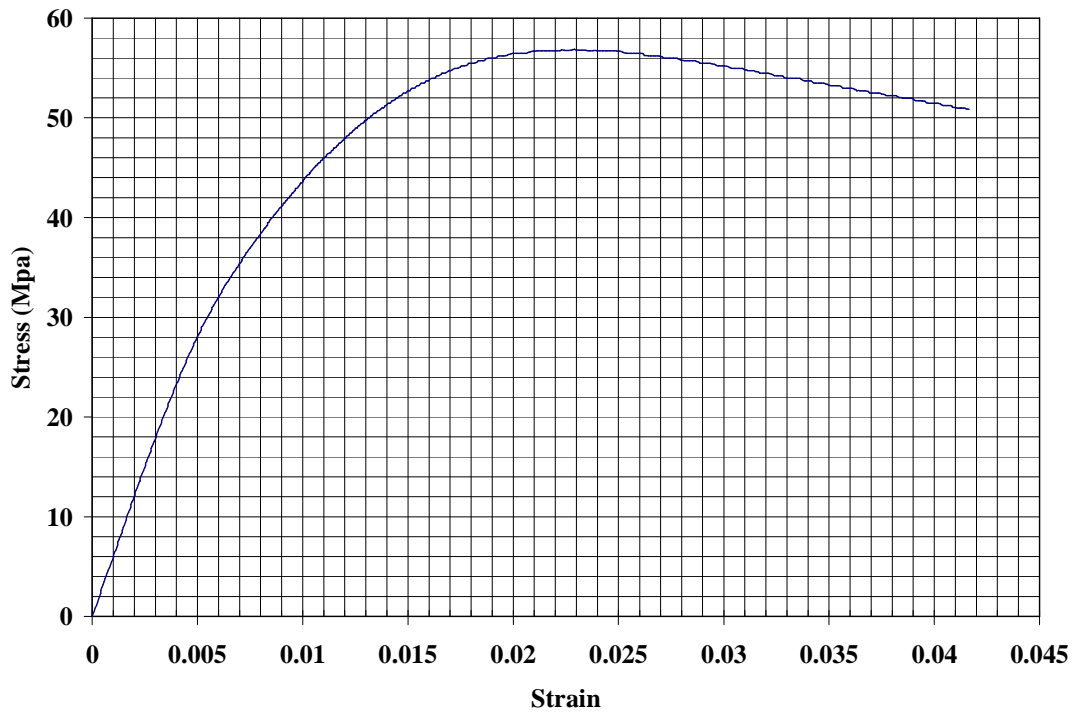


**Figure 127 Stress/Strain Curve for Biaxial  $\pm 45$  Carbon/Vinyl-ester Tensile Sample**

**References:**

Hull D. and Clyne T.W, “*An Introduction to Composite Materials, Second Edition*”, Cambridge Solid State Science Services, Cambridge 1996

Gibson R.F, “*Principles of Composite Material Mechanics*”, McGraw Hill, London 1994

Duckett M J, PhD Thesis “*Rate Dependent Effects on the Energy Absorption*

And Material Properties of Polymer Composites” University of Nottingham 2001

### Appendix 3 Theoretical Work – Stress Concentrations

As described earlier the equations described in Wu and Mu [81] based upon Lekkerkerker's work can be applied to the samples under study here as long as the following conditions are met.

Firstly, they state that  $\frac{d}{D} \ll \sqrt{\frac{2t}{D}}$  must be met.

In our case for a 5mm hole  $\frac{d}{D} = \frac{5}{38} = 0.132$

and  $\sqrt{\frac{2t}{D}} = \sqrt{\frac{2 \cdot 2}{38}} = 0.324$

so the criteria is met, however, for a 10mm hole  $\frac{d}{D} = \frac{10}{38} = 0.263$  this is possibly still within the bounds acceptable under their criteria, however, a 16mm hole (0.421) is not.

Using Equation (33)

$$K_{T,i,c,u}^{\infty,1} = 3 + \sqrt{\frac{3(m^2 - 1)}{m^2} \cdot \frac{\pi}{8} \cdot \frac{d^2}{Dt}} \quad (42)$$

(Where  $m = \frac{1}{\nu}$  where  $\nu$  is Poisson's ratio, and is equal to 0.3 for these materials [7])

**Table 34 Values Used in Calculation**

Symbol	Value
d (diameter of hole)	5mm
D (diameter of tube)	38mm
t (thickness of tube)	2mm
m	3.33

The stress concentration factors can be calculated using values from Table 34 and presented in Table 35.

**Table 35 Stress Concentration Factors for Isotropic Cylinder**

Hole size	$K^1$
5mm	3.21
10mm	3.85
16mm	5.19

If it is proposed that, the crushing stress multiplied by the stress concentration factor gives us a maximum value of stress, and if this is compared to the UCS then if it is greater the tube will fail globally, or if it is less the tube will crush progressively.

**Equation 1 Mode 2 failure Criteria**

$$\sigma_c * K^1 > UCS \quad (15)$$

Where  $\sigma_c$  is crushing stress and UCS is measured experimentally.

Using the data presented earlier in Table 18 with equation 15 the data in Table 36 is produced.

**Table 36 Failure Criteria Data**

Material Type	Hole size	$K^1$	$\sigma_c$ MPa	$\sigma_c * K^1$ MPa	UCS MPa
NCF 0-90	5mm	3.21	62.8	201.59	139.1
CoFRM (QS)	5mm	3.21	106.1	340.58	174.9
CoFRM (Dyn)	5mm	3.21	88.42	283.83	234

For the NCF 0-90 tubes,  $\sigma_C * K^1$  is approximately 1.5 times the size of the measured value. If the numbers and theory are correct then they indicate that the sample will fail globally. From our experimental testing we know that this type of tube with a 5mm holes crushes progressively under quasi-static conditions. For the CoFRM samples, the numbers again suggest that the sample will fail globally under quasi-static testing. The results presented show that there was global failure reported in one sample at this level. Dynamically, the UCS is still smaller than the calculated figure suggesting the sample will fail globally. The test results show that these sample crushes progressively under dynamic conditions, thus this suggests that these using calculations cause a conservative value for the stress concentration factor to be produced.

Quinn and Barton [80] have also suggested that many analytical methods are too conservative in their estimation of stress concentration factor, because for small d/D ratios the curvature does not play a significant role.

The next criticism that could be applied is that the tubes are not all isotropic. If the data was for a metallic tube then this equation could be used with greater accuracy. The composite NCF samples are orthotropic. The different in-plane properties of the samples will affect the stress concentration factor.

For an infinite orthotropic plate Wu and Mu propose the SCF to be

$$K_{T,o,p,u}^{\infty,1} = 1 + \sqrt{2 \left( \sqrt{\frac{E_y}{E_x} - \nu_{yx} + \frac{E_y}{2G_{yx}}} \right)} \quad (43)$$

Where  $E_x$  and  $E_y$  are Young's modulus in x and y directions and  $G_{yx}$  is shear modulus in x-y plane.

They then propose to multiply the SCF of the finite isotropic plate by ratio of the cylindrical isotropic SCF to the plate Isotropic SCF to account for the cylindrical effect, and then by the ratio of the orthotropic to isotropic plate values to account for the isotropic effect. This has the effect of increasing the overall SCF not reducing it.

**Equation 2 Formula for Stress Concentration factors about a hole from Roark [143]**

$$K_t = C_1 + C_2 \cdot \left( \frac{d}{D+2t} \right) + C_3 \cdot \left( \frac{d}{D+2t} \right)^2 + C_4 \cdot \left( \frac{d}{D+2t} \right)^3 \quad (44)$$

Valid for  $\frac{D}{D+2t} \leq 0.9$  and  $\frac{d}{D+2t} \leq 0.45$  (45)

And where:

$$C_1 = 3 \quad (46)$$

$$C_2 = 2.773 + 1.529 \cdot \left( \frac{D}{D+2t} \right) - 4.379 \cdot \left( \frac{D}{D+2t} \right)^2 \quad (47)$$

$$C_3 = -0.421 - 12.782 \cdot \left( \frac{D}{D+2t} \right) + 22.781 \cdot \left( \frac{D}{D+2t} \right)^2 \quad (48)$$

$$C_4 = 16.841 + 16.67 \cdot \left( \frac{D}{D+2t} \right) - 40.007 \cdot \left( \frac{D}{D+2t} \right)^2 \quad (49)$$

In this case the first criterion is not met as  $\frac{D}{D+2t} = 0.905$  thus is just slightly over the boundary. The second criterion is met for all values of  $d$  under test.

For any hole,  $C_1 = 3$ ,  $C_2 = 0.572$ ,  $C_3 = 6.663$ ,  $C_4 = -0.826$

Applying to the holes sizes used in this study:

For the 5mm hole  $K_t = 3.16$ , for a 10mm hole  $K_t = 3.50$  and for a 16mm hole  $K_t = 4.14$

These values show a reduction in SCF over the values produced by Savin's equation ((4)). These are still too high to produce results from the proposed equation that agree with the experimental observations.

FEA analysis, by Katherine Grenville-Jones at The University of Nottingham [155] upon a thin walled cylinder of Diameter 203.2mm, height 508mm and thickness 10.16mm was

undertaken with holes of diameter 7.62, 30.48, 76.2, and 127mm. The analysis was based upon Linear Elastic Analysis and the mesh used small elements around the hole and larger square elements away from the hole. The following values of SCF were calculated (Table 37)

**Table 37 SCF Values from FEA**

d/D	K <sup>I</sup>
0.038	2.938
0.150	3.292
0.375	3.870
0.625	4.375

These values can be plotted and a comparison between the previous theoretical equations can be shown.

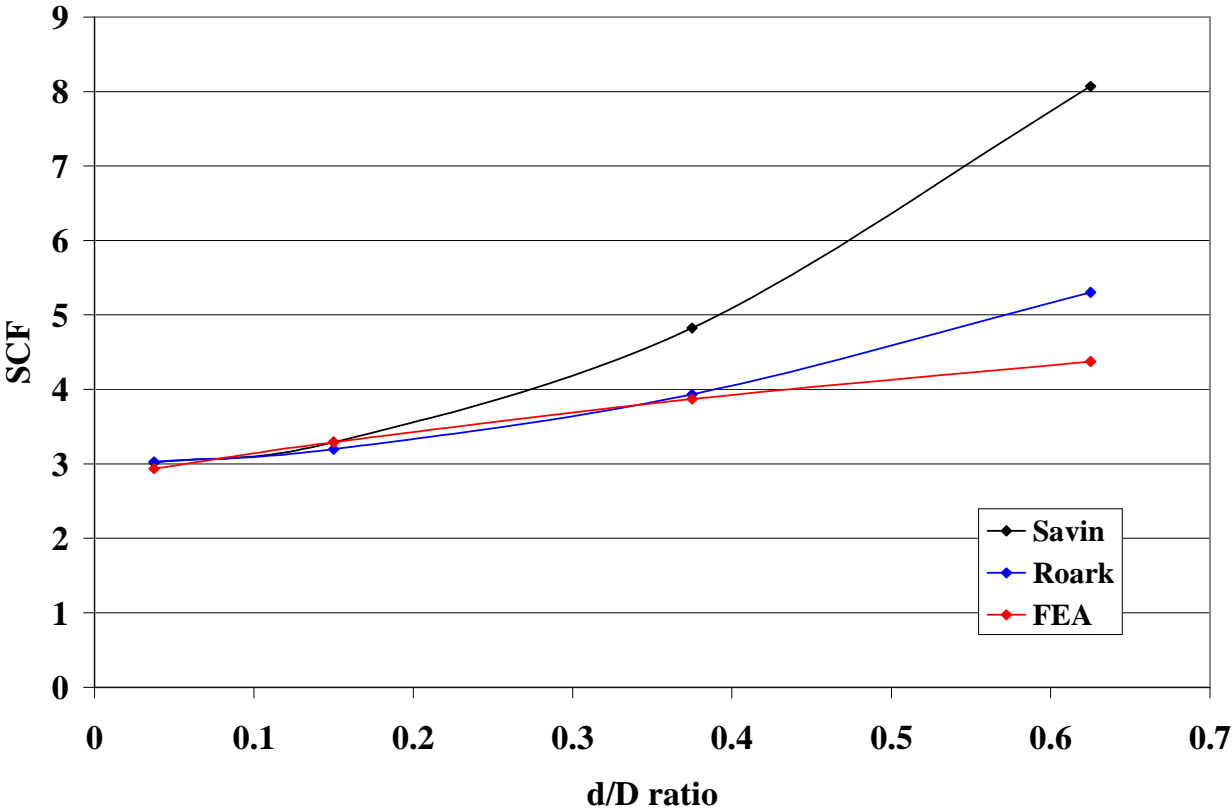


**Figure 128 Comparison of Theoretical Values**

At low values of  $d/D$  all 3 methods give a similar value for SCF, however, at  $d/D > 2$  they begin to diverge with the numbers produced from Savin's equation deviating the most. However, the FEA data still is based upon an isotropic cylinder thus its application can only be used as a guide.

Both Toubal et al [142] and Kaltakci's [83] results suggest that stress concentration factors are highly dependant on fibre angle. Noting that when the loading is parallel to the fibre orientation angles the stress concentrations are at a maximum, they also conclude that the maximum stress concentration and its location are not dependant on the stress which causes failure. Kaltacki used the Tsai-Hill failure criteria and Hencky-Von Mises distortion energy theory to gain an analytical value for stress concentrations. They were in the range of 2.24 for  $90^\circ$  to a maximum of 2.48 for  $0^\circ$  fibres, to compare with his FEA results, which gave SCFs in a range of 2.73 to 4 for fibre angles from 0 to  $90^\circ$ .

This suggests that for the tubes in this study the stress concentration will vary considerably and is highly dependant upon fibre architecture. Thus the NCF 0-90 tube will have a different SCF to an NCF 90-0 tube and an NCF  $\pm 45$  tube, suggesting a possible cause for the different threshold damage levels seen in the specimens.

Looking at Quinn and Barton's results [80] for a cylinder in tension with a  $d/D = 0.125$  they measure the SCF to be 2.22. This value is comparable to the 5mm hole ( $d/D = 0.132$ ). Interestingly they show a variation between compressive and tensile values for SCF values at the cylinder surface. For a cylinder with 2 holes drilled on opposite sides of the sample in tension the SCF is 2.35, in compression they record a decrease in SCF to 2.14. The value of 2.22 is for a cylinder in tension.